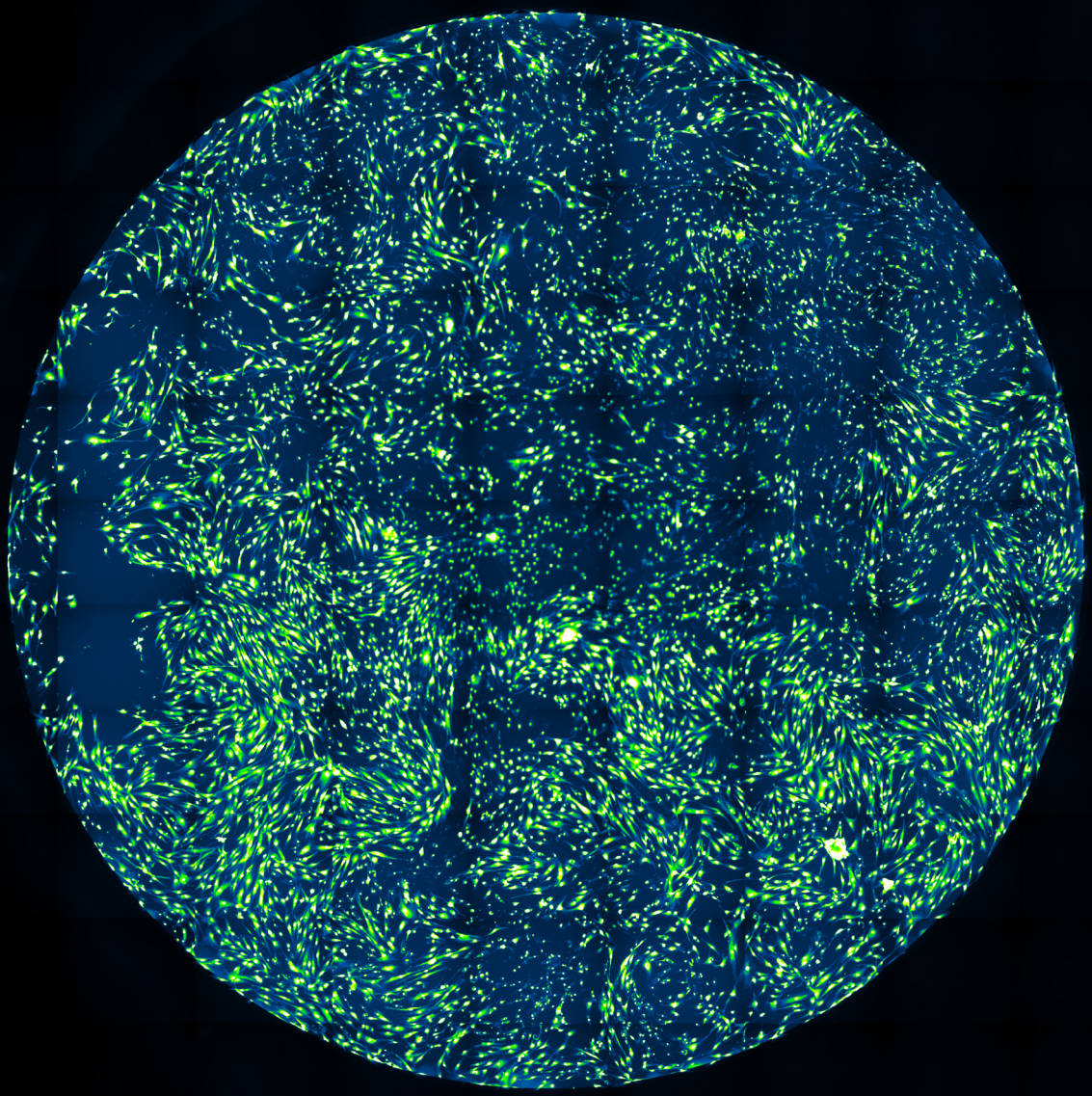
Cell-phenotypic profiling of mitochondrial dysfunction for target discovery and drug testing



Eligio Francesco Iannetti

Cell-phenotypic profiling of mitochondrial dysfunction for target discovery and drug testing

---

Proefschrift

ter verkrijging van de graad van doctor
aan de Radboud Universiteit Nijmegen,
op gezag van de rector magnificus prof. dr. J.H.J.M. van Krieken,
volgens besluit van het college van decanen
in het openbaar te verdedigen op vrijdag 26 juni 2020
om 15:30 uur precies

door
Eligio Francesco Iannetti
geboren op 23 Maart 1987
te Teramo, Italië

Promotor	Prof. dr. J.A.M. Smeitink
Copromotoren	Dr. W.J.H. Koopman
	Dr. J. D. Beyrath
Manuscriptcommissie	Prof. dr. P.H.A. Friedl
	Prof. dr. ir. J.H.L.M. van Bokhoven
	Dr. W. de Vos (Universiteit van Antwerpen, België)
Paranimfen	Sarah Foriel
	Renaud Vatrinet
	Jurre Floors

Cell-phenotypic profiling of mitochondrial dysfunction for target discovery and drug testing

---

Doctoral Thesis

to obtain the degree of doctor
from Radboud University Nijmegen
on the authority of the Rector Magnificus prof. dr. J.H.J.M. van Krieken,
according to the decision of the Council of Deans
to be defended in public on Friday, June 26, 2020
at 15:30 hours

by
Eligio Francesco Iannetti
born on March 23, 1987
in Teramo, Italy

Supervisor	Prof. dr. J.A.M. Smeitink
Co-supervisor	Dr. W.J.H. Koopman
	Dr. J. D. Beyrath
Manuscript committee	Prof. dr. P.H.A. Friedl
	Prof. dr. ir. J.H.L.M. van Bokhoven
	Dr. W. de Vos (University of Antwerp, Belgium)
Paranymphs	Sarah Foriel
	Renaud Vatrinet
	Jurre Floors

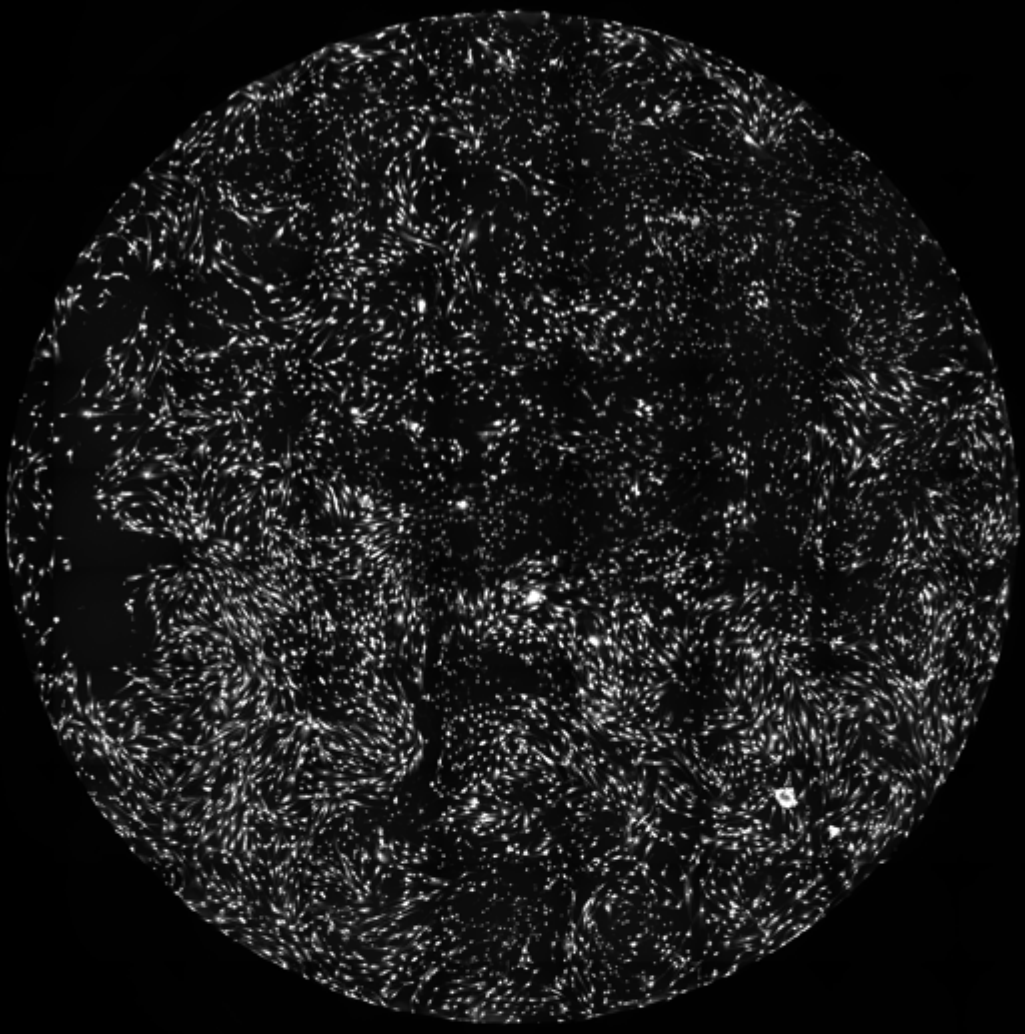
The research presented in this thesis was carried out at Khondrion BV, Nijmegen, The Netherlands in collaboration with Departmemt of Biochemistry, Radboud Insitute for Molecular Life Sciences (RIMLS) and Raboud University Medical Center (RadboudUMC), Nijmegen, The Netherlands. Eligio F. Iannetti was funded by Khondrion BV and Marie-Curie Initial Training Networks (ITN) grant 'MEET' (Mitochondrial European Educational Training; FP7-PEOPLE-2012-ITN). Publication of this thesis was financially supported by the RadboudUMC and RIMLS.

Printing:	Proefschriftmaken.nl
ISBN:	978-94-6380-749-4
Layout:	Anna C. Geuzebroek
Cover	Leigh Syndrome patient skin fibroblasts P5175 ("S7", NDUFS7) treated with BSO 30 μM for 14h. Whole well imaging of 96-well plate using 10x objective 10x10 frames using a BD Pathway 855 bioimager and Calcein-AM staining by Eligio F. Iannetti.

© **Eligio F. Iannetti, 2020**
All rights are reserved. No part of this thesis may be reproduced, distributed or transmitted in any form or by any means, electronic or mechanical, including photocopy, recording or otherwise without prior written permission of the author or of the publisher holding the copyright of the published articles.

Table of contents

Chapter 1	General introduction	7
Chapter 2	Live-imaging readouts and cell models for phenotypic profiling of mitochondrial function	19
Chapter 3	Toward high-content screening of mitochondrial morphology and membrane potential in living cells	35
Chapter 4	Multiplexed high-content analysis of mitochondrial morphofunction using live-cell microscopy	45
Chapter 5	Mitochondrial morphofunctional characterization of neuronal HT22 cells in response to SK channel activation in galactose based-medium	95
Chapter 6	Rescue from galactose-induced death of Leigh Syndrome patient cells by pyruvate and NAD^+	105
Chapter 7	Selective death of Complex I-deficient Leigh Syndrome patient skin fibroblasts upon glutathione depletion	145
Chapter 8	Summary, general discussion and future perspectives	169
Chapter 9	Appendix: References, Nederlanse Samenvatting, Acknowledgments, RIMLS PhD Portfolio, Curriculum Vitae	179



Chapter 1
General introduction

In order to highlight the importance of mitochondria in the overall cellular, tissue, organ, and organism homeostasis, it is useful to remind the origin of mitochondria. According to the endosymbiotic theory, mitochondria are directly descending from ancestral bacteria that about one and half billions of years ago existed outside from what today are the eukaryotic cells. Mitochondria ancestors survived the endocytosis by another cell type and became incorporated into the host cytoplasm developing together a highly productive molecular collaboration. The chance and the necessity that induced this successful and long symbiosis, changed the world and made the evolution of almost all the eukaryotic cell types possible. These compose all the tissues and organs of the animal species, including us humans. Since then, by a massive number of slow and incremental evolutionary changes, mitochondria acquired a pivotal role in the generation of cellular energy which earned them the name of the powerhouse of the cells. Besides their prominent role in cellular bioenergetics, they have many other diverse and crucial functionalities operating at the junction of numerous cellular, nuclear and subcellular signaling and metabolic pathways. Considering this extensive involvement of mitochondria in the cellular homeostasis, it is easy to understand their relevance in everyone's daily life. When something in the extremely sophisticated mitochondrial engines does not work or is less efficient, a devastating and heterogeneous set of diseases can develop affecting almost any part of the human body. These can range from rare primary and secondary mitochondrial diseases, but also include more common pathologies such as Alzheimer's, Parkinson's, and Huntington's disease, cardiovascular disease, cancer, diabetes, and epilepsy.

First, in this general introduction, I will give a brief molecular description of mitochondrial morphology and function ("morphofunction"), proceeding with some facts about the clinical manifestations of mitochondrial diseases and in particular of Leigh syndrome and mitochondrial oxidative phosphorylation complex I dysfunction. Hereafter, I will introduce the preclinical work-in-progress strategies to examine "broken" mitochondria. I will mainly focus on the technologies and challenges in drug discovery and the necessity of developing *in vitro* models recapitulating the disease phenotype in a dish.

1.1 Mitochondrial morphofunction: *"The structure without a function is a corpse. . . the function without structure is a ghost."*

Mitochondria, present in virtually all mammalian cells, have a crucial metabolic role as they convert food-derived metabolites into cellular energy. But mitochondria are also key players in other metabolic and signaling cellular processes including redox homeostasis, coordination of lipid biosynthesis, and cell death regulation (Nunnari and Suomalainen, 2012).
Already in 1953, Palade (PALADE, 1953) and Sjöstrand (Sjöstrand, 1953) independently described the ultrastructure of mitochondria for the first time. The individual mitochondrion consists of a mitochondrial outer membrane (MOM) and a mitochondrial inner membrane (MIM). Together these create two mitochondrial compartments; an inter-membrane space and a space enclosed by the inner membrane called the matrix. The MIM is highly folded and protrudes into the matrix with a number of invaginations, the so-called cristae. These determine an increase of the MIM surface which results in an increase of the chemical reaction's rate occurring in the matrix.
Mitochondrial functionality has considerable variations among different cytotypes and environmental conditions that is intrinsically linked to membrane ultrastructure and its protein distribution (Cogliati et al., 2016). In particular the MIM is the highest protein density membrane in the cell (Lackner, 2014) and remodeling of the MIM can thus regulate the dynamic distribution of proteins, lipids and soluble metabolites between individual mitochondrial sub-compartments (Zick et al., 2009).
The oxidative phosphorylation (OXPHOS) system is a crucial molecular machine responsible for the production of mitochondrial ATP and the overall mitochondrial and cellular homeostasis. Most of the OXPHOS proteins are embedded in the MIM. In mammals, the OXPHOS comprises five multi-protein enzyme complexes constituting the four electron transport chain (ETC) complexes (CI-CIV) and a fifth complex (CV) that is the ATP synthase. The highly energized electrons, coming from nutrients oxidation and transported

by the reduced nicotinamide adenine dinucleotide (NADH) and the reduced form of flavin adenine dinucleotide ($FADH_2$), enter into the ETC by CI and II, respectively. The electrons transfer from CI and CII along the ETC in a series of exergonic oxidation reactions that generate energy coupled to endergonic proton translocations. Protons are pumped from the matrix, across the MIM, to the intermitochondrial membrane space. This results in an electrochemical gradient or proton motive force: the mitochondrial membrane potential ($\Delta\psi$). $\Delta\psi$ reflects mitochondrial functionality and can be considered a crucial readout of mitochondrial "health". At the level of CV, another exergonic and endergonic series of reactions are coupled: protons passively flow back into the mitochondrial matrix according to their gradient, driving the synthesis of cellular energy in the form of ATP from ADP and inorganic phosphate.

Mitochondrial ultrastructural alterations have been linked to mitochondrial dysfunction contributing to pathological conditions (Vincent et al., 2016; Zick et al., 2009). Ultrastructural studies of mitochondria have been classically performed using electron microscopy in fixed tissues to analyze the structural organization of both mitochondrial tubules, MIM and MOM at the nanometer scale. In these studies, individual mitochondria have for a long time been depicted as isolated organelles with the typical bean-like structure.

However, in living cells mitochondria form a highly interconnected and dynamic tubular network in a continuous cycle of fission and fusion. The so-called net mitochondrial morphology is determined by mitochondrial dynamics such as swelling, shrinking, fragmentation, elongation etc. (Twig and Shirihai, 2010). The mitochondrial morphology has been described from discrete isolated organelles to a large continuous reticulum with a large variety that represent a continuum of states (Iannetti et al., 2015). Mitochondrial network morphology studies, depending from the specific cell type, size, thickness and other physical parameters, can measure geometrical features at the micron scale of the single mitochondria, single cell and cell population levels and can be performed in living cells using fluorescent microscopy. As for the mitochondria ultrastructural alterations, also aberration in mitochondrial network morphologies, have been associated with different physio-pathological states (Guillery

et al., 2008; Hoitzing et al., 2015; Koopman et al., 2007a; Willems, P. H. G. M. et al., 2015). Simultaneous aberrations in mitochondrial network morphology and $\Delta\psi$ have also been often observed at the same time (Hoitzing et al., 2015; Koopman et al., 2005c). We indeed defined mitochondrial "morphofunction" as a combined readout taking into consideration mitochondrial network morphology and $\Delta\psi$ simultaneously using live cell fluorescence microscopy (Iannetti et al., 2016). The importance of the simultaneous monitoring of functional and structural parameters is highlighted from the frequently quoted sentence of an American zoologist, Stephen A. Wainwright, who in 1969 wrote: *"the structure without a function is a corpse... the function without structure is a ghost"*. This general concept indicates how the relationship correlating structure to function, and vice versa, belongs inevitably to almost any biological system. Mitochondrial structure, morphology and functionality make no exception.

1.2 Mitochondrial diseases, Leigh Syndrome and complex I deficiency

Mitochondrial dysfunction can be caused by mutations directly in mitochondrial DNA genes, by mutations in nuclear DNA genes coding for mitochondrial proteins, but also by mutations in nuclear DNA genes controlling mitochondrial function, ultrastructure or network morphology. These conditions can be defined as a primary mitochondrial disease when caused by a mutation in one of the genes encoding a mitochondria-localized protein. In humans, with the use of mitochondrial proteome analysis, 1158 mitochondrial genes have currently been identified (Human MitoCarta 2.0; www.broadinstitute.org). These genes encode proteins with strong support of mitochondrial localization. *"In principle, a mutation in any of these genes can lead to mitochondrial dysfunction and induce a primary mitochondrial disorder. When mitochondrial dysfunction occurs for another reason, this gives rise to a secondary mitochondrial disorder"* (Koopman et al., 2013). Secondary mitochondrial diseases arise from external influences on mitochondria, such as environmental factors (Meyer et al., 2013) and off-target drug effects (Schirris et al., 2015).

Therefore, these have non-genetic causes and are non-hereditary. Both the disease types refer to a broad and heterogeneous group of disorders having in common mitochondrial dysfunctions and defective cellular energy production due to abnormal OXPHOS functioning.

Primary monogenic mitochondrial diseases are hereditary, relatively rare (prevalence ∼1:5000), chronic, metabolic and neurological disorders that can be present at birth, but can also occur at any age with any mode of inheritance. These can affect almost any part of the body, and in particular the cells of the brain, nerves, muscles, kidneys, heart, liver, eyes, ears or pancreas. This extremely broad range of affected organs can result in a wide range of serious and debilitating illnesses, signs and symptoms. As consequence of this clinical heterogeneity, mitochondrial disease diagnosis can be often a long, complex and burdensome process, consisting of multiple consultations and tests that can become an "odyssey" for patients (Grier et al., 2018). Even after the diagnosis, distinguishing between primary and secondary mitochondrial disease is still challenging (Niyazov et al., 2016).

Despite the significant advances in the molecular and biochemical understanding of the etiology and mechanism of these diseases, there are still no satisfactory approved therapies available. Mitochondrial patients lack therapeutic options that can significantly alter the course of the disease and ultimately stop and cure it. Mitochondrial patients currently only have access to supportive and symptomatic therapies (Koopman et al., 2016; Nightingale et al., 2016). Despite this high unmet medical need, the recent increased number of clinical trials evaluating different targets and drugs is promising (El-Hattab et al., 2017; Lehmann and McFarland, 2018).

Leigh Syndrome (LS) is the most common pediatric presentation of primary mitochondrial disease (Lake et al., 2016). It was first described by Dennis Leigh in 1951, and it is characterized by the degeneration of the central nervous system. This subgroup of mitochondrial diseases is still genetically extremely heterogeneous, and to date pathogenic mutations in more than 75 genes have been identified in mitochondrial and nuclear DNA (Lake et al., 2016). One of the main biochemical defects of the OXPHOS dysfunction in LS is complex I

(CI) deficiency (Ma et al., 2013). On the other hand, one of the most common clinical presentations of CI deficiency is LS (Fassone and Rahman, 2012).
CI is a multiprotein enzymatic complex composed of 45 subunits, 14 of which are defined core subunits. Seven of these core subunits are encoded by mitochondrial genes and seven by nuclear genes (Zhu et al., 2016). The function of the remaining 31 subunits, the so-called accessory subunits encoded by the nDNA, are crucial for assembly and function of CI and essential for cell viability (Stroud et al., 2016). The exact function of many of the accessory subunits is awaiting elucidation.
CI is an "L" shaped enzyme-complex composed of a hydrophilic arm protruding into the matrix and a hydrophobic or lipophylic arm embedded within the MIM, which includes the NADH binding site that accepts electrons and transfer these via a chain of Iron-Sulphur clusters to coenzyme Q. From a molecular point of view, CI deficiency is a quantity shortage of this multiprotein complex or a defect in its enzymatic activity. These can result from protein synthesis downregulation, instability or assembly aberration that can be caused by mutations in either mtDNA- or nDNA encoded CI structural subunits or nDNA-encoded CI assembly factors.
From a clinical point of view *"CI deficiency is the most frequently encountered single mitochondrial single enzyme deficiency in patients with a mitochondrial disorder"* (Rodenburg, 2016). Indeed, between 30% to 40% of the OXPHOS dysfunctions is associated with CI deficiency (Distelmaier et al., 2009b; Kirby et al., 1999; Koene and Smeitink, 2009). Therefore, *in vitro* LS CI models represent a crucial research tool to study OXPHOS pathogenesis and support the future design of rational drug intervention strategies.

1.3 Cell-based phenotypic screening for target discovery and drug testing

Currently, mitochondrial disease patients' clinical management is only symptomatic while mitochondrial dysfunction relentlessly progresses and causes devastating morbidity and premature death. Therefore, it is urgent to study new

candidate compounds improving or even better curing mitochondrial diseases. The process of getting a new drug approved to enter the market and make it available for patients, often named as *from bench-to-bedside*, is a more than a decade-long multi steps complex and expensive process. For simplicity, the drug development process can be summarized in three steps: (i) preclinical *in vitro* drug discovery, (ii) preclinical *in vitro* and *in vivo* drug testing and (iii) human clinical trials. In the rest of this chapter I will discuss the preclinical drug discovery (i) and testing (ii) steps focusing in particular on biological target identification, library drug screening, and *in vitro* drug efficacy and toxicity.

Historically, drugs were discovered by identifying the active ingredients by serendipitous findings coming mainly from plant sources. Today drug discovery and testing sit at the intersection of many different disciplines in particular: medicine, pharmacology, toxicology, biotechnology, genomics, bioinformatics and cellomics.

Drug discovery consist of target identification, candidate compounds identification, synthesis, characterization, screening and target validation. At the end of drug discovery, the first step (i), one or more "hit compound(s)" are identified. These are chemical molecules displaying pharmacological or biological activity likely to be therapeutically useful, but with a suboptimal chemical structure that requires modification to acquire better drug-like properties. These properties, analyzed and optimized during the second step (ii), drug testing, include: efficacy, potency, safety, synthesis route, cost, chemical stability, metabolic stability, and patentability. The rationale behind all these assays is to translate hit compounds into better candidates, lead compounds, for clinical evaluation.

In order to convey the urgency of new technologies development for mitochondrial disease drug development and for any other pathology, it is important to mention the Eroom's law (Scannell et al., 2012). It states that drug development is becoming slower and more expensive over time despite improvements in technology. This significant reduction in the number of newly approved drugs in the past decades has been partially attributed to failures in discovery and validation of new targets.

The two main strategies used by pharmaceutical companies for target discovery and validation include both molecular approaches referred to as target-based screening and empirical approaches referred to as phenotypic screening. The empirical phenotypic approaches seems to be the more successful strategy for small-molecule, first-in-class medicines (Swinney, 2013; Zheng et al., 2013).

Phenotypic screening is based on the use of *in vitro* models for cell-based assays. These model systems represent powerful and absolutely necessary tools for preclinical drug development (discovery (i) and testing (ii)). However, the choice of an appropriate cell model, recapitulating robust pathological readouts in vitro, appears to be the main challenge and goal to achieve for target discovery that highly relies on having a clear understanding of the cellular contribution to the disease.

High-content screening (HCS) is a key technology to perform phenotypic screening. It was created in 1996 when the company "Cellomics Inc." was incorporated to create a technological platform to perform large-scale screening of cells, with subcellular spatial and temporal resolution (Taylor, 2007; Taylor et al., 2001), HCS is defined as a cell-based phenotypic approach where readouts are imaged by multiplexed and automated microscopy and it is also referred to as cellomics. *"Because of the fast developments of technologies and applications the field of cellomics is now on the brink of catching up with the other–omics approaches."* (Iannetti et al., 2019). HCS combines the efficiency of acquiring large data sets typical of high-throughput techniques, with the ability of cellular imaging to collect quantitative data multiplexing different readouts proper of high-content techniques. HCS technology is integrated into all aspects of contemporary drug discovery (i) and testing (ii) due to its ability to study many features simultaneously in complex *in vitro* cell models.

The main challenges behind HCS depend on the specific assay complexity and the hardware used: the throughput magnitude, the data content and results reproducibility and robustness can vary substantially. Moreover, cell, drugs and microplates preparation processes are more complex to automate, as compared to the imaging and data analysis procedures. Therefore, these are often still executed manually and can represent a real bottleneck in data throughput,

reproducibility and robustness.

Another intrinsic challenge relies on the fact that live-cell imaging is technically complex. This is especially true when long kinetic measurements are necessary to study fast and dynamic biological events and cellular time-lapse monitoring, rather than end point measurements, is required.

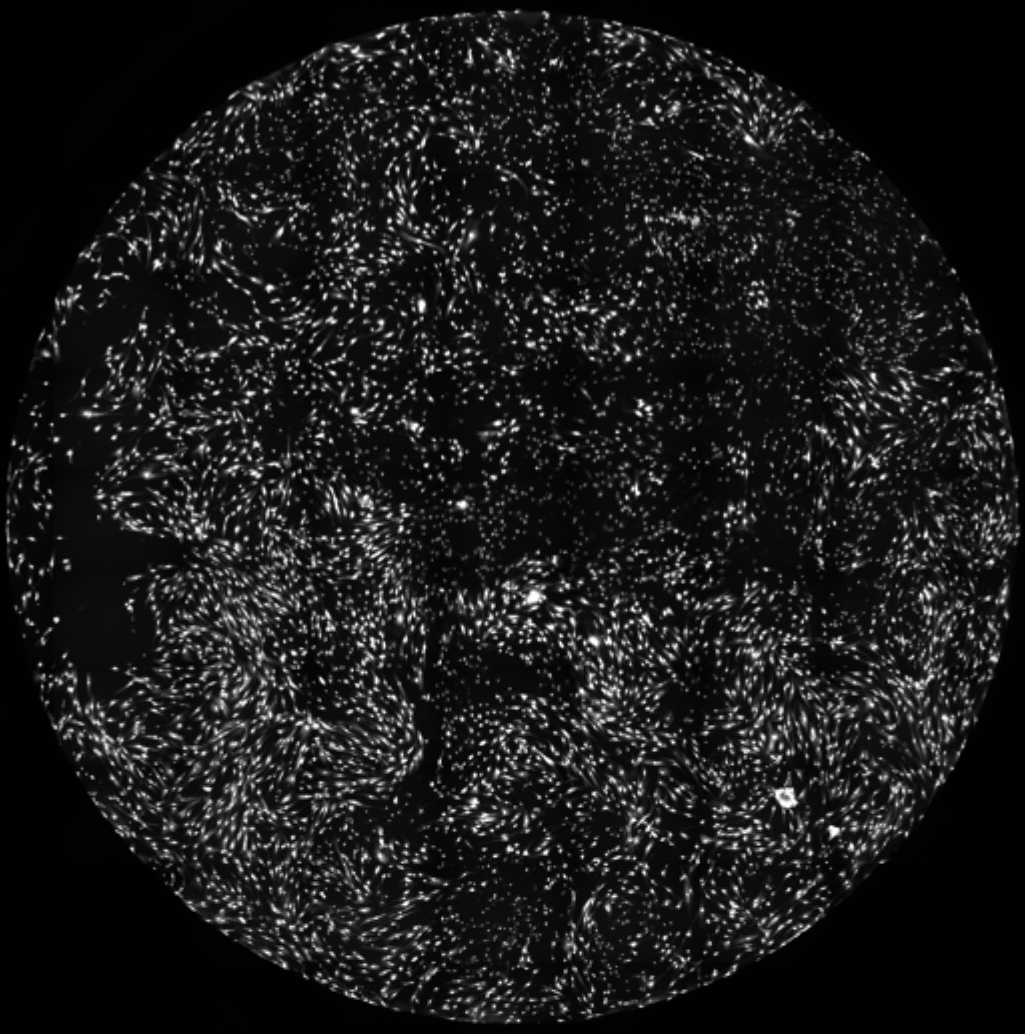
The last challenge regards the handling of complex and multivariate single-organelle, single-cell or cell population big data sets. These often require computational operations such as data management and data mining where strategies, coding languages and/or dedicated software packages are necessary to analyze multiparametric data extracted from biological systems (Kümmel et al., 2011; Smith et al., 2018).

1.4 Aim and outline of the thesis

The primary aim of this thesis is to characterize cellular consequences of mitochondrial dysfunction at the phenotypical level. To do so, this thesis focuses mainly on novel live-cell imaging technology development applied to patient-derived cell lines and predictive cell-based disease models. Fully automated microscopy and microplates were used throughout all this research to guarantee unbiased and high content image acquisition, and robust high throughput data generation. In order to better understand pathophysiological mitochondrial and cellular phenotypes, aberrations induced by inherited genetic mutations and/or by stress conditions were characterized. Particular emphasis was given to the mitochondrial morphofunctional method development and applications. This method and other cell-based assays were developed and applied to study OXPHOS dysfunctions mainly in isolated CI deficient *in vitro* Primary Human Skin Fibroblast (PHSF) models derived from healthy donors or LS patients.

The developed cell-based assays and the functional characterizations represent useful platforms to perform mode-of action studies, biological target identification, library drug screening but also to address fundamental questions in mitochondrial research. This thesis is part of a wider drug development strat-

egy, based on counteracting mitochondrial dysfunctions cellular consequences to stop disease progression and to restore normal cellular function.
Chapter 2 and 3 review the literature to critically discuss concepts not addressed in this chapter and to introduce the experimental Chapters 4, 5, 6 and 7. In particular **Chapter 2** provides an overview of available live-imaging readouts and cell models for phenotypic profiling of mitochondrial function. **Chapter 3** discusses strategies on how to implement high-content screening of mitochondrial morphology and membrane potential in living cells. **Chapter 4** presents a step-by-step protocol developed and optimized on multiplexed high-content analysis to allow unbiased and automated quantification of cellular and mitochondrial morphofunction in intact living PHSF. This protocol can be applied to both drug discovery and testing. **Chapter 5** translates the mitochondrial morphofunction protocol from PHSF to a different cell model, mouse hippocampal neuronal cells. This method application chapter served to evaluate the application of the technology to a different cell model and it was used as characterization analysis part of a bigger study focusing on metabolic flexibility in a nonapoptotic cell death. In **Chapter 6** and **7**, two different stress conditions are introduced, inducing respectively a metabolic and a redox unbalance, to enhance pathological aberrations of CI deficient PHSF derived from LS mitochondrial disease patients. While both these chapters are part of a drug discovery strategy for mitochondrial disease, and both focus on new targets identification, **Chapter 7** has also experiments related to *in vitro* drug efficacy and safety testing. In **Chapter 8** a general summary and discussion, and future perspectives for this field of research are proposed.



Chapter 2

Live-imaging readouts and cell models for phenotypic profiling of mitochondrial function

Published as: **Iannetti, E. F.**, Prigione, A., Smeitink, J. A. M., Koopman, W. J. H., Beyrath, J., and Renkema, H. (2019). Live-Imaging Readouts and Cell Models for Phenotypic Profiling of Mitochondrial Function. *Frontiers in Genetics. 10*, 1–9.

2.1 Introduction

Mitochondrial diseases can result from mutations in the nuclear (nDNA) or mitochondrial DNA (mtDNA). These mutations often lead to disruption of mitochondrial function and/or (ultra) structure leading to "primary mitochondrial disorders" (Koopman, Werner. Willems, Peter and Smeitink et al., 2012) that are progressive, multisystemic and relatively rare (prevalence ∼1:5000) (Parikh et al., 2015). Mitochondrial dysfunction is also a hallmark of various neurodegenerative disorders like Alzheimer's, Parkinson's, and Huntington's disease, cardiovascular disease, cancer, diabetes, and epilepsy (Koopman, Werner. Willems, Peter and Smeitink et al., 2012). Mitochondrial dysfunction can also be triggered by environmental factors (Meyer et al., 2013) and off-target drug effects (Schirris et al., 2015).
Mitochondrial function operates at the junction of numerous cellular signaling and metabolic pathways. At the metabolic level, the tricarboxylic acid cycle together with the four complexes (CI-CIV) of the electron transport chain (ETC) and the F_0F_1-ATP synthase (or CV) converts food-derived metabolites into ATP. This process consumes oxygen (O_C) and establishes a membrane potential ($\Delta\psi$) across the mitochondrial inner membrane (Mitchell, 1961). But mitochondria are also key players in cellular redox homeostasis, calcium signaling, branched-chain amino acid metabolism and the coordination of lipid biosynthesis (Nunnari and Suomalainen, 2012).
In this review, we summarize how live cell analysis using fluorescent reporter molecules and (semi)quantitative microscopy can be used to analyze mitochondrial phenotypes. We also discuss various cellular models of mitochondrial disease with respect to their benefits, disadvantages, technical applicability and appropriateness as a disease model. Finally, we present a collection of high-content microscopy strategies to evaluate mitochondrial contribution to disease and to perform drug toxicity and efficacy screening.

2.2 Live imaging of cell-based readouts to measure mitochondrial functions

Various experimental methodologies quantify mitochondrial dysfunction by focusing on activity measurements of specific mitochondrial enzymes and/or pathways following tissue/cells homogenization and/or using isolated mitochondria (Picard et al., 2011). By contrast, live-cell microscopy assays have the advantage to visualize and quantify functional and structural (sub)cellular (spatial dimension) components in situ in living cells. Moreover, microscopy uniquely allows for simultaneous time-lapse monitoring (temporal dimension) and (semi) quantitative measurements of multiple parameters by multispectral imaging (spectral dimension). In particular, developments in fluorescent reporter technology tremendously boosted the use of light microscopy for cell biology studies (Sbalzarini, 2016).

A limitation of fluorescent microscopy is the potential induction of phototoxic stress, which can be caused by illumination of the reporter molecules. Moreover, fluorophores themselves can perturb the physiological function of biomolecules and are subjected to photobleaching. Furthermore, due to calibration limitations, quantification of cellular parameters using single wavelength dyes can be challenging and, in some cases, only relative and qualitative measurements are possible. The application of ratiometric dyes, when possible, takes care of variable dye loading and extrusion responding with a (semi)quantitative change in fluorescence upon target binding. A drawback of the ratiometric dyes is related to their portability to high-throughput where doubling data dimension can create acquisition, storage and processing issues. Implementing ratiometric dyes in multispectral assays can be also inconvenient because of the wavelength limitation.

When mitochondrial contribution to disease is evaluated in living cells, we consider mitochondrial morphology and membrane potential, ROS, ATP and mitochondrial respiration crucial indicators of mitochondrial health status. Their compatibility with fluorescence microscopy assays will be presented in the next paragraphs and is summarized in Table 2.1.

Table 2.1: Live imaging cell-based mitochondrial readouts and probes.

Readouts and probes	Pros and cons	A	B	C	D	E
Mitochondrial morphology and Δψ						
TMRM (or TMRE)	Pros: fast equilibration, low non-specific bindings, low ETC inhibition, low toxicity.	c	m	553	576	Iannetti et al., 2016
rhod 123	Pros: can be used in quenching mode for fast resolving studies to monitor acute changes in Δψ.	c	m	507	529	Perry et al., 2011
DiOC6(3)	Cons: non-specific binding.	c	m	489	506	Perry et al., 2011; Zorova et al., 2018
JC-1	Pros: JC-1 aggregates emit at different λ discriminating high and low Δψ. Cons: Inconsistent experimental data.	c	d	498	525/595	Zorova et al., 2018
MitoTracker	Pros: retained after cell fixation. Cons: not suitable for Δψ live monitoring.	c	m	*	*	Chazotte, 2011
ROS						
CM-H2DCFDA	Cons: target aspecificity, no subcellular targeting.	c	m	495	529	Chen et al., 2010
DHE	Cons: target aspecificity, no subcellular targeting.	c	m	480	520	Zielonka and Kalyanaraman, 2010
MitoSOX	Pros: mitochondrial localization. Cons: target aspecificity.	c	m	510	580	Zielonka and Kalyanaraman, 2010
BODIPY 581/591 C11	Pros: intracellular membrane lipid targeting.	c	d	500/650	510/665	Pap et al., 1999
MitoPerOx	Pros: BODIPY 581/591 C11 properties with mitochondrial localization and faster equilibration.	c	d	580/600	590/520	Prime et al., 2012
rxYFP	Cons: pH sensitivity, target aspecificity.	g	m	513	527	Meyer and Dick, 2010; Pouvreau, 2014
roGFP	Pros: minor pH sensitivity than rxYFP, possibility to perform kinetic studies for long-lasting redox changes.	g	d	400/480	510	Meyer and Dick, 2010; Pouvreau, 2014
HyPer	Pros: specific indicator of H_2O_2. Cons: pH sensitivity.	g	d	420/500	516	Meyer and Dick, 2010; Bilan and Belousov, 2016
ATP						
ATeam	Cons: phototoxicity during long-time observation, pH sensitivity.	g	d	435	527/475	Imamura et al., 2009
BTeam	Pros: increased detection sensitivity, reduced phototoxicity for long kinetic measurement than ATeam.	g	d	460	455/527	Yoshida et al., 2016
ARP-1	Pros: pH independent, higher sensitivity, higher selectivity to distinguish ATP from its analogs.	c	m	500	557	Sunnapu et al., 2017
RSL+	Pros: mitochondrial localized, higher sensitivity, higher selectivity to distinguish ATP from its analogs.	c	m	520	583	De la Fuente-Herreruela et al., 2017

*General pros of genetic probes are: specifically targeted to different subcellular locations. General con of genetic probes is: transfection is required. General pros of ratiometric dual-wavelengths probes: quantitative measure is possible. A. Type of probe: Chemical (c) or genetic (g), B. mono-wavelength (m) or dual-wavelength (d). C. Maximal excitation wavelength. D. Maximal emission wavelength. E. References. *The MitoTracker® family includes several dyes with different spectral properties (e.g., MitoTracker Red Ex: 579, Em: 599; MitoTracker Green Ex: 490 Em: 516). λ = wavelength.*

2.3 Mitochondrial morphology and $\Delta\psi$

Mitochondrial dysfunction is often associated with simultaneous aberrations in mitochondrial morphology (e.g., fragmentation, roundness) and membrane potential ($\Delta\psi$). Fluorescence live-cell imaging is the most direct method for assessing their spatiotemporal dynamics (Koopman et al., 2008). Different lipophilic cell-permeant, cationic and fluorescent molecules have been presented, which diffuse across the plasma membrane of the cell and accumulate in the mitochondrial matrix in a $\Delta\psi$ dependent manner. These molecules include tetramethylrhodamine methyl ester (TMRM), tetramethylrhodamine

ethyl (TMRE) ester, rhodamine 123, DiOC6(3) (3,3'- dihexyloxacarbocyanine iodide), JC-1 (5,5',6,6'-tetrachloro-1,1',3,3'-tetraethylbenzimidazolylcarbocyanine iodide), and the MitoTracker© family. Among these molecules, TMRM was described to be the least toxic, the fastest in equilibrating across membranes, and displaying the lowest non-specific localization (Nicholls, 2012; Zorova et al., 2018). Therefore in our research we generally use TMRM to simultaneous analyze mitochondrial morphology and $\Delta\psi$ referred to as mitochondrial morphofunction (Koopman et al., 2008; Iannetti et al., 2016). The cell types, staining, imaging conditions and descriptors applicable for the analysis of mitochondrial morphofunction have been previously reviewed (Iannetti et al., 2015; Zorova et al., 2018) and are summarized in our recent study (Iannetti et al., 2016). To technically validate measurements of $\Delta\psi$ using TMRM, we performed oligomycin/bongkrekic acid, rotenone and FCCP acute injections while kinetically measuring mitochondrial TMRM fluorescence fluctuations (Iannetti et al., 2016). Although TMRM measurement, even under highly standardized experimental settings, have been considered still semi-quantitative (Leonard et al., 2015; Nicholls, 2018) attempts using this dye to perform more absolute measurements have been performed combining it with the analysis of the plasma membrane potential (Gerencser et al., 2016).

Protein-based probes targeted to the mitochondria, such as mito-GFP, are also a valid tool to study mitochondrial morphology and dynamics (Rizzuto et al., 1995; Nomura et al., 2009), however, these do not allow the simultaneous study of $\Delta\psi$.

2.4 Reactive Oxygen Species

Reactive oxygen species (ROS) is a general term that includes both oxygen radicals and non-radical agents that can be easily converted into radicals (Halliwell and Gutteridge, 1985). ROS are generated both in the cytosol and in mitochondria as (by) products of normal physiological cell metabolism (Murphy, 2009; Forkink et al., 2010). Depending on the chemical nature of the

ROS, the location at which they are generated and their (local) concentration, ROS can exert a signaling role or induce oxidative and/or redox stress (Lin and Beal, 2006; Smeitink et al., 2006) emphasizing the importance to determine their concentration, types, and localization with precision (Woolley et al., 2013).

Several non-microscopy based approaches are available (e.g., mass spectrometry, western blotting, and immunohistochemistry) to indirectly study ROS via the quantification of the accumulated reaction products (oxidized protein, lipid, and DNA)(McDonagh, 2017; Teixeira et al., 2018). Due to this accumulation these methods have an high sensitivity, however, they do not consider the spatial and temporal dimensions because cell lysates are usually analyzed at end points.

A wide range of chemical or proteinaceous fluorescent ROS probes has been developed (Zhang and Gao, 2015). The two most commonly used chemical ROS probes are 5-(and-6)-chloromethyl-2,7-
dichlorodihydrofluorescein diacetate (CM-H_2DCFDA) (Chen et al., 2010) and dihydroethidium (DHE) (Zielonka and Kalyanaraman, 2010). While CM-H_2DCFDA was initially developed and used to specifically detect H_2O_2 and DHE for superoxide detection, growing evidence indicates that these are both non-specific ROS indicators that should be used for qualitative analysis of total cellular oxidant stress rather than for specific ROS types (Koopman et al., 2006a; Chen et al., 2010; Zielonka and Kalyanaraman, 2010). Despite that, they currently are the most popular ROS sensors because of their technical ease of use that no alternatives can yet guarantee. Especially for CM-H_2DCFDA a rigorous monitoring of the experimental setup and in particular of the protection from environmental light, which is more easily executed with automated imaging, is required. Under tight quality controlled conditions these dyes can produce meaningful and robust qualitative information related to intracellular ROS bursts.

MitoSOX, which is DHE linked to a TPP moiety for rapid accumulation in mitochondria, would ideally allow detection of mitochondria specific ROS production (Robinson et al., 2006). However, this dye needs to be used with

caution, since oxidation of the probe may have happen before it enters the mitochondria (Connolly et al., 2017). Furthermore, the oxidized probe tends to bind to DNA upon which its fluorescence is much increased (Mukhopadhyay, 2008). In our experiments we take especial care to monitor the acquired images and exclude all data in which the staining is not strictly mitochondrial (Beyrath et al., 2018). Flow cytometric and plate reader experiments using mitoSOX should therefore be avoided or interpreted with great care.

Lipid peroxidation of the mitochondrial inner membrane represents a major cause of mitochondria disruption (Morris et al., 2018; Nielson and Rutter, 2018) and ferroptosis cell death (Yang et al., 2016) and it is also considered a crucial readout for evaluation of mitochondrial dysfunction. A ratiometric fluorescent probe, MitoPerOx, specific for mitochondrial fatty acid peroxidation was developed (Prime et al., 2012). MitoPerOx is the mitochondrial targeted version of the BODIPY 581/591 C11 used for the measurement of peroxyl radicals in the general cellular membrane fraction (Pap et al., 1999).

The major drawbacks of the currently available chemical fluorescent ROS probes are the non-specific photo- and chemical-oxidation and the limited availability of subcellular targeting options. This often causes an unclear temporal resolution dynamic: it is not clear where the oxidation of the probe happened. To overcome this limitation, genetically encoded ROS indicators have also been developed: redox-sensitive yellow fluorescent proteins (rxYFP family), redox-sensitive green fluorescent proteins (roGFP family) and the H_2O_2 probe HyPer (Pouvreau, 2014). The working principle of rxYFP and roGFP is based on a change in the oxidation state of the redox-reactive cysteines group that induces a conformational change in the fluorescent properties of the sensor protein (Meyer and Dick, 2010). HyPer instead works by an H_2O_2-sensing regulatory domain of a prokaryotic transcription factor which cysteine active site readily reacts with H_2O_2 inducing a conformational change of the fluorescent protein (Bilan and Belousov, 2016). These genetically encoded ROS and redox indicators have the advantage of providing more reliable real-time monitoring of specific ROS in subcellular compartments. However, using genetically encoded chimeric proteins that require cell transfection and gene expression, can

be technically challenging depending from the cell type (Kim and Eberwine, 2010).

2.5 ATP

ATP plays a central role in bioenergetics and intra/inter-cellular signaling. It can be considered an indicator of cellular and mitochondrial health status (Koopman, Werner. Willems, Peter and Smeitink et al., 2012). A number of well-established assays such as HPLC-based methods and biochemical assays based on luciferase-luciferin bioluminescence guarantee high specificity and accuracy to measure ATP (Vives-Bauza et al., 2007), however, these approaches are not applicable to study living cells because they require the physical extraction of the ATP from the cells by cell homogenization procedures.

Currently, luciferin-luciferase bioluminescence assays using plate readers represent still the gold standard to measure ATP in cells and robust kits are commercially available from different providers.

Significant advances have been made to image ATP using fluorescent, chemiluminescent, bioluminescent and resonance energy transfer technologies based on genetically encoded or chemical probes. Genetic approaches provide great flexibility in the subcellular localization to be targeted. In particular the fluorescence resonance energy transfer (FRET) sensors of the ATeam family (Imamura et al., 2009) that consist of a subunit of the bacterial F_0F_1-ATP synthase combined with fluorescent proteins of different colors, were developed to differentially target cytosol, nucleus or mitochondrial matrix and have been validated in several studies (Liemburg-Apers et al., 2011; Forkink et al., 2014). BTeam the next generation genetically encoded sensors to image ATP, have increased detection sensitivity and allow kinetic measurement of cytosolic ATP levels of the same cells (Yoshida et al., 2016).

Chemical probes that passively diffuse into the cells, such as the rhodamine-based chemical sensors, ARP-1 and RSL^+, have been recently developed for real-time imaging of mitochondrial ATP in living cells (De la Fuente-Herreruela et al., 2017; Sunnapu et al., 2017).

To the best of our knowledge, no chemical ATP probes are currently commercially available. Because ATP concentrations vary widely among tissues, cells and subcellular compartments and because local concentrations vary on a millisecond timescale, the availability of probes with a variety of ATP affinity ranges, fast ATP binding and response kinetics seem features necessary for future ATP probes (Rajendran et al., 2016).

2.6 Mitochondrial respiration

In the ETC the production of ATP is directly coupled to the consumption of molecular oxygen (O_2). Quantifying intracellular O_2 consumption (respirometry) is therefore a direct estimate of the mitochondrial respiratory activity and as such another crucial readout for the mitochondrial and cellular health status (Brand and Nicholls, 2011). The classical respirometry approaches are electrode-based systems like the Seahorse® XF Analyzers (Smolina et al., 2017) and the Oroboros O2k-Fluo Respirometer (Makrecka-Kuka et al., 2015). These are highly sensitive devices to quantify intracellular oxygen levels in living cells. However, these approaches lack spatial resolution to distinguish O_2 concentration at the single cell or subcellular level.

Imaging approaches using microscopy have been developed also for the quantification of O_2. These are mostly based on oxygen induced quenching of phosphorescence or luminescence generated by cell-permeable probes that all still are in an experimental phase. Extensive description of the pitfalls, advantages and opportunities were summarized by Dmitriev and Papkovsky (2015) and more recently by Yoshihara et al. (2017).

Despite all the research, further development is still necessary before O_2 imaging will be available for routine use (Dmitriev and Papkovsky, 2015). Therefore, we still consider electrode-based systems the benchmark to quantify intracellular O_2 consumption.

2.7 Human cell models in mitochondrial research

The choice of an appropriate cell model, recapitulating robust pathological read-out appears to be the first challenge and goal to achieve (Breuer et al., 2013) when evaluating mitochondrial contribution to disease.

Because cell specific metabolism is highly regulated at the genetic, transcriptional and post transcriptional level, every cell type has different energetic requirements. Therefore, mitochondrial physiopathology differs substantially between different cell models depending from their tissue of origin (Smeitink et al., 2006). Mitochondrial functionality can be differentially regulated, induced or even suppressed also depending from environmental factors such as nutrient availability, oxygen condition, differentiation, passage number and many other variables that should therefore be tightly controlled (Benard et al., 2010).

The human cell models most commonly used in mitochondrial research, with their advantages and disadvantages are discussed in the next paragraphs and listed in Table 2.2.

Table 2.2: Human cell models used in mitochondrial research.

Pros	Cons
Primary fibroblasts	
- relatively easy availability from patients and matched controls - easy isolation - robustness in culture, storage, and transport - low cost - not genetically modified - flat morphology and a relatively large size allow non-confocal imaging - present the biological aging of the patients and are usually sampled at the moment of diagnosis	- do not originate from the defective organs - stress conditions are often necessary to enhance pathological symptoms - slow proliferation - require large surface to grow significant number of cells - can be used only for a limited number of passages
Cybrids	
- relationship between mtDNA and phenotype can be studied - robustness in culture, storage, and transport - low cost	- nuclear-mitochondrial interactions are lost - cancer-like glycolytic bioenergetics profile - genetics aberrations - useful only to study mitochondrial encoded mutations
iPSc and iPSc-derived	
- mimic the defective organs - originate from the specific patient - pathological symptoms are usually present - derived from easily accessible patient material (skin, blood, urine) - can be differentiated into virtually any cell type of the body - open possibilities for precision medicine approaches	- genetically modified: mutagenesis risk - suboptimal standardization - mtDNA mutations can impair cellular reprogramming to iPSCs and differentiation - costly and timely procedure - iPSc heterogeneity can mask actual disease-associated phenotypes - low yield of differentiated cells

2.8 Primary culture

Primary cells are a good model to study disease-related phenotypes, since they do not undergo genetic manipulation, present the biological aging of the patients and are usually sampled at the moment of diagnosis. When using patients-derived primary cells, the use of adequate control cells to compare and normalize data to is crucial. The common approach is to use samples derived from healthy gender- and age-matched volunteers. However, because of the different genetic backgrounds between any two individuals, cell-specific non-pathological differences may be introduced. This makes comparison of multiple control and patient cell lines in parallel essential.

In mitochondrial research, the most used primary cell model is skin fibroblasts. A review by (Auburger et al., 2012) highlighted some of the advantages and drawbacks of primary skin fibroblast cultures. Easy availability from patients and matched controls and robustness in culture, storage, and transport were identified as some of the main advantages. In relation to microscopy, fibroblasts are also ideal for imaging simply by epifluorescence (non-confocal) microscopy. Thanks to their extremely flat morphology and a relatively large size, imaging one single focal plane is sufficient to have most of the cell body in focus. However, in mitochondrial disease, the cells with high bioenergetic requirements and concomitant reliance on mitochondrial ATP generation such as neurons, retinal, muscle cells, and in particular cardiomyocyte are often the most affected and often associated with malfunction of the corresponding organs (Breuer et al., 2013; Liang et al., 2014). Therefore, one of the possible concerns using fibroblasts in mitochondrial research regards the fact that these cells do not originate from a defective organ. Indeed, despite the presence of the pathogenic mutation, aberrant phenotypes are not always observed in primary fibroblasts in classical culture regimes. Therefore, different stress conditions have been used by the research community to enhance pathological symptoms and study the dysfunctions. Culture medium in which galactose replaces glucose to enforce ATP production to rely on mitochondrial metabolism (Robinson et al., 1992; Rossignol et al., 2004; Iannetti et al., 2018) and buthio-

nine sulfoximine treatment to reduce glutathione, the main cellular antioxidant (Shrader et al., 2011; Beyrath et al., 2018), are two well-known strategies to induce or enhance pathological mitochondrial phenotypes.

2.9 Cytoplasmic hybrids (cybrids)

Cytoplasmic hybrids (cybrids) are generated by fusing nuclear-depleted cells derived from patients carrying mtDNA mutations with cell lines in which the mtDNA has been removed (so called Rho Zero Cells). The cybrids model has been traditionally used to study mtDNA mutations and dissect the relationship between mtDNA and phenotype alterations (King and Attardi, 1989; Swerdlow, 2007; Wilkins et al., 2014). By introducing the patient-derived mtDNA into a healthy nuclear background, it is possible to dissect whether a certain mutation is sufficient to cause bioenergetics or cellular defects, making cybrids instrumental in dissecting the precise cellular and molecular consequences of a specific mtDNA mutations and the field of mtDNA-related diseases has greatly benefitted from this model.
Unfortunately, the patient-specific interplay between mitochondrial and nuclear genomes, which may play a contributing role in the OXPHOS dysfunction manifestation (Spinazzola and Zeviani, 2009), is lost in the cybrids model. Another disadvantage of cybrids, like other common immortal cell lines, is that they usually present genetic aberrations and relay on a glycolytic bioenergetics and not on OXPHOS like disease affected cells (Abramov et al., 2010). Moreover, cybrids are useful only to study mitochondrial encoded mutations and not for nuclear ones.

2.10 iPSCs and differentiated iPSC-derived cells

Human induced pluripotent stem cells (iPSCs) are obtained from somatic cells through the process of cellular reprogramming (Takahashi et al., 2007). iPSCs can be derived from easily accessible patient material (skin, blood, urine) and can be coaxed to differentiate into virtually any cell type of the body. Diseases

affecting the nervous system, like mitochondrial disorders, may particularly benefit from iPSC research, since the affected patient tissue is not readily available for testing. Genome editing techniques, such as CRISPR/Cas9, combined with iPSCs technology have opened unprecedented opportunities in manipulating nDNA to induce or correct specific mutations of interest. It is possible to generate isogenic iPSCs, which carry the same background (from a control or a patient individual) and differ only in one single disease-causing mutant gene (Grobarczyk et al., 2015). However, genome editing technology is well established only for nuclear DNA (Komor et al., 2017), as engineering of mitochondrial DNA still remain technically challenging (Patananan et al., 2016; Gammage et al., 2017). iPSCs can be applied in compound screens aimed at identifying treatments for mitochondrial diseases (Inak et al., 2017). In fact, one of the key advantages of iPSC-based models is that they may allow a precision medicine approach (Gibbs et al., 2018).

On the other hand, iPSCs also hold disadvantages. Some studies reported that mtDNA MELAS mutations impair cellular reprogramming to iPSCs (Yokota et al., 2015). Cellular fate-determination processes may also be affected, in particular neuronal and cardiac lineage commitment (Folmes et al., 2013; Hatakeyama et al., 2015; Yokota et al., 2017). This may be regarded as a possible readout for mitochondrial dysfunction, but also as a technical complication to generate patient iPSC derived cell lines. Furthermore, the generation of iPSCs is costly and time consuming. It is now apparent that different iPSC lines can be very heterogeneous, thereby masking actual disease-associated phenotypes. Unfortunately, the reprogramming process itself can also induce nuclear and mitochondrial DNA alterations (PERA, 2011; Perales-Clemente et al., 2016), and therefore the genome of all iPSC lines needs to be carefully monitored. The differentiation of iPSCs is time-consuming and often very challenging in obtaining robust and homogenous differentiated progeny (Saha and Jaenisch, 2010), resulting in a small number of obtained differentiated cells that can limit the scalability and the high-throughput applications of iPSC-derived cells. Finally, given that iPSCs rejuvenate the state of mitochondria (Lisowski et al., 2018) and the aging-associated epigenetic signature

(Mertens et al., 2018), it has been suggested to circumvent the generation of iPSCs by using a direct reprogramming approach (Vierbuchen et al., 2010). In this approach, patient-derived fibroblasts can be directly converted into neurons without going through the state of iPSCs, thereby retaining the aging signature (Mertens et al., 2015; Victor et al., 2018). Nonetheless, also directly reprogrammed cells carry disadvantages as they need to be generated newly continually and cannot be easily used for genome editing.

2.11 High-content screening applications to study mitochondrial functions

High-content screening (HCS) is defined as a cell-based phenotypic approach where readouts are imaged by multiplexed and automated microscopy (Zanella et al., 2010; Pegoraro and Misteli, 2017); this is also referred to as cellomics (Taylor, 2007).

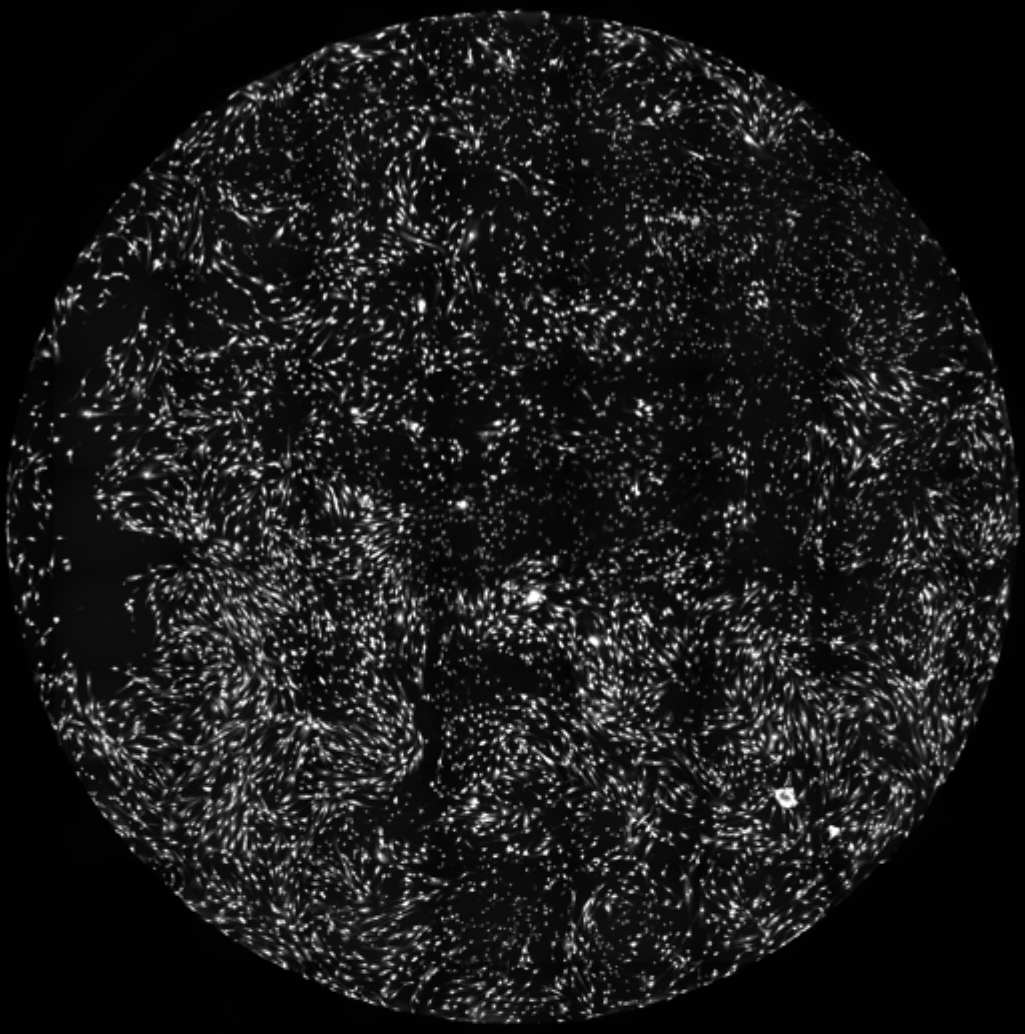
Because of the fast developments of technologies, probes and applications and the upcoming field of iPSCs technology generating faithful cell disease models, the field of cellomics is now on the brink of catching up with the other–omics approaches.

Already in 2007 an HCS method was developed combining $\Delta\psi$ analysis with other cellular parameters measured in human liver carcinoma cells (HepG2) grown in a microfluidics device (Ye et al., 2007). Also performed in HepG2 cells an HCS assays has been described to screen drugs based on six parameters among which $\Delta\psi$ and mitochondrial area (Persson et al., 2013) or intracellular redox state (Ye et al., 2007; Donato et al., 2012). A cellomics liver toxicity assay using iPSC-derived hepatocytes was recently published that focuses on drug development and toxicity testing, studying mitochondrial parameters as indicators of cellular health (Sirenko and Cromwell, 2018). Leonard et al. addressed more technical aspects of HCS application development combining the quantitative analysis of mitochondrial morphology and $\Delta\psi$ in living photoreceptor cells with supervised machine learning (Leonard et al., 2015). In 2016 we described a detailed protocol to optimize multiplexed high-content analysis

of mitochondrial morphofunction in primary human skin fibroblasts showing potential implementation of the protocol to HCS format (Iannetti et al., 2016). With this same cell type a high-content method was also developed to combine the study of cellular ROS levels and mitochondrial morphofunction (Sieprath et al., 2016). Other cellomics applications focused instead primarily on the identification of mitochondrial pathological phenotypes to evaluate their contribution to disease. Among these, a strategy based on iPSC-derived NPCs of mtDNA patients in which a $\Delta\psi$–related pathological phenotype was identified and used to screen a compound-library (Lorenz et al., 2017). A 384-well plates based HCS application, identifying reduced $\Delta\psi$ and mitochondrial morphology aberrations in iPSC-derived neurons from Parkinsons disease patients as compared to controls, was also recently published (Little et al., 2018).
All these studies show the applicability of mitochondrial morphofunction and ROS analysis as robust HCS/cellomics applications. These will likely in the near future be complemented with fluorescent imaging technologies to detect ATP and oxygen consumption, which, to the best of our knowledge, have not been explored yet.

2.12 Conclusion

Cellomics represents a powerful technology, already established in many research labs, to study in an unbiased manner mitochondrial functions monitoring multiple readouts, portable to different cells models and able to provide valuable insight in mitochondrial phenotypes and their contribution to disease.



Chapter 3

Toward high-content screening of mitochondrial morphology and membrane potential in living cells

Published as: **Iannetti, E. F.**, Willems, P. H. G. M., Pellegrini, M., Beyrath, J., Smeitink, J. A. M., Blanchet, L., Koopman, W. J. H. (2015). Toward high-content screening of mitochondrial morphology and membrane potential in living cells. *The International Journal of Biochemistry & Cell Biology. 63*, 66–70.

3.1 Introduction

Mitochondria are motile organelles that consist of a matrix compartment surrounded by an outer (MOM) and highly folded inner (MIM) membrane. The five complexes (CI–CV) of the mitochondrial oxidative phosphorylation (OXPHOS) system, involved in ATP generation, are embedded in the MIM. The OXPHOS system is composed of four electron transport chain (ETC) complexes (CI–CIV)and the ATP-producing F_0F_1-ATPase (CV). The ETC sustains the highly inside-negative mitochondrial membrane potential ($\Delta\psi$) across the MOM required to sustain the action of CV (Mitchell and Moyle, 1967) and many other mitochondrial functions (Koopman et al., 2010). Therefore the magnitude of $\Delta\psi$ can be considered a readout of mitochondrial "health". Within living cells, mitochondria are motile and continuously fuse and divide. The balance between these processes determines net mitochondrial morphology (Bereiter-Hahn and Vöth, 1994; Friedman and J., 2014). Simultaneous aberrations in mitochondrial function and dynamics have been observed during various patho-physiological conditions including human disease (Corrado et al., 2012; Archer, 2013). For instance, the degree of mitochondrial fragmentation and increase in reactive oxygen species (ROS) levels were proportional to the extent of CI deficiency in primary patient fibroblasts with isolated CI deficiency (Koopman et al., 2007a). In this sense, mitigative effects of antioxidants have been demonstrated in these cells (Blanchet et al., 2015), suggesting that mitochondrial morphology and increased ROS production constitute linked therapeutic targets.

Interestingly, MIM fusion appears to be $\Delta\psi$-dependent (Malka et al., 2005) and changes in mitochondrial function and morphology occur in parallel in many cellular systems of mitochondrial(dys)function (Benard and Rossignol, 2008; Guillery et al., 2008; Distelmaier et al., 2009b; Koopman, Werner. Willems, Peter and Smeitink et al., 2012; Koopman et al., 2013). Hence, simultaneous quantification of $\Delta\psi$ and mitochondrial morphology is important to better understand their interconnection during normal and pathophysiological conditions. At the single-organelle level, mitochondria display a large variety of

morphologies that represent a continuum of (probably functionally different) states.To properly describe this state continuum, multiple parameters are required. The latter are delivered by (live-cell) high content screening (HCS) strategies, which unite high content (HC, i.e.multi-parameter cell analysis) and high throughput (HT, i.e. auto-mated data acquisition for many cells) fluorescence microscopy and allows fully automated multi-parameter phenotypic cell analysis (Zanella et al., 2010; Kümmel et al., 2011; Buchser et al., 2012; Blanchet et al., 2015). This review focuses on the quantitative live-cell analysis of $\Delta\psi$ and mitochondrial morphology at the level of individual organelles, mainly illustrated using primary human skin fibroblasts. We will discuss how mitochondria can be stained and visualized using live-cell fluorescent microscopy (Section 3.2) and how numerical data can be extracted for unbiased explorative and statistical analysis (Section 3.3). Finally, we present some future perspectives on the role of HCS in mitochondrial research (Section 3.4).

3.2 Fluorescence microscopy imaging of $\Delta\pi$ and mitochondrial morphology

Our strategy for HCS analysis of $\Delta\psi$ and mitochondrial morphology in living cells is schematically depicted in Fig. 3.1 and consists of: (i) an experimental part (yellow), followed by (ii) image processing/quantification (green) and (iii) data analysis/mining(purple). In principle, this approach was developed for primary human skin fibroblasts. Thanks to their extremely flat morphology and a relatively large size, these cells are ideally suited for analysis by epifluorescence (non-confocal) microscopy (Koopman et al., 2006a). However analogous strategies can also be applied to other cells of similar size and axial dimensions, including human and mouse myoblasts, mouse skin fibroblasts, and Chinese hamster ovary (CHO) cells (Tronstad et al., 2014). As an alternative, cells dis-playing larger axial dimensions can be analyzed using 3D-confocalmicroscopy (e.g. Nicolaisen et al., 2014).

Cell growth conditions (e.g. cell culture medium, O_2 levels, time of cell seeding,

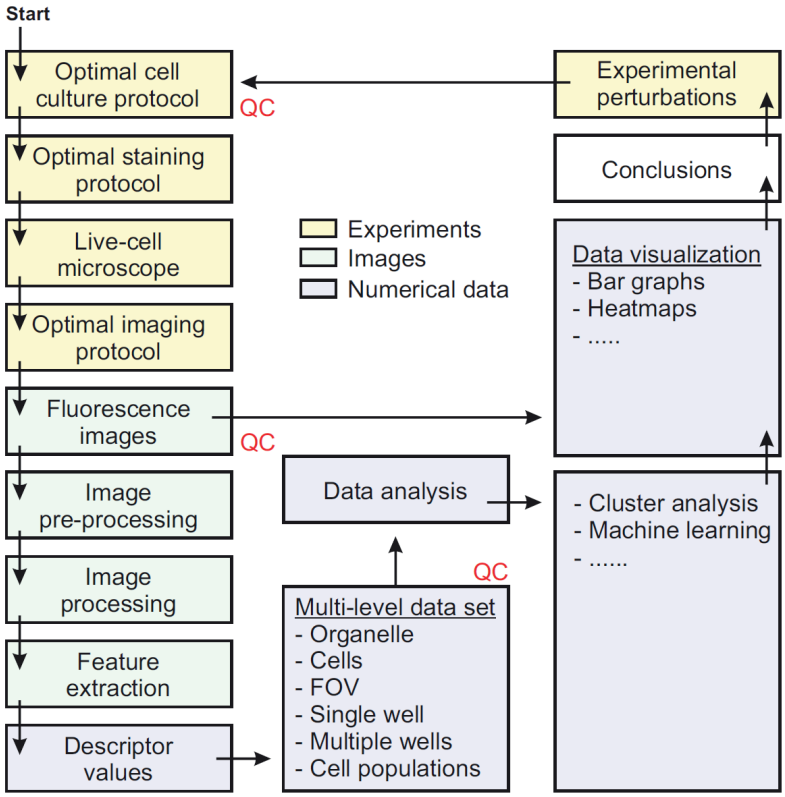


Figure 3.1: Integrated HCS strategy for analysis of $\Delta\psi$ and mitochondrial morphology.This approach represents a strategy developed for primary human skin fibroblasts and consists of three parts in which: (i) cells are cultured, stained with fluorescent reporter molecules and imaged using live-cell microscopy ("experiments"; yellow),(ii) microscopy images are processed and quantitative information is extracted("images"; green), and (iii) numerical data is analyzed and visualized ("numerical data"; purple). The depicted workflow includes various points for (fully automated)quality control (QC) focusing on cell quality, image quality and the obtained multi-level data. Abbreviation: FOV, field of view. (For interpretation of the references to color in this figure legend, the reader is referred to the web version of this article.)

temperature, pH) can strongly affect the outcome of the analysis in a cell type-dependent manner. For instance, mitochondrial morphology shifts toward a more filamentous ("hyperfused") state upon nutrient starvation (Gomes and Scorrano, 2011; Rambold et al., 2011). In addition, the various (energy) substrates of the cell culture medium affect mitochondrial morphological and func-

tional state (Zanna et al., 2008; Gomes et al., 2011). These findings highlight the prime importance of a highly standardized cell culture protocol (which closely mimics the normal physiological state of the cell) for successful development of a HCS approach. For automated strategies, it is further required that cell quality prior and during microscopy experiments is monitored using quality control (QC) tools (Bray and Carpenter, 2012).

Following culturing, cells are seeded and cultured in multi-well plates according to a standardized protocol, yielding a continuous supply of sub-confluent, non-senescent cells. This allows mitochondrial analysis in their "natural environment" (i.e. the cytosol of a living cell). As mentioned above, due to their flat morphology primary human skin fibroblasts are an ideal model system for microscopy analysis by epifluorescence (non-confocal) microscopy. Mitochondria can be visualized using organelle-specific fluorescent reporter molecules, like mitochondria-targeted fluorescent proteins. The latter are ideally suited for spatiotemporal analysis of mitochondrial dynamics (Collins et al., 2002) but require pre-microscopy cell transfection. Alternatively, chemical lipophilic cationic fluorescent probes of the "mitotracker" (MTR) family can be used to study live cell mitochondrial dynamics (Chazotte, 2011). These probes passively diffuse into the cells and accumulate in active mitochondria in a $\Delta\psi$-dependent manner. However, most MTR dyes are retained within mitochondria by reacting with mitochondrial biomolecules (Dong et al., 2013). As a consequence, MTR fluorescence intensity is generally not suited as a reliable readout of $\Delta\psi$. Fluorescent cations used for combined $\Delta\psi$ and mitochondrial morphol-ogy analysis include tetramethylrhodamine methyl (TMRM) and ethyl (TMRE) ester, rhodamine 123 (R123), DiOC6(3) (3,3-dihexyloxa carbocyanine iodide), and JC-1 (5,5',6,6'-tetrachloro-1,1',3,3'-tetraethyl benzimida-zolylcarbocyanine iodide. These dyes equilibrate across the plasma membrane and MIM in a potential dependent manner. Among these dyes, TMRM is best suited for the membrane potential measurement because it is least toxic, equilibrates fastest across membranes and displays lowest a specific binding (Nicholls, 2012). Using this cation, we previously presented an experimental and image quantification protocol for HC analysis of $\Delta\psi$ and mi-

tochondrial morphology in primary human skin fibroblasts (Koopman et al., 2006a, 2008). Proper image quantification requires images with a high signal-to-noise (i.e.mitochondrial-to-background) ratio, which are optimally focused and homogenously illuminated. Crucially, reliable analysis can only be performed when images are relatively free of a-specific noise and each mitochondrial object consists of a sufficient amount of pixels (Koopman et al., 2006a, 2008).

3.3 Image analysis and data mining

The microscopy system delivers "RAW" images that are first background-corrected (Fig. 3.1) and subsequently processed using a pipeline that highlights mitochondrial objects on a black background in a "masked" (MSK) image (Fig. 3.2B). This segmentation allows automated extraction of multiple morphology- and intensity-related parameters for each mitochondrial object within individual cells (Fig. 3.2C and D). In essence,the information in each image is condensed into a set of numerical descriptors (Fig. 3.1; "feature extraction"). This multi-level data set allows subsequent analysis at various levels (i.e. individual objects,single cells and cell populations; Fig. 3.1). Understanding complex HCS data sets requires application of multivariate statistics. The term "data mining" is used to designate computational strategies for pattern discovery in large data sets. These strategies consider all variables simultaneously in a multidimensional space and assume that each descriptor in the data set is (at least partially)correlated. In this context, data dimensionality reduction and graphical visualization tools, plays an important role in the discovery of hidden phenomena such as differences, similarities, trends and clusters between descriptor variables (Abraham et al., 2014).Importantly, the quality of the data extracted from microscopy images can suffer from low image quality and imaging artefacts.This means that QC metrics should be implemented in any HCS protocol to maximize the validity of the obtained descriptors (Bray and Carpenter, 2012). In this sense, QC algorithms can be used to exclude "aberrant" images from the analysis, both directly following

image acquisition and during analysis of the multi-level data set (Fig. 3.1). In HCS, machine-learning approaches are of value for explorative analysis and QC implementation (Sommer and Gerlich, 2013). In machine learning a computer algorithm is trained to recognize and/or discriminate between particular data sets (e.g. different cell lines, cell types or experimental interventions). "Unsupervised" machine learning attempts to recognize patterns or groups in the data. This classification is solely based on information inherently present in the data and not on what the user (supervisor) is looking for. For example, this type of analysis can be used to determine whether/which subpopulations are present in the total cell population. Unsupervised data analysis also allows detection of unexpected variation such as previously unknown phenotypes. However, unsupervised data analysis is sensitive to the presence of variance unrelated to the pattern of interest (Zhong et al., 2012). To determine what distinguishes two cell lines from each other (i.e. cells from a healthy individual and a patient with mitochondrial disease) a second family of algorithms is required. The latter generally are referred to as "supervised" methods, a term that originates from the fact that in these methods the operator supervises (or trains) the algorithm and "helps" it to learn the to-be-identified pattern (Held et al., 2010).

3.4 Applications and future perspectives

We are unaware of live-cell HCS studies in the literature focusing on simultaneous single-organelle $\Delta\psi$ and mitochondrial morphology analysis. However, particularly in analysis of mitochondrial drug toxicity, various combinations of mitochondrial and other cellular readouts have been assessed. These include: (i) $\Delta\psi$, mitochondrial area, number of nuclei, area of nuclei, plasma membrane integrity and lysosomal activity (Persson et al., 2013), (ii) CIV-subunit protein level and mtDNA-encoded protein synthesized on mitochondrial ribosomes (Nadanaciva et al., 2010), (iii) $\Delta\psi$, oxidative stress, nuclear morphology an cytosolic calcium levels (Tolosa et al., 2013), (iv) mitochondrial permeability transition pore opening, apoptosis induction and cytosolic calcium levels

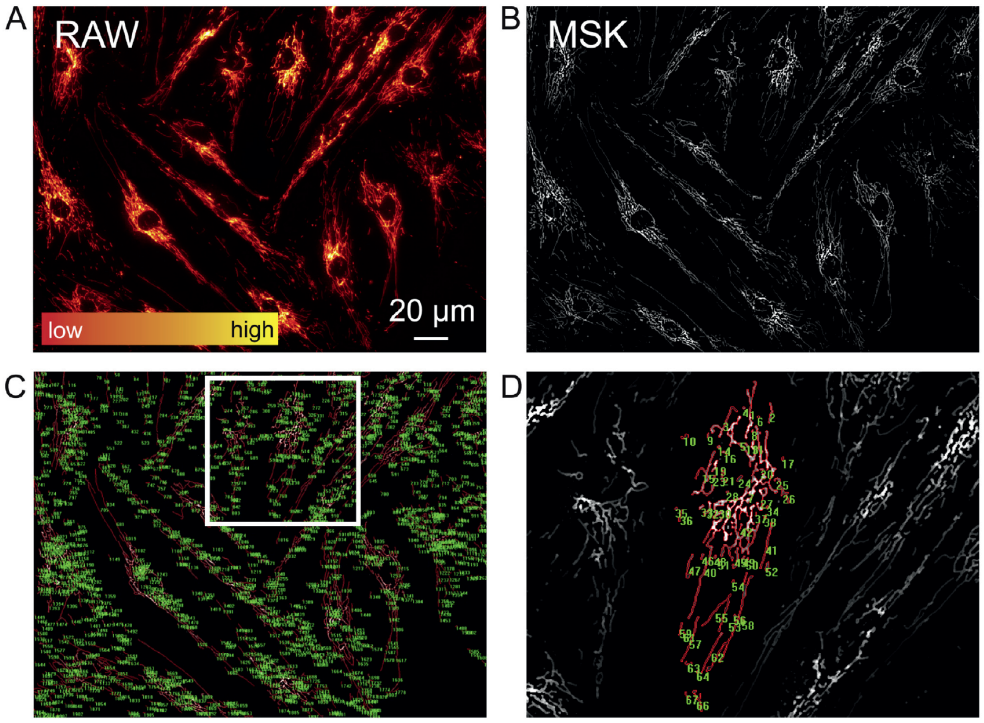
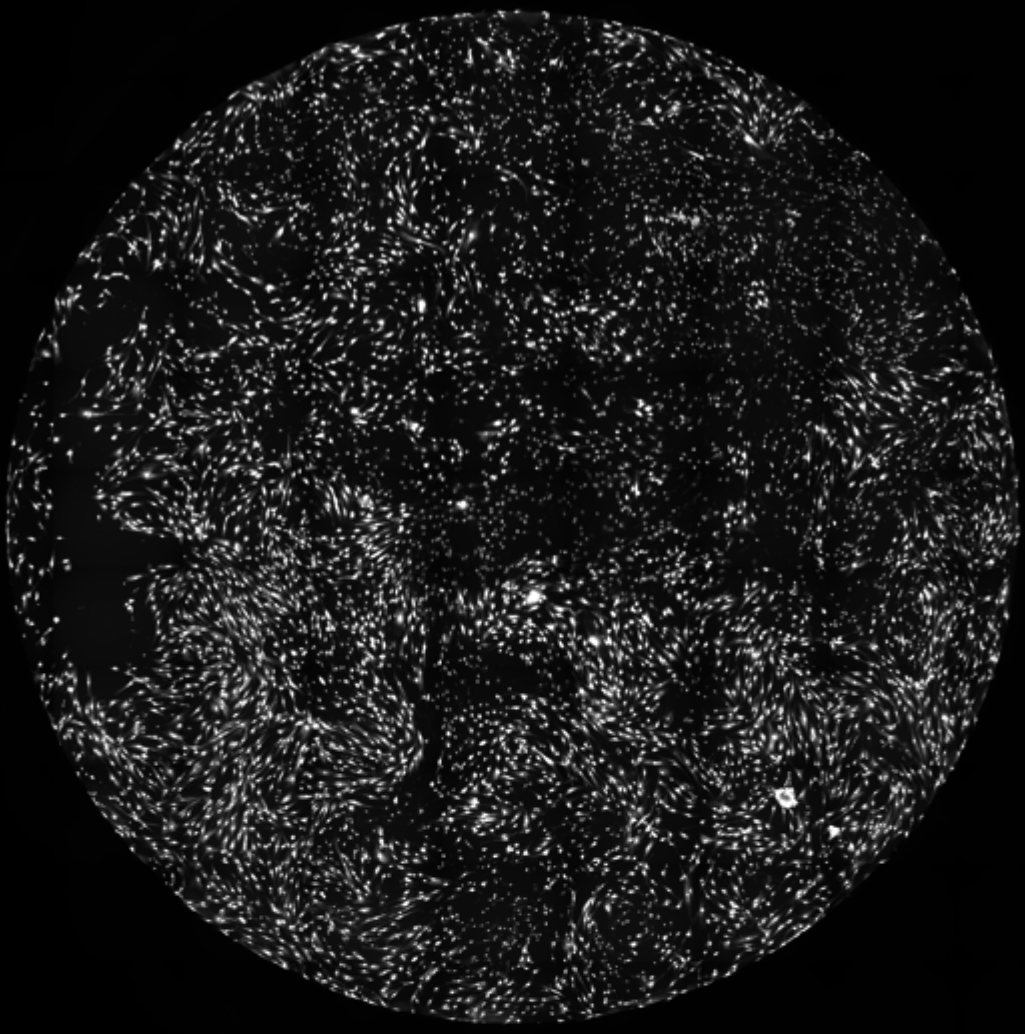


Figure 3.2: Processing and data extraction from images of TMRM-stained primary human skin fibroblasts. **A)** Recorded microscopy image (RAW) of primary human skin fibroblasts from a healthy individual. Cells were cultured in a 96-well plate, stained with TMRM and imaged by automated epifluorescence microscopy. TMRM fluorescence intensity was color-coded using a red to yellow scale (inset). **B)** Following background corrections and image processing of the RAW image, a masked image (MSK) is obtained which depicts mitochondrial objects on a black background. The intensity in this image represents TMRM fluorescence. **C)** Computer-assisted identification of mitochondrial (i.e.non-black) objects in the image. Each identified object is marked by a red boundary line and green numeral. **D)** Magnification of a region of interest in panel **C**. Multiple morphology- and intensity-related parameters can automatically be extracted from the image for each mitochondrial object within every individual cell. (For interpretation of the references to color in this figure legend, the reader is referred to the web version of this article.)

(Kim et al., 2012), (v) $\Delta\psi$, oxidative stress, lipid content, cell viability and nuclear morphology (Donato et al., 2012). Obviously, the above approaches can also be applied in fundamental mitochondrial research and therapeutics screening. For instance, correlations have been reported between mitochon-

drial morphology and apoptotic/bioenergetic state (Reis et al., 2012), caspase activation and mitochondrial dynamics (Peng et al., 2011) and mitochondrial content and cell size (Kitami et al., 2012).

In conclusion, we provide indications that combining HCS with machine learning approaches and QC algorithms is a promising strategy for unbiased automated analysis of $\Delta\psi$ and mitochondrial morphology. It is expected that this approach will be of value in enhancing our understanding of mitochondrial morpho-function as well as a powerful tool in drug-discovery and mode-of-action studies.



Chapter 4

Multiplexed high-content analysis of mitochondrial morphofunction using live-cell microscopy

Published as: **Iannetti, E. F.**, Smeitink, J. A. M., Beyrath, J., Willems, P. H. G. M., and Koopman, W. J. H. (2016). Multiplexed high-content analysis of mitochondrial morphofunction using live-cell microscopy. *Nature Protocols. 11*, 1693.

4.1 Introduction

Mitochondria are cellular organelles that fulfil a wide range of functions in cellular metabolism (Chandel, 2014). Within living cells, individual mitochondria are motile and display fission/fusion events(Westermann, 2010; Chan, 2012). The balance between these processes, in combination with mitochondrial swelling/shrinking and removal of mitochondria by mitophagy, determines net mitochondrial morphology (Twig et al., 2008; Willems, P. H. G. M. et al., 2015). Healthy mitochondria display an inside-negative electrical potential ($\Delta\psi$) across their inner membrane that is required to sustain mitochondrial ATP generation (Mitchell and Moyle, 1967) and can be considered as a semiquantitative functional readout of mitochondrial health (Koopman et al., 2008; Iannetti et al., 2015). Functional defects in mitochondrial and/or cellular metabolism are often associated with aberrations in mitochondrial morphology and vice versa (Mishra and Chan, 2016; Schrepfer and Scorrano, 2016; Toyama et al., 2016; Wai and Langer, 2016). Importantly, these defects are not only seen in rare monogenic mitochondrial disorders but are also associated with common pathologies such as Alzheimer's disease, Parkinson's disease, Huntington's disease, cancer, cardiac disease, diabetes, epilepsy and obesity. Moreover, a progressive decline in the expression of mitochondrial genes is a central feature of normal human aging (Koopman, Werner. Willems, Peter and Smeitink et al., 2012; Koopman et al., 2013). This means that maintaining normal mitochondrial morphofunction is of eminent importance for human health and, as a consequence, strategies for evaluation of this morphofunction are a subject of major interest in experimental research, pharmacological screening and clinical diagnostics (reviewed in Tronstad et al. (Tronstad et al., 2014)). Mitochondrial structure and metabolism are tightly interfaced with the rest of the cell (Rowland and Voeltz, 2012; Picard et al., 2013). Therefore, physiological analyses ideally are carried out using the natural mitochondrial 'habitat', being the cytosol of an intact living cell (Iannetti et al., 2015; Koopman, Werner. Willems, Peter and Smeitink et al., 2012; Koopman et al., 2013, 2010). In this respect, fluorescence microscopy is the most direct method for

assessing live-cell mitochondrial morphofunction. During the past decade, we have established an integrated experimental and computational strategy for semiautomatic quantification of mitochondrial morphofunction, on which the current protocol is based. In brief, our previously published strategy consists of the following parts:

- Staining of mitochondria in living cells with reporter molecules such as mitochondria-targeted fluorescent proteins (mtFPs; Koopman et al., 2007a) or fluorescent cations, including rhodamine 123 (Koopman et al., 2005c,a, 2006a) and TMRM23.
- Imaging of these cells (Koopman et al., 2006b; Willems et al., 2009) using a climate-controlled (video-rate) confocal microscope (Koopman et al., 2005c,a, 2006a) or an epifluorescence microscope (Koopman et al., 2008; Distelmaier et al., 2008; Nooteboom et al., 2012).
- Application of image processing techniques to allow extraction of relevant mitochondrial parameters such as fluorescence intensity and mitochondrial shape from the images (descriptors).
- Statistical evaluation and/or mining of the descriptor data for phenotypic classification of different cell lines and drug effects (Blanchet et al., 2011, 2015).

Importantly, in developing the above approach, a 'reverse strategy' was followed, meaning that the descriptors that should be extracted from the microscopy images were first defined. Next, an image processing pipeline was designed to obtain these descriptor values. Then, the image properties that were required to allow successful descriptor extraction were determined. Finally, a cellular staining and image acquisition workflow compatible with these image requirements was implemented. Development of the protocol was initiated and first presented in 2005 for quantitative analysis of mitochondrial morphofunction in PHSFs (Koopman et al., 2005c,a). Using PHSFs from patients with mitochondrial disease, morphofunction was quantitatively compared with reactive oxygen species levels (Koopman et al., 2008, 2007b), cytosolic calcium

homeostasis (Koopman et al., 2008; Willems et al., 2009), enzyme activities (Koopman et al., 2005a) and clinical data (Blanchet et al., 2011). In later years, the 2005 protocol was further validated using genetic mtFPs such as the enhanced yellow fluorescent protein (Koopman et al., 2007a,b) and was successfully applied in other cell types (Table S1). In essence, our 2005 method involves manual acquisition of single microscopy images, followed by semiautomatic image processing and quantification. Here, this method is adapted for use with multiple reporter molecules ('multiplexed') (Lansing-Taylor, 2007) and 96-well plates. High-content (multi descriptor) analysis is particularly important in drug discovery, as therapeutic small molecules generally exert subtle pleiotropic effects via (a)specific targeting of (multiple) effectors, which might be overlooked by single-descriptor analysis (Blanchet et al., 2015; Feng et al., 2009; Zanella et al., 2010; Bast and Haenen, 2013). The protocol presented here combines quantitative analysis of mitochondrial morphology and $\Delta\psi$ with that of cell size/confluence and nuclear number/morphology. After cell staining, each well is automatically imaged and analyzed (high throughput), yielding multiple descriptors (high content). We also provide an automated QC algorithm, which allows large-scale statistical evaluation and classification of mitochondrial morphofunctional phenotypes.

4.1.1 Comparison with other methods

Many strategies for the quantification of mitochondrial morphology have been presented in the literature, several of which are included in Table S1. With respect to image quantification, these strategies are often similar to the one that we initially described for PHSFs (Koopman et al., 2005c,a). However, other studies were performed using different cell types (e.g., HEK293, HeLa and HUVECs) and fluorescent markers. In various studies, including our own, only a limited number of mitochondrial morphology descriptors were quantified (Wiemerslage and Lee, 2016). Fortunately, mitochondrial morphology can be described well using only a few 'biologically relevant' descriptors (i.e., the number of mitochondria per cell, mitochondrial size, mitochondrial mass, mitochondrial aspect ratio and mitochondrial formfactor (Tronstad et al., 2014)).

However, using a relatively low number of descriptors might be disadvantageous for phenotypic analysis and/or drug-screening studies (Blanchet et al., 2015). As an alternative to our presented PCA-based strategy, mitochondrial morphology can also be analyzed by machine-learning strategies (Sommer and Gerlich, 2013). For instance, unsupervised machine learning was applied to define six morphological phenotypes in CHO cells and the effects thereupon of caspase inhibition (Peng et al., 2011). Similarly, supervised machine-learning and fuzzy logic methods were used to study mitochondrial morphology, $\Delta\psi$ and Bax activation in human epithelial cells treated with mitochondrial inhibitors (Reis et al., 2012; Ahmad et al., 2013). In these two studies, classification of mitochondrial shape was based on three predefined phenotypes ('tubular', 'donut-shaped' and 'swollen'). A similar approach was applied in another machine-learning study (Leonard et al., 2015). In contrast to the protocol presented here, these predefinition strategies might introduce an undesirable bias. Therefore, we recently used a supervised machine-learning approach for data mining and visualization, but, similar to the current protocol, we did not assume the existence of predefined mitochondrial morphology phenotypes (Blanchet et al., 2015).

4.1.2 Limitations of the protocol

A limitation of this method is that the cell seeding and staining procedures have to be carried out manually, which requires time investment. Moreover, because a non confocal mode of imaging is used, the protocol performs best with relatively large cells displaying a flat morphology (e.g., PHSFs). This is because results obtained by 2D image analysis are representative of 3D mitochondrial morphofunctional properties in such cells (Nikolaisen et al., 2014). When analysis of 'thick' and/or small cells is required, the protocol can be adapted using the information provided in Section *Troubleshooting*; otherwise, alternative strategies should be used. The latter include 3D mitochondrial morphology analysis, super-resolution microscopy and 2-photon microscopy (Farrand et al., 2013; Rizk et al., 2014; Lautenschläger et al., 2015; Lihavainen et al., 2015; Hugelier et al., 2016; McClatchey et al., 2016). In contrast to

those from other studies (Leonard et al., 2015), the numerical data obtained in this protocol represent average descriptor values for each image/well (i.e., containing multiple cells). This means that data for individual cells are not available. In its current form, the presented protocol cannot be used to quantify mitochondrial motility or ultrastructure. However, in this respect, various other strategies have been described (Giuly et al., 2012; Lihavainen et al., 2012; Mumcuoglu et al., 2012; Dietlmeier et al., 2013; Bros et al., 2015; Kandel et al., 2015; Tasel et al., 2016).

4.2 Experimental design

Overview of the protocol. The full protocol is summarized in a flowchart (Fig. 4.1), and it combines three fluorescent reporter molecules into a single live-cell assay. PHSFs are cultured on 96-well plates, after which the main emphasis is on the correct use of the mitochondria-selective fluorescent cation TMRM to quantify mitochondrial morphology and $\Delta\psi$. To this end, cells are also stained with calcein and Hoechst 33258 (Hoechst) to co-assess cellular and nuclear parameters, respectively. For each well, a TMRM, calcein and Hoechst image is acquired (Fig. 4.1a) and processed (Fig. 4.1b,c) to extract quantitative descriptors (Table 4.1). From the TMRM images, 33 different descriptors are extracted, including the mitochondrial aspect ratio (AR; a measure of mitochondrial length), the average mitochondrial TMRM signal (Dm; a semi-quantitative measure of $\Delta\psi$) and the mitochondrial 'roundness' (formfactor (F), a combined measure of mitochondrial length and degree of branching). The calcein image is used to quantify the total cell area (CaSum) and integrated intensity (CaIOD). Hoechst staining is analyzed to determine the total number of nuclei (Nn), as well as their area (An) and formfactor (Fn). Integration of the various descriptors allows calculation of various 'derived descriptors', including the cell-size-corrected mitochondrial mass (Mm), mitochondrial size (Am; Am=Asum/Ot), the number of mitochondria per cell (Nc) and cell size (Casum/Nn). In total, automated image processing and quantification (Fig. 4.1b) yields 44 descriptors for each well (Fig. 4.1c).

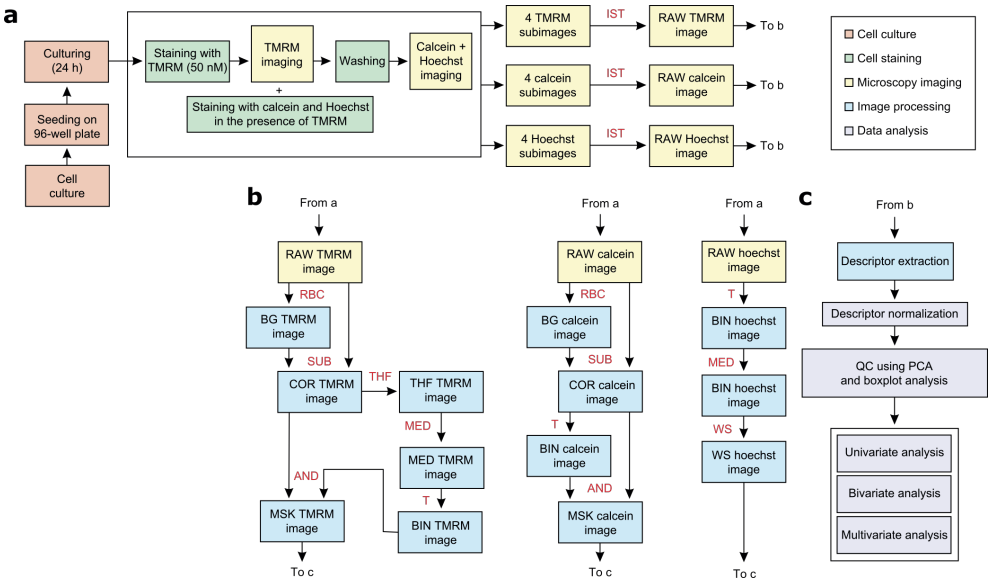


Figure 4.1: Overview of the protocol. A–C) The presented approach consists of five distinct parts (colorized) involving experiments (cell culture, cell staining and microscopy imaging) and computational analysis (image processing, data analysis). **A)** Cells are cultured under highly standardized conditions and seeded in a 96-well plate. After 24 h, cells are stained with TMRM, calcein and Hoechst and imaged using an automated microscope. During acquisition, four subimages are combined in real time into a 2×2 mosaic using image stitching (IST). This yields 3 'RAW' images (TMRM, calcein and Hoechst) for each well. **B)** Image processing pipeline for the RAW images obtained in a. After processing, each RAW image is converted into an image suited for descriptor extraction: a 'masked' TMRM image (MSK TMRM), a 'masked' calcein image (MSK calcein) and a 'watershed' Hoechst image (WS Hoechst). **C)** Descriptor data are extracted from the processed images, normalized and subjected to a QC step. The resulting data set can then be analyzed and visualized by various means (see main text for details). AND, Boolean AND operator; BG, background image, BIN, binary image; COR, background-corrected image; MED, median-filtered image; MSK, masked image; RAW, image directly from microscope; RBC, rolling-ball correction; SUB, background subtraction; T, thresholding; THF, top-hat filter, WS, watershed operation.

Table 4.1: Descriptors calculated for each well.

No[a]	Reporter	Descriptor	Symbol	Definition/meaning of descriptor[b]
1	TMRM	Aspect ratio	AR	Ratio between major axis and minor axis of an ellipse equivalent to the object: measure of mitochondrial length
2	TMRM	Area/Box	Ab	The ratio between the area of an object and the area of its bounding box
3	TMRM	Box XonY	Bxy	Ratio between the width and height of the object's bounding box
4	TMRM	Density mean	Dm	Average intensity of the object (grayvalue): average mitochondrial intensity of the TMRM signal
5	TMRM	Axis minor	Axm	Length of the minor axis of the ellipse with same moments of order 1 and 2 as the object (pixels)
6	TMRM	Diameter max	Dimax	Length of the longest line joining two points of the object's outline and passing through the object's centroid (pixels)
7	TMRM	Diameter min	Dimin	Length of shortest line joining two points of the object's outline and passing through the object's centroid (pixels)
8	TMRM	Diameter mean	Dim	Average length of diameters measured at 2-degree intervals and passing through the object's centroid
9	TMRM	Radius max	Rmax	Maximum distance between the object's centroid and outline (pixels)
10	TMRM	Radius min	Rmin	Minimum distance between the object's centroid and outline (pixels)
11	TMRM	Perimeter ellipse	Pe	The perimeter of the ellipse surrounding the outline of each object (pixels)
12	TMRM	Radius ratio	Rr	Ratio between Rmax and Rmin
13	TMRM	Roundness	*F*	Perimeter2/(4 × π × Area; AKA formfactor): measure of mitochondrial length and degree of branching
14	TMRM	Length	Le	Feret diameter (caliper length) along the major axis of the object (pixels)
15	TMRM	Width	Wi	Feret diameter (caliper length) along the minor axis of the object (pixels)
16	TMRM	Perimeter2	P2	Chain code length of the outline (pixels)
17	TMRM	IOD	IOD	Integrated optical density of all objects (grayvalue): sum of all mitochondrial TMRM pixel intensity values
18	TMRM	Perimeter convex	Pc	Perimeter of the convex outline of the object (pixels)
19	TMRM	Perimeter	Pe	Length of the object's outline (pixels)
20	TMRM	Perimeter ratio	Pr	Ratio of convex perimeter to perimeter
21	TMRM	Area polygon	Ap	Area included in the polygon defining the object's outline (same polygon as used for Perimeter)
22	TMRM	Count	Cou	Size-weighted object 'count' (number of objects)
23	TMRM	Box width	Bw	Width of the object's bounding box (pixels)
24	TMRM	Box height	Bh	Height of the object's bounding box (pixels)
25	TMRM	Feret min	Fmin	Smallest feret (caliper) length (pixels)
26	TMRM	Feret max	Fmax	Longest feret (caliper) length (pixels)
27	TMRM	Feret mean	Fm	Average feret (caliper) length (pixels)
28	TMRM	Density min	Dmin	Minimum density inside the object (grayvalue)

Table 4.2: Descriptors calculated for each well (continued).

No[a]	Reporter	Descriptor	Symbol	Definition/meaning of descriptor[b]
29	TMRM	Density max	Dmax	Maximum density inside the object (grayvalue)
30	TMRM	Density s.d.	Dstdv	Standard deviation of intensity or density inside the object (grayvalue)
31	TMRM	Margination	Ma	The distribution of intensity between the center of an object and the edge of the object
32	TMRM	Area sum	Asum	Total area of the mitochondrial objects (pixels). The average size of the mitochondrial objects (Am) is given by Asum/Ot
33	TMRM	Objects total	Ot	Total number of objects: total number of mitochondria
34	Calcein	Area sum	Casum	Total area of the objects (pixels)
35	Calcein	IOD sum	CaIOD	Integrated pixel intensity of the objects (grayvalue)
36	Hoechst	Nn	Nn	Total number of objects: total number of nuclei/cells (assuming 1 nuclear object per cell)
37	Hoechst	H. area	An	Average area of the objects (pixels): average area of the nuclei
38	Hoechst	H. roundness	Fn	Roundness of objects: describing nuclear shape
39	Derived	Cell mito ratio	Mm	Given by Asum/Casum: A measure of mitochondrial mass
40	Derived	Norm mito area	Amt	Given by Asum/Nn: equaling the total mitochondrial area (in pixels) per cell
41	Derived	Norm mito number	Nc	Given by Ot/Nn: equaling the average number of mitochondrial objects per cell. Asum/Ot equals the area (size) of individual mitochondrial objects (Am)
42	Derived	Norm cyto area	Casum/Nn	Average size of the object (pixels): a measure of average cell size
43	Derived	Confluence (%)	C%	Fraction/percentage of the image covered: a measure of cell confluence
44	Derived	Calcein fluoresence	CaIOD/ Casum	Average intensity per cellular pixel

[a]Corresponding to the number of the descriptor in the provided MATLAB m-file (*Iannetti_MATLAB.m*). [b]Adapted from the definitions in the Image Pro Plus software. Where the unit measurement is not differently specified in parentheses after the meaning in the definition column, it is arbitrary units (a.u.). The first 31 descriptors were used in a previous study for PCA and machine learning[27].

Fluorescent reporters. TMRM (Fig. 4.2a) is a fluorescent lipophilic cation that accumulates within the mitochondrial matrix in a $\Delta\psi$-dependent manner. This results in a mitochondria-specific fluorescence signal that allows the analysis of mitochondrial morphology and semiquantitative $\Delta\psi$ analysis. TMRM is maximally excited by 552-nm light and maximally emits fluorescence light at 578 nm (Fig. 4.2b). Importantly, matrix accumulation of TMRM depends not only on $\Delta\psi$, but also on the electrical potential of the plasma membrane (ΔV; ref. Koopman et al., 2008). Therefore, if there is doubt about potential ΔV changes, they should be quantified using electrophysiological techniques54 or an alternative strategy (Nicholls, 2006). In addition, when its concentration in the mitochondrial matrix exceeds a certain threshold, TMRM quenches its own fluorescence ('autoquenching'). This leads to a reduction in the TMRM

fluorescence signal and erroneous underestimation of $\Delta\psi$. When illuminated using an inappropriately high excitation intensity or for a long period of time, TMRM can display substantial photobleaching and, by acting as a photosensitizer, can stimulate the opening of the mitochondrial permeability transition pore (Hüser et al., 1998; Falchi et al., 2005; Blanchet et al., 2014). Of note, to detect hyperpolarization (i.e., $\Delta\psi$ values becoming more negative) TMRM needs to be present outside the cells during the measurement (Forkink et al., 2014). Calcein is used to label living cells in cell viability and cytotoxicity assays (Wang et al., 1993). Its non fluorescent AM form (calcein–AM) is taken up by the cells. There it is converted by intracellular esterases into the fluorescent and hydrophilic calcein molecule by cleavage of its AM tail (Fig. 4.2a). This process traps the calcein inside the cell. Calcein is maximally excited by 493-nm light, and it maximally emits fluorescence light at 514 nm (Fig. 4.2b). Of note, AM-ester-based fluorescent molecules, but not their de-esterified forms, can be actively extruded from the cell by multidrug transporters (Homolya et al., 1993). Hoechst (Fig. 4.2a) is one of the most widely used stains for DNA quantification. It is a cell-permeable fluorescent molecule that specifically binds to the A–T base pairs in the minor groove of double-stranded DNA (dsDNA). By itself Hoechst displays a weak fluorescence, which is greatly enhanced upon DNA binding. Hoechst is maximally excited by 352-nm light and maximally emits fluorescence light at 455 nm (Fig. 4.2b).

Microscopy hardware. In this protocol, a BD Pathway 855 system (Fig. 4.2c–e) is used to perform automated image acquisition. This microscope is equipped with an environmental control system (temperature and CO_2), which is necessary for live cell imaging, and a shielded measuring chamber that prevents interference from ambient light. It also features an automated pipetting robot, which is not used in this protocol. Excitation light is provided by two mercury arc lamps (Lamp A and Lamp B; Figs. 4.2d and 4.3a,b), from which the required wavelength is selected by two excitation filter wheels (Wheel A and Wheel B). Excitation light intensity can be independently controlled for both lamps via two dichroic mirror wheels (Wheel 1 and Wheel 2); excitation light

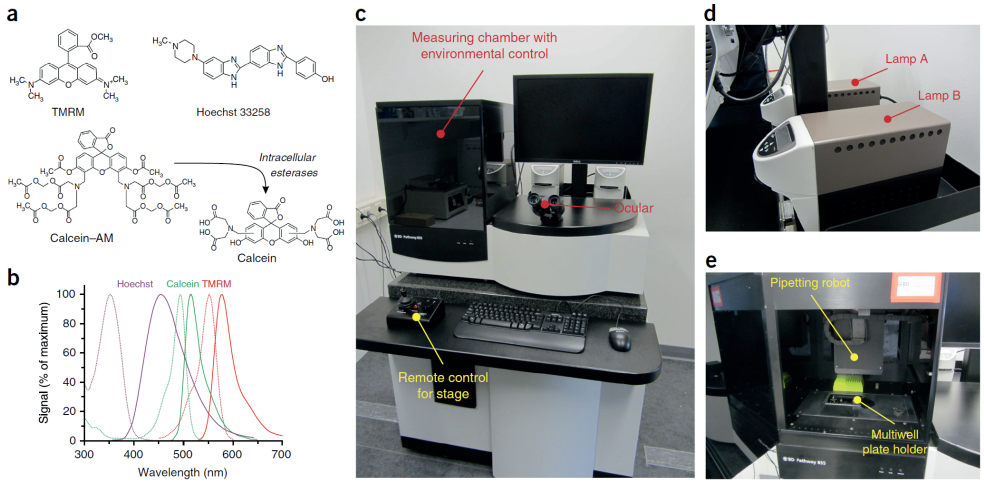


Figure 4.2: Spectral properties of the fluorescent reporter molecules and microscopy hardware. **A)** Chemical structures of TMRM, calcein–AM, calcein and Hoechst 33258 ('Hoechst'). Structures were obtained from http://www.lifetechnologies.com. **B)** Excitation (dotted lines) and emission (continuous lines) of the used reporter molecules. Spectral information was obtained from http://www.chroma.com. **C)** Front-view of the BD Pathway 855 automated microscopy system showing the light-shielded and environment-controlled measuring chamber, the ocular and the remote control of the microscopy stage. **D)** View of the two mercury arc lamps (lamp A and lamp B) used for excitation. **E)** Inside view of the measuring chamber revealing the pipetting robot and the holder for the 96-well plate.

is directed to the cells via an air (dry) 40× objective. In this protocol, wide-field images are acquired, and therefore the spinning disk confocal optics of the Pathway 855 system are not used. TMRM/calcein/Hoechst emission light is directed toward a cooled CCD (charge-coupled device) camera via Wheel 2 and an emission filter wheel. Taking into account the spectral properties of the reporter molecules (Fig. 4.2b), appropriate excitation ('Ex'), dichroic ('Dich') and emission ('Em') filters were selected (Fig. 4.3c–e). This allowed acquisition of specific TMRM, calcein and Hoechst fluorescence images from co-stained cells.

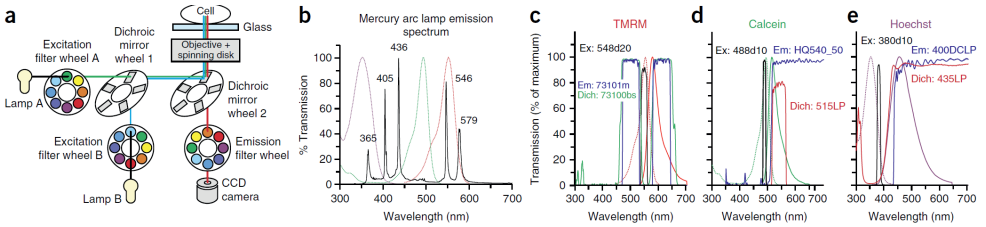


Figure 4.3: Microscopy light path and spectral properties of the excitation source and filters. A) Light path and filter configuration of the BD Pathway 855 system (see main text for details). **B)** Emission spectrum of the mercury arc lamps used for excitation (black curve). Numerals indicate peak wavelengths, and dotted lines represent the excitation spectrum of TMRM (red), calcein (green) and Hoechst (purple). **C)** The filter configuration used for TMRM. **D)** The filter configuration used for calcein. **E)** The filter configuration used for Hoechst. Information for this figure was obtained from http://www.bdbiosciences.com (**A**), http://searchlight.semrock.com (**B**), http://www.lifetechnologies.com (**B-E**) and http://www.chroma.com (**C**–**E**).

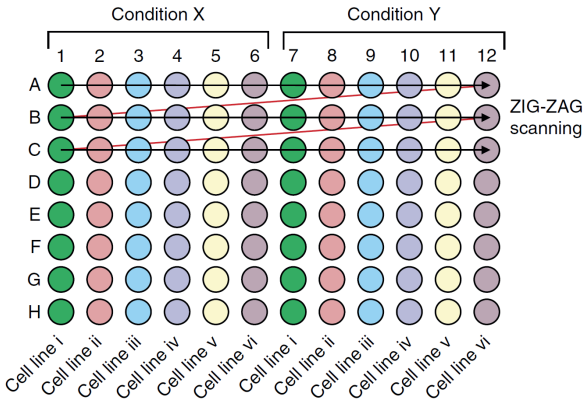


Figure 4.4: Layout of the 96-well plate and image acquisition strategy. Typical layout of the 96-well plate, allowing analysis of six different cell lines (i–vi) under two experimental conditions (X and Y). Images from individual wells are acquired, starting at the top left of the plate (well A1) and moving downward toward the lower right of the plate (well H12), using 'ZIG-ZAG' scanning mode (i.e., once well A12 is reached, imaging continues with well B1 and so on).

Image acquisition and image properties. The cell lines to be analyzed are seeded in a column-wise manner on the 96-well plate (see the 'Control cell lines and replicates' section for details) and imaged using the 'ZIG-ZAG'

scanning mode option (Fig. 4.4). Automatic focusing is carried out using an integrated laser-based autofocus system. The microscope stage was motionless, so images of subsequent wells were acquired by moving the objective. For each well and reporter molecule, four sub images with a bit depth of 12-bit (i.e., containing a maximum of 4,096 grayvalues) were acquired and automatically combined during acquisition by 'image stitching' (Fig. 4.1a). The resulting 2 × 2 RAW image was stored as an uncompressed 16-bit TIFF (tagged image file format) file (i.e., with a range of 216 = 65,536 grayvalues) having a file size of 2,679 kb. Each RAW image had a dimension of 1,344 × 1,024 pixels (equalling 210.5 μm × 160.4 μm). In total, 288 RAW images were obtained for each plate (with a total file-size of 771 Mb) and stored to the hard-disk.

4.3 Image processing and descriptor extraction.

Automated image processing and descriptor extraction/calculation is carried out using Image Pro Plus (IPP) and MATLAB software. Once acquired, each RAW TMRM, calcein and Hoechst image (set) is processed independently (Fig. 4.1b). The processing pipeline for each reporter molecule is described in more detail directly below. From the RAW TMRM image (Fig. 4.5a; left panel of top row), a background image was calculated using the 'rolling ball' correction algorithm (Sternberg, 1983; Russ and Neal, 2016). This algorithm filters out objects and requires one parameter: the rolling ball 'feature width'. The latter should be set to at least the size of the largest object that is not part of the background. For TMRM-stained PHSFs, a feature width of 140 was empirically determined. Subtraction of the background image from the RAW image yielded a background-corrected image (COR). The COR image was processed using a top-hat spatial filter (THF, 7 × 7 kernel, 1 pass, strength 10). The top-hat filter functions as a 'particle isolator' that increases the grayvalue of mitochondrial objects (see Box 1 for details). To remove noise pixels, the THF image is subsequently median-filtered (MED, 3 × 3 kernel, 6 passes; see Box 1) and 'thresholded' to yield a binary (BIN) image. An optimal threshold (T) value of 40 grayvalues was empirically determined (Fig. 4.1). In the BIN image,

white mitochondrial objects (grayvalue of 65,535) are represented on a black background (which has a grayvalue of 0). Finally, the COR image is combined with the BIN image using a Boolean AND operator. This operator will keep only pixels that are 'on' (i.e., that have a grayvalue that is not 0) in both the COR and BIN images. This generates a 'masked' image (MSK) in which the background is black (grayvalue = 0) and each mitochondrial object pixel retains its TMRM grayvalue from the COR image. The MSK image (Fig. 4.5a; left panel of lower row) is used for descriptor extraction. The various processing steps of the TMRM images (Fig. 4.1b) are summarized in Fig. 4.5b. Once the MSK image is obtained, a look-up table (LUT) can be used to color-code intensity values (Fig. 4.5b; 'MSK+LUT' image). As a first example of data visualization, mitochondrial objects can be sorted to yield a 'mitogram' according to the numerical value of a specific descriptor, here according to their form factor (F; Fig. 4.5c; left panel). Magnification of the mitogram (white box) can be used to visually inspect heterogeneities in TMRM staining for individual mitochondrial objects (F; Fig. 4.5c; right panel). Quantification of mitochondrial descriptors in the mitogram (Fig. 4.5d) can, for instance, be used to assess the average mitochondrial object length (Le), width (Wi), F, margination (Ma) and TMRM fluorescence intensity (Dm). The RAW calcein image (Fig. 4.5a; middle panel of upper row) is first processed using the rolling ball algorithm (using an empirically determined feature width of 140) to obtain a background image (Fig. 4.1a; lower row). The COR image is then obtained by subtracting the background image from the RAW image. The latter is thresholded (T value set to 40; Fig. S1), resulting in the BIN image. Like the TMRM images, the calcein COR and BIN images were combined to obtain a calcein MSK image. The MSK image (Fig. 4.5a; middle panel of lower row) is used for descriptor extraction. The RAW Hoechst image (Fig. 4.5a; right panel of upper row) was first thresholded (T) to obtain a binary image (using an empirically determined cutoff grayvalue of 500; Fig. 4.1b). This image was subsequently filtered by applying a 7 × 7 MED filter (1 pass). The resulting BIN image is then subjected to a watershed-split operation (WS) to separate nuclear objects that are touching. The WS image (Fig. 4.5a; right panel of

lower row) is used for descriptor extraction.

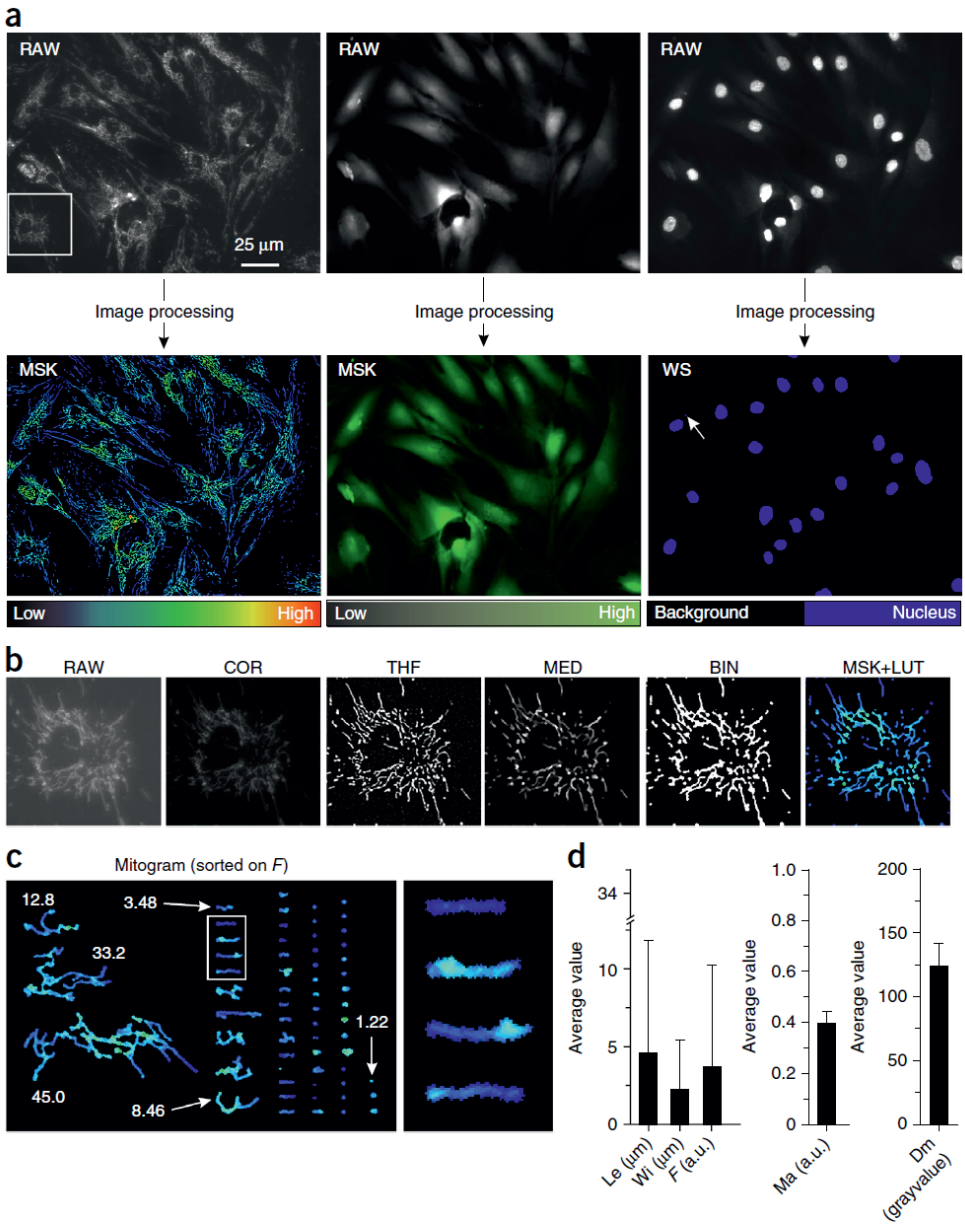


Figure 4.5: Overall image quantification strategy. (See caption on next page.)

Figure 4.5: A) Upper row: typical example of a 16-bit TMRM, calcein and Hoechst image obtained from the same well (RAW images; grayvalue range: 0 – 65,535). For visualization purposes, grayvalues between 0 and 700 are depicted. Lower row: images obtained after image processing. **B)** Illustration of the TMRM image processing pipeline for the cell highlighted (box) in a (see main text for details). **C)** Mitogram calculated from the MSK+LUT image in **B**. Mitochondrial objects are depicted according to their form factor (F) (left panel) reflecting the degree of mitochondrial length and degree of branching. Numerals indicate the F value of the various mitochondrial objects. The colors reflect the intensity of the TMRM fluorescence signal, ranging between low (black background) and high (green). The magnification (white box and right panel) shows four individual mitochondrial objects to illustrate heterogeneous TMRM fluorescence. **D)** Average value of five descriptors (Table 4.1) calculated for the 61 objects in the MSK+LUT image in **B**. Descriptors are mitochondrial length (Le), mitochondrial width (Wi), mitochondrial form factor (F), margination (Ma) and average mitochondrial TMRM intensity (Dm). Spatial descriptors (obtained in pixel units) were calibrated (to micrometers) using a pixel size of 0.157 μm/pixel. Bars represent standard deviation. BIN, binary image; COR, background corrected image; MED, median-filtered image; MSK, masked image; RAW, image directly from microscope; LUT, look-up table; THF, top-hat filter; WS, image after watershed-split operation.

Control cell lines and replicates. The cell lines to be compared and experimental conditions should be part of the same plate (Fig. 4.4; ref. Bray and Carpenter, 2004). The well replicates are oriented from the top to the bottom of the plate (columns) to make sure that replicates of the same cell line and/or condition are acquired with the same time delay during ZIG-ZAG scanning. In a typical experiment, eight replicates (i.e., one column of 8 wells) are performed per plate (technical replicate) in at least three different plates from three different cell cultures (biological replicates). Technical variation can arise from (combined) errors in reagent preparation, concentration changes due to solvent evaporation, anomalies in liquid handling, pipetting errors and pipette malfunction, variations in incubation times, temperature differences and plate imaging artefacts (column effects, border effects). Biological variation can be considered an intrinsic property of living cells but might also be related to the cell system used. In the case of PHSFs (et al. Tigges, 2014), it is well established that growth and biological characteristics change at high passage number and high cell density (even occurring in the culture flask before seed-

Box 1 | Median and top-hat spatial filtering

Spatial filtering[62,73]: The properties of a spatial filter are given by a square $N \times N$ matrix of numbers (a 'kernel'), which operates on pixels in the image. Because the value of N is uneven, this means that each filter kernel has a center 'pixel'. For instance, a 3 × 3 filter kernel h and a (partial) 3 × 3 image I (with the numbers indicating pixel intensity) could be

$$h = \begin{bmatrix} 0 & -1 & 1 \\ 0 & 2 & 1 \\ 1 & 2 & 3 \end{bmatrix} \quad I = \begin{bmatrix} 1 & 0 & 1 \\ 1 & 3 & 0 \\ 1 & 2 & 2 \end{bmatrix}$$

The result of applying the spatial filter h on the image I will be calculated as follows:

1. Each pixel in the image I is multiplied by the corresponding element in the kernel h:

$$0 \times 1 + (-1) \times 0 + 1 \times 1 + 0 \times 1 + 2 \times 3 + 1 \times 0 + 1 \times 1 + 2 \times 2 + 3 \times 2 = 18$$

2. The result of this multiplication is divided by the sum of the kernel h: 18/(0 – 1 + 1 + 0 + 2 + 1 + 1 + 2 + 3) = 2
3. The result is scaled and boosted (facultative).
4. The center pixel in the original image (i.e., 3) is replaced by its filtered value (i.e., 2)

In practice, images are much larger than 3 × 3 pixels, and the kernel is moved across the image to process each pixel. Importantly, the new (filtered) value of each pixel is calculated from its original (unfiltered) value.

The median filter (MED): the median filter replaces the center pixel with the median value in its neighborhood, thereby removing noise from an image. For instance, for the 3 × 3 image above, the pixel values can be ranked from low to high as follows: 0 – 0 – 1 – 1 – 1 – 1 – 2 – 2 – 3. The central (median) value of this sequence equals 1, meaning that the original pixel value of 3 is replaced by 1. The median filter can be applied multiple times ('passes'), thereby amplifying its effect with each pass (**Supplementary Fig. 6A**). For effective use, the kernel size of the median filter should be smaller than that of the objects that need to be retained in the image (**Supplementary Fig. 6A**).

The top-hat filter (THF): This filter is suited for isolation of bright objects from a dark background[24]. Its 7 × 7 kernel h is

$$h = \begin{bmatrix} 0 & 0 & -1 & -1 & -1 & 0 & 0 \\ 0 & -1 & -1 & -1 & -1 & -1 & 0 \\ -1 & -1 & 3 & 3 & 3 & -1 & -1 \\ -1 & -1 & 3 & 4 & 3 & -1 & -1 \\ -1 & -1 & 3 & 3 & 3 & -1 & -1 \\ 0 & -1 & -1 & -1 & -1 & -1 & 0 \\ 0 & 0 & -1 & -1 & -1 & 0 & 0 \end{bmatrix}$$

Like the median filter, the top-hat filter can be applied multiple times (passes), which amplifies its effect with each pass (**Supplementary Fig. 6B**). The 'strength' of the top-hat filter can be varied from 1 to 10, and this determines how much of the filtering effect is applied to the image (**Supplementary Fig. 6B**). A value of 10 specifies that the full strength (100%) of the filtered result should be applied to each pixel. Values below 10 reduce the weight of the filter—i.e., a value of 1 indicates that only 10% of the difference between the filtered pixel value and the original pixel value is applied. For effective use, the kernel size of the top-hat filter should be larger than that of the objects that need to be retained in the image (**Supplementary Fig. 6B**).

ing the cells on the 96-well plates). In our experience, an absolute minimum of 24 wells need to be imaged for each individual condition (i.e., 8 wells in three different plates). At least one previously characterized (control) cell line should be present on each plate to allow normalization, plate-to-plate comparison and detection of anomalies (Bray and Carpenter, 2004). As a rule of thumb, we established, by manual analysis of rhodamine 123–, TMRM- and mtFP-stained cells7,19–23, that a typical primary human fibroblast cell line from a healthy volunteer (CT5120) displays key descriptor values between 3

and 6 (F), 2 and 3 (AR) and 50 and 150 (number of mitochondria per cell; Nc). Once it is established that the descriptor values of the control are within these previously established boundaries, it can be used for intraplate normalization of descriptor values for the other cell lines and experimental conditions (Fig. 4.1c).

Data analysis and quality control (QC). In this protocol, we apply PCA, which simultaneously considers all variables in a multidimensional space (Iannetti et al., 2015; Blanchet et al., 2011; Massart and Al., 1997), to analyze the obtained data set. PCA is a mathematical technique that reduces the dimensionality of the data while retaining most of the variation in the data set, thereby facilitating graphic visualization (Massart and Al., 1997) and explorative data analysis (Tukey, 1977). Dimensionality reduction is achieved by identifying directions, called PCs, along which the variation in the data is maximal. The sum of variation accounted for by each PC determines how many PCs are required to faithfully represent the data set (Ringnér and Ringner, 2008; Bro, 2014). There are several 'rules' for determining the number of PCs to include, such as 'Kaiser's stopping rule' and the 'Screen test' (Brown, 2009). In our experience, two PCs suffice to allow proper multivariate analysis and QC for the type of data generated in this protocol. Alternatively, other multivariate approaches, including cluster analysis and machine learning (Blanchet et al., 2015), can be applied (Massart and Al., 1997). Data analysis and quality control can be performed using the supplied MATLAB code in the m-file *Iannetti_ MATLAB.m* (Table 4.3 and the Supplementary Software), which carries out the following operations:

- It imports the numerical data generated by IPP into MATLAB.
- It calculates the derived descriptors (i.e., descriptor 39 to 44; see Table 2.1).
- It normalizes the data.
- It performs a PCA and creates a PCA graph and boxplot graph to visualize the data.

- It performs a QC step, to identify and remove outliers (i.e., individual wells) from the data set.
- It performs a second PCA after removal of the outliers (generates 'cleaned data').
- It calculates the 95% conidence ellipses of the 'cleaned' PCA data.
- It generates a PCA graph for visualization of the cleaned data and its 95% confidence ellipses.

Technical details related to the above operations are embedded in the *Iannetti_ MATLAB.m* file.

Table 4.3: Processing scripts and tutorial data files.

File name	Content of file
Files for image processing and extraction with IPP (directory: \Tutorial\IPP_processing_analysis\)	
Iannetti_IPP.bas	IPP script for image processing and quantification
RAW_TMRM.tif	RAW 16-bit TMRM image directly from the microscope (TIFF format)
RAW_Calcein.tif	RAW 16-bit calcein image directly from the microscope (TIFF format)
RAW_Hoechst.tif	RAW 16-bit Hoechst image directly from the microscope (TIFF format)
TMRM.cnt	Numerical data file: quantification data for the RAW_TMRM.tif image
Calcein.cnt	Numerical data file: quantification data for the RAW_Calcein.tif image
Hoechst.cnt	Numerical data file: quantification data for the RAW_Hoechst.tif image
Files for data visualization and QC with MATLAB (directory: \Tutorial\MATLAB_QC\)	
Iannetti_MATLAB.m	MATLAB m-file that performs the PCA and QC
auto.m	MATLAB m-file used by Iannetti_MATLAB.m
ellipses.m	MATLAB m-file used by Iannetti_MATLAB.m
import_cnt.m	MATLAB m-file used by Iannetti_MATLAB.m
headers.mat	MATLAB MAT-file used by Iannetti_MATLAB.m
ConditionX_ci.cii_TMRM.cnt	Numerical data file: TMRM quantification data for cell lines 1 and 2 (condition X)
ConditionX_ci.cii_Calcein.cnt	Numerical data file: calcein quantification data for cell lines 1 and 2 (condition X)
ConditionX_ci.cii_Hoechst.cnt	Numerical data file: Hoechst quantification data for cell lines 1 and 2 (condition X)
ConditionY_ci.cii_TMRM.cnt	Numerical data file: TMRM quantification data for cell lines 1 and 2 (condition Y)
ConditionY_ci.cii_Calcein.cnt	Numerical data file: calcein quantification data for cell lines 1 and 2 (condition Y)
ConditionY_ci.cii_Hoechst.cnt	Numerical data file: Hoechst quantification data for cell lines 1 and 2 (condition Y)
Other files (directory: \Tutorial\)	
DataExtraction.xlsm	Excel file that automatically extracts descriptor values from a .cnt file

4.4 Materials

4.4.1 Reagents

- Suitable cells of interest. The procedure below is optimized for PHSFs taken from human skin biopsies **! CAUTION** Take the necessary precautions when working with human samples. They should be handled in a biological safety cabinet. Experiments with human cell lines must adhere to the relevant local institutional and governmental regulations and generally require informed consent.

- Medium 199 with HEPES and Phenol Red (Invitrogen, cat. no. 12340-030)

- Medium 199 without HEPES and Phenol Red (Invitrogen, cat. no. 11043-023)

- FBS (Greiner Bio-One, cat. no. 758093) Penicillin–streptomycin solution, 100× (Corning, cat. no. 30-002-CI)

- HEPES (1 M; Invitrogen, cat. no. 15630-08)

- DMSO (MW = 78.134 g/mol; CAS: 67-68-5; Sigma-Aldrich, cat. no. D5879-100ML) **! CAUTION** DMSO is skin-permeable and irritating.

- Trypsin–EDTA (0.5% (wt/vol)) solution, without Phenol Red, 10× concentrated (Gibco/Life Technologies, cat. no. 15400-054). Store the solution between -5 and -20 °C for up to 18 months

- PBS (pH 7.2; Gibco/Life Technologies, cat. no. 20012-068)

- Tetramethyl rhodamine methyl ester (TMRM; MW = 500.93 g/mol; CAS: 115532-50-8; Invitrogen, cat. no. T668)

- Calcein–AM (MW = 622.53 g/mol; CAS: 154071-48-4; Ebioscience, cat. no. 65-0853-39)

- Hoechst 33258 (MW = 533.88 g/mol; CAS: 23491-45-4; Invitrogen, cat. no. 94406) **! CAUTION** Hoechst stains are known mutagens and should be handled with care. The dye must be disposed of safely and in accordance with applicable regulations.

4.4.2 Equipment

- Culture lasks (Greiner Bio-One): 75 cm^2 (cat. no. 658170) and 175 cm^2 (cat. no. 661160)
- Centrifuge tubes (Greiner Bio-One): 15 ml (cat. no. 188271) and 50 ml (cat. no. 227261)
- Reagent reservoir (35 ml; Greiner Bio-One, cat. no. 9103006)
- Polystyrene 96-well cell culture microplates (μClear/black; working volume: 25-340 μl; total well volume: 392 μl; growth area per well 34 mm^2; glass thickness: 190 μm; Greiner Bio-One, cat. no. 655090)
- Cell culture low cabinet (Model EF/S 4; Telstar Laboratory Equipment)
- Incubator for cell culture (Heracell 150i; Thermo Fisher Scientiic)
- Water bath (Model 1003; GFL)
- Neubauer hemocytometer (Hausser Scientiic)
- Multi-(12-)channel pipette (Model m300; Biohit/Sartorius)

Microscopes

- An inverted microscope for cell culture (Model DM IL; Leica Microsystems)
- An automated multiwell luorescence microscope with environmental (CO_2 and temperature) controls: Pathway 855 High-content Bioimager (Becton Dickinson). This system features two mercury arc lamps A and B (Becton Dickinson, cat. no. 341032)

Computing hardware and software

- A PC workstation (Windows 7 Pro 64-bit; Dell T7500; Xeon E5620 2.40 GHz; 24 GB RAM, Nvidia Quadro 2000; Dell Computer Corp.)
- MATLAB 8.2.0.701 (R2013b; The MathWorks)
- MATLAB Statistics Toolbox 8.3 (R2013b; The MathWorks)
- Image Pro Plus 6.3 (IPP; Media Cybernetics)
- Microsoft Excel (Microsoft Ofice 2010, Microsoft)
- Origin Pro 2015 (OriginLab Corp.)

4.4.3 Reagent setup

Culture medium Medium 199 (M199) is used for cell culture, and it contains HEPES and Phenol Red. This medium should be supplemented with 10% (vol/vol) FCS, 100 IU/ml penicillin and 100 IU/ml streptomycin. The solution should be stored at 4 °C in the dark and used within 1 month after preparation. The complete formulation of this medium is provided in Table S2.

Assay medium This is based on a special variant of the culture medium (M199) that does not contain Phenol Red or HEPES. This medium should be supplemented with 25 mM HEPES and is used for diluting the fluorescent probes and for washing the cells. The assay medium should be stored at 4 °C in the dark and used within 1 month after preparation. The complete formulation of this medium is provided in Table S2.

TMRM stock (500 mM) TMRM is provided as a lyophilized off-white powder (25 mg) that should be protected from light/moisture and stored at -20° C. The solid should be dissolved in dry (water-free) DMSO from a freshly opened bottle to prepare a TMRM stock solution of 500 μM. This solution should be divided into 10-μl aliquots, which should be stored at -20 °C in the dark. Each aliquot should be freshly thawed and used only

once to avoid repeated freezing and thawing. The TMRM stock solution can be used for at least a year.

Calcein–AM stock (5 mM) Calcein–AM is provided as a lyophilized off-white solid (typically in 20 × 50-μg batches). It should be shielded from light/moisture and stored at -20 °C. The solid should be dissolved in dry (water-free) DMSO from a freshly opened bottle, yielding a stock solution of 5 mM. This solution should be divided in 10-μl aliquots, which should be stored at -20 °C in the dark. Each aliquot should be used while fresh and discarded after use to avoid repeated freezing and thawing. The calcein–AM stock solution can be used for at least a year.

Hoechst 33258 stock (1 mg/ml) Hoechst 33258 is delivered as a 1 mg/ml stock solution in water (1.87 mM), and it should be stored at 2–8 °C in the dark. The Hoechst 33258 stock solution can be used for at least a year.

4.5 Procedure

Seeding of the cells on a 96-well plate • *TIMING* ∼90 min/plate

1. Wash the cells twice with 1× PBS.
2. Add an adequate volume of 1× Trypsin–EDTA (diluted in PBS) to cover the cell-containing surface of the culture flask (typically 1 ml for a T75 culture flask), and incubate it for 5 min (37 °C, 5% (wt/vol) CO2).
3. Resuspend the cells in assay medium prewarmed to 37 °C (typically by adding 9 ml of medium for a T75 culture flask).
4. Perform a thorough cell count using a cell counting chamber or Coulter counter.
5. Resuspend the cells and seed the cells into a 96-well plate so that each well contains 2,000–3,000 cells in 100 μl of culture medium. Culture the cells for 24 h (37 °C, 5% (wt/vol) CO_2) to reach a final confluence of 50–60%.

The number of cells to be seeded to reach this confluence generally differs per cell line or type, and it needs to be empirically determined. For a typical cell seeding example, see Fig. 4.4.

▲ ***CRITICAL STEP*** Reaching a correct level of cell confluence after 24 h (illustrated in Fig. S2) is crucial for reliable image quantification.

? TROUBLESHOOTING

Cell staining and imaging • *TIMING* ~90 min/plate

6. 1 h before image acquisition, set the temperature (to 37 °C) and the CO_2 control (to 5%), and turn on lamps A and B (excitation sources) of the microscope.

7. Mount the 40× objective on the microscope and allow it to thermally equilibrate.

8. Prewarm the assay medium to 37 °C in a water bath.

9. Prepare a 250 nM TMRM 'loading solution' by diluting the 500 μM TMRM stock solution in the prewarmed assay medium. Take care that the final DMSO concentration in the loading solution does not exceed 0.1% (vol/vol). Use the same TMRM loading solution for all plates measured on the same day to reduce technical variation.

10. To start TMRM staining, add 20 μl of the TMRM loading solution from Step 9 (250 nM) to each well using the 12-channel pipette. This yields a final TMRM concentration of 50 nM.

    ▲ ***CRITICAL STEP*** Because of evaporation, the total volume of culture medium in each well will be reduced. We empirically established that only 80 μl of the initial 100 μl of culture medium is left in each well after 24 h of cell culture. There was no substantial difference in TMRM intensity, calcein intensity or Hoechst intensity between the wells at the outer rim and those in the central part of the plate.

11. Carefully check whether the volume of TMRM loading solution in each pipette tip is correct (air bubbles should be absent) before pipetting.

12. To mix, gently pipette up and down four times after addition of the TMRM loading solution.

13. Incubate the cells for 30 min at 37 °C, 5% CO_2.

14. During the cells' incubation with TMRM, prepare a loading solution containing a 5 μM final concentration of calcein and a 1.5 μg/ml final concentration of Hoechst in prewarmed assay medium. Use the same calcein/Hoechst loading solution for all plates measured on the same day to reduce technical variation.

15. After the 30-min TMRM incubation, add 100 μl of the calcein/Hoechst loading solution to each well using the 12-channel pipette, without washing or mixing. Add the calcein/Hoechst loading solution at the edge of each well (so not directly on top of the cells), holding the pipette horizontal. Addition of the calcein/Hoechst loading solution dilutes the extracellular TMRM concentration, which is required for signal stability (Fig. S3). The final extracellular concentrations should now equal 25 nM (TMRM), 2.5 μM (calcein) and 0.75 μg/ml (Hoechst).

16. Place the 96-well plate in the BD Pathway 855 measuring chamber, and manually focus on a random well. (For this microscopy system, typically a Z-position value near 5,200 is required.) Start the TMRM image acquisition using a predefined macro (full macro settings are provided in Table S4). This acquisition will take 15 min. Next, keep the plate inside the measuring chamber and incubate for another 5 min to complete the calcein/Hoechst staining (20 min in total will have passed after completion of Step 15).
? TROUBLESHOOTING

17. Discard the TMRM/calcein/Hoechst–containing medium by turning the plate upside down in a single fluid motion.

18. Gently wash each well in the plate 2 times (12-channel pipette) with 100 μl of assay medium. This will remove extracellular calcein, which would otherwise induce a continuous increase in calcein signal over time.

19. Pipette 100 μl of assay medium into each well (12-channel pipette).

20. Start the calcein/Hoechst image acquisition (this will take 20 min).
    ? TROUBLESHOOTING ■ ***PAUSE POINT*** Images are automatically saved on the microscope computer; the rest of the protocol can be carried out at any moment later in time.

Image processing and descriptor extraction with IPP • *TIMING* ∼30 min/plate

▲ ***CRITICAL*** For this part of the protocol, as well as the next section, we provide tutorial data files (Supplementary Software). The .zip file needs to be copied onto a hard-drive and extracted, yielding a directory named `\Tutorial\`, the contents of which are given in Table 4.3. Processing and quantification of the RAW images, as visualized in the flowchart (Fig. 4.1b), is performed by a single IPP Basic script (*Iannetti_IPP.bas*) that automatically carries out the various image processing described in the *'Image processing and descriptor extraction*' Section by applying built-in IPP functions. Further technical details related to the image processing and descriptor extraction code are embedded within the *Iannetti_IPP.bas* file. Typical results obtained in this section are shown in Fig. 4.6.

21. Start the IPP software. Load the *Iannetti_IPP.bas* script. To do this, click 'Macro' 'Macro' > 'Change', select *Iannetti_IPP.bas* and click 'Open' > 'OK'. The Macro menu now contains the following six items: TMRM_Processing, TMRM_DescriptorExtraction, Calcein_Processing, Calcein_DescriptorExtraction, Hoechst_Processing and Hoechst_DescriptorExtraction.

22. The provided IPP script assumes a fixed directory for data storage. In the provided code, this is `c:\Users\Khondrion\Desktop\cnt\` Adjust the script to your working directory, changing the below code. Click 'Macro' > 'Macro' > 'Edit' and replace the directory name with your working directory:

    In the section 'Sub TMRM_DescriptorExtraction', change the line

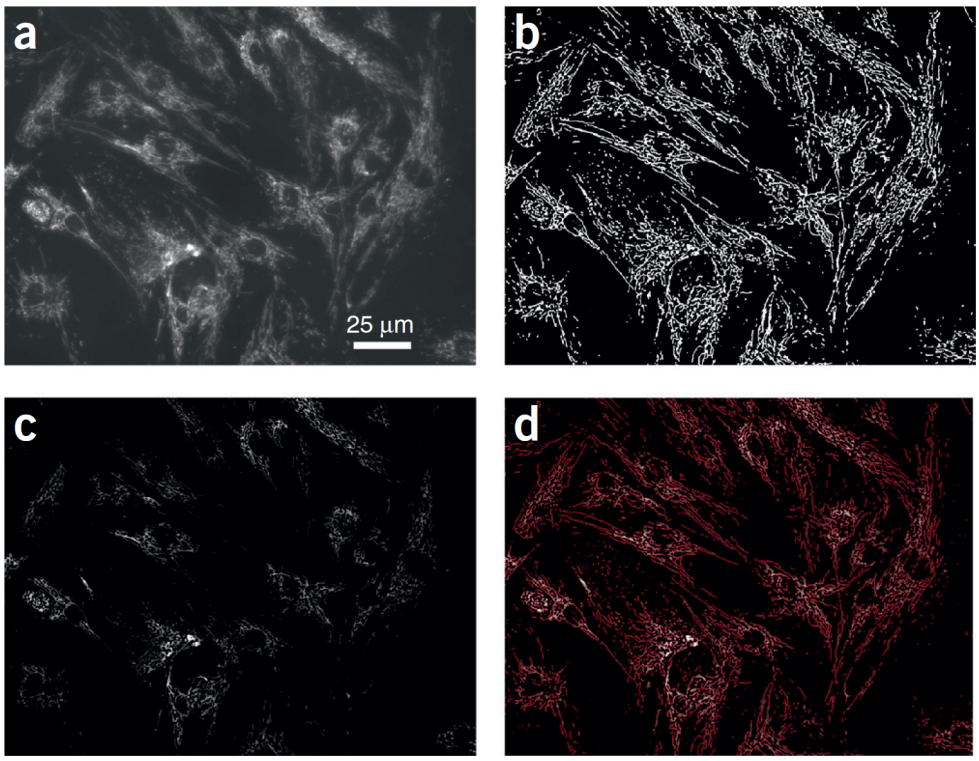


Figure 4.6: Image processing of the TMRM image. A) The *RAW_ TMRM.tif* image. **B)** The BIN image calculated from the *RAW_ TMRM.tif* image. **C)** The MSK image calculated from the *RAW_ TMRM.tif* image. **D)** Highlighted mitochondrial objects (red outlines) that are quantified.

"ret = IpBlbSaveData("`C:\Users\Khondrion\Desktop\cnt\`...",
In the section 'Sub Calcein_DescriptorExtraction', change the line
"ret = IpBlbSaveData("`C:\Users\Khondrion\Desktop\cnt`..."
In the section 'Sub Hoechst_DescriptorExtraction', change the line
"ret = IpBlbSaveData(`C:\Users\Khondrion\Desktop\cnt`..."

23. Save the script with the new working directory by clicking 'File' > 'Save'.

24. Load the provided TMRM example image into IPP. To do this, click 'Sequence' > 'Merge files...', select 'RAW_TMRM.tif' and click 'Open'. The igure should appear as in Fig. 4.6a.

▲ ***CRITICAL STEP*** The IPP macro was designed to also operate on a sequence of multiple images (i.e., obtained from a 96-well plate; not provided here). To use the IPP macro on an image sequence, this first needs to be created by using the 'Sequence' > 'Merge files' menu option in IPP, followed by selection of the first and last image and clicking 'Open'.

25. Perform the image processing of the 'RAW_TMRM.tif image', by clicking 'Macro' > 'TMRM_Processing'. This creates the BIN image (Fig. 4.6b) and an MSK image (Fig. 4.6c).
? TROUBLESHOOTING

26. Perform the image quantiication by clicking on the MSK image, and then click 'Macro' > 'TMRM_DescriptorExtraction'. The quantified individual mitochondrial objects are now highlighted by a red outline (Fig. 4.6d), and the numerical data are saved in the working directory (TMRM.cnt file).
▲ ***CRITICAL STEP*** For convenience, example .cnt files have been included in the Supplementary Software. These files should be moved from the `Tutorial\IPP_processing_analysis\` directory to another directory before re-executing Step 27 to prevent them being overwritten.

27. Repeat Steps 25 to 27 to process and quantify the provided Calcein.tif and Hoechst.tif images to obtain the Calcein.cnt and Hoechst.cnt files
▲ ***CRITICAL STEP*** For each 96-well plate, descriptor data are stored in three files: TMRM.cnt (33 descriptors of interest), Calcein.cnt (2 descriptors of interest) and Hoechst.cnt (3 descriptors of interest). These files can be opened and further `processed/analyzed/visualized` using Excel, MATLAB, Origin Pro or other data analysis software. We provide an Excel file (DataExtraction.xlsm) in the Supplementary Software for easy inspection of the .cnt files and extraction of numerical values for specific descriptors by drag-and-drop.
■ ***PAUSE POINT*** After generation of the .cnt files, the remainder of the protocol can be carried out at a later time.

Data visualization and QC with MATLAB • *TIMING* 15 min/plate

▲ ***CRITICAL*** To illustrate this part of the protocol, we provided the .cnt files for a larger data set obtained from a 96-well plate (Table 4.3). In this experiment, we aimed to quantify mitochondrial morphofunction in two primary human fibroblast cell lines (1 and 2) that were cultured under two experimental conditions (X and Y). In this example, 48 wells were measured for each condition (i.e., 16 wells in three independent experiments/plates). Importantly, optimal results required a plate layout compatible with Fig. 4.4, in which both cell lines were measured under both conditions in the same plate. Cell line 1 was used as a control, and the average descriptor values obtained with this cell line were used to normalize the data for cell line 2 on the same day/plate.

29. Start the MATLAB software. Before performing the MATLAB analysis, the relevant files from the Supplementary Software (see 'Files for data visualization and QC with MATLAB' in Table 4.3) have to be present in the same directory. If other file names are required, they can be manually changed in the Iannetti_MATLAB.m file (line 53–59).

30. If it is not open yet, activate the Current Folder window by clicking /Desktop/Current Folder/ and navigate to the folder containing the tutorial files above.

31. Execute the file Iannetti_MATLAB.m by right-clicking on its filename and clicking /Run. In the MATLAB command window, the following instruction appears: 'Specify the condition you want to analyse:'

32. Perform the analysis for condition X (by typing 'x' followed by Enter) or condition Y (by typing 'y' followed by Enter). This process will take ∼50 s. For both conditions X and Y (run the Iannetti_MATLAB.m file twice), MATLAB will generate three figures (Fig. 4.7). The first figure contains the result of the PCA visualized by plotting principal component 1 (PC1; x axis) versus principal component 2 (PC2; y axis) before the QC (Fig. 4.7a,d). The second figure contains a box-plot of PC1 and PC2

revealing the outliers (QC; Fig. 4.7b,e). The third figure contains the result of the PCA analysis visualized by plotting PC1 versus PC2 with the outliers removed (Fig. 4.7c,f). In our experience, visual inspection of the images revealed that such outliers (e.g., condition X: well 54 and condition Y: well 13) displayed aberrant staining (Fig. 4.8a).

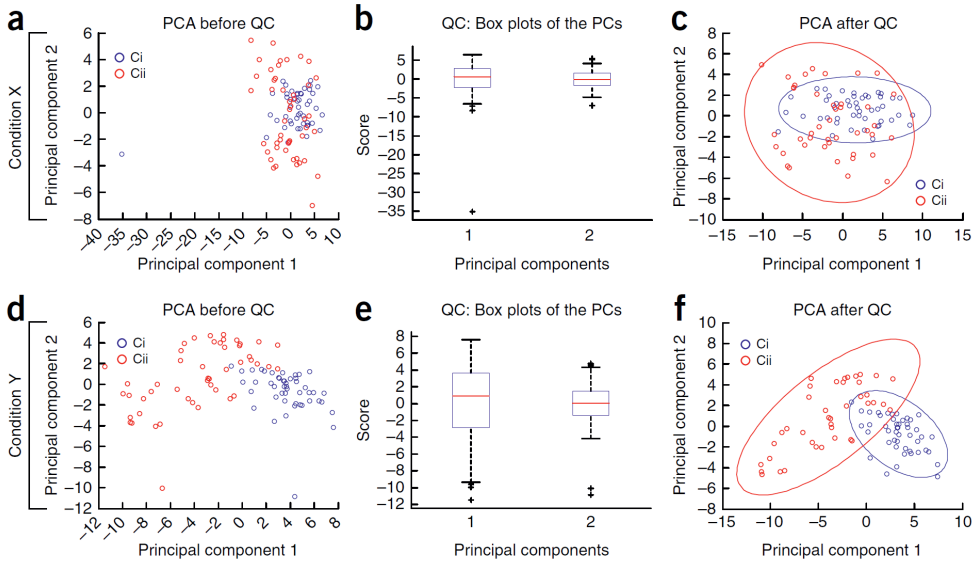


Figure 4.7: Descriptor extraction, data visualization and QC procedure. **A)** Graphical output of the MATLAB analysis. PCA for all wells under experimental condition X. Each symbol corresponds to an individual well for cell line 1 ('Ci', blue symbols) or cell line 2 ('Cii', red symbols). **B)** Detection of outlier wells (crosses) in the PCA of a using a boxplot analysis of principal component 1 (PC1) and 2 (PC2) for condition X. Box-plot settings: the top and bottom of each box reflects the 25th and 75th percentile, respectively. The median value is indicated by a horizontal red line within the box. The error bars ('whiskers') extend to the furthest observations within the whisker length, which was set at 1.0-times the interquartile range. Observations outside the whiskers were considered outliers (marked by '+'). **C)** Same as a, but now the outlier wells that were detected in b have been removed. This panel demonstrates that cell lines 1 and 2 are similar under experimental condition X. **D)** Same as A, but now showing analysis for experimental condition Y. **E)** Same as B, but now showing analysis for experimental condition Y. **F)** Same as C, but now showing analysis for experimental condition Y. In the latter condition, cell lines 1 and 2 are dissimilar.

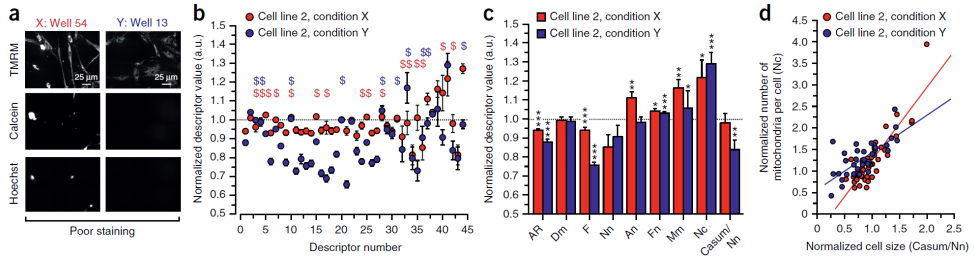


Figure 4.8: Quality control and monovariate and bivariate data visualization. Two cell lines (1 and 2) were cultured under two experimental conditions (X and Y) on three different plates using the plate layout in Fig. 4.5. **A)** Examples of staining aberrations detected by the analysis in Fig. 4.7b,e (condition X: well 54 and condition Y: well 13). **B)** Average normalized values of the 44 descriptors in Table 2 for cell line 2 cultured under experimental conditions X (red) and Y (blue). The data were normalized on the average value obtained for cell line 1 on the same day/plate (i.e., cell line 1 is characterized by a y value of 1.0, marked by the horizontal dotted line). Statistical analysis revealed that the marked descriptors ($ signs) for cell line 2 did not significantly differ ($P > 0.05$) from cell line 1 in condition X (red symbols) or condition Y (blue symbols). **C)** Average values of a selected subset of 'biologically meaningful' descriptors for cell line 2 cultured under experimental condition X (red) and condition Y (blue). The data were normalized on the average value obtained for cell line 1 on the same day/plate (dotted line). Statistical analysis revealed significant differences between various descriptors. **D)** Example of a bivariate analysis using the number of mitochondria per cell (Nc; y axis) and cell size (Casum/Nn; x axis) for cell line 2 cultured under experimental condition X (red) and condition Y (blue). Both descriptors were normalized on the average value obtained for cell line 1 on the same day/plate. A linear fit to the data revealed that Nc increases with Casum/Nn (Red line: $P < 0.0001$, $R = 0.88$; Blue line: $P < 0.0001$, $R = 0.71$), demonstrating that the number of mitochondria per cell increases as a function of cell size. Statistics: mean values were compared (b,c) using an unpaired independent t-test (Bonferroni-corrected). $^{*}P < 0.05$, $^{**}P < 0.01$ and $^{***}P < 0.001$.

4.5.1 *? TROUBLESHOOTING*

The presented protocol was specifically developed for quantitative analysis of mitochondrial morphology, $\Delta\psi$ and cellular/nuclear parameters in PHSFs using 96-well plates. To this end, we used a combined staining of TMRM/calcein/Hoechst, which was imaged using a BD Pathway 855 microscopy system. However, our strategy is compatible with any microscopy system that features an environmental control system, allows automated image acquisition and

meets the spectral requirements (excitation, emission) for combined and specific imaging of TMRM, calcein and Hoechst. For successful implementation of the protocol, one needs to establish the following (see also Figs. S2-S5):

- The PHSFs are viable when cultured on multiwell plates and are firmly attached.
- The cell density (confluence) is appropriate (Fig. S2).
- Each well is properly mixed after TMRM addition (Fig. S3).
- TMRM photobleaching during image acquisition is absent or does not interfere with descriptor extraction (Fig. S3).
- The automatically acquired images are in focus (Fig. S4).
- TMRM autoquenching is absent (Fig. S5).
- The TMRM signal is able to report both $\Delta\psi$ depolarization and hyperpolarization (Fig. S5).

With regard to TMRM staining, the most crucial part of the procedure is the dilution of the extracellular TMRM concentration following TMRM staining and before TMRM image acquisition (Lemasters and Ramshesh, 2007). For PHSFs, the extracellular TMRM loading concentration needs to be twofold diluted to allow signal stability over time (Fig. S3). This dilution factor is probably cell-type-specific. Once the cell culture and staining conditions are optimal, successful image processing and descriptor extraction requires that the acquired microscopy images display certain properties. The key part of the TMRM image processing pipeline is the generation of the BIN image, in which white mitochondrial objects are represented on a black background. Faithful calculation of the BIN image from the background-corrected TMRM image (COR) requires that the mitochondria-specific TMRM signal is high enough, that the image is relatively noise-free (i.e., contains few noise-related pixels introduced by defocusing and/or the optical/electronic systems of the microscope) and that each true mitochondrial object consists of enough pixels

to avoid its erasure from the image by the median filtering (MED). In case of other cell types, the THF and MED filtering used in this protocol can be directly applied if:

- Mitochondrial TMRM signals are sufficiently above background (i.e., cytosolic, nuclear and extracellular TMRM signals).
- The acquired TMRM images are relatively noise-free.
- The cell type displays axial dimensions ('latness') similar to those of PHSFs.
- The cells contain mitochondrial objects with a (pixel) size (Am) similar to that of PHSFs.

When (several of) these four criteria are not met, we strongly advise against blindly applying our protocol but instead to empirically assess whether alternative settings of the THF and MED filters might be appropriate (Fig. S6). Changing these settings is often required when small cells, small mitochondrial objects in close vicinity to each other and/or cells displaying a considerable axial dimension are imaged. In these cases, 3D analysis using confocal microscopy might be an option (Koopman et al., 2013; Nikolaisen et al., 2014). Descriptors that are particularly informative during troubleshooting include the following:

- Nn and confluence % (C%; fraction/percentage of the image covered), to detect cell densities that are too low or too high (Nn; Fig. S2).
- Am, AR, F and Nc, which are collectively sensitive to defocusing or the presence of noise in the image (Fig. S4).
- Descriptors such as Dstdv, which is suited to detect fluorescence saturation and the presence of objects with a very high fluorescence intensity.

Additional troubleshooting advice can be found in Table 4.4. By using the information provided in this protocol and the fully annotated IPP and MAT-

LAB scripts, the presented image processing/quantification and data analysis/visualization strategies can be implemented with relative ease using open-source software (see Eliceiri et al. (Eliceiri et al., 2012) for an overview).

Table 4.4: Troubleshooting table.

Step	Problem	Possible reason	Solution
Cell culture			
5	Cell confluence is too low	Too few cells seeded or a low proliferation rate. Error made during cell counting	Seed more cells or culture for longer time
	Cell confluence is too high	Too many cells seeded or a high proliferation rate. Error made during cell counting	Seed fewer cells or culture for shorter time
	Low cell proliferation rate	The cell passage number is too high (PHSFs; ref. 64)	Use a fresh batch of cells
		The cell confluence reached in the culture flask before seeding cells on the 96-well plate is too high	Split the cells in a new flask and allow them to recover for at least 48 hrs before 96-well plate seeding
Cell staining			
16	TMRM fluorescence is too low	TMRM is bound to medium components during the staining period, which reduces its effective concentration	Reduce the serum amount. Use a different medium
20	Calcein fluorescence is too low	The AM tail of calcein-AM is hydrolyzed before cell staining	Use a fresh batch of calcein-AM. Prevent hydrolysis by aliquotting and avoiding repeated freezing and thawing
		Low esterase activity in cells	Use another cell type
		Calcein-AM binds to serum in the medium, thereby reducing its effective concentration	Reduce the amount of serum. Use another serum batch. Increase the concentration of calcein-AM
		Calcein-AM is actively extruded from the cell[60]	Block multidrug transporter, and stain at a lower temperature
Microscopy imaging			
16	TMRM intensity is not stable	Excitation intensity is too high (photobleaching)	Reduce image acquisition time; reduce intensity of excitation light
		Changes in ΔV	Quantify ΔV using electrophysiology[54]. Use a ΔV correction technique[55]
		TMRM is leaking out of the mitochondria/cell	Increase the extracellular TMRM concentration and test with FCCP
		TMRM is still accumulating in the cell after the staining period because of improper mixing	Properly dilute the extracellular TMRM after the staining period by thorough mixing
		Illumination of TMRM photoactivates mPTP opening, e.g., ref. 58	Reduce image acquisition time; reduce intensity of excitation light
16 and 20	Cells die during imaging	Excitation intensity is too high	Reduce excitation intensity or acquire fewer images per well
	Fluorescence image is not sharp	Focus drift, autofocus problem, optical misalignment	Allow the microscopy system to warm up before experiments. Adjust autofocus settings. Service the microscopy system
		Cell has considerable axial dimensions	Increase the time for cell attachment to glass, use CLSM imaging and analysis of single optical slices, or use 3D imaging strategy[40]
	Mitochondrial objects are blurred	Mitochondria move during the acquisition of the image	Use faster imaging. If possible, perform image acquisition at a lower temperature (e.g., 20 °C)
20	Calcein intensity is not stable	Calcein-AM is still present extracellularly and taken up by the cells	Wash the cells more thoroughly to remove extracellular calcein-AM

Table 4.5: Troubleshooting table (continued).

Step	Problem	Possible reason	Solution
Image processing			
26	True mitochondrial objects are erased during processing	Mitochondrial pixel size is too small	Use an objective with a higher magnification
		The settings of the MED filter are incorrect	Check and/or use alternative MED filter settings
		The settings of the THF filter are incorrect	Check and/or use alternative THF filter settings
	False mitochondrial objects are introduced during processing	The TMRM image is too noisy	Increase TMRM concentration during cell staining, increase excitation intensity during image acquisition.
		Mitochondria-specific signal is too low	Use an alternative reporter molecule for mitochondrial staining (e.g., MTDR or MTR, thereby losing $\Delta\Psi$ information)

$\Delta\psi$, mitochondrial membrane potential; ΔV, plasma membrane potential; AM, acetoxymethylester; CLSM, confocal laser scanning microscopy; FCCP, mitochondrial uncoupler p-trifluoromethoxy carbonyl cyanide phenyl hydrazine; MED, median spatial filter; mPTP mitochondrial permeability transition pore; MTDR, MitoTracker Deep Red; MTR, MitoTracker Red CMXRos; PHSF, primary human skin fibroblast; THF, top-hat spatial filter; TMRM, tetramethyl rhodamine methyl ester.

4.5.2 • *TIMING*

Steps 1–5, seeding of the cells on a 96-well plate: ∼90 min/plate
Steps 6–20, cell staining and imaging: ∼ 90 min/plate
Steps 21–28, image processing and descriptor extraction with IPP: ∼30 min/plate
Steps 29–32, data visualization and QC with MATLAB: ∼15 min/plate (depends on the type of analysis)

4.6 Anticipated results

After removal of the outliers, the two PCs in condition X accounted for 58% of the total variation, and in condition Y they accounted for 67% of the total variation. Visual inspection of the two scatter plots of PC1 and PC2 revealed that cell lines 1 and 2 were very similar under condition X (Fig. 4.7c); in contrast, cell lines 1 and 2 were dissimilar in condition Y (Fig. 4.7f). For statistical analysis (e.g., to determine whether the two cell lines significantly differ from each other in conditions X and Y), the centroid (average) values of PC1 and PC2 for the two cell lines under conditions X and Y can be compared. To this end, it first should be assessed whether the individual values for PC1 and PC2 are normally distributed. This was carried out by performing a Shapiro–Wilk

test, which showed that the PC2 data for cell line 2 in condition Y was not normally distributed. This means that in this example a non-parametric test is required to compare the data. For independent samples, as is the case in this protocol, a Mann–Whitney or Kolmogorov–Smirnov test can be applied (Massart and Al., 1997). Using the latter test, the following results were obtained for condition X (PC1: cell lines 1 and 2 are significantly different, P = 0.00987; PC2: cell lines 1 and 2 are significantly different, P = $8.61e^{-5}$) and condition Y (PC1: cell lines 1 and 2 are significantly different, P = $8.65e^{-15}$; PC2: cell lines 1 and 2 are significantly different, P = $2.57e^{-5}$). This means that cell lines 1 and 2 are better separated for condition Y, especially with respect to PC1. After the PCA approach shown in Figure 4.7, single descriptors (univariate) were compared between cell lines 1 and 2 in conditions X and Y (Fig. 4.8b). After QC, various descriptors are suited for direct 'biological' interpretation (Tronstad et al., 2014). For instance, under conditions X and Y, cell line 2 displayed a reduction in AR and F, and an increase in Nc (Fig. 4.7c). This means that the mitochondria are smaller (lower AR, F), less branched (lower F) and more abundant (increased Nc) than in control cell line 1, which is indicative of mitochondrial fragmentation. The latter was paralleled by condition-specific changes in nuclear morphology, as indicated by the alterations in An (the average nuclear size) and Fn (a measure of nuclear 'roundness'). Moreover, an increase in mitochondrial mass (Mm; both conditions) and decrease in average cell size (Casum/Nn; condition Y) were observed. By contrast, the Dm value (a measure of average mitochondrial TMRM intensity) for cell line 2 was similar to that of cell line 1 (i.e., the normalized Dm value was close to 1). This suggests that the $\Delta\psi$ value is similar for cell lines 1 and 2 in both conditions. In addition to comparing single descriptors, the relationship between two variables can also be informative (bivariate analysis). For example, plotting the Nc as a function of cell size (Casum/Nn) revealed a linear correlation (Fig. 4.8d). This demonstrates that larger cells contain more mitochondria (Kitami et al., 2012). For this reason, in our protocol the total number of mitochondrial objects in an image (Ot) was normalized to the total cell area in the image (Casum).To estimate the true number of mitochondria per cell.

Supplementary

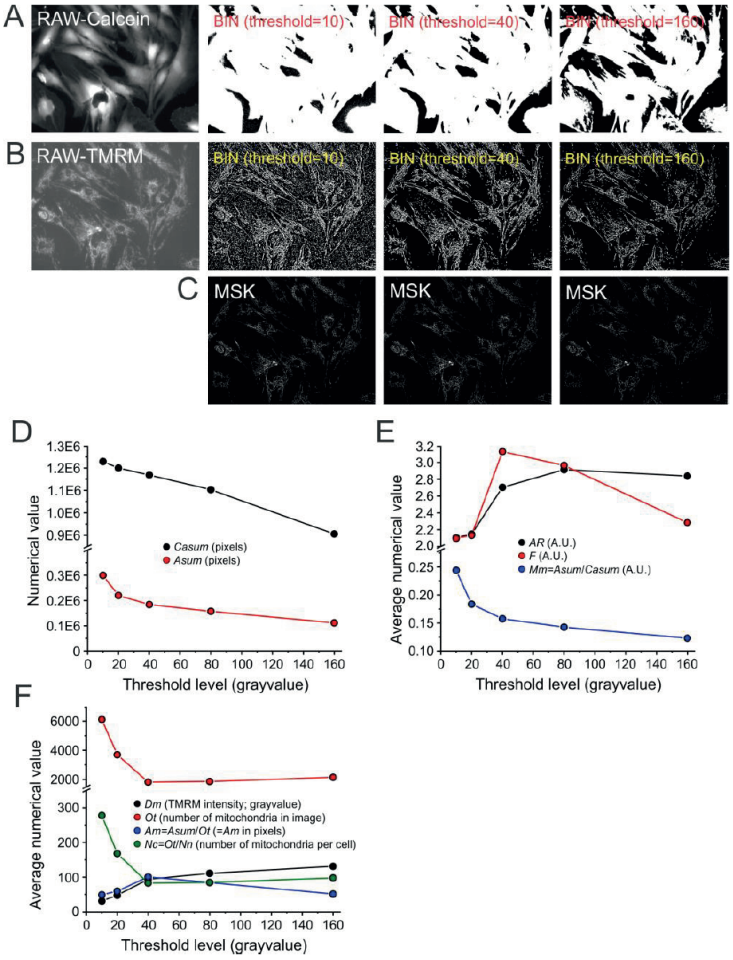


Figure S1: Importance of the threshold (T) gray value for correct calculation of the BIN and MSK images. **A)** Typical RAW calcein image (left image) and the effect of various thresholds (numerals depict the threshold gray value) on the resulting binary (BIN) image. **B)** Same as panel A but now for the RAW TMRM image of the same cells. **C)** TMRM MSK image calculated using the BIN images in panel B. **D)** Average value of Casum (total area of the objects in the calcein BIN image) and Asum (total area of the mitochondrial objects in the TMRM MSK image) for various threshold values.

Figure S1: E) Average value of AR (aspect ratio of mitochondrial objects), F (form factor: length and degree of branching of mitochondrial objects) and Mm (mitochondrial mass) in the TMRM MSK image for various threshold values. **F)** Average value of Dm (mitochondrial TMRM intensity in TMRM MSK image), Ot (the total number of mitochondrial objects in the TMRM MSK image), Am (the area of individual mitochondrial objects in the TMRM MSK image) and Nc (the number of mitochondria per cell; calculated by combining information from the TMRM MSK and Hoechst BIN image) for various threshold values. Using a threshold value of 40 yielded the correct values of key descriptors between 3-6 (F), 2-3 (AR) and 50-150 (Nc), compatible with previous manual analysis (e.g. Koopman et al., 2005a,b, 2006a, 2008; Distelmaier et al., 2008, 2012, 2015.

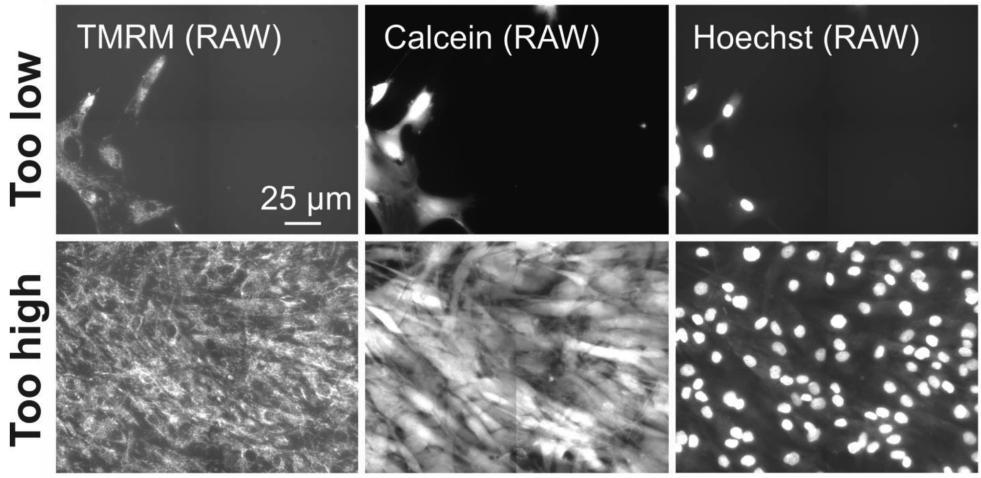


Figure S2: Illustration of too low and too high cell density. Since images are automatically acquired for each well there is no user-control regarding which cells are imaged. Although this strategy avoids user-induced bias, it requires that the average number of imaged cells is similar between individual wells. The latter is also important to allow standardized image processing, statistical analysis and QC. This figure provides typical examples of too low and too high cell densities (relative to the proper density depicted in Fig. 4.5). The protocol described in the main text was used to acquire the images in this figure.

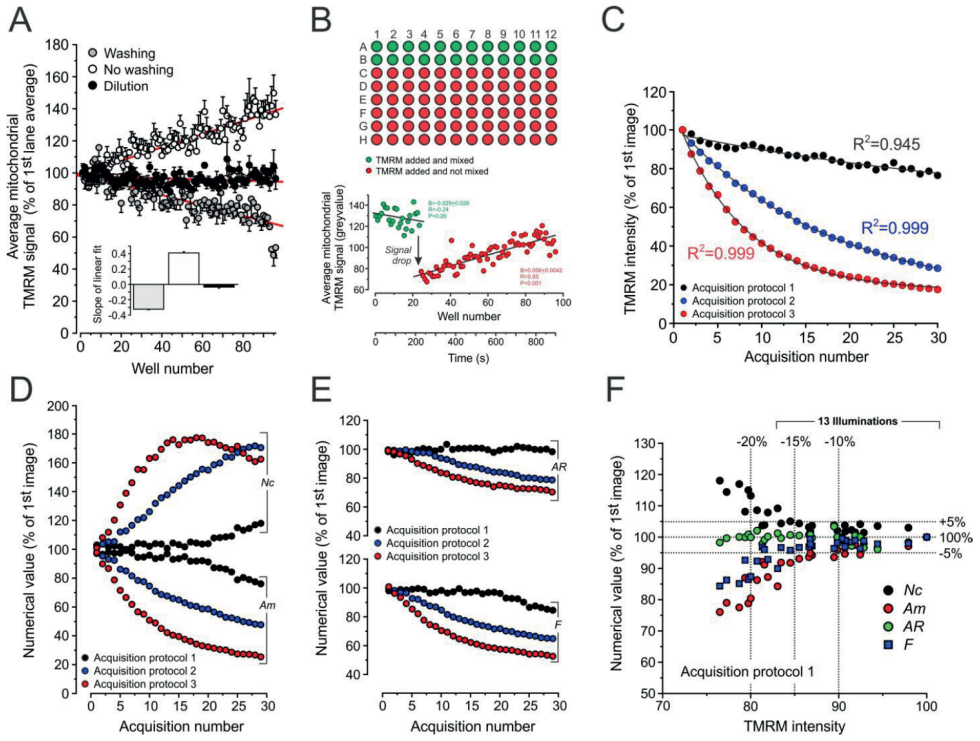


Figure S3: Importance of the presence of extracellular TMRM, well mixing and illumination intensity for TMRM descriptor analysis. This figure illustrates why it is important to have TMRM present outside the cell during image TMRM acquisition, why wells need to be properly mixed following TMRM addition, and the artefact-inducing effect of too high illumination intensities. Unless stated otherwise, the experimental data in this figure was acquired using the experimental protocol described in the main text. **A)** Importance of the presence of extracellular TMRM during TMRM image acquisition. In this experiment the calcein/Hoechst loading and imaging steps were omitted. Three different manoeuvres were tested (using 5 plates/days for each condition), thereby modifying step 15 of the protocol as follows: "Washing" condition (gray symbols; two washing steps were performed using 100 μl assay medium; 100 μl of assay medium was present in each well during image acquisition); "No washing" condition (open symbols; nothing was done to the plate after step 13); "Dilution" condition (black symbols; 100 μl assay medium was added to each well without washing and mixing). Only for the last condition, the fluorescence signal remained stable as indicated by the slope (inset) of a linear fit (red line). All data were normalized to the average of the first row (row A) of the plate. **Fitting results:** $P < 0.001$, $R = -0.83$ (Washing condition); $P < 0.001$, $R = 0.91$ (No washing condition); $P = 0.029$, $R = -0.22$ (Dilution condition; Caption continues at the next page)

Figure S3: B) Importance of mixing after TMRM addition to the well. The following steps of the protocol were modified: Step 13 (TMRM was added and mixed by pipetting up and down 4 times, but only in row A and B. For row C to H, TMRM was added but not mixed. Calcein/Hoechst staining and imaging were not required here. Only in the mixed wells (green), the TMRM signal was stable (i.e. the fitted line had no significant slope). **C)** Effect of TMRM illumination intensity on the TMRM fluorescence signal. In this experiment, 30 subsequent images of the same well were acquired at the same position (Option in BD AttoVision Software: image acquisition option/acquire button/30 data points. Three different acquisition protocols were used with the following settings: Protocol 1 (Exposure time: 0.1 s; Excitation B: 548/20; Excitation dichroic: 40%; Lamp B intensity: 60%), protocol 2 (Exposure time: 0.1 s; Excitation B: 548/20; Excitation dichroic: open; Lamp B intensity: 80%), protocol 3 (Exposure time: 0.1 s; Excitation B: 548/20; Excitation dichroic: open; Lamp B intensity: 100%). Acquisition protocol 1 (used in the protocol) displayed the lowest drop in TMRM signal. **Fitting results**: TMRM intensity curves were fitted using a mono-exponential equation ($y = y_0 + A_1 * e^{-t/\tau}$, with τ being the decay time constant). The fitted values equalled: 44.0 ± 23.4 (acquisition protocol 1), 17.4 ± 0.384 (acquisition protocol 2) and 7.56 ± 0.129 (acquisition protocol 3). **D)** Effect of the three illumination protocols on the calculated mitochondrial area (Am) and number of mitochondrial objects per cell (Nc). The more the TMRM signal drops, the greater the erroneous apparent increase in Am and Nc. **E)** Similar to panel D but now for the calculated mitochondrial aspect ratio (AR) and form factor (F). **F)** Values of calculated key mitochondrial descriptors (Nc, Am, AR and F; y-axis) as a function of TMRM intensity (x-axis) for acquisition protocol 1. About 13 illuminations can be carried out (i.e. 13 images can be acquired) before the (10-15%) drop in TMRM intensity affects descriptor quantification.

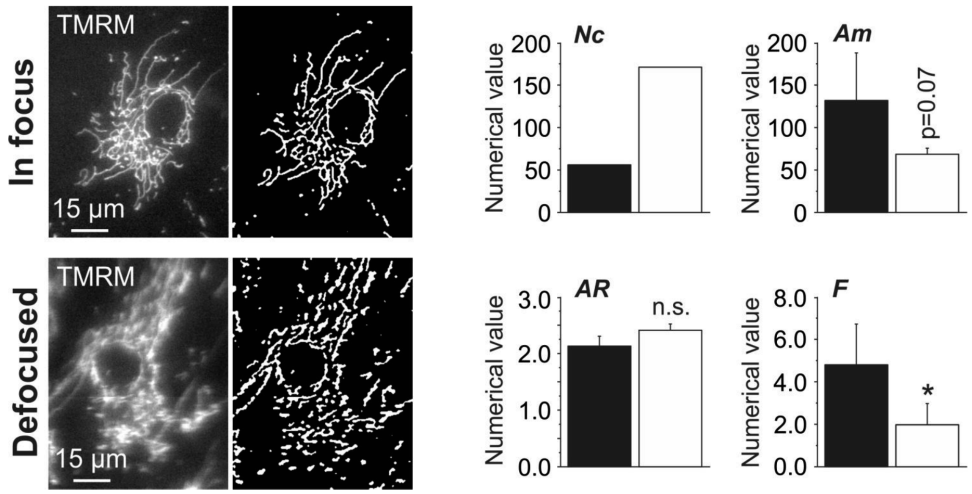


Figure S4: Illustration of the effect of image defocusing on TMRM-reported mitochondrial morphology descriptors. It is of the greatest importance that the acquired images are optimally focused, since defocusing will affect the extracted numerical data in a descriptor-dependent manner. This figures illustrates the effects of image defocusing on key mitochondrial descriptors. Typically, defocused images contain "artificial" small non-mitochondrial objects after image processing. The latter results in an apparent increase in the number of mitochondrial objects per cell (N_c), and a decrease in mitochondrial size (A_m) and form factor (F). Statistics: Significant differences between the focused and defocused condition were assessed using an unpaired independent Student's test and presented by: * $P < 0.05$, the actual P-value (A_m) and by non-significant (n.s.). The protocol described in the main text was used to acquire the images in this figure.

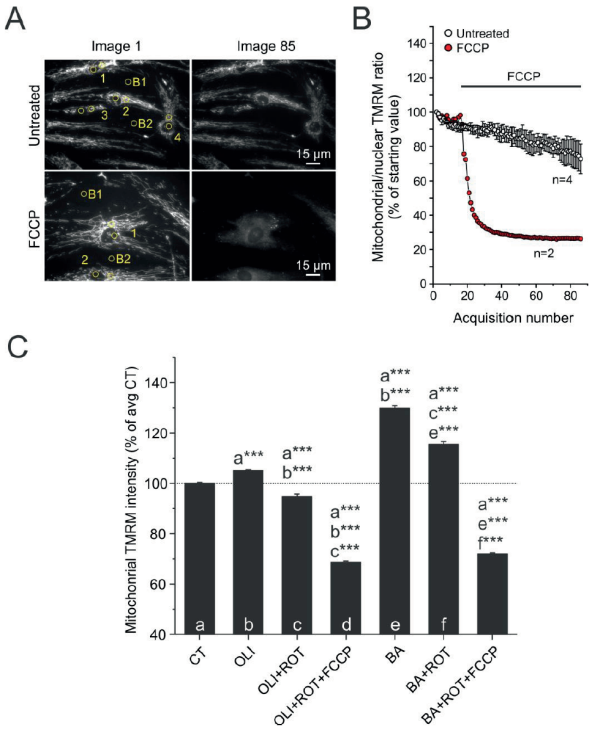


Figure S5: Control for TMRM autoquenching, detectability of hyperpolarization and effect of the mitochondrial uncoupler FCCP. This figure illustrates how to check if the TMRM fluorescence signal is affected by autoquenching and whether depolarization and hyperpolarization can be detected by decreased and increased mitochondrial TMRM accumulation, respectively. **A)** Eighty-five consecutive TMRM images were acquired from the same well. The displayed typical image-pairs illustrate the effect of the mitochondrial uncoupler p-trifluoromethoxy carbonyl cyanide phenyl hydrazine (FCCP, 10 μM; #370-86-5; Sigma-Aldrich, St. Louis, MO, USA) on mitochondrial TMRM staining (upper vs. lower panel). Numerals mark individual cells and regions of interest (ROIs; yellow) mark the nuclear and mitochondrial compartment (yellow circles). **B)** Average ratio between TMRM intensity in the mitochondrial and nuclear compartments calculated using the ROIs in panel A for untreated (n = 4) and FCCP-treated (n = 2) cells. Repeated illumination induces a gradual drop in ratio (photobleaching) in the untreated cells. FCCP induces a smooth drop in the ratio signal, indicating the absence of TMRM autoquenching. If the latter would be the case, FCCP would first induce an increase in the signal (due to TMRM dequenching in the mitochondrial matrix), followed by a decrease. (Caption continues at next page.)

Figure S5: C) Effect of subsequent acute addition of the F_0F_1-ATPase inhibitor Oligomycin A (OLI; 1 μM; #1404-19-9; Sigma-Aldrich), the mitochondrial complex I inhibitor Rotenone (ROT; 1 μM; #83-79-4; Sigma-Aldrich) and FCCP (10 μM) on mitochondrial TMRM fluorescence intensity. In a second type of experiment, Bonkrekic acid (BA; 50 μM; #11076-19-0; Sigma-Aldrich) was acutely added to inhibit the electrogenic mitochondrial ATP/ADP translocator (ANT). This was followed by subsequent addition of ROT and FCCP. **Statistics:** Significant differences with the indicated columns (a, b, c, d, e, f) was assessed using an unpaired independent Student's test (Origin Pro 6.1) and presented by: *** $P < 0.001$. **Experimental details:** Options used in the BD attovision software: "Montage Capture Setup", "INACTIVE MONTAGE", "1 Frame". MACRO on BD attovision software: Experiment 1 (30 (CT) TMRM image acquisitions of the same well; 30 s pause during which 1 μM Oligomycin (OLI) is added by pipetting; 30 TMRM image acquisitions of the same well; 30 s pause during which 1 μM Rotenone (ROT) is added; 30 TMRM image acquisitions of the same well; 30 s pause during which 10 μM FCCP is added; 30 TMRM image acquisitions of the same well); Experiment 2 (30 (CT) TMRM image acquisitions of the same well; 30 s pause during which 50 μM Bongkrekic acid (BA) is added; 30 TMRM image acquisitions of the same well; 30 s pause during which 1 μM Rotenone (ROT) is added; 30 TMRM image acquisitions of the same well; 30 s pause during with 10 μM FCCP is added; 30 TMRM image acquisitions of the same well). Remarks: Care should be taken that during addition of the inhibitors the pipette tip does not touch the plate to avoid altering the field of view. Inhibitors are added at twice their final concentration in a (relatively large) volume of 100 μl to each well (which contains 100 μl of fluid). This ensures complete and rapid mixing.

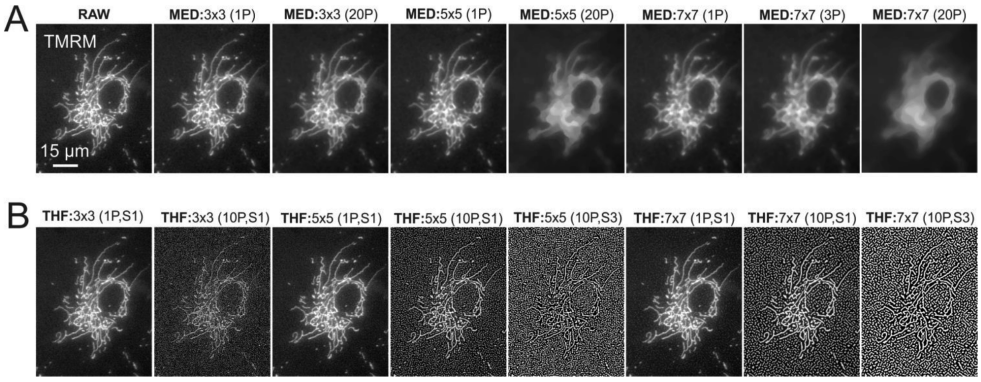


Figure S6: Visualization of the effect of median (MED) and top-hat (THF) spatial filtering on the TMRM image. Proper use of the MED and THF filters to reduce noise and isolate mitochondrial objects, respectively, is crucial for proper subsequent calculation of the binary image (BIN). The latter image represents white mitochondrial objects on a black background (for the complete processing pipeline see Fig. 4.5C). In this protocol, we have established the correct size of the MED and THF filter, how often they should be applied ("passes") and, in case of the THF filter, its strength ("S"). For details about these parameters see the information in Box 1 provided in the main text. (A) Effect of various MED filter settings on the TMRM image (RAW). (B) Effect of various THF filter settings on the TMRM image (RAW).

Table S1: Use of the quantification protocol in various cell types.

Cell type	Staining	Imaging	Descriptors	Reference
BGM	mtEYFP	V-CLSM	*Am, AR, F, Nc, Mm*	Tronstad et al., 2014
CE	mtGFP	CLSM	*AR, F*	Hoffmann et al., 2009
CV1-4A	mtDsRed1	EPIF	*Am, AR, Nc*	De Vos et al., 2005
CHO	R123	EPIF	*F, Nc*	Distelmaier et al., 2012
Clone 9	mtRFP/mtGFP	EPIF	*AR, F*	Hom et al., 2007
COS-7	MTDR/mtGFP	EPIF	*AR, F*	Buhlman et al., 2014
CPA	TMRM	CLSM	*Am, AR, F, Fi*	Matthews et al., 2010
CPH	TMRM	CLSM	*Am, AR, F, Fi*	Matthews et al., 2010
H9c2	mtRFP	EPIF	*AR, F*	Yu et al., 2006
H9c2	MTR	EPIF	*AR, F*	Yu et al., 2008
HEK293	MTR	V-CLSM	*F, Nc*	Vogel et al., 2007
HeLa	R123	V-CLSM	*F, Nc*	Distelmaier et al., 2012
HPM	R123	V-CLSM	*AR, F, Nc*	Eisenberg et al., 2008
HUVECs	MTG	EPIF	*AR, F*	Lugus et al., 2011
HUVECs	mtGFP	CLSM	*Am, F, Nc, Pm*	Nikolaisen et al., 2014
M17HN	mtDsRed2	CLSM	*AR*	Wang et al., 2012b
MEFs	TMRM	EPIF	*F, Nc, Fi*	Distelmaier et al., 2012
MEFs	TMRM	EPIF	*Am, F, Mm, Nc*	Heeman et al., 2011
MM	Mt-roGFP2	EPIF	*F*	Cunniff et al., 2013
MPM	MTR	V-CLSM	*Am, AR, F, Nc, Mm*	Tronstad et al., 2014
N2a	R123	V-CLSM	*AR, F, Nc*	Coussee et al., 2011
PHSF	R123	V-CLSM	*AR, F, Fi, Nc, F/Nc*	Koopman et al., 2005a
PHSF	R123	V-CLSM	*AR, F, Nc*	Koopman et al., 2005b
PHSF	R123	V-CLSM	13 different	Koopman et al., 2006
PHSF	TMRM	EPIF	*Am, F, Fi, Nc*	Komen et al., 2007
PHSF	mtEYFP	V-CLSM	*F, Nc*	Koopman et al., 2007b
PHSF	mtGFP/TMRM	EPIF	*Fi*	Distelmaier et al., 2008
PHSF	TMRM	EPIF	*Fi*	Hoefs et al., 2008
PHSF	mtGFP/TMRM	EPIF	*Am, AR, F, Fi, Lm, Mm, Nc, Wm*	Koopman et al., 2008a
PHSF	R123	V-CLSM	*AR, F, Nc*	Mortiboys et al., 2008
PHSF	TMRM	EPIF	*Fi*	Distelmaier et al., 2009
PHSF	R123	V-CLSM	*F, Nc*	Willems et al., 2009
PHSF	MTG	EPIF	*AR, F*	Burbulla et al., 2010
PHSF	TMRM	EPIF	*AR, F, Fi, Nc*	Jonckheere et al., 2011
PHSF	TMRM	EPIF	*Am, F*	Baracca et al., 2013
PHSF	MTG	EPIF	*Am, AR, F*	Grau et al., 2013
PHSF	TMRM	EPIF	*F, Nc*	Szklarczyk et al., 2013
PHSF	TMRM	EPIF	*Am, AR, F, Fi, Mm, Nc*	Szklarczyk et al., 2013
PHSF	TMRM	EPIF	*Am, AR, F, Nc*	Willems et al., 2013
PHSF	TMRM/CM-H_2DCF	EPIF	*Am, AR, F, Nc, Ac*	Distelmaier et al., 2015
PHSF	TMRM	EPIF	31 different	Blanchet et al., 2015
PMMF	R123	V-CLSM	*Am, F, Nc*	Valsecchi et al., 2013
PMSF	R123	V-CLSM	*Am, F, Nc*	Valsecchi et al., 2013
RPAC	R123	V-CLSM	*Am, AR, F, Nc, Mm*	Tronstad et al., 2014
SH-SY5Y	mtDsRed1	EPIF	*AR, F*	Burbulla et al., 2010
SH-SY5Y	MtDsRed2	CLSM	*AR*	Wang et al., 2011
SH-SY5Y	MtDsRed2	CLSM	*AR*	Wang et al., 2012a

Abbreviations: *Ac*, area of cell; *Am*, area of mitochondrial object; *AR*, aspect ratio of mitochondrial object; BGM, Buffalo Green Monkey kidney cells; CE, intact *C. elegans*; CHO, Chinese Hamster Ovary cells; Clone9, Rat liver cells; CLSM, Confocal Laser Scanning Microscopy; CM-H_2DCF, 5-(and-6)-chloromethyl-2',7'-dichlorodihydrofluorescein; COS-7, African green monkey kidney cells; CPA, Chicken Primary Astrocytes; CPH, Chicken Primary Hepatocytes; EPIF, epifluorescence microscopy; *F*, formfactor of mitochondrial object; *Fi*, fluorescence intensity of mitochondrial object; H9c2, Rat heart myoblasts; HEK293, Human Embryonic Kidney cells; HeLa, Human epitheloid cervix carcinoma; HPM, Human Primary Myoblasts; HUVECs, Human Umbilical Vein Endothelial Cells; *Lm*, length of mitochondrial object; M17HN, M17 Human Neuroblastoma; MEFs, Mouse Embryonic Fibroblasts; *Mm*, mitochondrial mass; MM, Malignant Mesothelioma cells; MPM, Mouse Primary Myoblasts; MTDR, Mitotracker Deep Red; mtEYFP, mitochondria-targeted Enhanced Yellow Fluorescent Protein; MTG, Mitotracker Green; mtGFP, mitochondria-targeted Green Fluorescent Protein; MTR, Mitotracker Red CMXRos; MtRFP, mitochondria-targeted Red Fluorescent Protein; Mt-roGFP2, mitochondria-targeted redox-sensitive GFP2; N2a, Mouse Neuroblastoma cells; *Nc*, number of mitochondrial objects per cell; PHSF, Primary Human Skin Fibroblasts; *Pm*, perimeter of mitochondrial object; PMMF, Primary Mouse Muscle-derived Fibroblasts; PMSF, Primary Mouse Skin-derived Fibroblasts; R123, rhodamine 123; RPAC, Rat Primary Pancreatic Acinar Cells; SH-SY5Y, Human neuroblastoma cells; TMRM, tetramethyl rhodamine methyl ester; V-CLSM, Videorate Confocal Laser Scanning Microscopy; *Wm*, width of mitochondrial object. This table was adapted from: Tronstad et al., 2014.

Table S2: Composition of the used media.

CULTURE MEDIUM		ASSAY MEDIUM	
Components	**mM**	**Components**	**mM**
Amino Acids		**Amino Acids**	
Glycine	0.66667	Glycine	0.66667
L-Alanine	0.28090	L-Alanine	0.28090
L-Arginine hydrochloride	0.33175	L-Arginine hydrochloride	0.33175
L-Aspartic acid	0.22556	L-Aspartic acid	0.22556
L-Cysteine hydrochloride-H_2O	0.00057	L-Cysteine hydrochloride-H_2O	0.00057
L-Cystine 2HCl	0.10833	L-Cystine 2HCl	0.10833
L-Glutamic Acid	0.51020	L-Glutamic Acid	0.51020
L-Glutamine	0.68493	L-Glutamine	0.68493
L-Histidine hydrochloride-H_2O	0.10419	L-Histidine hydrochloride-H_2O	0.10419
L-Hydroxyproline	0.07634	L-Hydroxyproline	0.07634
L-Isoleucine	0.30534	L-Isoleucine	0.30534
L-Leucine	0.45802	L-Leucine	0.45802
L-Lysine hydrochloride	0.38251	L-Lysine hydrochloride	0.38251
L-Methionine	0.10067	L-Methionine	0.10067
L-Phenylalanine	0.15152	L-Phenylalanine	0.15152
L-Proline	0.34783	L-Proline	0.34783
L-Serine	0.23810	L-Serine	0.23810
L-Threonine	0.25210	L-Threonine	0.25210
L-Tryptophan	0.04902	L-Tryptophan	0.04902
L-Tyrosine disodium salt dihydrate	0.22222	L-Tyrosine disodium salt dihydrate	0.22222
L-Valine	0.21368	L-Valine	0.21368
Vitamins		**Vitamins**	
Alpha-tocopherol Phosphate	0.00001	Alpha-tocopherol Phosphate	0.00001
Ascorbic Acid	0.00028	Ascorbic Acid	0.00028
Biotin	0.00004	Biotin	0.00004
Choline chloride	0.00357	Choline chloride	0.00357
D-Calcium pantothenate	0.00002	D-Calcium pantothenate	0.00002
Folic Acid	0.00002	Folic Acid	0.00002
Menadione (Vitamin K3)	0.00006	Menadione (Vitamin K3)	0.00006
Niacinamide	0.00020	Niacinamide	0.00020
Nicotinic acid (Niacin)	0.00020	Nicotinic acid (Niacin)	0.00020
Para-Aminobenzoic Acid	0.00036	Para-Aminobenzoic Acid	0.00036
Pyridoxal hydrochloride	0.00012	Pyridoxal hydrochloride	0.00012
Pyridoxine hydrochloride	0.00012	Pyridoxine hydrochloride	0.00012
Riboflavin	0.00003	Riboflavin	0.00003
Thiamine hydrochloride	0.00003	Thiamine hydrochloride	0.00003
Vitamin A (acetate)	0.00030	Vitamin A (acetate)	0.00030

Table S3: Composition of the used media (continued).

Vitamin D2 (Calciferol)	0.00025	Vitamin D2 (Calciferol)	0.00025
i-Inositol	0.00028	i-Inositol	0.00028
Inorganic Salts		**Inorganic Salts**	
Calcium Chloride ($CaCl_2$) (anhyd.)	1.80180	Calcium Chloride ($CaCl_2$) (anhyd.)	1.80180
Ferric nitrate ($Fe(NO_3)$-$9H_2O$)	0.00173	Ferric nitrate ($Fe(NO_3)$-$9H_2O$)	0.00173
Magnesium Sulfate ($MgSO_4$) (anhyd.)	0.81392	Magnesium Sulfate ($MgSO_4$) (anhyd.)	0.81392
Potassium Chloride (KCl)	5.33333	Potassium Chloride (KCl)	5.33333
Sodium Bicarbonate ($NaHCO_3$)	26.1904	Sodium Bicarbonate ($NaHCO_3$)	26.1904
Sodium Chloride (NaCl)	**105.172**	**Sodium Chloride (NaCl)**	**117.241**
Sodium Phosphate monobasic (NaH_2PO_4)	1.01449	Sodium Phosphate monobasic (NaH_2PO_4)	1.01449
Other Components		**Other Components**	
2-deoxy-D-ribose	0.00373	2-deoxy-D-ribose	0.00373
Adenine sulfate	0.02475	Adenine sulfate	0.02475
Adenosine 5'-phosphate	0.00058	Adenosine 5'-phosphate	0.00058
Adenosine 5'-triphosphate	0.00165	Adenosine 5'-triphosphate	0.00165
Cholesterol	0.00052	Cholesterol	0.00052
D-Glucose (Dextrose)	5.55556	D-Glucose (Dextrose)	5.55556
Glutathione (reduced)	0.00016	Glutathione (reduced)	0.00016
Guanine hydrochloride	0.00160	Guanine hydrochloride	0.00160
HEPES	**25.0420**	**HEPES (add yourself)**	**25.0420**
Hypoxanthine Na	0.00294	Hypoxanthine Na	0.00294
Phenol Red	**0.05313**	**Phenol Red**	**0.0**
Ribose	0.00333	Ribose	0.00333
Sodium Acetate	0.60976	Sodium Acetate	0.60976
Thymine	0.00238	Thymine	0.00238
Tween 80®	Infinity	Tween 80®	Infinity
Uracil	0.00268	Uracil	0.00268
Xanthine-Na	0.00224	Xanthine-Na	0.00224

Culture medium: Cells were cultured in culture medium (Medium 199, HEPES; #12340-030, Invitrogen, Breda, The Netherlands). To the culture medium was added: 10% (v/v) fetal calf serum (FBS; #758093, Greiner Bio-One, Gmbh, Germany), 100 IU/ml penicillin and 100 IU/ml streptomycin (#30-002-CI, Corning, NY, USA).

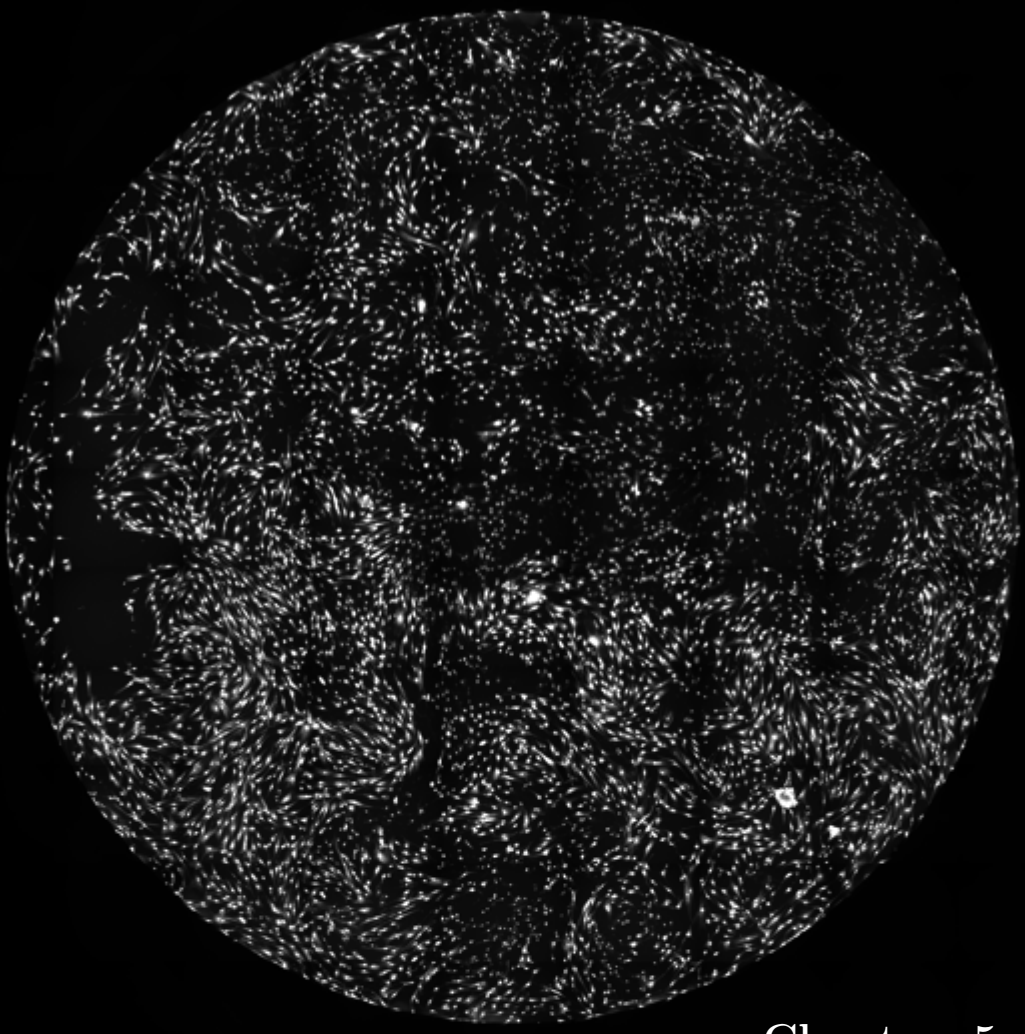
Assay medium: TMRM, Calcein-AM and Hoechst 33258 were diluted in assay medium (Medium 199, no phenol red; #11043-023; Invitrogen, Breda, The Netherlands). To the assay medium was added: 25 mM HEPES (HEPES (1M); #15630-08, Invitrogen, Breda, The Netherlands). Washing steps were done with the assay medium; images were acquired in the assay medium.

Table S4: Detailed BD Pathway® 855 settings

96 WELL PLATE GREINER 655090 CELLSTAR® 96W Microplate

Setting	Calcein	Hoechst 33258	TMRM
Geometry setup			
Objective	40x Olympus	40x Olympus	40x Olympus
Ring value	0.17	0.17	0.17
Binning	1x1=0.156617µm/pixel	1x1=0.156617µm/pixel	1x1=0.156617µm/pixel
Light path			
Lamp A Transmittance	100%	100%	n.a.
Lamp B Transmittance	n.a.	n.a.	60%
Excitation A	488/10	380/10	n.a.
Excitation B	n.a.	n.a.	548/20
Excitation Dichroic	OPEN	OPEN	40%B
Emission	FURA/FITC	400DCLP	FURA/TRITC
Epifluorescence dichroic	515LP	435LP	FURA/TRITC
Auto-focus settings			
LaserAutofocus	x	x	x
Offset	1.0	1.0	1.0
Gain	40	40	40
Z-axis Relative Displacement	100 µm	100 µm	100 µm
Data points	2000	2000	2000
Sampling Rate	12000 Hz	12000 Hz	12000 Hz
Algorithm type	Double threshold	Double threshold	Double threshold
Use Rolling average	On	On	On
Rolling average size	20	20	20
Montage Capture Setup			
Active	x (4 frames)	x (4 frames)	x (4 frames)
Frames width	2	2	2
Frames height	2	2	2
Use laser autofocus during capture every 4 frames starting at frame 1	x	x	x
Dye setup			
Numerator	Exposure 0.015s	Exposure 0.01s	Exposure 0.1s
Gain	0	0	0
Offset	255	255	255
Exposure mode	Capture=on	Capture=on	Capture=on
Dynamic range	200-4095	200-4095	140-3000
Wavelength	Light path = Calcein	Light path = Hoechst	Light path = TMRM
Macro:	Calcein+Hoechst	Calcein+Hoechst	TMRM
Z-position	~5200	~5200	~5200

[&]Neutral density filters; % indicates the transmission from lamp A and B. Filters are denoted by their center wavelength and bandwidth (*e.g.* 470/40 = center wavelength=470 nm, bandwidth=40 nm (*i.e.* ±20 nm). **Abbreviations:** N.a. Not appropriate; ND, neutral density.



Chapter 5

Mitochondrial morphofunctional characterization of neuronal HT22 cells in response to SK channel activation in galactose based-medium

Adapted from: Krabbendam, I. E., Honrath, B., Dilberger, B., **Iannetti, E. F.**, Branicky R. S., Meyer T., Evers, B., Dekker F. J., Koopman, W. J. H., Beyrath, J., Bano, D., Schmidt, M., Bakker, B., M., Hekimi, S., Culmsee, C., Eckert, G.P., Dolga, A. M. (under revision *Cell death & disease*). SK channel-mediated metabolic escape to glycolysis inhibits 1 ferroptosis and supports stress resistance in C. elegans.

5.1 Introduction

In order to adapt to quick environmental changes, cells and mitochondria are fully interconnected in a continuous crosstalk where mild mitochondrial stress rapidly activate cytosolic signalling pathways that makes the cell less susceptible to subsequent perturbations (Yun J et al., 2014). This phenomenon is called mitohormesis or mitochondrial preconditioning and it is related to cellular reactive oxygen species (ROS). While high levels of ROS cause cellular damage, low levels of ROS have crucial physiological intracellular signalling functions and also improve systemic defence mechanisms by inducing adaptive responses or mitohormesis (Tapia, 2006; Ristow et al., 2014).

Recently, it has been shown that activation of mitochondrial calcium-activated potassium (mito K_{Ca}) channels mediated neuroprotection and attenuated mitochondrial dysfunction in different models of oxidative toxicity (Dolga et al., 2013; Gáspár et al., 2009). In particular, activation of small-conductance calcium-activated potassium (SK/K_{Ca}) channels preserved cell survival in conditions of oxidative stress by attenuating mitochondrial calcium uptake, preventing opening of the mitochondrial permeability transition pore and, thereby, inhibiting the release of apoptosis inducing factor (Dolga et al., 2013). In a previous study, it was observed that SK channel activation alone induced a mild increase in mitochondrial ROS levels (Honrath et al., 2017), leading to the hypothesis that SK channels might render neuroprotective effects via mitohormesis (Ristow et al., 2014; Tapia, 2006).

In the presence of glucose, cells are able to use both glycolysis and the mitochondrial Oxidative Phosphorylation System (OXPHOS) to meet their energetic demands. Many cell models cultured in vitro generate almost all ATP via glycolysis despite a fully functional mitochondrial OXPHOS system. This phenomenon called the Crabtree effect (Crabtree, 1929), describes cells as more resistant to stress targeting mitochondrial functions. In galactose-based medium where no glucose is present, galactose enters glycolysis via the Leloir pathway at a much slower rate than glucose, preventing ATP production via rapid glucose-to-pyruvate conversion (Frey, 1996). The cells are therefore forced to rely on

OXPHOS metabolism for energy production (Robinson et al., 1992). As a consequence, replacing media glucose with galactose increases susceptibility to mitochondrial toxicants (Marroquin et al., 2007). Cell culture medium where glucose is replaced by galactose is a common experimental practice to prevent glycolysis up-regulation, limit metabolic flexibility and induce metabolic stress (Rossignol et al., 2004; Iannetti et al., 2018). This also allows to study mitochondrial metabolic functionality in a partially isolated experimental model where compensatory mechanisms are limited.

The work presented here is part of a wider research project investigating whether SK channel activation and protection from ferroptosis happened via mitohormesis (Krabbendam et al., 2017 submitted). Ferroptosis is a non-apoptotic form of cell death associated with formation of lipid peroxides and, according to recent findings, also with mitochondrial dysfunction (Neitemeier et al., 2017; Gao et al., 2018)

In this part of the research, we studied phenotypical consequences induced by SK channel activation to validate a metabolic shift to a more glycolytic metabolism induced by SK channel activation and protection from ferroptosis. In order to answer this research questions, we used the mouse hippocampal neuronal cell line HT22 that has been proven to be a good model to study oxidative stress and cellular neurodegenerative mechanisms, including oxytosis and ferroptosis (Neitemeier et al., 2017). CyPPA, a pharmacological positive SK channel modulator was used to induce opening of SK channels and study its consequence at the level of mitochondrial and cellular morphofunctional phenotype in glucose or galactose containing media.

Our results indicate that inhibiting glucose up-regulation by using galactose-based medium, SK channel activation induces more severe mitochondrial phenotypical aberration as compared to a condition of glucose availability. This, together with the additional data from the rest of the research (Krabbendam et al., 2019) indicates that CyPPA-mediated effects on mitochondrial function and cell survival are linked to glycolytic events.

5.2 Materials and methods

5.2.1 Cell culture

Mouse Hippocampal Neuronal Cell Line HT22 cells were cultured in cell culture medium prepared supplementing DMEM, high glucose (#41965039; Thermo Fisher) with: 10% (v/v) Fetal Bovine Serum (FBS; #758093; Greiner Bio-One, Kremsünster, Austria), 100 IU/ml penicillin/streptomycin (#30-002-CI; Corning). The assay medium was prepared supplementing DMEM, no glucose, no glutamine, no phenol red (#A1443001; Thermo Fisher) with: 1 mM sodium pyruvate (#11360070, Life Technologies, Carlsbad, CA, USA), 1 mM L-glutamine (GlutaMAX®; #35050061; Thermo Fisher), 10% (v/v) Fetal Bovine Serum (FBS; #758093; Greiner Bio-One, Kremsmünster, Austria), 10mM HEPES (#15630080; Thermo Fisher), 100U/ml penicillin/streptomycin (#30-002-CI; Corning), 0.05mM Phenol Red (#3532; Sigma-Aldrich) and 25.5mM glucose (#G8270; Sigma-Aldrich, St. Louis, MO, USA) for sglucose assay medium or 25.5mM galactose (#G0750, Sigma-Aldrich) for galactose assay medium. Glucose and galactose assay media were stored at 4°C in the dark for a maximum of one month.
SK2 channels were pharmacologically activated with the selective SK2/SK3 channel activator NCyclohexyl-N-[2-(3,5-dimethyl-pyrazol-1-yl)-6-methyl-4-spyrimidinamine (CyPPA). CyPPA was freshly dissolved in DMSO and diluted in assay medium to a final concentration of 1μM before every experiment.
Cells were seeded in culture medium in black 96-well plates (#655090, Greiner Bio-one) at a density of 4,000 cells/well, and incubated overnight in a humidified atmosphere (95% air, 5% CO_2) at 37°C. The next day, culture medium was removed and glucose or galactose assay medium was added. Then, the cells were cultured in these media for 24h and 48h when mitochondrial and cellular morphofunctional analysis was performed.

5.2.2 Mitochondrial and cellular morphofunctional assay

Fluorescence microscopy images were acquired from 96-well plates (#655090, Greiner Bio-One) using a BD Pathway 855® High-Content Bioimager (Becton Dickinson, Franklin Lakes, NJ, USA) using a protocol previously described (Iannetti et al., 2016). A minor adjustment introduced in the protocol was related to the microscope exposure time during image acquisition. An optimal exposure time of 0.2 s was empirically determined. All other settings were as previously described. In brief, cells were co-stained with three fluorescent membrane-permeable chemical reporters: TMRM (Tetramethyl rhodamine methyl ester, #T668, Invitrogen), Calcein-AM (#65-0853-39; Thermo Fisher) and Hoechst 33258 (#94406, Invitrogen). TMRM is a cation that accumulates in the mitochondrial matrix according to the magnitude of the MMP (depicted in white). Calcein-AM passively accumulates in the cytosol and upon esterase-mediated cleavage of its AM (acetoxymethyl) ester tail it becomes green fluorescent. Hoechst 33258 binds to the AT base pairs in the minor groove of double-stranded DNA greatly increasing its blue fluorescence signal.

5.2.3 Image processing, data analysis and statistics

For the mitochondrial and cellular morphofunctional analysis the image processing, quantification and data extraction was performed using Image Pro Plus® software (Media Cybernetics, Rockville, MD, USA) and MATLAB® scripts (Mathworks, Natick, MA., USA), as previously described (Iannetti et al., 2016). A minor adjustment introduced in the protocol during image processing was related to the threshold value to yield binary images (Fig 5.1B). An optimal threshold value of 60 gray values was empirically determined. All other settings were as previously described. Data analysis was performed using Graphpad PRISM® software (Graphpad Software, San Diego, CA, USA). Three independent experiments with sixteen technical replicates each experiment, for a total of forty-eight replicates per conditions, were performed. Statistical significance was assessed using one-way analysis of variance

(ANOVA) followed by Tukey's comparison (GraphPad Prism 5.0), unless otherwise stated. P-values indicating statistically significant differences between the mean values are defined as follows: *p $<$ 0.05, **p $<$ 0.01, and ***p $<$ 0.001. Data are presented as mean $\pm$ standard deviation (SD).

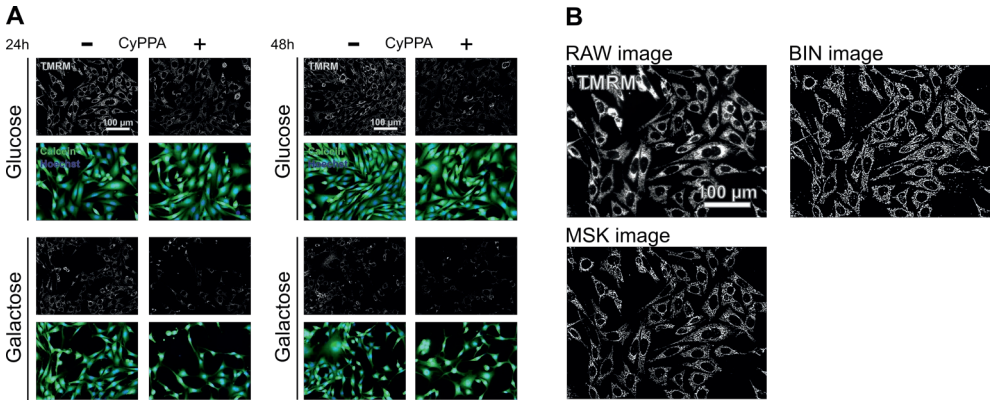


Figure 5.1: Representative microscopy images and TMRM image processing. A) Representative panel of microscopy images of HT22 cells in different conditions (glucose and galactose, vehicle and CyPPA (1μM)) and time points (24h and 48h) where TMRM is visualized in white, calcein in green and Hoechst in blue are overlayed. **B)** Image processing of TMRM-stained HT22 cells; original image recorded from the microscope (RAW); Binary image (BIN); Masked image (MSK).

5.3 Results

5.3.1 SK channel activation exerts differential effects in glucose and galactose-based media

In order to delineate the different effects of the SK channel activation on mitochondria phenotypical homeostasis in the presence of cell culture media containing glucose or galactose, automated quantification of mitochondrial 'morphofunction' (i.e., morphology and membrane potential), cellular parameters (size, confluence) and nuclear parameters (number, morphology) was performed. In this study, we focused specifically on the effects of CyPPA in glucose versus galactose media rather than on the differential effects of the two media

themselves that has been already addressed somewhere else in different cell models (Iannetti et al., 2018).

Our protocol, based on high content automated fluorescence live cell microscopy, developed in intact living primary human skin fibroblasts (PHSFs) (Iannetti et al., 2016) was here applied to neuronal HT22 cells. The phenotypical characterization was performed upon SK channel pharmacological activation induced by 24h and 48h of CyPPA treatment. In particular the cell-permeant, cationic, fluorescent dye TMRM was used as reporter for both mitochondrial morphology and mitochondrial membrane potential (mitochondrial morphofunction) that together can be considered a readout of mitochondrial health (Iannetti et al., 2016). Two additional cell-permeant fluorescent reporters, calcein and hoechst, were also used to co-assess cellular and nuclear parameters, respectively. A representative panel of microscopy images of the different conditions and time points is shown in figure 5.1A (TMRM in white, calcein in green and hoechst in blue). Image processing (TMRM image processing is shown in Fig. 5.1B) and data extraction was performed as described in our protocol with minor adjustments as described in materials and methods.

Univariate analysis of selected descriptors of biological interest was performed (Figure 5.2). To study mitochondrial morphology, we looked at two descriptors, "1. Aspect ratio" and "13. Roundness", respectively a combined measure of mitochondrial length and degree of branching. "1. Aspect Ratio" was significantly reduced in cells treated with CyPPA in galactose while the same treatment did not have any significant effect in glucose after both 24h and 48h of treatment. "13. Roundness" was significantly reduced upon CyPPA treatment in both glucose and galactose -based cell media both at 24h and 48h. Reduction of both aspect ratio and roundness upon CyPPA treatment indicated a reduction of mitochondrial length and branching, therefore a shift of the mitochondrial network from a tubulated towards a more fragmented morphology induced by SK activation. This effect on mitochondrial morphology is enhanced in galactose medium where a decreased was described in both the descriptors (1. Aspect Ratio" and "13. Roundness").

Two derived descriptors, "39. Cell Mito Ratio" and "42. Norm Cyto Area" re-

spectively reflecting a measure of mitochondrial mass and a measure of average cell size, were also analyzed. “39. Cell Mito Ratio” was significantly reduced in cells treated with CyPPA in galactose at both 24h and 48h of treatment, while the treatment had an effect in glucose only after 48h. “42. Norm Cyto Area” was increased following CyPPA treatment in both glucose and galactose medium at both time points. These data would indicate that CyPPA treatment induced a cell size increase that is not coupled with a mitochondrial mass increase but rather with a decrease of it. These phenotypical changes, CyPPA induced, are again more pronounced in galactose as compared to glucose.
The average mitochondrial fluorescent intensity of the TMRM signal “4. Density Mean” was also analyzed to monitor mitochondrial functionality and estimate mitochondrial membrane potential. CyPPA treatment both at 24h and 48h reduced the mitochondrial fluorescent signal in both glucose and galactose medium. However, the reduction is more severe in glucose medium rather than in galactose. This is consistent with the data measured with a different combination of technology and probe: TMRE/FACS (Krabbendam et al., 2019), *submitted* versus TMRM/microscopy presented here. As an indirect measure of cell viability, by looking at calcein and hoechst staining, cell confluence and density “34. Casum” and number of cell nuclei “36. Nn” were studied. Cell density (“34. Casum”) was not affected by CyPPA treatment in neither glucose nor galactose medium at 24h, but a significant decrease was observed after 48h in both the media. The number of cell nuclei (“36. Nn”), was slightly reduced by CyPPA treatment in galactose medium, however, not in glucose medium at 24h. After 48h, in both media the number of nuclei was reduced upon CyPPA treatment. Also, these two descriptors, indirectly describing cell viability, indicates a more sever effect of CyPPA in galactose as compared to glucose.
Overall, these data indicate that cells growing in galactose-based medium, where glycolysis up-regulation is inhibited, are more sensitive to phenotypical perturbation induced by SK channel activation as compared to cells with glucose availability.

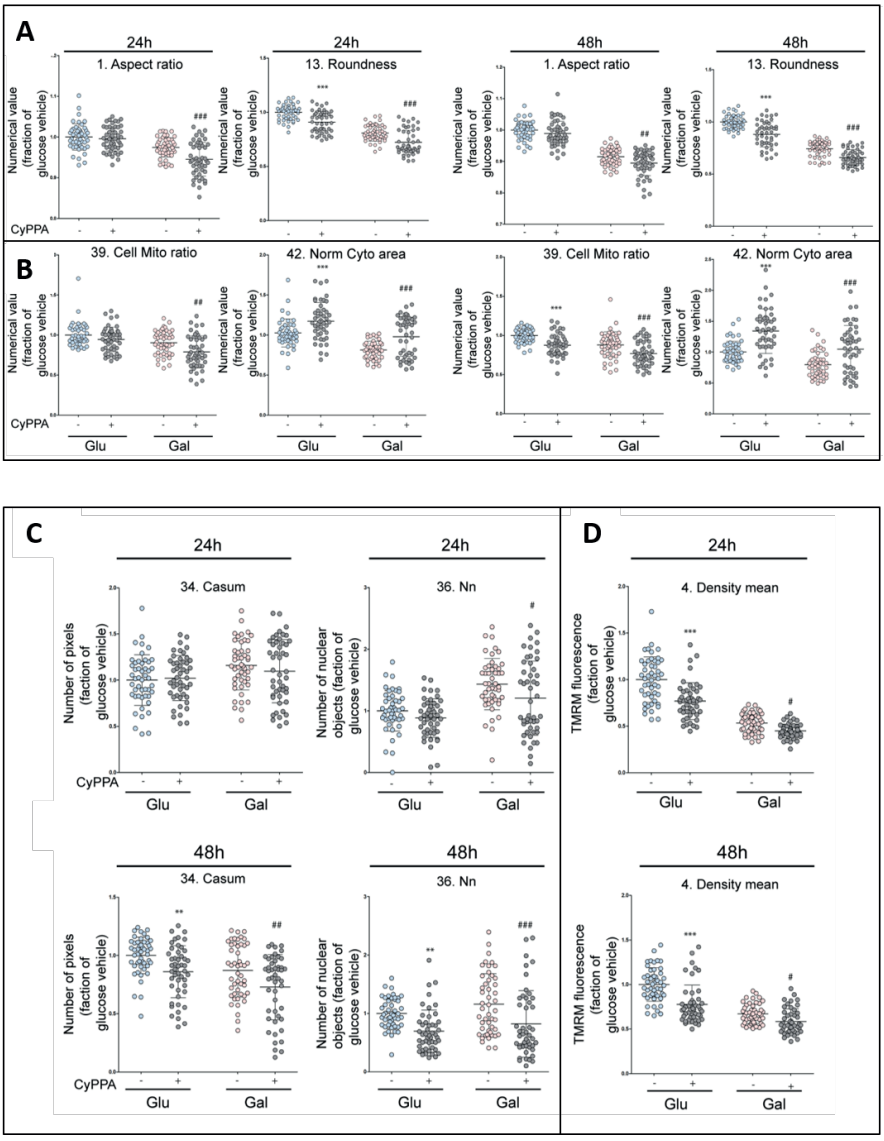
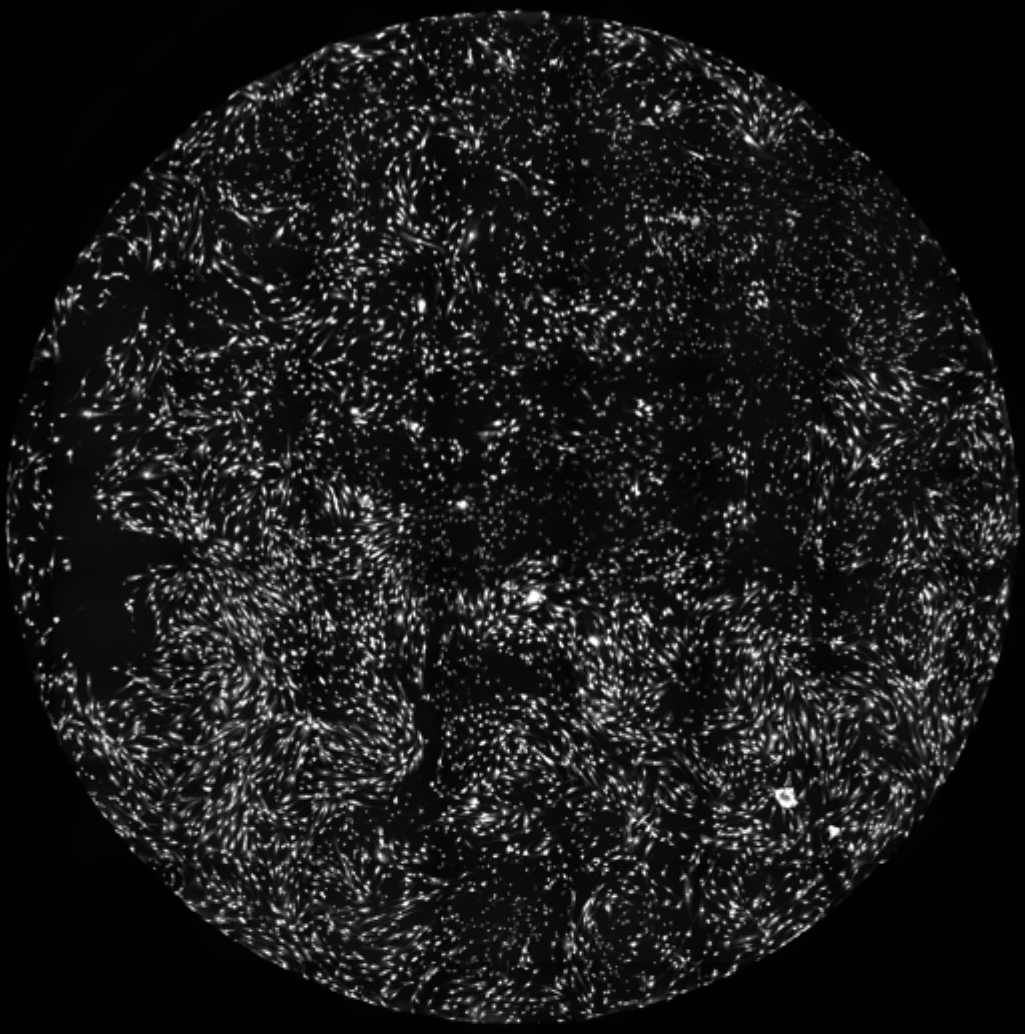


Figure 5.2: SK channel activation effects on mitochondrial and cellular morphofunction. Mitochondrial and cellular morphofunction descriptors extracted by high content microscopy images recorded in cells growing in glucose- and galactose-based media treated with CyPPA (vehicle, 1μm) are shown. Descriptors numbers are identified accordingly to the original code in "TABLE 1. Descriptors calculated for each well" (Iannetti et al., 2016).

Figure 5.2: A) Mitochondrial geometrical descriptors, "1. Aspect ratio" and "13. Roundness", extracted from the TMRM images. **B)** Derived descriptors, "39. Cell Mito Ratio" and "42. Norm Cyto Area", calculated by numerical integration of descriptors extracted from TMRM, calcein and hoechst images. **C)** Cellular and nuclear descriptors, "34. Casum" and number of cell nuclei "36. Nn", extracted from calcein and Hoechst images. (D) Average mitochondrial fluorescent intensity of the TMRM signal, "4. Density Mean", as estimation of mitochondrial membrane potential. Data are presented as mean ± SD, n = 3, $^{**}p < 0.01$, $^{***}p < 0.001$ versus glucose alone, $^{\#}p < 0.05$, $^{\#\#}p < 0.01$, $^{\#\#\#}p < 0.001$ versus galactose only treated cells.

5.4 Discussion

In this study we showed a specific mitochondrial susceptibility increase upon activation of SK channel chemically induced by CyPPA in galactose-based medium as compared to glucose-based medium. This hyper sensitivity was shown in mitochondrial morphology and cell viability descriptors, while surprisingly not at the level of mitochondrial membrane potential, that was less affected in galactose as compared to glucose medium. This might be explained by the fact the mitochondrial membrane potential, being already dramatically compromised from the galactose medium itself (50% drop), is less susceptible to extra toxicants as CyPPA because minimum mitochondrial membrane potential has to be maintained to avoid the complete collapse of the mitochondrial functionality. Using HT22 cells growing either in glucose or galactose, we delineated consequences of the ability of cells to use glycolysis or not as an energy source in conditions of SK channel activation. This phenotypical mitochondrial and cellular morphofunctional analysis presented here, is part of a wider study recently submitted for publication Krabbendam et al., 2019 that together with a previously published study (Honrath et al., 2017) shows that the activation of SK channels provides protection against ferroptosis or oxidative stress-induced cell death by mitohormesis that initiate a metabolic shift towards glycolysis.



Chapter 6

Rescue from galactose-induced death of Leigh Syndrome patient cells by pyruvate and NAD^+

Published as: **Iannetti, E. F.**, Smeitink, J. A. M., Willems, P. H. G. M., Beyrath, J., and Koopman, W. J. H. (2018). Rescue from galactose-induced death of Leigh Syndrome patient cells by pyruvate and NAD_+. *Cell Death & Disease, 9*, 1135.

6.1 Introduction

Oxidative phosphorylation (OXPHOS) is carried out by five protein complexes (CI-CV) and constitutes a prime source of mitochondrial ATP (Smeitink et al., 2001). OXPHOS dysfunction and isolated CI deficiency (OMIM 252010) is often associated with Leigh Syndrome (LS), a rare metabolic disorder with poorly understood pathophysiology (Pfeffer et al., 2013; Koopman et al., 2016; Nightingale et al., 2016; Gorman et al., 2016; Rodenburg, 2016). Functionally, CI couples the transfer of electrons from NADH to oxidized ubiquinone-10 to the transport of H^+ from the mitochondrial matrix across the mitochondrial inner membrane (MIM).This process provides the electron transport chain (ETC) with reducing equivalents to sustain a trans-MIM pH gradient (ΔpH) and electrical potential ($\Delta\psi$). Moreover, CI action allows operation of the tricarboxylic acid (TCA) cycle by NADH-to-NAD^+ recycling (Vinogradov and Grivennikova, 2001; Christensen et al., 2014; Titov et al., 2016; Hosios and Vander Heiden, 2018). We previously demonstrated that primary skin fibroblasts of pediatric LS patients exhibit disturbed calcium/ATP homeostasis (Willems et al., 2008), partial $\Delta\psi$ depolarization (Distelmaier et al., 2009b), altered mitochondrial morphology (Koopman et al., 2007a), and increased reactive oxygen species (ROS) levels (Verkaart et al., 2007a). However, we neither detected increased lipid peroxidation nor alterations in thiol redox state in LS cells (Verkaart et al., 2007a). It was hypothesized that mitochondrial (CI-mediated) NADH recycling is required to prevent "reductive stress" (as opposed to "oxidative" stress) and allow cell proliferation (Titov et al., 2016). Various CI deficiency models display an apparent reduction in NAD^+/NADH ratio (Verkaart et al., 2007a; Valsecchi et al., 2012; Karamanlidis et al., 2013), compatible with the key role of CI in oxidizing NADH to NAD^+ (Brandt, 2006) and supporting the reductive stress hypothesis. In primary skin fibroblasts, the free cytosolic NAD^+/NADH ratio is coupled to the lactate/pyruvate (L/P) ratio (Christensen et al., 2014; Robinson, 1996). Compatible with the reductive stress idea, patients with CI deficiency displayed a mild/severe lactic acidemia paralleled by an increased L/P ratio in the cor-

responding skin fibroblasts (Pitkanen and Robinson, 1996). In CI-inhibited human skin fibroblasts and other cell models of CI deficiency a parallel increase in lactate production and glycolytic flux was demonstrated (Valsecchi et al., 2012; Forkink et al., 2014; Distelmaier et al., 2015; Liemburg-Apers et al., 2015, 2016). Although the latter is important to sustain cell viability, it might prevent triggering or interfere with the detection of other relevant consequences of CI deficiency(Schöckel et al., 2015; Basit et al., 2017). Here we studied the cellular effects of genetic CI deficiency by comparing control and LS patient primary skin fibroblasts cultured in (pyruvate-free) glucose-containing or galactose-containing media. The latter enters glycolysis via the Leloir pathway at a much slower rate than glucose, preventing ATP production via rapid glucose-to-pyruvate conversion (Robinson et al., 1992; Frey, 1996). We demonstrate that glucose-by-galactose replacement specifically induces the death of LS fibroblasts, and that this dead is rescued by pyruvate and exogenous NAD^+ (eNAD) via different mechanisms.

6.2 Materials and methods

6.2.1 Cell lines

Fibroblasts were obtained following informed parental consent and according to the relevant Institutional Review Boards from skin biopsies of healthy individuals and various Leigh Syndrome (LS) patients with isolated complex I (CI) deficiency (OMIM 252010). These cell lines were previously fully characterized at the genetic, biochemical and cellular level in our group (reviewed in ref. Distelmaier et al., 2009b). Control cell lines included: #CT5120 ("CT1"), #CT5119 ("CT2"), and #CT5118 ("CT3"), which all displayed a similar and normal phenotype during their previous characterization (reviewed in ref. Distelmaier et al., 2009b). Patient cell lines harbored mutations in various genes encoding CI structural subunits: #P5175 ("S7", NDUFS7-V112M mutation), #P6603 ("S8", NDUFS8-R94C mutation), and #P5866 ("V1", NDUFV1-R59X/T423M mutations). S8 cells display a very low residual CI activity (i.e., 18% of the lowest control value) whereas this activity is higher for S7 (68%) and V1 (64%)

fibroblasts (Koopman et al., 2007a). Fibroblasts were cultured in Medium 199 (M199; #22340–020; Thermo Fisher Scientific, Waltham, MA, USA) in a humidified atmosphere (95% air, 5% CO_2) at 37°C. This medium contained no pyruvate, 25 mM HEPES, 5.5 mM D-glucose, 0.7 mM L-glutamine, and 0.05 mM phenol red. To this medium was added: 10% (v/v) Fetal Bovine Serum (FBS; #758093; Greiner Bio-One, Kremsmünster, Austria), 100 IU/ml penicillin/streptomycin (#30–002-CI; Corning, NY, USA). Cells were passaged every 4–5 days when reaching 90% confluence by trypsinization (#15400054; Corning) and were mycoplasma negative (Mycoalert® mycoplasma detection kit; Lonza, Allendale, NJ, USA).

6.2.2 Preparation of glucose and galactose media

As a starting point we used DMEM without glucose, pyruvate, glutamine and phenol red (#A1443001; Thermo Fisher). From this DMEM a "glucose medium" was prepared by adding 5.5 mM glucose (#G8270; Sigma-Aldrich, St. Louis, MO, USA). Similarly, a "galactose medium" was prepared by adding 5.5 mM galsactose (#G0750, Sigma-Aldrich). To both the glucose/galactose media was added: 1 mM L-glutamine (GlutaMAX®; #35050061; Thermo Fisher), 10% (v/v) dialyzed Fetal Bovine Serum (FBS; #26400044; Thermo Fisher), 10 mM 4-(2-hydroxyethyl)-1-piperazineethanesulfoni acid (HEPES; #15630080; Thermo Fisher), 100 IU/ml penicillin/streptomycin (#30–002-CI; Corning), and 0.05 mM Phenol Red (#3532; Sigma-Aldrich). Glucose and galactose media were stored at 4°C in the dark for a maximum of 1 month.

6.2.3 Medium additions

In certain experiments (one of) the following compounds was/were added to the medium: sodium pyruvate (#11360070, Life Technologies, Carlsbad, CA, USA), L-aspartic acid (#A7219, Sigma-Aldrich), 2-ketobutyric acid (#K401, Sigma-Aldrich), oxaloacetic acid (#O4126, Sigma-Aldrich), sodium L-lactate (#L7022, Sigma-Aldrich), L-(-)-malic acid (#M1000, Sigma-Aldrich), sodium succinate dibasic hexahydrate (#S9637, Sigma-Aldrich), dimethyl α-keto-glutarate (#349631, Sigma-Aldrich), uridine (#U3003, Sigma-Aldrich),

β-nicotinamide adenine dinucleotide hydrate (#43410, Sigma-Aldrich), Oleamide (#O2136, Sigma-Aldrich). These compounds were dissolved directly in the medium after which its pH was adjusted to 7.2 with NaOH. Media were freshly prepared prior to each experiment.

6.3 Cell functional and viability analysis

Cells were suspended in M199 culture medium, seeded in black 96-well plates (#655090, Greiner Bio-one) at a density of 2500 cells/well, and incubated overnight in a humidified atmosphere (95% air, 5% CO^2) at 37°C. On the next day, M199 culture medium was removed, cells were washed twice during 1 min with PBS and glucose or galactose medium was added.Then, the cells were cultured in these media and analyzed at 24h (functional analysis) and 96h (cell viability analysis).

6.4 Live-cell high-content microscopy

Fluorescence microscopy images were acquired from 96-well plates using a BD Pathway 855® High-Content Bioimager (Becton Dickinson, Franklin Lakes, NJ, USA) using a protocol described previously (Iannetti et al., 2016). For viability analysis, cells were stained with (a combination of) Calcein-AM (#65–0853–39; Thermo Fisher) and Hoechst 33258 (#94406, Invitrogen). Calcein-AM is membrane-permeable and accumulates in the cytosol upon esterase-mediated cleavage of its AM (acetoxymethyl) ester tail. Hoechst 33258 is also membrane-permeable and binds to the AT base pairs in the minor groove of double-stranded DNA, which greatly increases its fluorescence signal. For integrated analysis of cellular and mitochondrial morphological/functional parameters ("morphofunction"; Table S1), cells were co-stained with Calcein-AM, Hoechst 33258, and TMRM (Tetramethyl rhodamine methyl ester, #T668, Invitrogen). The latter is a fluorescent lipophilic cation that accumulates in the mitochondrial matrix depending on the magnitude of the mitochondrial membrane potential ($\Delta\psi$). Importantly, under our experimental conditions TMRM

operated in non-quenching mode and was present in the medium during image acquisition (Iannetti et al., 2016). Calcein, Hoechst, and TMRM images were quantified as described in detail previously (Iannetti et al., 2016).

6.4.1 Quantification of total cellular ATP and NAD^+ content

Using a ×10 objective (UPlanSApo, NA 0.4, Olympus, Leiderdorp, The Netherlands), 96-well plates were imaged and the total number of Calcein-positive pixels ("Casum") was determined from the center of each well (2×2 image montage; 4 images in total) by live-cell high-content microscopy (see above). Next, the total cellular ATP content was determined using the CellTiter-Glo® Luminescence Cell Viability Assay according to the manufacturer's protocol (#G7570, Promega Corporation, Madison, WI, USA). Luminescence signals were quantified using a scanning microplate reader (FLUOstar Omega®, BMGLabtech, Cary, NC, USA). This signal was divided by Casum for each well to normalize for the total cell volume in each well. The latter is possible given the flat morphology of the fibroblasts (i.e., their dimensions in the XY direction greatly exceed their height in the Z-direction; Koopman et al., 2005c). In certain experiments, cells were pre-incubated for 20 min with 10 μM of Oligomycin A (#O4876, Sigma-Aldrich) prior to ATP quantification20. Total cellular NAD^+ content was determined using the NAD/NADH-Glo® Luminescence Assay (#G9071, Pro-mega) according to the manufacturer's protocol and quantified as described for the ATP measurement.

6.4.2 Reactive oxygen species measurement

The levels of cellular reactive oxygen species (ROS) were measured in 96-well plates by quantifying the oxidation of two ROS reporter molecules (Forkink et al., 2010, 2015; Oparka et al., 2016): 5-(and-6)-chloromethyl-2',7'-dichloro dihydrofluorescein diacetate (CM-H_2DCFDA, #C6827, Thermo Fisher) and Hydroethidine (HEt, #D11347, Thermo Fisher). To this end, the cells were stained in DMEM medium (#A1443001; Thermo Fisher), which was supplemented with 10 mM HEPES (#15630080; Thermo Fisher) and contained either CM-H_2DCFDA (1 μM) or HEt (10 μM) for 30 min (37°C, 5% CO_2) in the

dark. After this incubation, cells were washed twice with and placed in Dulbecco's phosphate-buffered saline (DPBS containing calcium and magnesium, #14040133, Thermo Fisher). Next, fluorescence signals were visualized using the high-content microscopy system described above (2×2 image montage; 4 images in total) using a ×20 objective (UApo/340, NA 0.75, Olympus). Following acquisition, each image (RAW) was processed using the rolling ball algorithm28 with a feature width of 80 pixels to generate a background (BG) image. Next, the BG image was subtracted from the RAW image to obtain a background-corrected (COR) image. Noise pixels were removed from the COR image using a median filter (MED, 3×3 kernel, 2 passes). Then the image was thresholded using a cut-off of 20 gray values yielding a binary (BIN) image. The latter was combined with the COR image using a Boolean AND operation (Iannetti et al., 2016) to obtain a masked (MSK) image. In the latter image, the average fluorescence intensity was quantified by dividing the integrated pixel intensity (gray value) by the total number of pixels. This parameter is computationally equivalent to CaIOD/Casum (Table S1) and reflects the average cllular fluorescence intensity of the ROS reporter molecule.

6.4.3 Data analysis

Image visualization, processing and quantification was carried out using Image Pro Plus® software (Media Cybernetics, Rockville, MD, USA) and custom MATLAB® algorithms (Mathworks, Natick, MA., USA), as described in detail previously (Iannetti et al., 2016). Data visualization and analysis was performed using Origin Pro® (OriginLab, Northampton, MA, USA) and Graphpad PRISM® software (Graphpad Software, SanDiego, CA, USA). The number of independent experiments and replicates are indicated by N and n, respectively. Unless stated otherwise, data from multiple experiments is presented as the mean ± standard error of the mean (SEM) and statistical significance was assessed using an independent two-population Student's t-test with Bonferroni correction (*$P < 0.05$; **$P < 0.01$; ***$P < 0.001$).

6.5 Results

6.5.1 Galactose specifically induces death of LS fibroblasts in a time-dependent manner

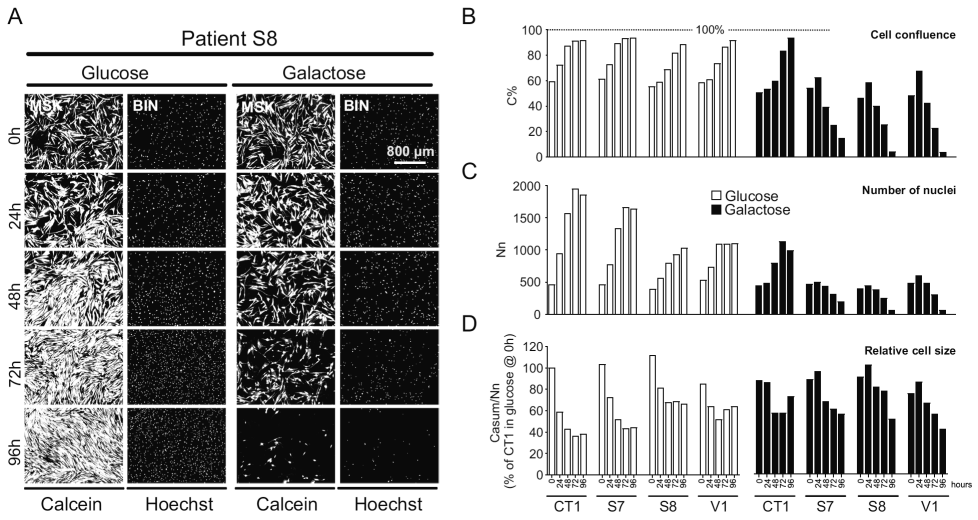


Figure 6.1: Galactose specifically reduces the viability of LS fibroblasts in a time-dependent manner. A) Time-dependent effect of glucose and galactose in LS fibroblasts (S8 cells shown as a typical example). The cells were co-stained with Calcein-AM and Hoechst 33258 to visualize the cytosol and nuclei, respectively. Image processing was applied to calculate "masked" (MSK) and black-and-white "binary" (BIN) images (see *Results* for details). **B)** Time-dependent analysis of control (CT1) and LS cells (S7, S8, V1) cultured in glucose-containing or galactose-containing medium (N = 1, n $\geq$ 2). The y-axis represents C%, the percentage of total pixels in the BIN image that was Calcein-positive. C% is a measure of cell confluence. **C)** Same as **b** but now for the number (Nn) of Hoechst-positive objects (nuclei; middle panel), calculated from the Hoechst BIN image. Nn is used as a measure of cell number. **D)** Same as **b** but now for the total number of Calcein-positive pixels (Casum; a measure of cell area) divided by the number of nuclei (Nn). This reflects the relative size of the cells (expressed as % of CT1 in glucose at 0 h). Results for the individual cell lines are presented in Fig. S1, S2, S3, S4.

Fibroblasts from control subjects (CT1, CT2, CT3) and LS patients with isolated CI deficiency (S7, S8, V1) were routinely cultured in glutamine-containing DMEM without pyruvate to which 5.5 mM glucose or galactose was added. Vi-

ability analysis revealed that control cells proliferated in glucose and galactose medium (Fig. 6.1b), whereas LS cells proliferated in glucose medium but died in galactose medium (Fig. 6.1a). CT1 and LS cells gradually decreased in size in glucose and galactose medium (Fig. 6.1d). These results demonstrate that glucose-by-galactose replacement specifically reduces the viability of LS cells relative to CT1 cells in a time-dependent manner. However, performing experiments over a time course of 18 months (Table S2) revealed that S8 patient cells invariably died in galactose medium, whereas death was variably induced in S7 and V1 cells. A correlation was observed between the time point at which a freshly prepared galactose medium was used for the first time and a change in the galactose-induced killing efficiency (Fig. S6). Since a medium change might affect cell growth, we determined whether the LS cell seeding density affected their galactose-induced killing at 96 h. Higher seeding densities protected LS fibroblasts against galactose-induced cell death (Fig. 6.2a). Therefore, we routinely seeded 2500 cells/well and only analyzed experiments where glucose-by-galactose replacement significantly reduced LS cell viability. This yielded consistent results (Fig. 6.2b), allowing cell functional and viability analyses (Fig. 6.2c). Given the similar response to galactose with in the control and LS patient cell group (Fig. 6.2b) we compared CT1 with average LS cell data in the remainder of the study (the full dataset is presented in the Supplementary materials).

6.5.2 Galactose-induced death of LS fibroblasts is rescued by specific metabolites in an oleamide-sensitive manner

Galactose-induced LS cell death was dose-dependently inhibited by pyruvate in the presence of glutamine and vice versa (Fig. 6.2d, e). Supplementation of the galactose medium with malate, oxaloacetate, α-ketoglutarate or aspartate also (partially) rescued LS cell death (Fig. 6.2f, g). Lactate, succinate, α-ketobutyrate or uridine displayed no rescue (Fig. 6.2f, g). None of the metabolites affected LS cell viability in glucose medium (Fig. S7a). Various rescuing metabolites (e.g. pyruvate, oxaloacetate, α-ketoglutarate) increased cellular NAD^+ content (iNAD; Fig. 6.3a). Although α-ketobutyrate

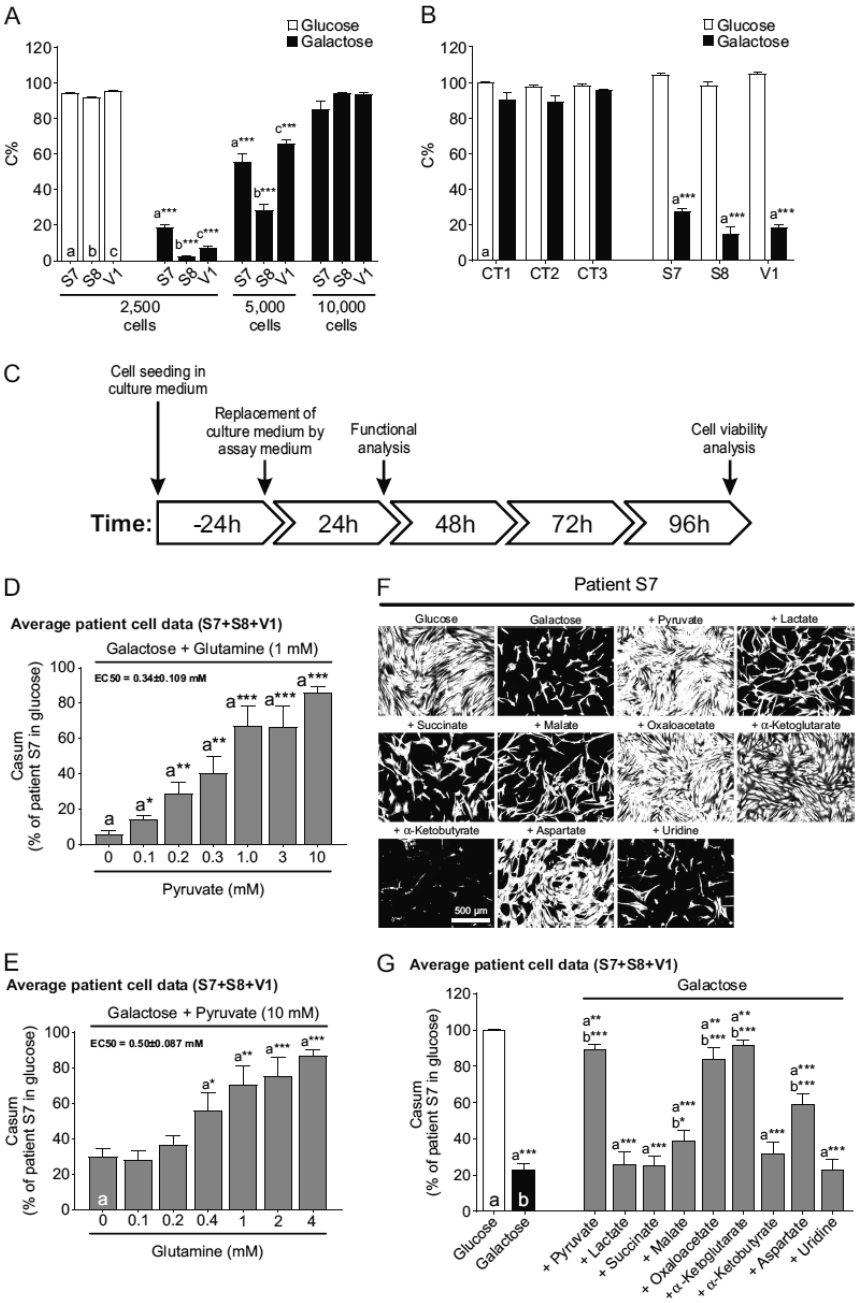


Figure 6.2: The viability of LS fibroblasts is reduced in galactose medium in a cell density-dependent manner and rescued by specific metabolites. . (Caption continues on next page.)

Figure 6.2: A) Effect of cell seeding density on the galactose-induced reduction in viability of LS cells (S7, S8, V1; measured at 96 h; N = 1, n = 8). **B)** Specificity of the galactose-induced reduction in viability (2500 cells seeded; measured at 96 h; N = 3, n ≥ 12) for LS cells relative to CT cells (CT1, CT2, CT3)**C)** Experimental protocol used in this study to quantify the effects of galactose and other treatments on control and LS cells. **D)** Dose dependent rescue of the galactose-induced reduction in viability of LS cells (S7, S8, V1) at 96 h by pyruvate in the presence of a constant glutamine concentration (N = 3, n ≥ 9). The EC50 value was determined by fitting a Hill equation to the data ($R^2 = 0.97$). **e)** Same as **d**, but now for the dose-dependent effect of glutamine in the presence of a constant pyruvate concentration (N = 3, n ≥ 18). The EC50 value was determined by fitting a Hill equation to the data ($R^2 = 0.98$). **f)** Rescuing effect of specific metabolites on the galactose-induced reduction in LS cell viability (96 h; Calcein MSK images for patient S7 are shown as a typical example): sodium pyruvate (10 mM), sodium L-lactate (10 mM), sodium succinate dibasic hexahydrate (10 mM), L-(-)-malic acid (10 mM), oxaloacetic acid (10 mM), dimethyl α-ketoglutarate (10 mM), 2-ketobutyric acid (10 mM), L-aspartic acid (15 mM), and uridine (1 mM). The "+" conditions reflect combined galactose + metabolite treatment. **g)** Quantification of the rescuing effect of the metabolites (N = 3, n ≥ 18) in LS patient cells (S7, S8, V1) at 96 h (N = 3, n ≥ 18). Statistics: $^*P < 0.05$, $^{**}P < 0.01$, $^{***}P < 0.001$, relative to the marked conditions (a, b, c). Results for the individual cell lines are presented in Fig. S6, S7.

also increased iNAD (Fig. 6.3a), galactose-induced LS cell death was not rescued (Fig. 6.2g). This demonstrates that the rescuing effects of the above metabolites are not unequivocally linked to increased iNAD levels. Next, we evaluated the effect of extracellular NAD^+ (eNAD) on iNAD (Pittelli et al., 2011) and cell viability. Adding eNAD to the galactose medium increased iNAD (Fig. 6.3b) and rescued galactose-induced LS cell death (Fig. 6.3c, d). This rescue was prevented by oleamide (Fig. 6.3e), an inhibitor of gap-junction hemichannel-mediated NAD^+ entry34. These findings demonstrate that eNAD application increases iNAD and inhibits galactose-induced death of LS cells via an oleamide-sensitive mechanism.

6.5.3 Rescue of galactose-induced death of LS fibroblasts by eNAD is enhanced by pyruvate

Supplementation with eNAD increased iNAD levels to a greater extent than pyruvate supplementation (Fig. 6.3a, b). However, pyruvate rescued galactose-

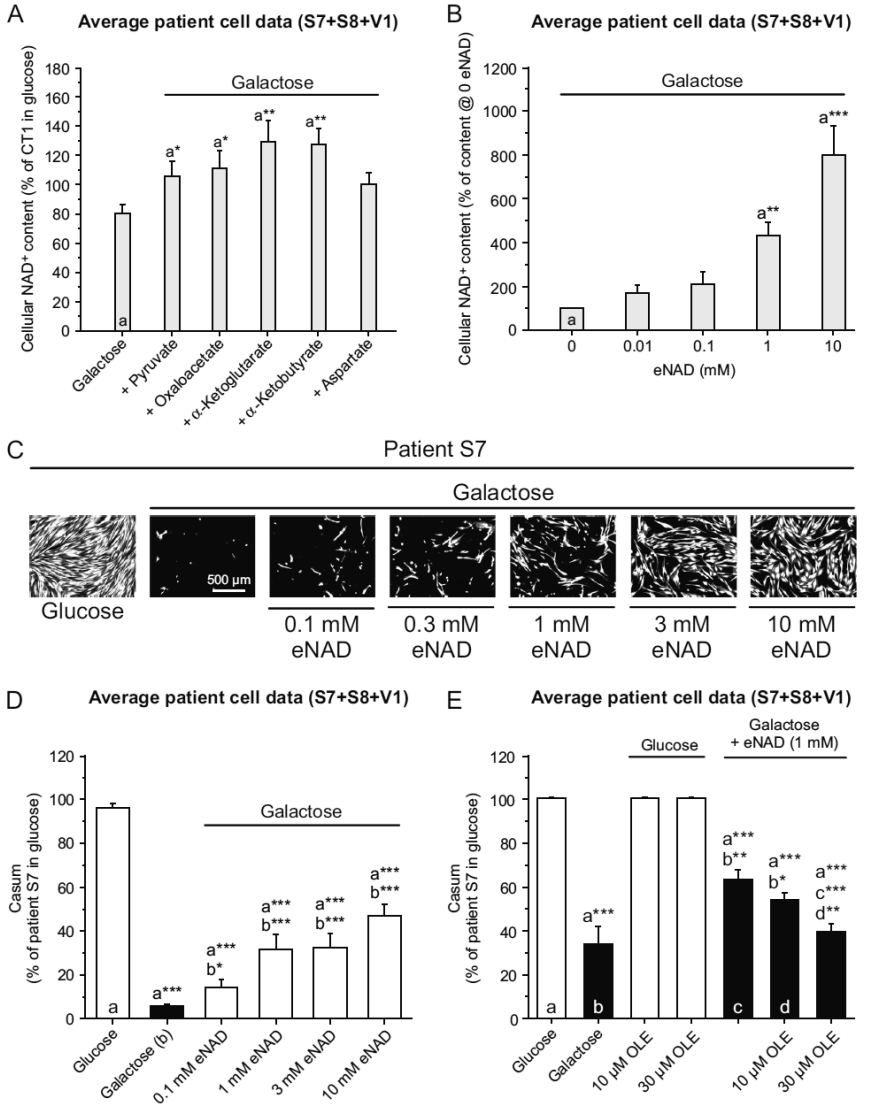


Figure 6.3: Exogenous NAD$^+$ (eNAD) rescues the galactose-induced reduction in cell viability and intracellular NAD$^+$ (iNAD) content in LS fibroblasts. A) Dose-dependent effect of extracellular sodium pyruvate (10 mM), oxaloacetic acid (10 mM), dimethyl α-ketoglutarate (10 mM), 2-ketobutyric acid (10 mM), and L-aspartic acid (15 mM) on intracellular NAD (iNAD) levels in LS cells (24 h; N = 1, n = 3). **B)** Dose-dependent effect of extracellular NAD (eNAD; β-nicotinamide adenine dinucleotide hydrate) on intracellular NAD (iNAD) levels (24 h; N =1, n $\geq$ 6). (Caption continues on next page.)

Figure 6.3: C) Dose-dependent rescue of the galactose-induced reduction in viability of LS cells (Calcein MSK images) by eNAD (β-nicotinamide adenine dinucleotide hydrate; S7 shown as a typical example; 96 h). **D)** Quantification of the rescuing effect of eNAD in LS patient cells (96 h; N = 2 n $\geq$ 9). **E)** Dose-dependent inhibition of the rescuing effect of eNAD by oleamide (OLE) in LS patient cells (96 h; N = 3, n = $\geq$ 6). Statistics: *P $<$ 0.05, **P $<$ 0.01, ***P $<$ 0.001, relative to the marked condition (**a**, **b**, **c**, **d**). Results for the individual cell lines are presented in Fig. S8.

induced LS cell death to a greater extent than eNAD (e.g., Fig.6.2g and 6.3d, e). Combination experiments demonstrated that, in the absence of pyruvate, eNAD concentrations up to 1mM partially rescued galactose-induced LS cell death (Fig. 6.4; red line). By itself, pyruvate inhibited galactose-induced LS cell death to a greater extent than eNAD (Fig. 6.4; dark gray bars vs. red line). Moreover, rescue was always larger for pyruvate + eNAD than for eNAD alone (Fig. 6.4; light gray bars vs. red line). In contrast, pyruvate-induced rescue was not stimulated by the presence of eNAD. These results suggest that the rescue of galactose-induced LS cell death by pyruvate is not primarily due to its iNAD-increasing effect.

6.5.4 Mitochondrial morphofunctional analysis demonstrates differential effects of pyruvate and eNAD

High-content microscopy analysis (Fig. 6.5a) of TMRM/Calcein/Hoechst-stained cells(Iannetti et al., 2016) was applied to analyze mitochondrial morphology and function ("morphofunction"). This yielded 44 descriptor values (Table S1), which were normalized to the glucose condition and visualized using a heatmap (Fig. 6.5b). Exploratory analysis (Fig. S11) revealed that: (i) mitochondrial morphofunction is differentially affected by galactose in CT1 and LS fibroblasts, and (ii) the galactose-induced phenotypic differences between CT1 and LS cells disappear upon supplementation with eNAD, but not pyruvate. Regression analysis (Fig. S11C-D) was used to highlight the descriptors most differentially altered between CT1 and LS cells (Fig. 6.5b; red characters). In glucose medium LS cells contained a larger number of mitochondria (Nc) than CT1 cells (Fig. S11C). This difference was enhanced by galactose

treatment (Fig. 6.5c). Pyruvate and eNAD supplementation inhibited the galactose-induced Nc increase in LS cells but not in CT1 cells (Fig. 6.5c). In glucose medium, the total mitochondrial area per cell (Amt) was higher in LS cells than in CT1 cells and this difference was enhanced by galactose treatment (Fig. 6.5d). Pyruvate supplementation did not prevent the galactose-induced increase of Amt in LS and CT1 cells, whereas eNAD was effective in LS cells but not in CT1 cells (Fig. 6.5d). Adding eNAD to the galactose medium increased various descriptors (Dstdv, Dmax, Dmin, and Dm) in LS but not in CT1 cells (Fig. S11E). These parameters are all related to the TMRM fluo-

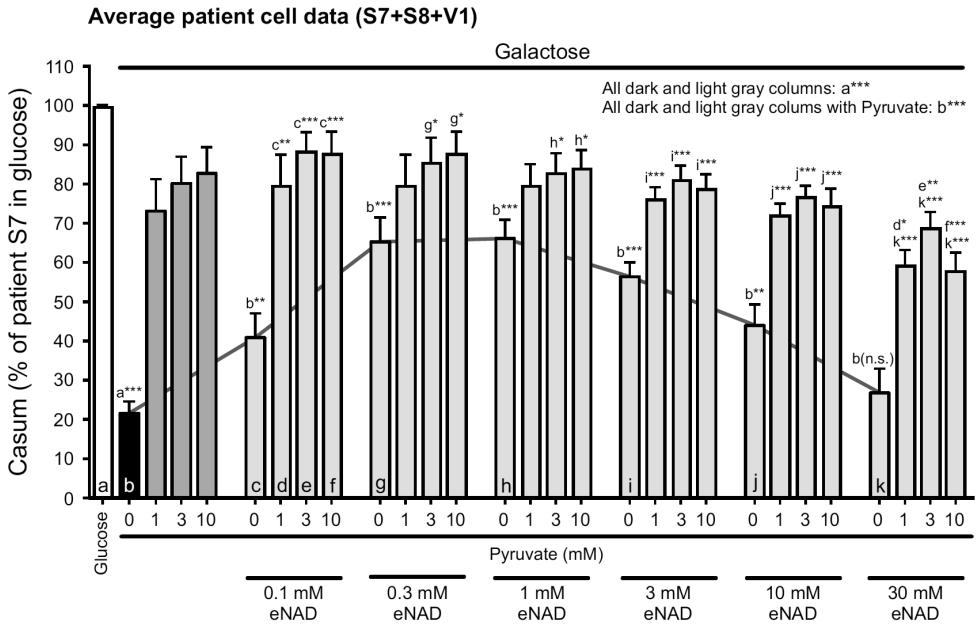


Figure 6.4: Combined effect of pyruvate and exogenous NAD$^+$ (eNAD) on the galactose-induced reduction in cell viability of LS fibroblasts. Effect of pyruvate and eNAD on the viability of LS cells (S7, S8, V1) cultured in galactose medium (N = 1, n $\geq$ 9; 96 h). Casum, the number of white pixels in the Calcein BIN image, was expressed as percentage of the total number of pixels for patient S7 in glucose medium. The red line highlights the effect of eNAD in the absence of pyruvate. Statistics: $^*P < 0.05$, $^{**}P < 0.01$, $^{***}P < 0.001$, relative to the marked condition (**a**, **b**, **c**, **d**, **e**, **f**, **g**, **h**, **i**, **j**, **k**). Results for the individual cell lines are presented in Fig. S9.

rescence intensity (Table S1), with Dm representing the average mitochondrial TMRM fluorescence. In glucose medium, LS cells displayed a lower Dm than CT1 cells, indicating a less negative $\Delta\psi$ (Fig. 6.5e). Galactose treatment in the absence/presence of pyruvate did not affect this difference (Fig. 6.5e). In LS cells but not CT1 cells, eNAD but not pyruvate supplementation increased Dm, suggesting that eNAD partially restored $\Delta\psi$ (Fig. 6.5e).

6.5.5 Pyruvate and eNAD reduce the levels of CM-H_2DCFDA-oxidizing ROS

Extracellular pyruvate displays antioxidant properties in human cells35–38. In glucose medium, LS cells displayed higher levels of CM-H_2DCFDA- and HEt-oxidizing ROS than CT1 cells (Fig. 6a, b). Galactose treatment increased CM-H_2DCFDA oxidation to a similar level in CT1 and LS cells (Fig. 6.6a) without affecting HEt oxidation(Fig. 6.6b). Similarly, pyruvate and eNAD lowered CM-H_2DCFDA oxidation (Fig. 6.6a) without affecting HEt oxidation (Fig. 6.6b). In S8 cells the glutathione precursor N-acetylcysteine (NAC) prevented galactose-induced LS cell death, whereas the vitamin E-derivative Trolox (6-hydroxy-2,5,7,8-tetramethylchroman-2-carboxylic acid) was ineffective (Fig. 6.6c, d). These results suggest that galactose-induced cell death co-involves CM-H_2DCFDA oxidizing and NAC-sensitive ROS.

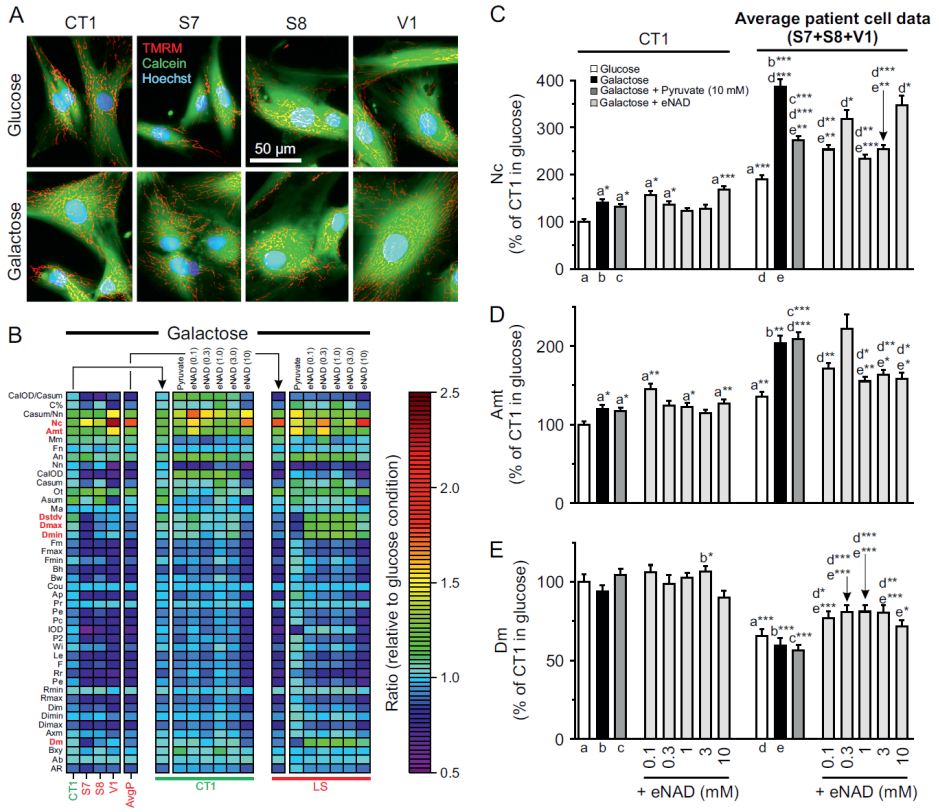


Figure 6.5: Effect of galactose, pyruvate and exogenous NAD+ (eNAD) on mitochondrial morphofunction in LS fibroblasts. CT1 and LS cells (S7, S8, V1) were cultured in glucose or galactose medium for 24 h and analyzed. **A)** Typical microscopy images of cells stained with TMRM (mitochondria), Calcein-AM (cytosol) and Hoechst 33258 (nuclei). **B)** Heatmap displaying the average value of the morphofunctional descriptors (y-axis; normalized on the glucose condition). The left group of panels depict results obtained using the galactose medium (CT1, S7, S8, V1, and average patient data; AvgP). The middle group of panels depict results obtained using the galactose + pyruvate (10 mM) and galactose + eNAD (0.1, 0.3, 1, 3, and 10 mM) medium (CT1 cells). The right group of panels is similar to the middle group of panels but now depicting the average results obtained with LS cells. **C)** Values of Nc, representing the the number of mitochondria per cell. **D)** Values of Amt, representing the total mitochondrial area per cell. **E)** Values of Dm, representing the average mitochondrial TMRM intensity (a measure of the mitochondrial membrane potential $\Delta\psi$). Statistics: Glucose and galactose conditions (CT1, S7, S8: N = 2, n = 60; V1: N = 1, n = 12). Galactose + pyruvate condition (CT1, S7, S8, V1: N = 1, n = 12). Galactose + eNAD condition (CT1, S7, S8, V1: N = 1, n = 12; all concentrations). Results for the individual cell lines and detailed data analysis are presented in Fig. S10, S11.

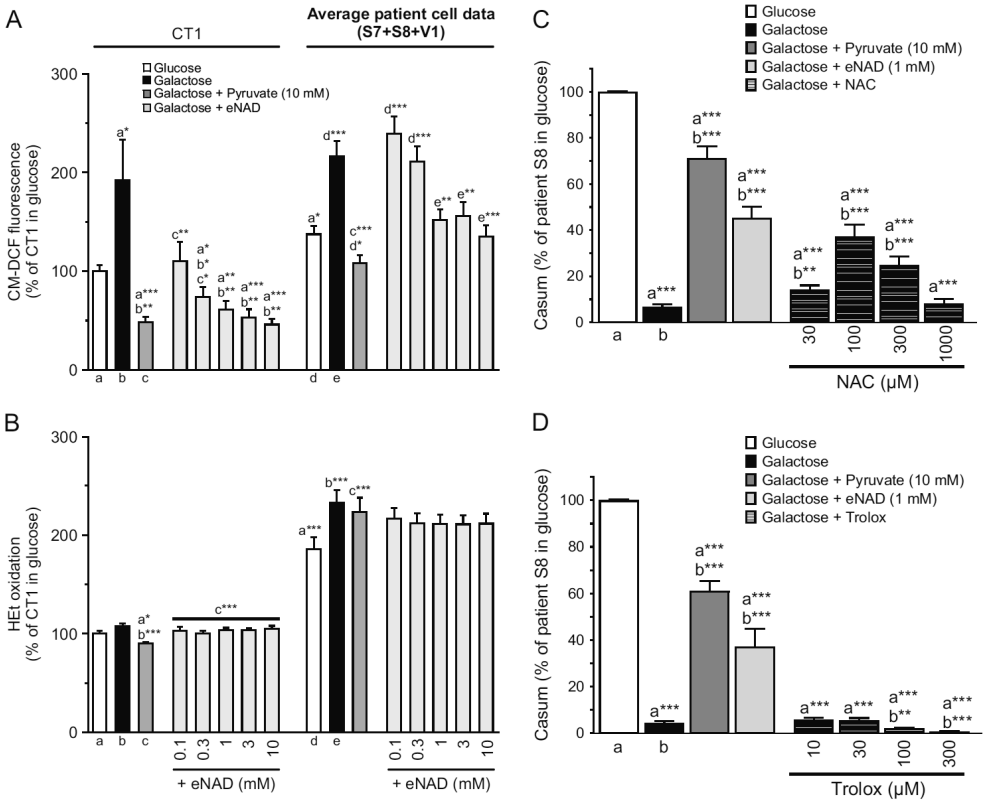


Figure 6.6: Effect of galactose, pyruvate and exogenous NAD$^+$ (eNAD) on cellular ROS levels and of exogenous antioxidants on the viability of LS fibroblasts. CT1 and LS cells (S7, S8, V1) were cultured in glucose or galactose medium and analyzed at 24 h (CM-DCF fluorescence and HEt oxidation) and at 96 h (viability). **A)** Effect of the various treatments on cellular ROS levels as reported by CM-DCF fluorescence (N = 4, n $\geq$ 36). **B)** Same as **A** but now for HEt oxidation (N = 4, n $\geq$ 36). **C)** Effect of the antioxidant N-acetylcysteine (NAC) on the viability of S8 cells in galactose medium (N = 3, n = 12). **D)** Same as **C** but now for the antioxidant Trolox (N = 3, n =12). Statistics: $^*P < 0.05$, $^{**}P < 0.01$, $^{***}P < 0.001$, relative to the marked condition (**a**, **b**, **c**, **d**, **e**). Results for the individual cell lines are presented in Fig. S12.

6.5.6 Cellular ATP content decreases in galactose medium and is normalized by eNAD but not by pyruvate in LS cells

Pyruvate and eNAD differentially affected $\Delta\psi$ in galactose-cultured LS cells (Fig. 6.5e), potentially impacting on mitochondrial ATP production. In glucose medium, the ATP content of LS fibroblasts exceeded that of CT1 cells (Fig. 6.7a). Glucose-by-galactose replacement reduced ATP content to a greater extent in LS cells than in CT1 cells (Fig. 6.7a). In both CT1 and LS cells, eNAD supplementation normalized the galactose-induced reduction in ATP content, whereas pyruvate did not (Fig. 6.7a). Preventing mitochondrial ATP production by the F_0F_1-ATPase (CV) inhibitor Oligomycin A (OLI) reduced the ATP content of CT1 and LS cells under all conditions (Fig. 6.7b). This demonstrates that mitochondrial ATP production is active. In glucose medium, quantification of this ATP reduction revealed that mitochondria contribute twofold less to total ATP levels in LS cells than in CT1 cells (Fig. 6.7c). Given their higher ATP level(Fig. 6.7a; white bars), this suggests that glycolysis is more active in LS cells. Galactose treatment induced a threefold and sixfold increase in the mitochondrial contribution to total ATP content in CT1 and LS cells, respectively (Fig. 6.7c). Addition of eNAD did not affect the mitochondrial ATP contribution in CT1 but further increased this parameter in LS cells (Fig. 6.7c).

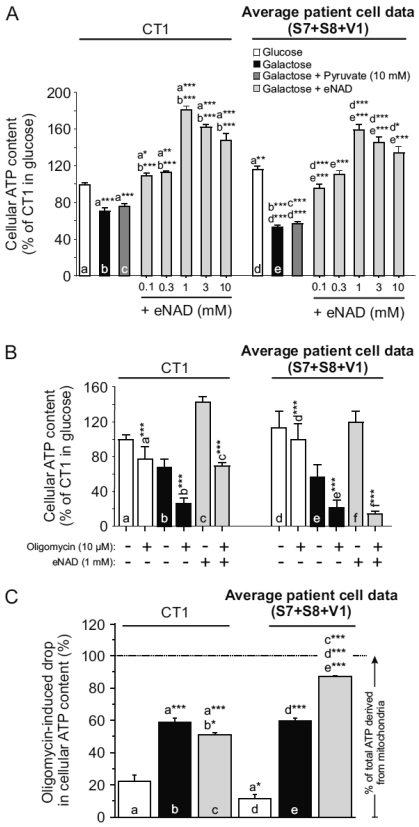


Figure 6.7: Effect of galactose, pyruvate and exogenous NAD$^+$ (eNAD) on cellular ATP content and mitochondrial ATP production. CT1 and LS cells (S7, S8, V1) were cultured in glucose-or-galactose medium for 24 h and analyzed. **A)** Effect of the various treatments on the average cellular ATP content in control (CT1) and LS cells (N = 5, n $\geq$ 45). **B)** Effect of the various treatments (see legend in **A**), in the absence and presence of Oligomycin (10 μM, 30 min), on the average cellular ATP content in control (CT1) and LS cells (N = 4, n $\geq$ 36). **C)** Effect of the various treatments (see legend in **A**) on the Oligomycin-induced drop in cellular ATP content, reflecting the contribution of OXPHOS-derived ATP production (calculated from the data in **B**). Statistics: $^*P < 0.05$, $^{**}P < 0.01$, $^{***}P < 0.001$, relative to the marked condition (**a**, **b**, **c**, **d**, **e**, **f**). Results for the individual cell lines are presented in Fig. S13.

6.6 Discussion

Activation of glycolysis during CI dysfunction can mask deficiency-induced aberrations in cell physiology (Fig. 6.8a). Here we prevented this activation by culturing CT and LS fibroblasts in pyruvate-free media containing galactose. In glucose medium, LS fibroblasts exhibited a partially depolarized $\Delta\psi$, increased HEt and H_2DCFDA oxidation and altered mitochondrial morphology (Fig. 6.8b), compatible with our previous findings (Distelmaier et al., 2009b). In addition, we here demonstrate that LS cells display a higher ATP content than CT1 fibroblasts and derive less of their total ATP from mitochondria. This suggests a mechanism in which: (i) the CI-deficient state stimulates glycolytic lactate and ATP generation, there by reducing the mitochondrial contribution to cellular ATP content, and (ii) NADH levels increase as the combined result of glycolytic upregulation and hampered mitochondrial NADH-to-NAD^+ conversion by CI (Fig. 6.8a).

6.6.1 Galactose induces specific death of LS cells

Glucose-by-galactose replacement induced the specific death of LS fibroblasts without affecting CT1 cell viability, providing that a sufficiently low cell seeding density was used. We speculate that cell-cell adhesion might play a role in counteracting the galactose effect (Bergin et al., 2000) and/or death-suppressing pathways might become activated at high cell densities (Reuven et al., 2013). Galactose treatment invariably reduced the viability of S8 fibroblasts with a low residual CI activity (18% of lowest control value) whereas variable results were obtained with S7 and V1 cells displaying a moderate reduction in CI activity (68–64%). This is compatible with previous findings (Robinson et al., 1992) and suggests a mechanism in which the degree of CI deficiency determines the extent of compensatory glycolysis activation and, as a consequence, the cellular sensitivity to glucose-by-galactose replacement. Indeed, CI inhibition dose-dependent increased lactate production in mouse fibroblasts (Yang and Balcarcel, 2003) and NADH-cytochrome *c* reductase activity inversely correlated with the L/P ratio in primary fibroblasts from OXPHOS-deficiency

patients (linear correlation: R =-0.61; p = 0.01; data from ref. (Pitkanen and Robinson, 1996).

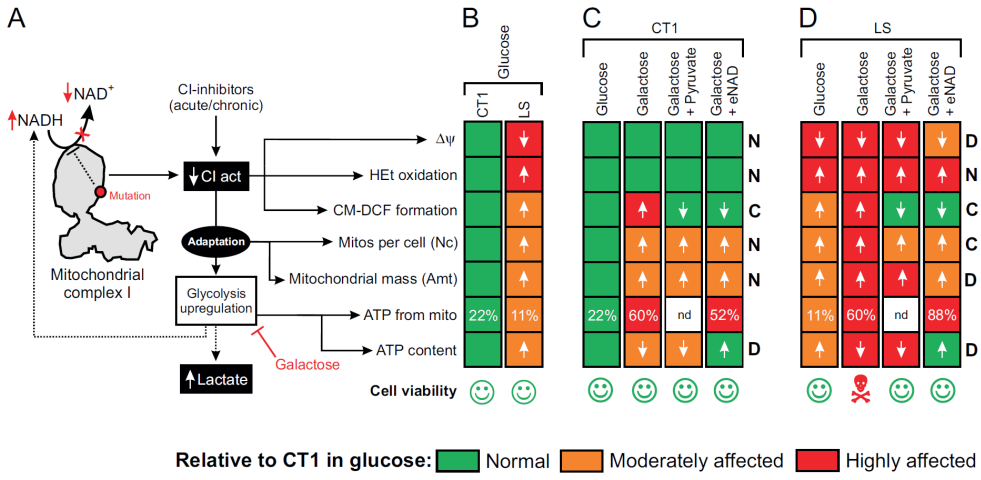


Figure 6.8: Differential effects of galactose, pyruvate and eNAD on live-cell functional parameters in CT1 and LS fibroblasts. a) Mutations in mitochondrial complex I (CI) or chemical CI inhibition reduce the conversion of NADH into NAD$^+$ and CI catalytic activity (CIact), associated with increased NADH and reduced NAD$^+$ levels ("reductive stress"). The reduced CI activity is associated with alterations in mitochondrial membrane potential($\Delta\psi$), the levels of HEt- and H_2DCFDA-oxidizing ROS, the number of mitochondria per cell (Nc), mitochondrial mass (Amt), mitochondrial ATP production and cellular ATP levels. As an adaptation to CI deficiency, glycolysis is upregulated leading to increased production of NADH and lactate. In this study, glucose in the culture medium was replaced by galactose to inhibit glycolysis upregulation. **b)** Functional changes associated with glucose-by-galactose replacement in control (CT1) fibroblasts. The magnitude of each change is color coded in green (no effect), orange (moderately affected) or red (highly affected). Cell viability is indicated by pictograms. **c)** Same as **b** but now also including the effects of pyruvate and exogenous NAD$^+$ (eNAD) supplementation on CT1 cells. For each measured parameter, it is indicated whether both supplements displayed a common effect("C"), differential effect ("D") or no effect ("N"). The glucose condition was reproduced from **b**. **d)** Same as **c**, but now for fibroblasts from Leigh Syndrome (LS) patients with isolated CI deficiency. The glucose condition was reproduced from **b**

6.6.2 Pyruvate rescues galactose-induced death of LS cells

Galactose only induced specific death of LS fibroblasts in the absence of pyruvate. Since pyruvate is normally produced by the glycolysis pathway (Lunt and Vander Heiden, 2011), this suggests that: (i) the reduced glycolytic flux in galactose-treated cells induces pyruvate shortage, and (ii) this pyruvate shortage is responsible for the specific galactose-induced death of LS cells. Pyruvate-mediated rescue of galactose-induced LS cell death was glutamine-dependent. However, although glutamine was present in all galactose media it did not prevent LS cell death in the absence of pyruvate. In HeLa cells, glutamine fuels OXPHOS-mediated mitochondrial ATP production via the TCA cycle, providing more than half of the ATP in the presence of glucose and virtually all ATP upon replacing glucose by galactose (Reitzer and Wice, 1979). In addition, inhibition of the mitochondrial pyruvate carrier in cancer cells activated glutamate dehydrogenase and rerouted the glutamine metabolism to generate oxaloacetate and acetyl-CoA, there by sustaining TCA cycle function (Yang et al., 2014). This situation might also be present in our galactose-treated LS cells, where the glycolytic pyruvate production flux is expected to be low. Alternatively, in case of OXPHOS-deficient cells with mitochondrial DNA (mtDNA) mutations, it was proposed that impaired NADH utilization by the mitochondrial ETC triggers reductive carbonylation of glutamine in the cytosol catalyzed by malate dehydrogenase 1 (Gaude et al., 2018). This study proposed a mechanism in which reduced mitochondrial NADH turnover inhibits the mitochondrial malate-aspartate shuttle (MAS), leading to cytosolic NADH accumulation. The latter then induces cytosolic reductive carbonylation of glutamine, which provides carbons for NADH-coupled MDH1 and thereby regulates NAD^+ redox state and enhances the activity of the glycolysis enzyme GAPDH. This then increases glycolytic flux to enhance ATP production in the cytosol (Gaude et al., 2018). However, since this mechanism requires a highly active glycolysis pathway it is unlikely that it explains the glutamine-dependence of the pyruvate rescue of galactose-induced LS cell death observed in our experiments. Previous evidence suggests that inhibited cell proliferation during ETC disruption is rescued by pyruvate supplementa-

tion via restoration of NAD^+/NADH balance mediated by lactate dehydrogenase in the cytosol (Titov et al., 2016; King and Attardi, 1989). Compatible with this mechanism, we observed that pyruvate slightly increased cellular NAD^+ content. However, pyruvate also displays antioxidant activity. Here, pyruvate rescue of galactose-induced LS cell death was paralleled by normalization of the galactose-induced increase in CM-H_2DCFDA oxidizing ROS levels (Fig. 6.8d). In contrast, the increased levels of HEt-oxidizing ROS in LS cells were neither stimulated further by galactose treatment nor affected by pyruvate. This suggests that pyruvate might rescue galactose-induced LS cell death by lowering the levels of CM-H_2DCFDA-oxidizing ROS. Supporting this idea, pyruvate protected human fibroblasts against hydrogen peroxide (H_2O_2)-induced cell death, by lowering CM-H_2DCFDA-oxidizing ROS levels and preventing $\Delta\psi$ depolarization (Ramos-Ibeas et al., 2017). Related to this, three other molecules that rescued galactose-induced LS cell death in the current study (pyruvate, oxaloacetate, and α-ketoglutarate) also reduced the levels of CM-H_2DCFDA-oxidizing ROS and protected against H_2O_2-induced toxicity (Sawa et al., 2017). Similarly, non-rescuing molecules in the current study (lactate, succinate, malate, and α-ketobutyrate) were also ineffective in the H_2O_2-induced toxicity model (Sawa et al., 2017). This suggests that (part of) the rescuing effects of pyruvate, oxaloacetate, and α-ketoglutarate is due to their antioxidant properties. Although glutamine also can act as an (in)direct antioxidant (Yang et al., 2017), its presence in the galactose medium did not prevent LS cell death. This means that it displays no antioxidant properties in our experimental system and/or its medium concentration is too low. Functionally,pyruvate supplementation did not affect $\Delta\psi$, Nc, Amtorthe decreased ATP content in galactose-treated CT1 cells (Fig. 6.8c). In galactose-treated LS cells, pyruvate slightly reduced Nc but did not restore $\Delta\psi$, Amt or cellular ATP content (Fig. 6.8c). Therefore we propose that pyruvate does not rescue galactose-induced LS cell death by restoring mitochondrial function but by its ability to prevent the galactose-induced increase CM-H_2DCFDA oxidizing ROS levels. This means that, under galactose conditions, pyruvate rescue of LS viability requires TCA fueling by glutamine to sustain biomolecule synthesis

and cell proliferation (Reitzer and Wice, 1979; Yang et al., 2014).

6.6.3 eNAD rescues galactose-induced death of LS cells

For the metabolites tested in this study, their ability to rescue the galactose-induced death of LS cells was not unequivocally paralleled by an iNAD increase. As mentioned above, this likely relates to fact that several of these metabolites also can act as antioxidants (pyruvate, oxaloacetate, and α-ketoglutarate). However, supplementation of the galactose medium with eNAD increased iNAD (Pittelli et al., 2011) and dose-dependently rescued LS cells from galactose-induced death. Oleamide dose dependently and completely inhibited thee NAD-induced rescue of galactose-induced death in LS cells, suggests that eNAD exerts its protective effects by increasing iNAD via gap junction hemichannels. Combined treatment with pyruvate and eNAD revealed that pyruvate alone rescued galactose-induced LS cell death to a larger extent than eNAD alone. In addition, rescue was always greater for combined pyruvate and eNAD supplementation than for eNAD alone. Remarkably, eNAD increased iNAD levels to a much greater extent than pyruvate. These results suggest that the rescuing effect of pyruvate is not due to its iNAD-increasing effect, which supports the above conclusion that pyruvate prevents galactose-induced LS cell death by acting as an antioxidant. Similar to pyruvate, eNAD lowered the galactose-induced increase in CM-H_2DCFDA-oxidizing ROS levels in galactose-treated CT1 (Fig. 6.8c) and LS cells (Fig. 6.8d). Although this suggests that iNAD directly lowers these ROS levels, the latter was not observed in HeLa cells (Pittelli et al., 2011)33. At the functional level, and similar to pyruvate, eNAD supplementation did not affect the normal $\Delta\psi$, the normal HEt oxidation, the moderately increased number of mitochondria per cell, the moderately increased mitochondrial mass or the moderately decreased ATP content in galactose-treated CT1 cells (Fig. 6.8c). In contrast, eNAD fully restored the galactose-induced reduction in ATP content of CT1 cells. In the case of galactose-treated LS cells, and in sharp contrast to pyruvate, eNAD partially restored the depolarized $\Delta\psi$ and fully restored the galactose-induced reduction in ATP content (Fig. 6.8d).

6.7 Conclusions

Our results establish a cell-based strategy for intervention testing and analysis of the pathophysiological consequences and adaptive responses in CI deficiency. We propose a mechanism in which pyruvate rescues the galactose-induced death of LS cells by directly lowering the levels of CM-H_2DCFDA-oxidizing and NAC-sensitive ROS, during which glutamine (and not pyruvate) is used for TCA cycle fueling. In the case of eNAD, we conclude that it rescues galactose-induced death of LS cells by partially restoring $\Delta\psi$ depolarization and fully normalizing their greatly reduced cellular ATP content. This is compatible with CI-deficient LS cells suffering from galactose-induced reductive stress. Whether NAD^+ lowers the levels of CM-H_2DCFDA-oxidizing ROS by reducing mitochondrial ROS production or via (indirectly) acting as an antioxidant remains to be determined.

Supplementary

Table S1: Meaning of descriptors extracted from Calcein/Hoechst/TMRM images.

Table S1: Meaning of descriptors extracted from Calcein/Hoechst/TMRM images

Nr[#]	Reporter	Descriptor	Symbol	Definition/meaning of descriptor[&]
1	TMRM	Aspect ratio	AR	Ratio between major axis and minor axis of an ellipse equivalent to object: measure of mitochondrial length.
2	TMRM	Area/Box	Ab	The ratio between the area of an object and the area of its bounding box.
3	TMRM	Box XonY	Bxy	Ratio between width and height of object's bounding box.
4	TMRM	Density mean	Dm	Average intensity of object (grayvalue): average mitochondrial intensity of TMRM signal.
5	TMRM	Axis minor	Axm	Length of minor axis of ellipse with same moments of order 1 and 2 as object (pixels).
6	TMRM	Diameter max	Dimax	Length of longest line joining two points of object's outline and passing through the object's centroid (pixels).
7	TMRM	Diameter min	Dimin	Length of shortest line joining two points of object's outline and passing through the object's centroid (pixels).
8	TMRM	Diameter mean	Dim	Average length of diameters measured at 2 degree intervals and passing through the object's centroid.
9	TMRM	Radius max	Rmax	Minimum distance between object's centroid and outline (pixels)
10	TMRM	Radius min	Rmin	Maximum distance between object's centroid and outline (pixels)
11	TMRM	Perimeter ellipse	P1	The perimeter of the ellipse surrounding the outline of each object (pixels)
12	TMRM	Radius ratio	Rr	Ratio between Rmax and Rmin
13	TMRM	Roundness	F	Perimeter2/(4*π*Area; a.k.a. Formfactor or F): measure of mitochondrial length and degree of branching.
14	TMRM	Length	Le	Feret diameter (caliper length) along the major axis of the object (pixels).
15	TMRM	Width	Wi	Feret diameter (caliper length) along the minor axis of the object (pixels).
16	TMRM	Perimeter2	P2	Chain code length of the outline (pixels)
17	TMRM	IOD	IOD	Integrated optical density of all objects (grayvalue): sum of all mitochondrial TMRM intensity values.
18	TMRM	Perimeter convex	Pc	Perimeter of the convex outline of the object (pixels)
19	TMRM	Perimeter	P3	Length of the object's outline (pixels)
20	TMRM	Perimeter ratio	Pr	Ratio of convex perimeter to perimeter
21	TMRM	Area polygon	Ap	Area included in the polygon defining the objects outline (same polygon as used for Perimeter)
22	TMRM	Count	Cou	Size weighted object "count" (number of objects).
23	TMRM	Box width	Bw	Width of the object's bounding box (pixels).
24	TMRM	Box height	Bh	Height of the object's bounding box (pixels).
25	TMRM	Feret min	Fmin	Smallest feret (caliper) length (pixels).
26	TMRM	Feret max	Fmax	Longest feret (caliper) length (pixels).
27	TMRM	Feret mean	Fm	Average feret (caliper) length (pixels).
28	TMRM	Density min	Dmin	Minimum density inside object (grayvalue).
29	TMRM	Density max	Dmax	Maximum density inside object (grayvalue).
30	TMRM	Density std dev	Dstdv	Standard deviation of intensity or density inside object (grayvalue).
31	TMRM	Margination	Ma	The distribution of intensity between the center of an object and the edge of the object.
32	TMRM	Area sum	Asum	Total area of the mitochondrial objects (pixels). The size of individual mitochondrial objects (Am) is given by Asum/Ot.
33	TMRM	Objects total	Ot	Total number of objects: total number of mitochondria.
34	Calcein	Area sum	Casum	Total area of the objects (pixels).
35	Calcein	IOD sum	CaIOD	Integrated pixel intensity of the objects (grayvalue)
36	Hoechst	*Nn*	Nn	Total number of objects: total number of nuclei/cells (assuming 1 nuclear object per cell).
37	Hoechst	H. area	An	Average area of the objects (pixels): average area of the nuclei.
38	Hoechst	H. roundness	Fn	Roundness of objects: describing nuclear shape.
39	Derived	Cell mito ratio	Mm	Given by: Asum/Casum, a measure of mitochondrial mass.
40	Derived	Norm mito area	Amt	Given by: Asum/Nn; equalling the total mitochondrial area (in pixels) per cell.
41	Derived	Norm mito number	Nc	Given by: Ot/Nn; equalling the average number of mitochondrial objects per cell. Asum/Ot equals the area (size) of individual mitochondrial objects (Am).
42	Derived	Norm cyto area	Casum/Nn	Average size of object (pixels): a measure of average cell size.
43	Derived	Confluence (%)	C%	Percentage image pixels that are cellular calculated from Casum; a measure of cell confluence.
44	Derived	Calcein fluoresence	CaIOD/Casum	Average intensity (grayvalues) per cellular pixel.

[#]Adapted from: **Blanchet et al., Sci. Rep., 2015; Iannetti et al., Nat. Protoc., 2016.** [&]As defined in the Image Pro Plus software. If the measurement unit is not specified in the definition column, it is Arbitrary Units (A.U.).

Table S2: Analysis of experimental variability in glucose and galactose viability experiments.

	DATE			MEDIUM				PN				Casum in glucose (% of patient S7 in glucose)				Casum in galactose (% of patient S7 in glucose)			
#	Y	D.M.	P	DP	A	SB	O	CT1	S7	S8	V1	CT1	S7	S8	V1	CT1	S7	S8	V1
1	1	14.03	1	10.03	4	#1	A	16	16	15	14	98.7	100.0	97.5	99.5	99.0	100.3	28.7	6.7
2	1	14.03	2	10.03	4	#1	A	16	16	15	14	97.4	97.9	93.3	96.8	96.6	98.4	25.6	3.2
3	1	18.03		14.03	4	#1	A	17	17	16	15	93.2	100.0	95.3	98.4	95.3	49.8	8.6	74.1
4	1	29.03		25.03	4	#1	A	19	19	18	17	98.4	100.0	95.3	100.4	98.1	31.9	8.9	7.8
5	1	16.04	1	29.03	19	#1	A	17	17	18	15	97.1	99.9	91.8	100.1	89.4	31.4	4.5	16.6
6	1	16.04	2	29.03	19	#1	A	17	17	18	15	98.4	99.9	94.8	100.7	77.2	21.8	4.5	35.7
7	1	18.04	1	29.03	21	#1	A	18	18	19	16	96.9	100.0	94.2	99.7	97.0	19.4	6.6	94.9
8	1	18.04	2	29.03	21	#1	A	18	18	19	16	96.7	99.9	88.7	98.9	96.5	15.4	3.9	84.6
9	1	21.04		29.03	24	#1	A	19	19	20	17	95.6	100.3	97.5	98.9	96.6	12.3	13.1	61.1
10	1	24.05	1	19.05	5	#1	A	17	18	19	17	94.6	98.3	99.7	101.5	89.8	21.6	32.9	16.0
11	1	24.05	2	19.05	5	#1	A	17	18	19	17	116.3	109.1	117.2	119.1	67.0	13.6	30.7	6.4
12	1	24.05	3	19.05	5	#1	A	17	18	19	17	152.7	99.9	153.0	155.9	30.3	25.3	26.4	15.6
13	1	07.06		03.06	4	#1	A	--	22	21	19	--	100.0	99.4	99.6	--	76.1	24.1	38.6
14	1	14.06		09.06	5	#1	A	--	17	16	16	--	100.0	102.1	103.4	--	10.3	2.7	9.9
15	1	28.06		24.06	4	#1	B	18	16	16		98.6	100.0	82.2	--	98.0	41.8	1.5	--
16	1	02.07		02.07	0	#1	B	14	15	14	18	95.5	100.0	94.2	92.1	94.0	47.2	2.8	5.7
17	1	19.09		15.09	4	#2	B	14	15	14	16	95.1	100.0	90.4	90.3	94.3	21.1	2.2	3.1
18	1	26.09		15.09	11	#2	B	15	16	17	15	97.6	100.0	98.9	98.7	97.5	17.7	6.1	8.6
19	1	01.10		15.09	16	#2	B	--	17	16	18	--	100.0	101.2	100.6	--	38.3	13.0	19.0
20	1	10.10	1	15.09	25	#2	B	--	18	19	17	--	100.0	97.2	94.6	--	14.5	3.8	4.7
21	1	10.10	2	15.09	25	#2	B	--	18	19	17	--	100.0	96.3	94.1	--	18.9	4.2	3.6
22	1	15.10	1	15.09	30	#2	B	18	19	17	18	95.5	100.0	98.9	99.5	97.2	7.2	1.9	1.4
23	1	15.10	2	15.09	30	#2	B	18	19	17	18	96.8	100.0	98.7	99.4	95.7	5.7	2.5	2.8
24	1	18.10		15.09	33	#2	B	--	18	19	20	97.8	100.1	95.1	95.2	93.0	6.7	3.2	4.2
25	2	07.03		16.02	21	#2	C	--	12	12	15	--	100.0	100.3	89.6	--	15.0	9.2	3.1
26	2	14.03	1	10.03	4	#2	C	12	13	12	16	98.6	100.0	86.0	97.4	97.2	31.4	2.5	7.7
27	2	14.03	2	10.03	4	#2	C		13	12	16	--	100.0	70.4	99.6	--	32.1	3.2	14.4
28	2	15.04	1	11.04	4	#2	C	14	17	16	16	98.8	100.0	107.6	73.7	92.7	16.3	4.9	28.8
29	2	15.04	2	11.04	4	#2	C	--	17	16	16	--	100.0	122.4	110.2	--	28.9	5.3	35.3
30	2	13.05		11.04	35	#2	C	13	16	15	13	99.6	100.0	83.6	88.2	87.8	14.4	0.4	2.2
31	2	16.05		12.05	4	#2	C	--	17	15	13	--	100.0	96.3	100.7	--	38.0	9.7	22.9
32	2	21.08	1	03.08	18	#2	A	--	17	18	19	--	100.0	99.7	99.8	--	59.0	5.9	78.4
33	2	21.08	2	03.08	18	#2	A	--	17	18	19	--	100.0	100.4	100.2	--	44.9	2.2	61.2
34	2	29.08	1	03.08	26	#2	A	--	16	14	15	--	100.0	98.5	100.1	--	64.0	8.8	85.3
35	2	29.08	2	03.08	26	#2	A	--	16	14	15	--	100.0	97.6	100.7	--	57.7	7.3	82.5
36	2	04.09	1	31.08	5	#3	A	--	17	15	16	--	100.1	99.2	100.0	--	99.5	5.0	91.5
37	2	04.09	2	31.08	5	#3	A	--	17	15	16	--	103.9	100.4	100.0	--	101.8	3.7	96.3
											Total number of wells:	105	171	171	163	139	211	211	199
											Total number of days (independent experiments):	16	25	25	24	16	25	25	24

Abbreviations: -- = not measured; A = Age; D.M = Day.Month; DP = Date prepared; O = Operator; P = Plate; PN = Passage Number; SB = Serum Batch; Y = Year.

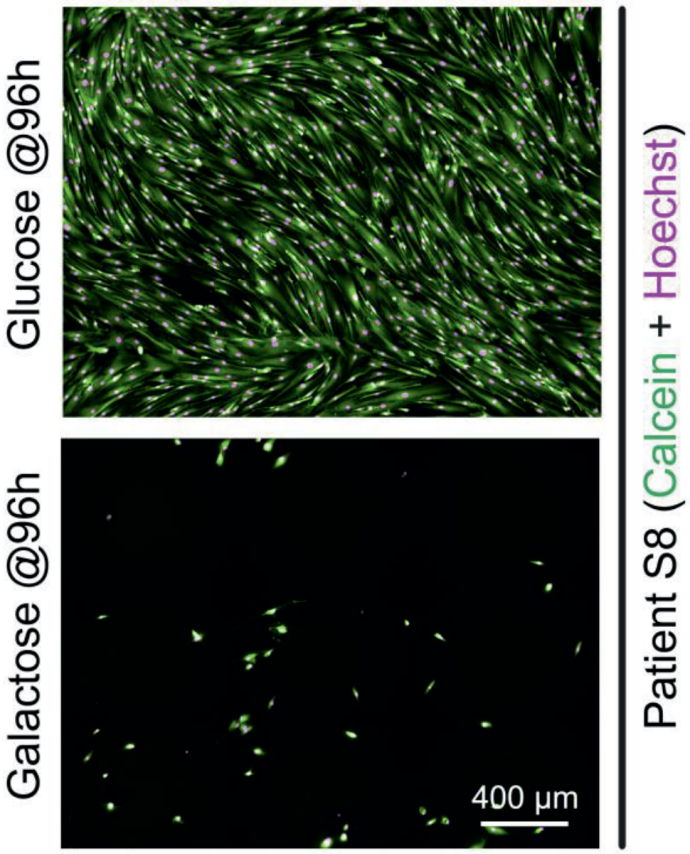


Figure S1: Magnification of the MSK image in panel A (96 h) of Fig. 6.1A for S8 patient fibroblasts. It depicts the co-localization of Calcein (green) and Hoechst (purple) staining for the glucose and galactose condition.

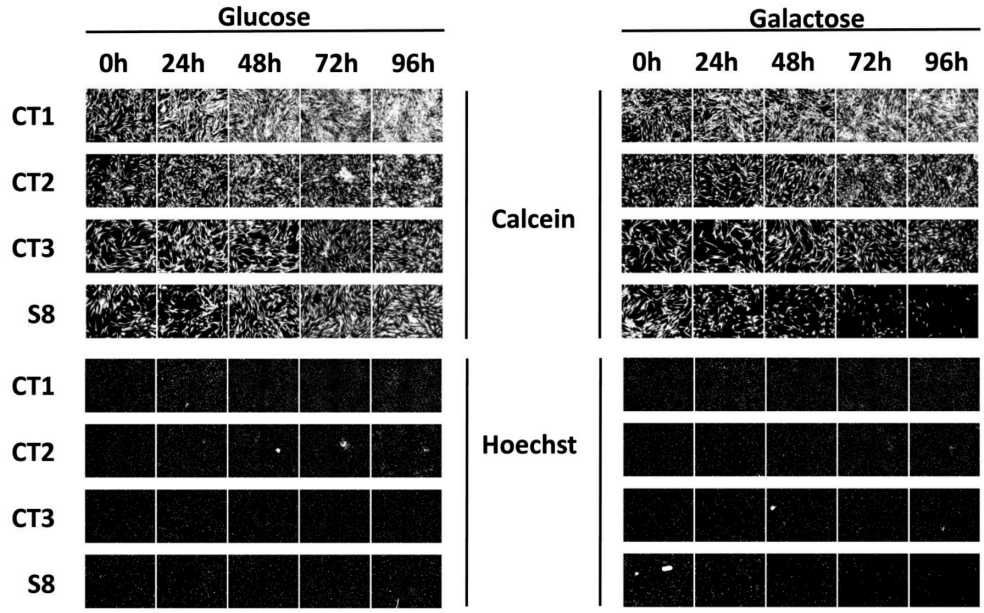


Figure S2: Galactose specifically reduces the viability of LS fibroblasts in a time-dependent manner. The cells were co-stained with Calcein-AM and Hoechst 33258 to visualize the cytosol and nuclei, respectively. Image processing was applied to calculate "masked" (MSK) and black-and-white "binary" (BIN) images (see Results for details). A time-dependent analysis was performed ($N = 3$, $n \geq 2$) of control (CT1, CT2, CT3) and LS cells (S8) cultured in glucose-medium (left panel) or galactose-medium (right panel). The viability of LS fibroblasts was specifically reduced in the galactose medium in a time-dependent manner, whereas this phenomenon was not observed in the glucose medium. A quantitative analysis is presented in Fig. S3.

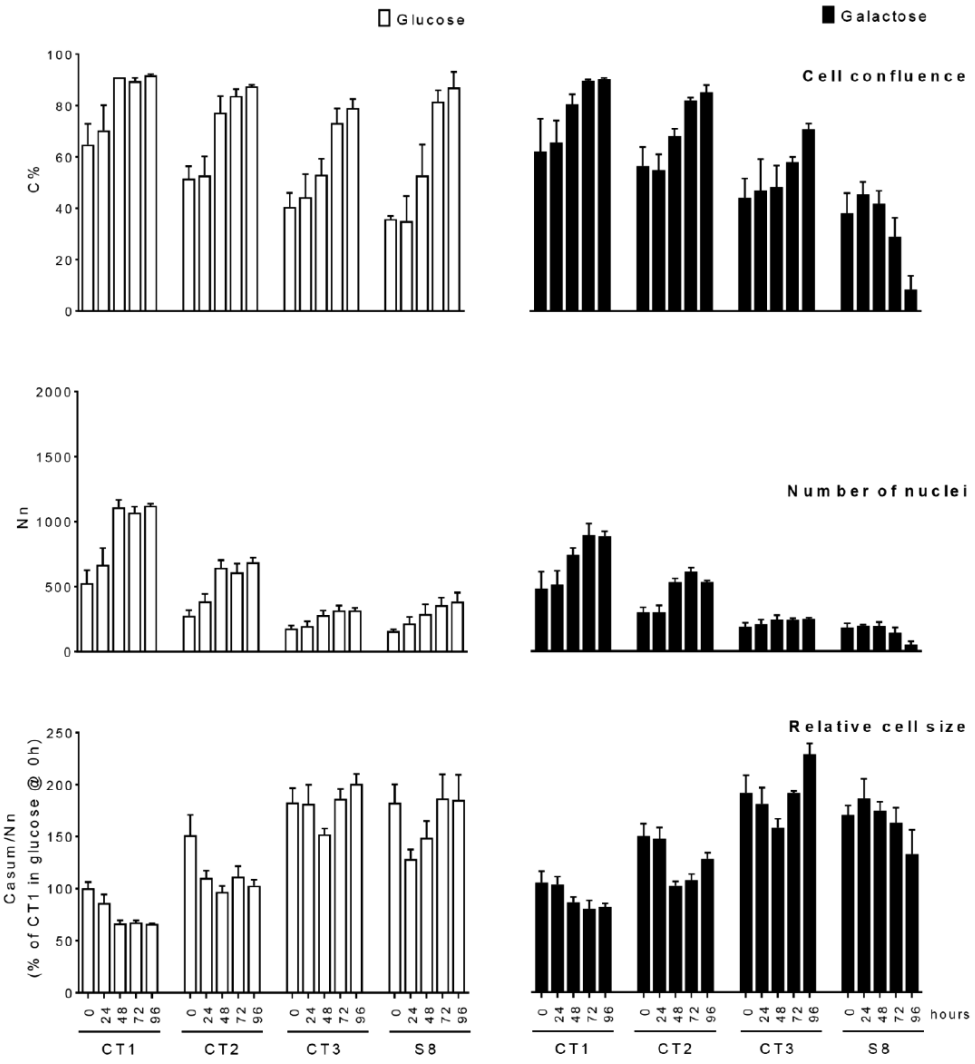


Figure S3: Galactose specifically reduces the viability of LS fibroblasts in a time-dependent manner. Quantification of the experiments described in Fig. S2. **Upper panel**: the y-axis represents C%, the percentage of total pixels in the BIN image that was Calcein-positive. C% is a measure of cell confluency. **Middle panel**: The y-axis represents the number (Nn) of Hoechst-positive objects (nuclei), calculated from the Hoechst BIN image. Nn is used as a measure of cell number. **Lower panel**: The y-axis reflects the total number of Calcein-positive pixels (Casum; a measure of cell area) divided by the number of nuclei (Nn). This reflects the relative size of the cells (expressed as % of CT1 in glucose at 0 h). See *Results* and Fig. 6.1 for details.

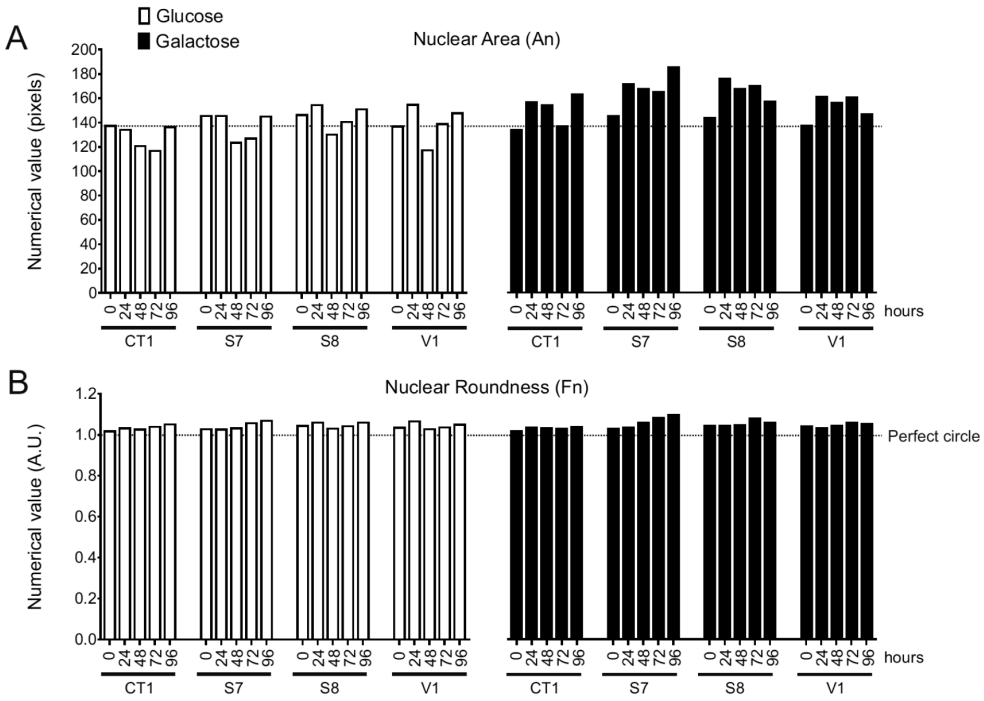


Figure S4: Nuclear morphological parameters derived from the Hoechst binary images in Fig. 6.1. A) Time dependent effect of glucose and galactose in CT1 and LS patient cells (S7, S8, V1) on the Nuclear Area (An) given in pixels (N = 1, n $\geq$ 2). **B)** Same as panel A but now for the Nuclear Roundness (or Formfactor; Fn). Dotted lines indicate the value of An in CT1 cells at 0 hours (panel A) and Fn (i.e. a value of 1) for a perfect circle in panel B (see also Table S1). An was larger in galactose than in glucose medium for both CT1 and LS cells, whereas Fn was not affected. This demonstrates that nuclear fragmentation is absent for all cell lines in glucose and galactose medium and, therefore, Nn is a true measure of the number of nuclei.

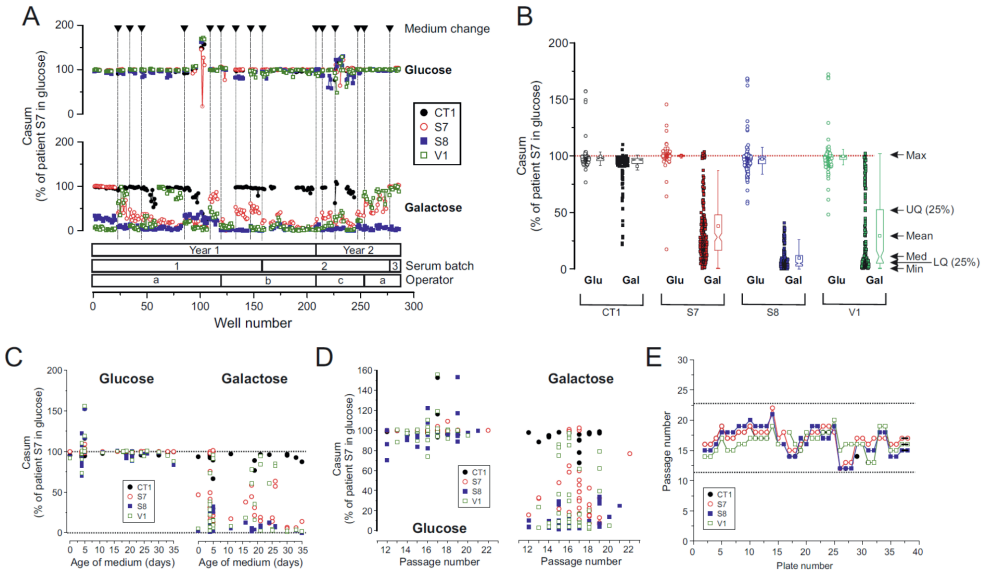


Figure S5: Effect of galactose treatment on the viability of CT1 and LS cells in multiple experiments performed over a time period of 18 months. The numerical data for this figure is provided in Table S1. A) The effect of galactose treatment (96 h) on cell viability was quantified in multiple experiments performed using different batches of serum ("serum batch") by different researchers ("Operator") over a period of 18 months ("year 1" and "year 2"). Black triangles and dotted vertical lines indicate the time points when a freshly prepared galactose medium was used for the first time. The upper and lower halves of the graph displays the effect of culturing in glucose and galactose medium, respectively. A total number of 105-199 wells (individual symbols; x-axis) were analyzed in 16-25 independent experiments (plates) for control (CT1; black circles), NDUFS7 ("S7", red circles), NDUFS8 ("S8", blue squares) and NDUFV1 ("V1", green squares) fibroblasts. Since S7 cells were present in every experiment, Casum was normalized on the value obtained for S7 cells in glucose, since this condition was present on every plate. **B)** Alternative representation of the galactose data depicted in panel A using a box and whisker plot. The latter indicates the highest value (Max), upper 25% quartile (UQ), average value (Mean), median value (Med), lower 25% quartile (LQ) and lowest value (Min) in the data set. **C)** Cell viability (96 h) of the various cell lines cultured in glucose (left panel) and galactose medium (right panel) as a function of the age of the culture medium. **D)** Similar to panel C, but now for cell passage number. **E)** Passage number of the various cell lines used in the experiments.

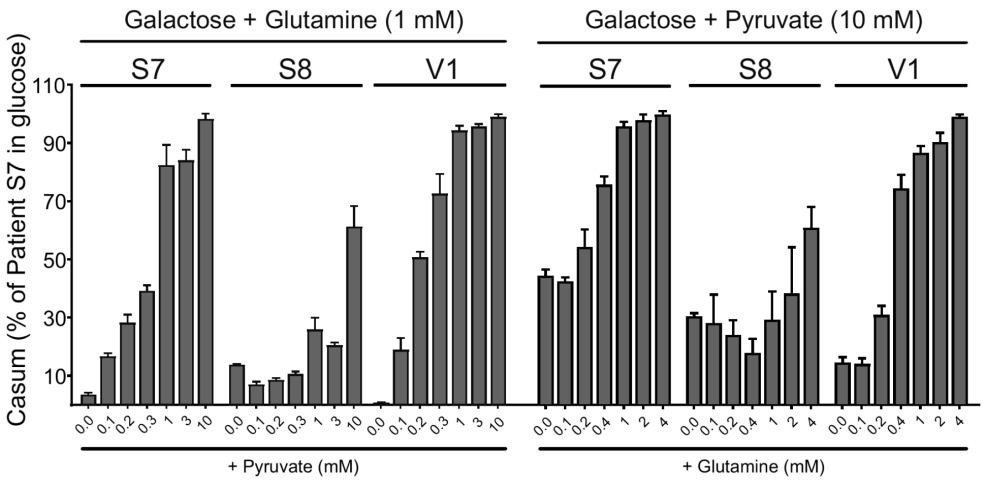


Figure S6: Data for individual cell lines (S7, S8, V1) used to create Fig. 6.2D and E. See *Results* for details.

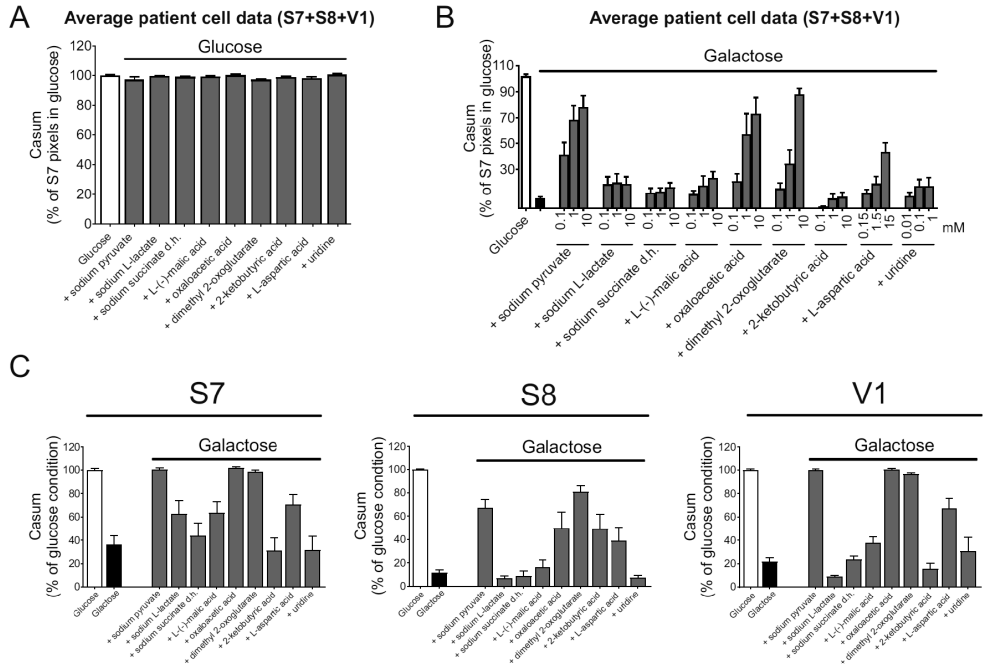


Figure S7: Data for individual cell lines (S7, S8, V1) used to create Fig. 6.2G. See *Results* for details.

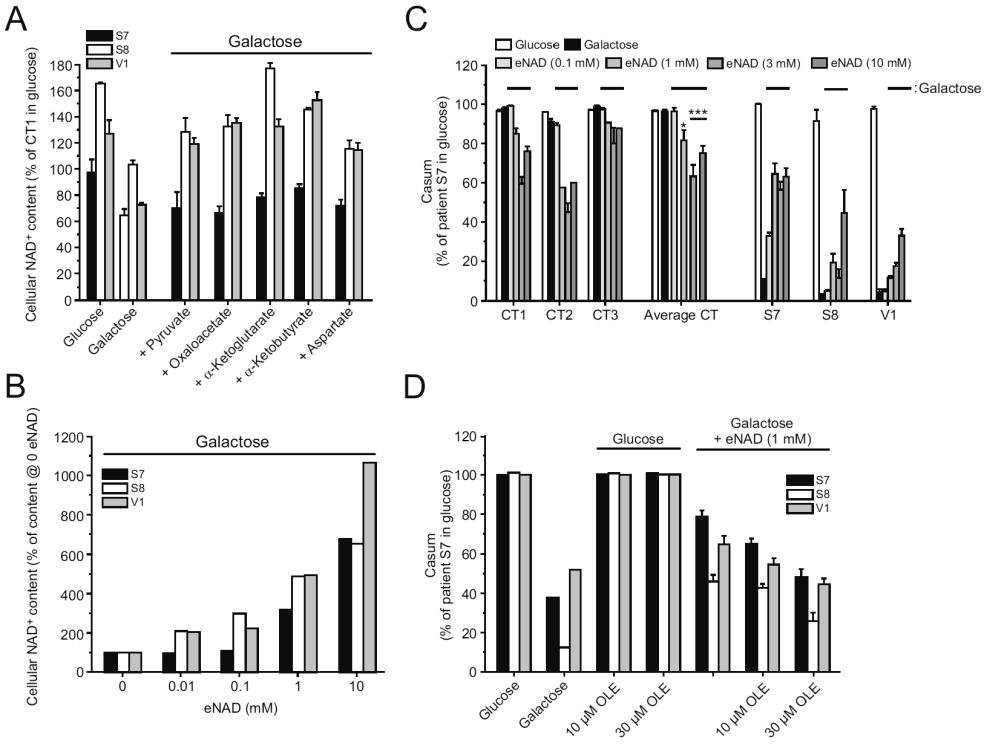


Figure S8: Data for individual cell lines (S7, S8, V1) used to create Fig. 6.3A, B, D and E. See *Results* for details.

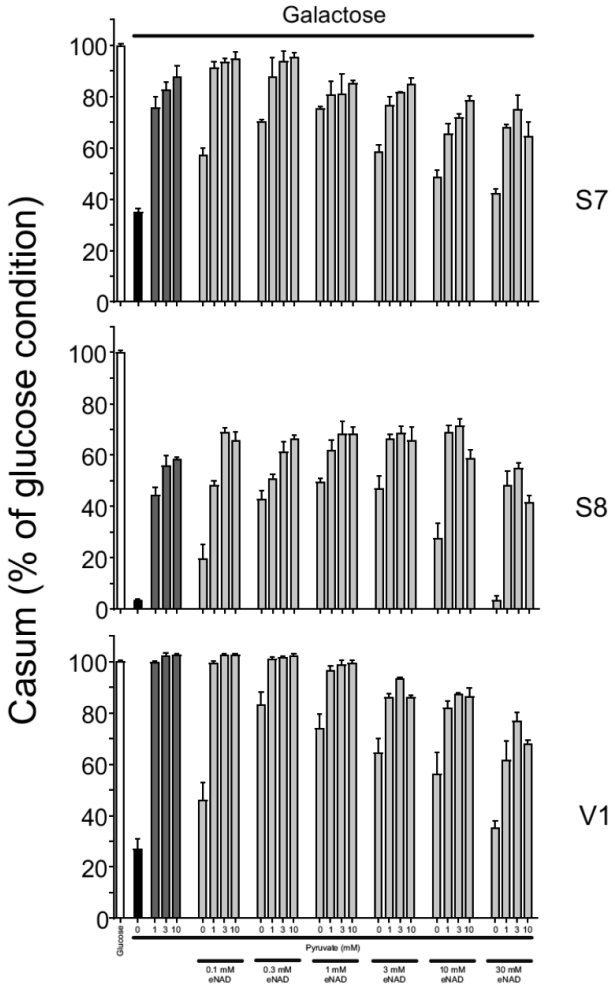


Figure S9: Data for individual cell lines (S7, S8, V1) used to create Fig. 6.4. See *Results* for details.

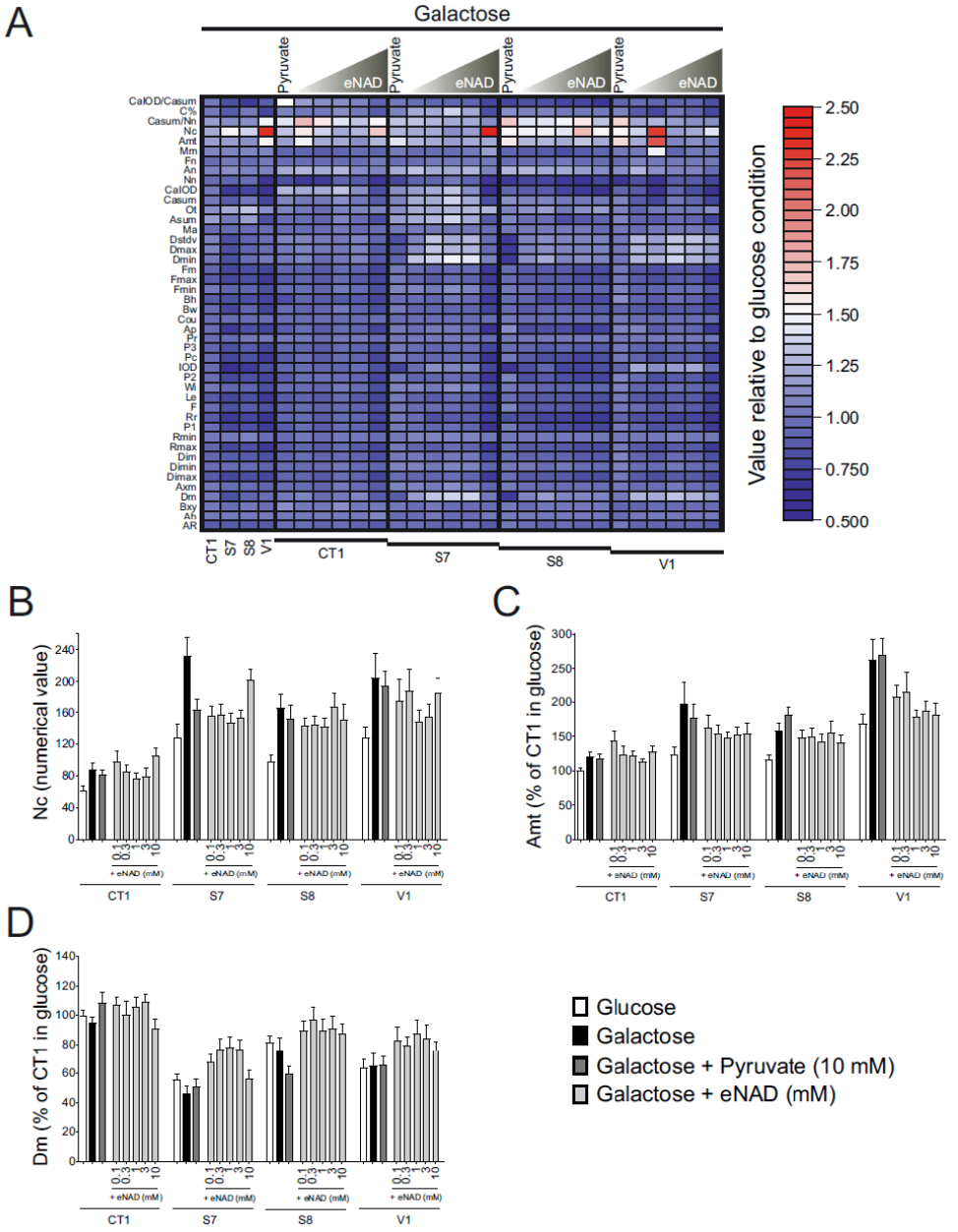


Figure S10: Data for individual cell lines (CT1, S7, S8, V1) used to create Fig. 6.5B, C, D and E. See *Results* for details.

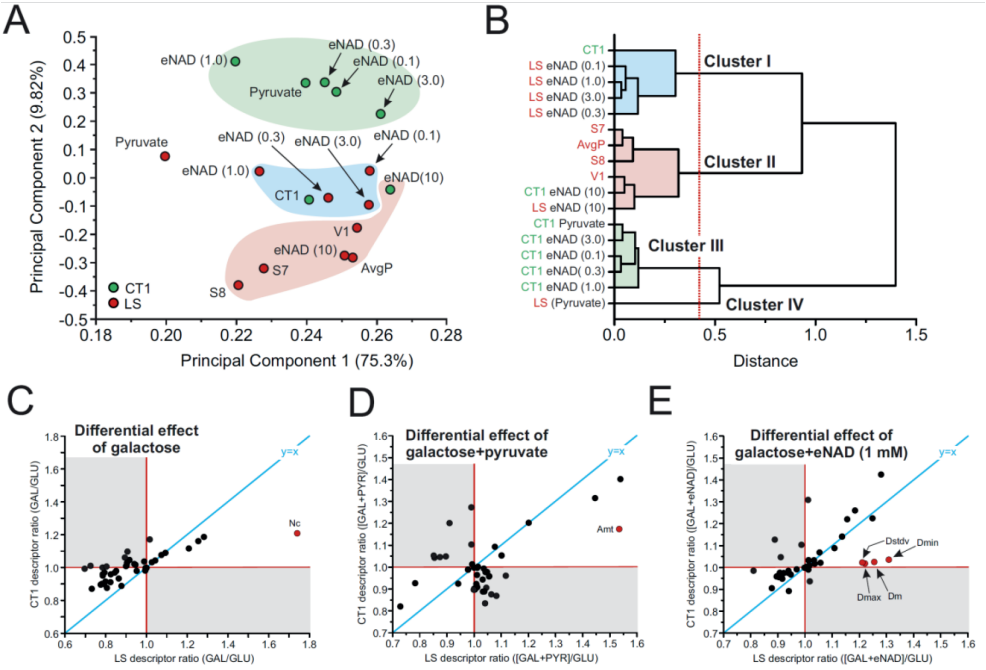


Figure S11: Analysis of the mitochondrial morpofunctional data in Fig. 6.5B. (A) Principal component analysis (PCA) of the data depicted in Fig. 6.5B. The colour of the symbols indicates CT1 (green) and LS patient (red) data. Three groups (marked by different colors) were detected in the data using cluster analysis (see panel B). **B)** Cluster analysis of the data depicted in Fig. 6.5B (using the Ward clustering method and correlation as a distance measure). **C)** To gain more detailed insight into the morphofunctional consequences of the various treatments, we determined which descriptors were differentially affected the most in CT1 vs. LS cells. To this end the average numerical value for each descriptor for CT1 cells was plotted as a function of its numerical value in LS cells. Descriptors for CT1 that are not affected by the treatment fall on the horizontal red line. Descriptors for LS cells that are not affected by the treatment fall on the vertical red line. Descriptors that are similarly affected by the treatment in CT1 and LS cells fall on the line y = x (blue). Grey boxes mark the regions were the treatments induced opposite changes in CT1 and LS cells. In case of the differential effect of galactose (relative to the glucose condition) on CT1 (y-axis) and LS patient cells (x-axis), this analysis yielded Nc (the number of mitochondria per cell) as the most extreme differential descriptor (red symbol). **D)** Same as panel C, but now for the differential effect of galactose + pyruvate on LS and CT1 cells. The most extreme differential descriptor was Amt (red symbol). **E)** Same as panel C, but now for the differential effects of galactose + 1 mM eNAD on LS and CT1 cells. The most extreme differential descriptors were Dstdv, Dmax, Dm and Dmin (red symbols). (Caption continues on next page)

Figure S11: ***Panel A and B*** demonstrate that galactose treatment induces a different phenotype in CT1 and LS cells, as exemplified by the CT1 condition being part of cluster I (blue), whereas the S7, S8 and V1 conditions are part of cluster II (pink). Moreover, CT1 and eNAD-treated LS cells (0.1, 0.3, 1.0 and 3.0 mM) part of cluster I, demonstrating that their mitochondrial morphofunctional phenotypes are highly similar. In contrast, LS cells cultured in galactose medium supplemented with a higher eNAD concentration (10 mM) or pyruvate were not part of cluster I. This means that the galactose-induced phenotypic difference between CT1 and LS cells disappears upon supplementation with eNAD (up to a concentration of 3.0 mM), whereas a high eNAD concentration (10 mM) and pyruvate do not have this effect.

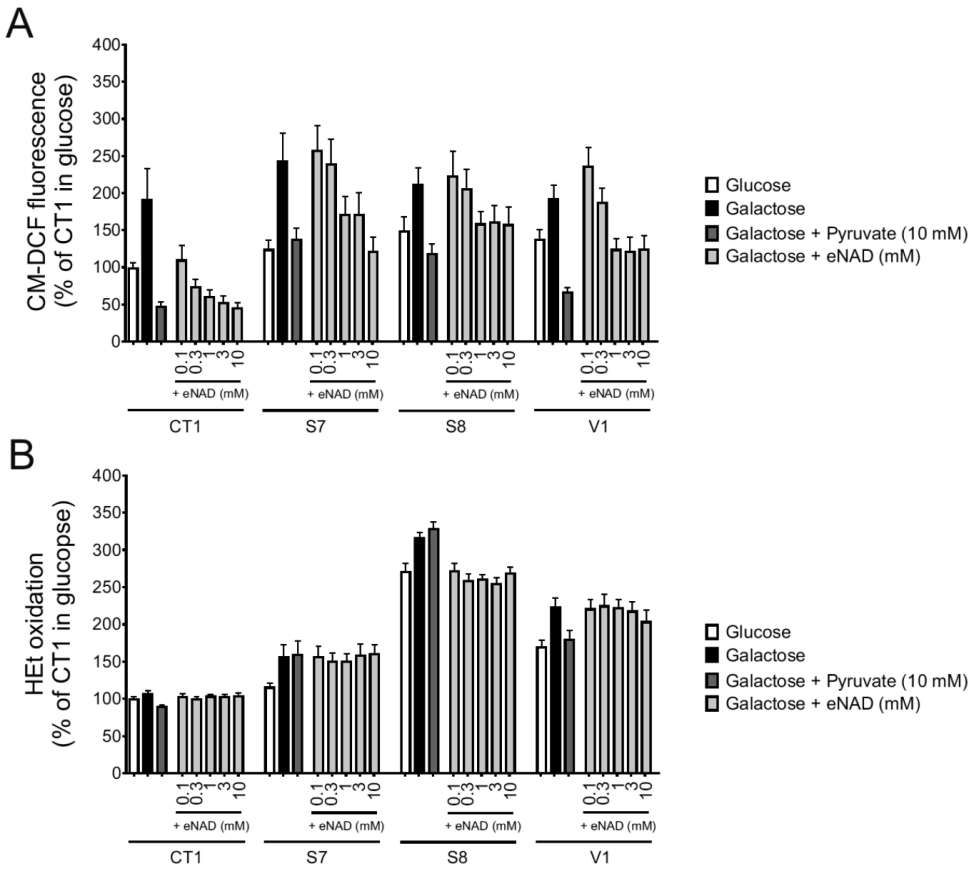


Figure S12: Data for individual cell lines (CT1, S7, S8, V1) used to create Fig. 6.6A and B. See *Results* for details.

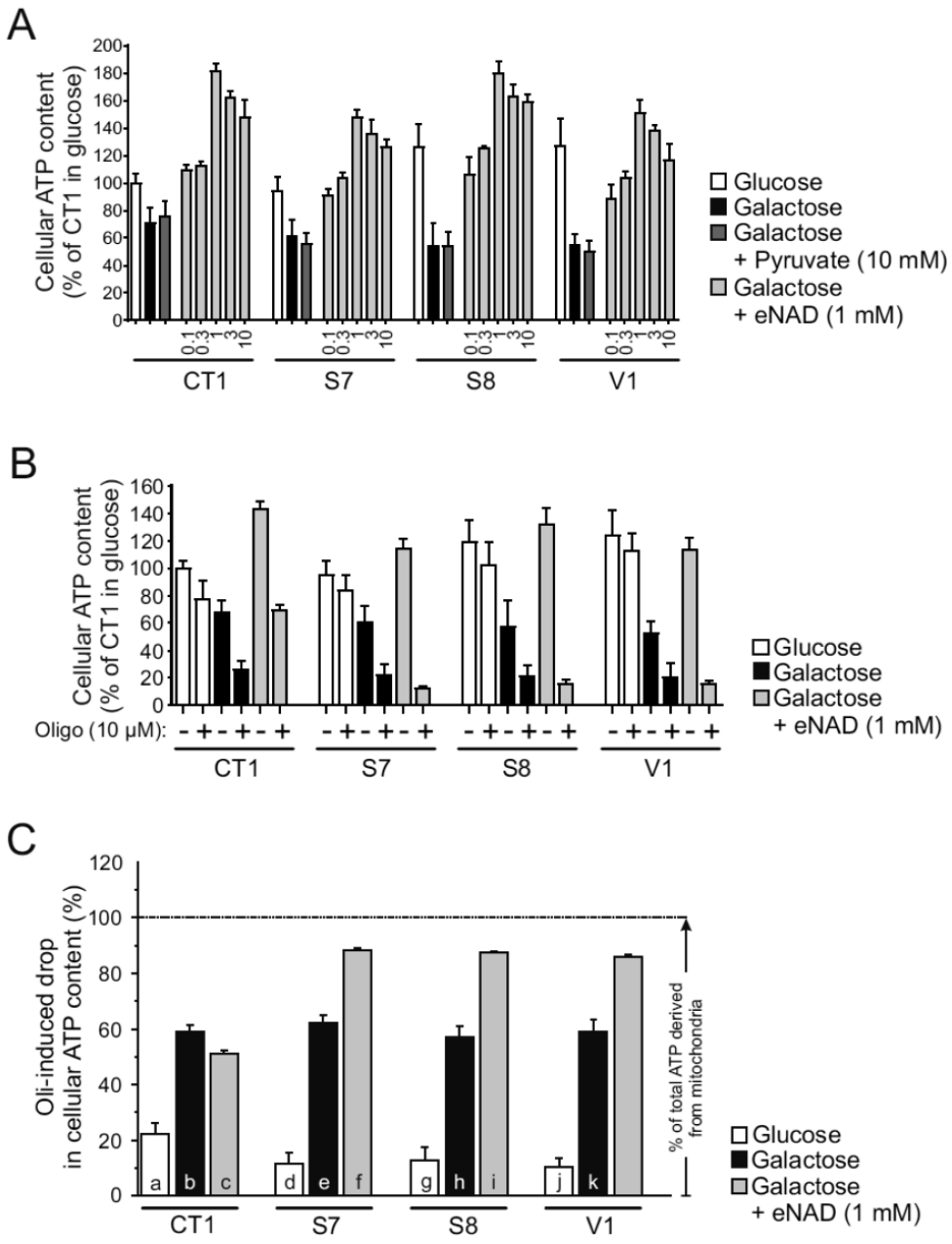
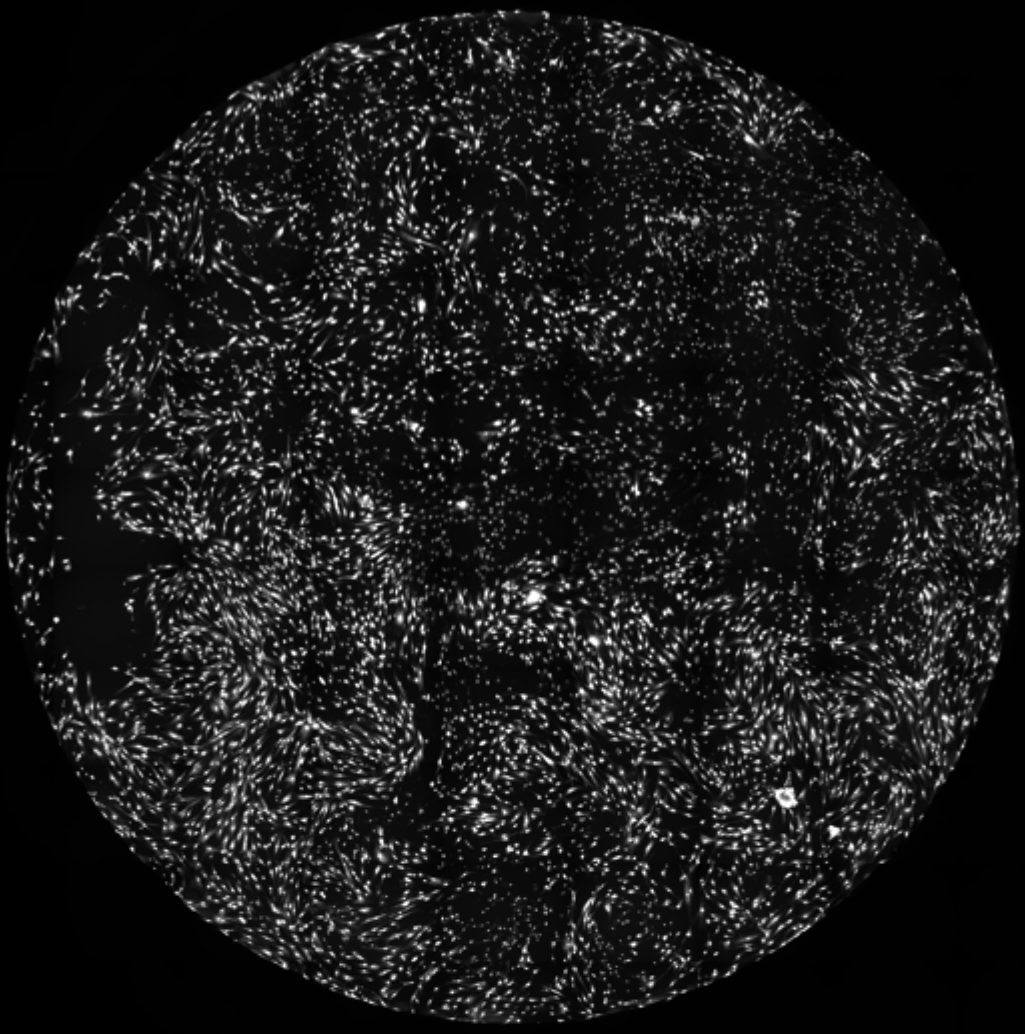


Figure S13: Data for individual cell lines (CT1, S7, S8, V1) used to create Fig. 6.7A, B and C. See *Results* for details



Chapter 7

Selective death of Complex I-deficient Leigh Syndrome patient skin fibroblasts upon glutathione depletion

Unpublished: **Iannetti, E. F.**, Renkema, H, Smeitink, J.A.M., Koopman, W.J.H., Beyrath, J.

7.1 Introduction

Primary mitochondrial diseases are a heterogenous group of genetic pathologies caused by changes in macromolecules (proteins or RNA) required for the normal function of the oxidative phosphorylation system. Often these changes result in altered function of one or more of the mitochondrial oxidative phosphorylation enzyme complexes (Gorman et al., 2016). In particular, Leigh Syndrome (LS), is a severe, neurodegenerative disorder representing the most frequent paediatric presentation of mitochondrial disease (Lake et al., 2016). The most common biochemical basis of LS is the deficiency of the mitochondrial respiratory chain enzyme complex I (CI) (Ma et al., 2013).

Many studies have reported that different cell models for CI deficiency display higher content of reactive oxygen species (ROS) (Distelmaier et al., 2009b; Iuso et al., 2006; Leipnitz et al., 2018; Lopez-Fabuel et al., 2016; Sharma et al., 2011; Tretter et al., 2004; Verkaart et al., 2007a,b). ROS increase can lead to oxidation of macromolecule such as lipids, however we could not detected any evidence that cellular lipid peroxidation is increased in CI-deficient PHSFs (Verkaart et al., 2007b) and scant evidence is published on the direct consequence of CI deficiency/inhibition on lipid peroxidation in other cell models (Abeti et al., 2016; Barrientos and Moraes, 1999; Basit et al., 2017). Nevertheless recent studies indicate lipid peroxidation of the mitochondrial inner membrane, among various ROS, as a major cause of mitochondrial disruption during mitochondrial dysfunction (Gao et al., 2018; Nielson and Rutter, 2018). Lipid peroxidation also plays a crucial role in ferroptosis (Yang et al., 2016). Ferroptosis is described as a nonapoptotic but regulated form of cell death, driven by loss of activity of the lipid repair enzyme GPX4 and subsequent accumulation of lipid hydroperoxides (Yang et al., 2016). This mode of cell death is also described for neurodegenerative diseases (Morris et al., 2018). Mitochondrial involvement in the ferroptosis pathway has been recently investigated, however, its exact role is still under debate (Basit et al., 2017; Dixon et al., 2012; Gao et al., 2018; Neitemeier et al., 2017; Yang et al., 2016).

The inhibition of ferroptosis may protect from neurodegeneration and therefore

a dedicated effort has been put into the discovery and optimization of specific ferroptosis inhibitors. Ferrostatin-1 was the first identified potent and specific drug-like small-molecule inhibitor of ferroptosis (Dixon et al., 2012) and it still remains the reference compound.

Primary human skin fibroblasts (PHSFs) are an established model to study mitochondrial disease-related cellular phenotypes, however exogenous stress inducers are often necessary to expose pathological symptoms and study the dysfunctions. In a recent work, we studied PHSFs replacing glucose cell culture medium by galactose. The latter enters glycolysis at a much slower rate than glucose preventing ATP production via rapid glucose-to-pyruvate conversion but enforcing it to rely on mitochondrial metabolism (Iannetti et al., 2019). Treating cells with L-buthionine-(S,R)-sulfoximine (BSO) is another cell culture strategy to enhance pathological mitochondrial dysfunctions in PHSFs (Beyrath et al., 2018; Enns et al., 2012). BSO is an inhibitor of gamma-glutamylcysteine synthetase, the rate limiting enzyme in the glutathione (GSH) biosynthesis and treatment of cells with this compound results in reduced intra cellular GSH levels (Shrader et al., 2011). GSH plays a key role in the general cellular free radical defence by working as an essential cofactor of the lipid repair enzyme glutathione peroxidase 4 (GPX4) amongst others (Brigelius-flohé and Maiorino, 2013). Depletion of GSH inhibits GPX4 leading to the accumulation of lipid peroxides potentially triggering ferroptosis (Dixon et al., 2012; Yang et al., 2014).

We previously showed that upon BSO-induced GSH depletion and consequent redox perturbation, the viability of CI deficient LS mitochondrial diseased PHSFs is severely affected, while CT cells remained viable. Moreover, we reported the development of KH176, a new clinical-stage drug candidate acting as a ROS-Redox modulator. We showed that KH176 and its quinone metabolite KH176m rescue BSO-induced cell death without restoring the GSH level (Beyrath et al., 2018).

The exact causes underlying the difference in sensitivity to BSO for CT and LS cells is not yet fully understood. Here we aimed to characterize the chain of events leading to the selective BSO-induced death of CI deficient LS patient

PHSFs. We measured indicators of mitochondrial (dys)function at different time points preceding loss of cellular integrity without detecting any pathological aberration in cellular and mitochondrial GSH depletion, mitochondrial morphofunction and cellular ATP content. However, just prior to cell death we detected a pathological burst of lipid peroxidation specifically in LS patient cells. In addition, we provide preliminary results showing that KH176m prevents this increased lipid peroxidation, suggesting that the latter plays a key role in BSO-induced death of LS cells. KH176m is described here as a new inhibitor of lipid peroxidation and BSO-induced cell death more potent than the reference compound Ferrostatin-1.

7.2 Materials and methods

7.2.1 Primary human skin fibroblasts

Primary Human Skin Fibroblasts (PHSFs) of healthy individuals and Leigh Syndrome (LS) patients with isolated Complex I (CI) deficiency (OMIM 252010) were obtained from skin biopsies following informed patient or parental consent in accordance to the relevant Institutional Review Boards. Control cell lines included #CT5120 ("CT1"), #CT5119 ("CT2") and #CT5118 ("CT3") which all displayed similar phenotype during their previous characterization (Distelmaier et al., 2009a). Patient cell lines harbored mutations in various genes encoding CI structural subunits: #P5175 ("S7", NDUFS7), #P7277 ("S2", NDUFS2), and #P5866 ("V1", NDUFV1). For the first cell viability experiment the full panel of six cells was used, for all the other experiments only S7, with or without CT1, cells were used.

7.2.2 Cell culture procedure

PHSFs were cultured in a humidified atmosphere (95% air, 5% CO_2) at 37° C in medium 199 (M199; #22340-020; Thermo Fisher Scientific, Waltham, MA, USA). The medium was supplemented with 10% (v/v) Fetal Bovine Serum (FBS; #758093; Greiner Bio-One, Kremsmünster, Austria) and 100

IU/ml penicillin/streptomycin (#30-002-CI; Corning, NY, USA). Cells were mycoplasma-negative (Mycoalert® mycoplasma detection kit; Lonza, Allendale, NJ, USA). Every 3-5 days, when the cells reach about 80-90% confluence as evaluated by visual inspection using transmitted-light microscopy, they were detached from culture flasks by using trypsin (#15400054; Corning) and were either passaged for further culturing (not above passage twenty) or seeded at a density of 3.5 × 103 cells/well into 96-wells black plates (#655090, Greiner Bio-one) to prepare for the different assays. All cell incubation and staining procedures were performed in a humidified atmosphere (95% air, 5% CO_2) at 37° C. 24h after the cells were seeded, the medium was removed, and redox stress was induced as described in section 7.2.3.

7.2.3 Redox stress induction

To induce redox stress, L-buthionine-(S,R)-sulfoximine (BSO, #B2515, Sigma Aldrich) was dissolved in phosphate buffered saline solution (PBS) and further diluted in the culture medium, which was used to replace the growth medium. Depending on the experiment, up to 7 semi-logarithmic dilutions (up to 100 μM) of BSO were used.

To test compounds rescuing capacity, cells were treated with 30 μM BSO in co-incubation with semi-logarithmic dilutions of the test compounds KH176m (Beyrath et al., 2018), and Ferrostatin-1 (#SML0583, Sigma Aldrich) up to 1 μM. Stock solutions (1000 × the final concentration) were prepared in dimethylsulfoxide (DMSO) and a 0.1% DMSO vehicle condition was used for background correction. BSO and/or compound treatments were incubated for different durations depending on the specific experiment/assay and measurements, indicated in the corresponding figures.

7.2.4 Cell viability and living cells area assay

Cell viability was assessed using intracellular conversion of calcein-AM into fluorescent calcein by esterase-mediated cleavage in living cells. Briefly, after the growth medium was discarded, cells were loaded with 2.5 μM green

calcein-AM (#65-0853-39, Affimetrix eBioscience) or violet calcein-AM (#65-0854-39, Thermofisher) dissolved in M199 without phenol red for 10 min after which the dye excess was washed twice with M199 without phenol red. Calcein was measured by live-cell automated microscopy using a BD Pathway 855® High-Content Bioimager (Becton Dickinson, Franklin Lakes, NJ, USA) with environmental control (CO_2 and temperature) using a 10× objective (UPlanSApo, NA 0.4, Olympus, Leiderdorp, The Netherlands) and Ex. 488/10 nm, Em. FURA/FITC filters for green calcein or using Ex. 380/10 nm, Em. 400DCLP filters for violet calcein. Calcein image processing and data extraction was performed as previously described (Iannetti et al., 2016). The "Casum", total number of calcein-positive pixels per well, was quantified from the calcein images to calculate the total living cells area per well. This was used as measurement of cell viability and to normalize other parameters described in the following sections (number of mitochondria, cell size, lipid peroxidation content, ATP content).

7.2.5 Mitochondrial morphofunction assay

For integrated analysis of cellular and mitochondrial morphological/functional parameters ("morphofunction"), MRM, calcein green and Hoechst fluorescent dyes were imaged as previously described (Iannetti et al., 2016) by live-cell automated microscopy using a BD Pathway 855® High-Content Bioimager (Becton Dickinson, Franklin Lakes, NJ, USA) with a 40x objective (UApo/340, NA 0.9 Olympus, Leiderdorp, The Netherlands). Image processing, data quantification, univariate and multivariate (Principal Component Analysis) were performed as previously described (Iannetti et al., 2016). Univariate analysis was performed focusing on six biologically relevant descriptors of mitochondrial morphology (Fig. 4B) and one descriptor of mitochondrial membrane potential TMRM Density mean (Fig. 5A) measured at 10h after BSO treatment.

7.2.6 Lipid peroxidation assay

Lipid peroxidation endpoint measurements were assessed 10h after BSO-induced redox stress using BODIPY 581/591 C11 (#D3861, Thermo Fisher), here-

after indicated as BODIPY. Cell viability and living cells area measurements were performed prior to the lipid peroxidation measurements using calcein violet that does not interfere with the lipid peroxidation fluorescent sensor wavelength. Immediately following the calcein violet measurements, the cells were incubated with 500 nM BODIPY in M199 without phenol red for 30 min. Upon oxidation, the BODIPY red emitting form (595 nm) is converted into a green emitting form (520 nm) (Koopman et al., 2005b; Verkaart et al., 2007a). After two washes the oxidized BODIPY was imaged using automated microscopy using a BD Pathway 855® High-Content Bioimager (Becton Dickinson, Franklin Lakes, NJ, USA) with a 20× objective (UApo/340, NA 0.475 Olympus, Leiderdorp, The Netherlands) and Ex. 488/10 nm, Em. 540/50 nm. Lipid peroxidation kinetic measurement was performed using 10 μM BODIPY by imaging each wells every 20 minutes for 18h following treatment with 30 μM BSO (30 μM) and imaged using the same microscope setting described for the endpoint measurement. Calcein violet was measured before to start the BODIPY kinetic measurement to measure the starting cell viability and living cells area used to normalize the lipid peroxidation content. Image processing for both the end point and the kinetic BODIPY measurements was performed as described previously for the CM-H2DCFDA (5-(and-6)- chloromethyl-2',7'-dichlorodihydrofluorescein diacetate) and HEt (dihydroethidium) measurements (Iannetti et al., 2018). The cut-off used to threshold the signal and generate the binary (BIN) image was visually determined and set at 40 gray values in the image processing algorithm. The total number of BODIPY-positive pixels per well was quantified from the BODIPY BIN images and corrected for the calcein violet "Casum" for normalisation. As described also above, the "Casum" represent the total number of calcein-positive pixels per well, and it was quantified from the calcein images to calculate the total living cells area per well.

7.2.7 Cytosolic and mitochondrial GSH content assay

The clinical-stage drug candidate KH176, and its quinone metabolite KH176m, can prevent BSO-induced cell death. However, the compounds did not restore

GSH content, indicating that their mode of action did not involve competition with BSO-induced inhibition of gamma-glutamylcysteine synthetase nor alternative mechanisms to restore the GSH levels. BSO was shown to induce a similar decrease of GSH in both patient and control cells when measured in total cells homogenate (Beyrath et al., 2018). To measure cytosolic and mitochondrial glutathione (GSH) content, cells were treated with a subtoxic dose of BSO (1 μM) for 24h. To confirm that the cells were not dead and morphologically unperturbed, visual inspection using transmitted light microscope was performed. After harvesting the cells, they were resuspended and incubated for ten minutes in a hypotonic solution (10 mM Tris pH 7.6 at +4° C) to induce cell swelling. Physical rupture of the cell membranes was performed using a handheld 2 ml Potter-Elvehjem homogenizer (glass on glass, 30 strokes). Isotonicity was re-established by the addition of 1,5 M sucrose. A first 10 min centrifugation at +4° C and 600g was performed to discard nuclei and intact cells. The supernatant was subjected to a second centrifugation (10 min at +4° C and 14.000g), after which the supernatant, representing the cytosolic fraction, was transferred to a new tube. The pellet, representing the crude mitochondria fraction, was resuspended in 10 mM Tris pH 7.6 +1,5 M sucrose. The two fractions were stored at -80° C. Citrate synthase, a soluble mitochondrial matrix enzyme was measured as a marker for intact mitochondria as previously described (Rodenburg, 2011). GSH measurement was performed on the cytosolic and crude mitochondrial fractions using the GSH-Glo™ Glutathione Assay (#V6911, Promega Corporation, Madison, WI, USA) according to the manufacturer's protocol measuring luminescence with a scanning microplate reader (FLUOstar Omega®, BMG Labtech, Cary, NC, USA).

7.2.8 ATP content assay

ATP was measured 10 h after redox stress induction by BSO treatment. Before measuring ATP, cells were imaged with calcein green to measure cell viability and living cells area. Total cellular ATP content was determined using the CellTiter-Glo® Luminescence Cell Viability Assay (#G7570, Promega Corporation, Madison, WI, USA) according to the manufacturer's protocol measur-

ing luminescence with a scanning microplate reader FLUOstar Omega®, BMG Labtech, Cary, NC, USA). The luminescent signal of each well was divided by the respective calcein green "Casum" to normalize ATP for the living cells area.

7.2.9 Data analysis

Image visualization, processing and quantification was carried out using Image Pro Plus® software (Media Cybernetics, Rockville, MD, USA) and custom MATLAB® algorithms (Mathworks, Natick, MA., USA), as previously described (Iannetti et al., 2016). Data visualization and analysis was performed using Graphpad PRISM® software (Graphpad Software, San Diego, CA, USA). The number of independent experiments and replicates are indicated by N and n, respectively. For some of the experiments only one independent experiment was performed, therefore additional experiments are necessary to validate a confirm the preliminary conclusions. Data from multiple experiments is presented as the mean ± standard deviation (SD). Statistical analysis of each experiment is described in the figure legends.

7.3 Results

7.3.1 Mitochondrial and cytosolic GSH level decrease at the same rate in CT ad LS cells upon BSO treatment

To validate the panel of cell lines used for this study we first confirmed our previous results (Beyrath et al., 2018) and demonstrated that BSO dose-dependently reduced the viability of LS but not of CT fibroblasts after 24 h incubation (Fig. 7.1). Although the LS cells displayed different sensitivities to BSO, their viability was similarly reduced using a concentration above 30 μM (Fig. 7.1B).

GSH synthesis occurs in the cytosol where most molecules remain localized, the rest being distributed between various subcellular compartments. The mitochondrial GSH pool represents about 10-15% of the total GSH with a

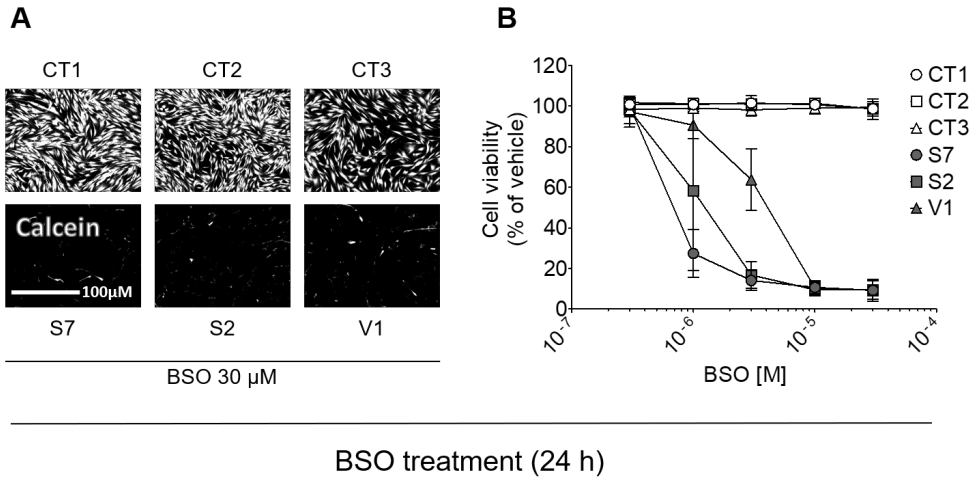


Figure 7.1: Cell viability of CI deficient PHSFs is abolished upon BSO treatment. A) Representative microscopy pictures of PHSFs stained with calcein, derived from three healthy controls (CT1 to CT3) and three LS patients (S7, S2b, V1) bearing mutations in different nuclear encoded CI subunits, upon 24h treatment with 30 μM of BSO. **B)** Cell viability data quantified from the calcein pictures of the same panel of cell lines upon 24h treatment with six semi-logarithmic dilutions up to 30 μM of BSO. N $\geq$ 2, n $\geq$ 8.

similar cytosolic concentration of 10-14 mM (Marí et al., 2013). Although BSO induced a similar decrease in cytosolic GSH level in both CT and LS cells (Beyrath et al., 2018, and Fig. 7.2A) we hypothesized that the mitochondrial pool of GSH might be consumed faster in the LS CI-deficient context upon BSO treatment. We therefore measured GSH separately in the mitochondrial and cytosolic fractions of both CT and LS cells untreated and treated with a subtoxic dose of BSO (1 μM) for 24h. No significant difference in mitochondrial or cytosolic GSH content was detectable between CT and LS cells in the untreated condition. Additionally, the GSH pools were depleted to the same extent in CT and LS cells treated with BSO (Fig. 7.2A). The purity of the cytosolic and mitochondrial fraction was controlled by measuring the activity of citrate synthase, a soluble mitochondrial matrix enzyme (Fig. 7.2B).

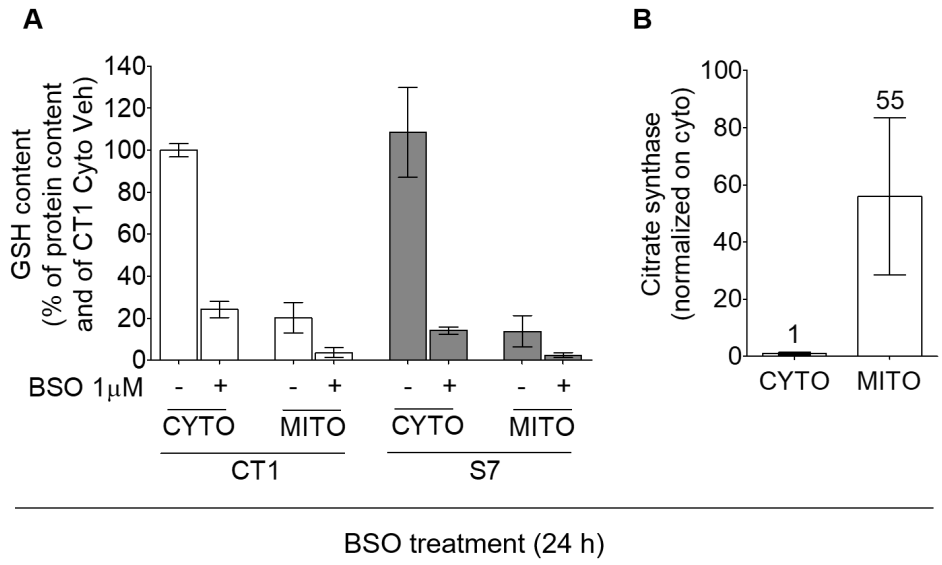


Figure 7.2: GSH measurement in cytosolic and mitochondrial fractions 24h after treatment with a subtoxic dose of BSO. A) CT1 and S7 PHSFs GSH measurements in the cytosolic and mitochondrial fractions upon 24h treatment with 1 μM of BSO (N = 3, n = 9). Statistical analysis was performed with GrapPad Prism using one-way ANOVA followed by Tukey's comparison. No significant differences (P>0.05) were found when comparing CT1 and S7 in the different conditions. **B)** Mitochondrial enzyme citrate synthase quantification in the cytosolic and mitochondrial fractions to validate the isolation procedures (N = 1, n = 1).

7.3.2 Mitochondrial morphofunction, ATP and lipid peroxidation were not affected two hours prior to the decrease in cell viability

In order to characterize the kinetic of the BSO-induced cell death, we measured cell viability 12h, 14h, 16h and 18h after BSO treatment (Fig. 7.3). We confirmed that CT cells remain viable at all concentrations and time points of BSO treatment (Fig. 7.3A), as already shown in Fig. 7.1 for measurement acquired after 24h. Up to 12h after BSO treatment the cell viability of patient cells was not significantly affected at any doses. Later time points revealed the LS time and dose sensitivity to BSO treatment with a dramatic loss of cell viability after 18h exposure to concentration above 10μM BSO (=10^{-5} M).

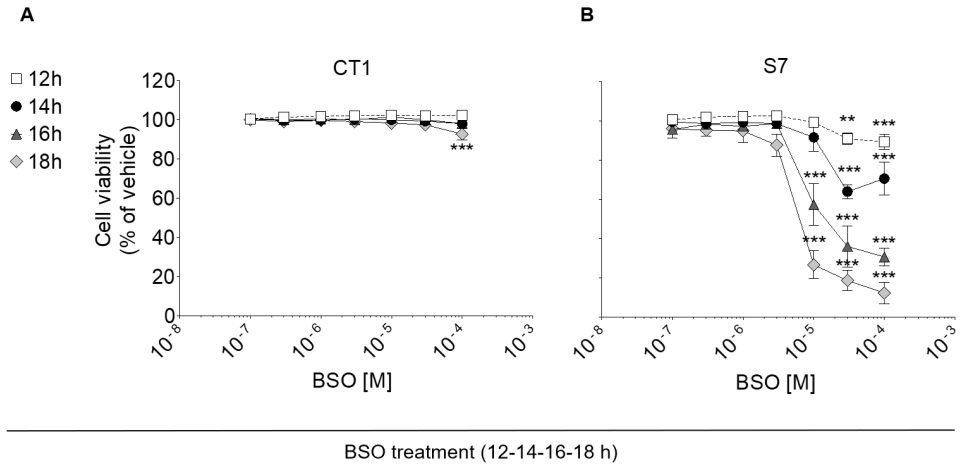


Figure 7.3: BSO-induced cell death kinetics. Cell viability data quantified from the calcein pictures of **A)** CT1 and **B)** S7 PHSFs upon 12, 14, 16, and 18h treatment with 7 semi-logarithmic dilutions up to 100 μM (=10^{-4} M) of BSO (N = 1, n = 3). Statistical analysis was performed with GrapPad Prism using one-way ANOVA followed by Tukey's comparison. When statistically significant differences are present are indicated by *(P<0.05), **(P<0.01) and ***(P<0.001) and are relative to their respective time point vehicle condition.

Based on these results we chose a time point of 10h to study the molecular events preceding BSO-induced LS cell death in order to avoid potential measurement artifacts caused by dead cells. Mitochondrial morphofunction (Fig. 7.4 and 7.5A), ATP content (Fig. 7.5B) and lipid peroxidation (Fig. 7.5C) were quantified as end point measurements at 10h after BSO treatment (10, 30, and 100 μM).

The results revealed that all the measured cellular parameters remained unchanged at 10h after the treatment with high doses of BSO (10, 30, 100 μM of BSO). Principal Component Analysis of multiple mitochondrial morphologic and functional parameters was also performed as previously described Iannetti et al. (2016) but no relevant BSO-induced clusters were identified (data not shown).

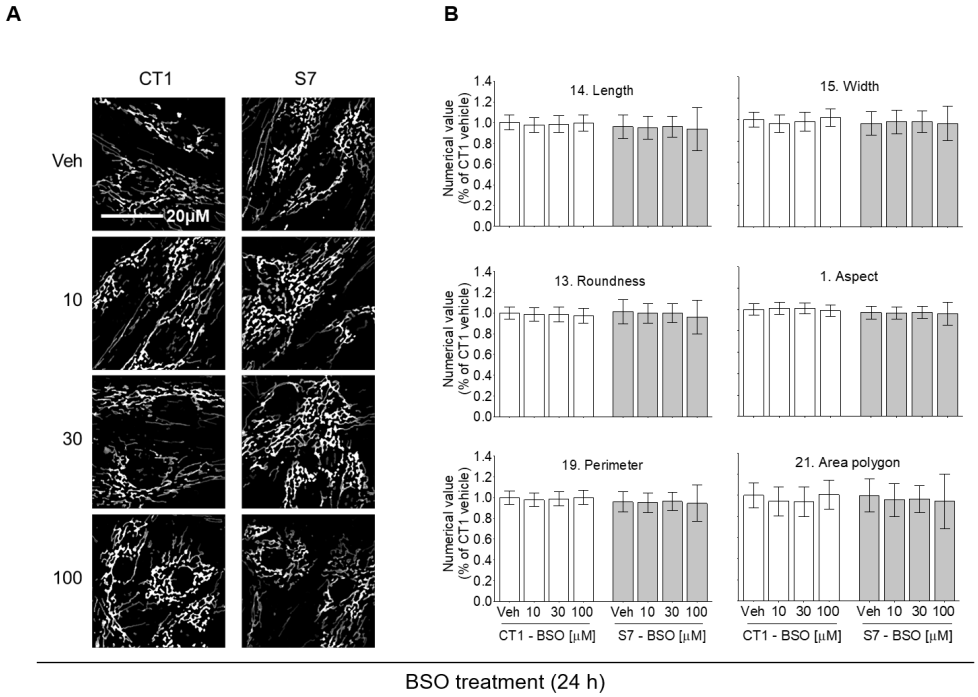


Figure 7.4: Mitochondrial morphology 10h after BSO treatment. Upon 10h treatment with 10, 30, 100 μM of BSO **A)** Representative microscopy pictures of CT1 and S7 cells stained with TMRM after 10h treatment with 10, 30, 100 μM of BSO. **B)** Six biological relevant descriptors extracted from TMRM microscopy pictures were selected to describe mitochondrial morphology: 14. Length, 15. Width, 13. Roundness, 1. Aspect (ratio), 19. Perimeter, 21. Area polygon (the descriptors numbers correspond to our previous published labels Iannetti et al., 2016). (N = 3, n = 30). Statistical analysis was performed with GrapPad Prism using one-way analysis of variance (ANOVA) followed by Tukey's comparison. BSO treatment did not induce any significant differences (P>0.05) in CT1 and S7.

7.3.3 Lipid peroxidation increases in patient cells concomitantly with their loss of viability

BSO-induced GSH depletion was shown to initiate ferroptosis (Yang et al., 2014). One of the main hallmark of ferroptosis pathway is the accumulation of lipid-based reactive oxygen species (Yang et al., 2016). Although we did not observe an increase in lipid peroxidation 10h after treatment with BSO (Fig.

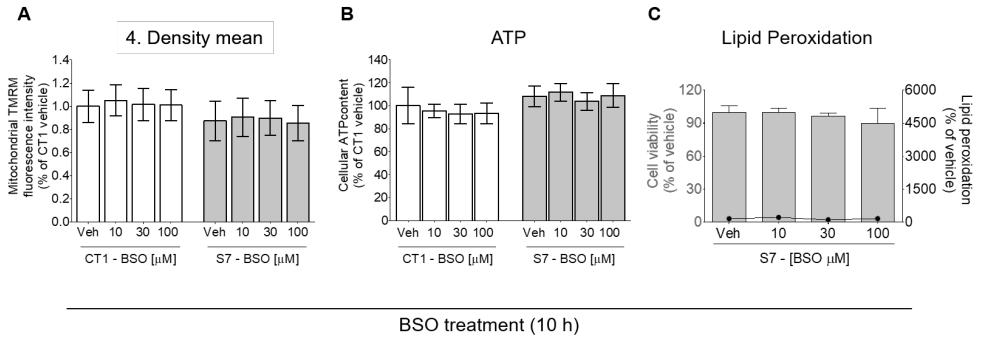


Figure 7.5: Mitochondrial functionality, ATP and lipid peroxidation 10h after BSO treatment. Upon 10h treatment with 10, 30, 100 μM of BSO **A)** 4. Mitochondrial TMRM Density mean (mitochondrial membrane potential; the descriptors number correspond to our previous published labels Iannetti et al., 2016). (N = 3, n = 15). **B)** Intracellular ATP content measured in cell lysate with a luminescent sensor (N = 3, n = 18). **C)** Lipid peroxidation content measured with BODIPY in parallel to the cell viability using calcein violet (N = 1, n = 4). Statistical analysis was performed with GrapPad Prism using one-way analysis of variance (ANOVA) followed by Tukey's comparison. BSO treatment did not induce any significant differences (P>0.05) in CT1 or S7.

7.5C), we repeated the experiment measuring lipid peroxidation along with cell viability every two hours starting from the time of BSO addition (t=0) up to 18h. In Fig. 7.6A and B the two most relevant time point (12h and 14h) are showed. At 12h, the highest dose of BSO (100 μM) induced a small reduction of cell viability (70% of cells are still viable as compared to the vehicle). At 12h, we instead already observed a large and dose-dependent increase of lipid peroxidation (8-fold with 10 μM; 22-fold with 30 μM; 43-fold with 100 μM BSO as compared to the vehicle). At 14h cell viability was drastically reduced dose-dependently (60% with 10 μM, 30% with 30 μM, 15% with 100 μM BSO as compared to the vehicle) (Fig. 7.6A). Lipid peroxidation decreased compared to the 12h time point because of the detachment of dead cells as indicated by representative microscopy images (Fig. 7.6B). It is interesting to note that there was only limited overlay of BODIPY and calcein signals indicated by yellow regions (Fig. 7.6B). This suggests that in our experimental conditions lipid peroxidation burst was mainly observed consecutively to the cell membrane in-

tegrity disruption. To increase the time resolution of the lipid peroxidation, we performed a kinetic measurement for 18h after BSO treatment of CT and LS cells. Figure 7.6C shows that the kinetics of lipid peroxidation differed significantly between LS and CT cells. In patient cells a peak of 29-fold increase was observed after 8 hours incubation with BSO, as compared to the control cell treated with vehicle, followed by a decrease certainly due to cell death and detachment from the assay plate. In control cells the lipid peroxidation signal only started to increase at 8h with a maximal 14-fold increase measured at the last data point of 18h. Therefore, BSO-induced lipid peroxidation burst happened earlier and reached higher intensity in LS cells as compared to CT cells.

Figure 7.6: Kinetic of lipid peroxidation in cells treated with BSO. A) Data quantification of S7 cells co-stained with BODIPY and calcein 12h and 14h after treatment with 10, 30, 100 μM of BSO (N = 1, n = 4). One single representative data set is here shown because the lipid peroxidation burst started in the different replicate experiments with ± 30 minutes difference making datasets merging not possible. Statistical analysis was performed with GrapPad Prism using one-way analysis of variance (ANOVA) followed by Tukey's comparison. Statistically significant differences are indicated by ns($P>0.05$), *($P<0.05$), **($P<0.01$) and ***($P<0.001$). **B)** Representative microscopy pictures of the data quantified in Fig. 7.6A. **C)** 18h kinetic BODIPY measurement of CT1 and S7 PHSFs normalized for the area of living cells measured at 0h with calcein and CT1 vehicle (N = 1, n = 6). (Figure follows on the next page.)

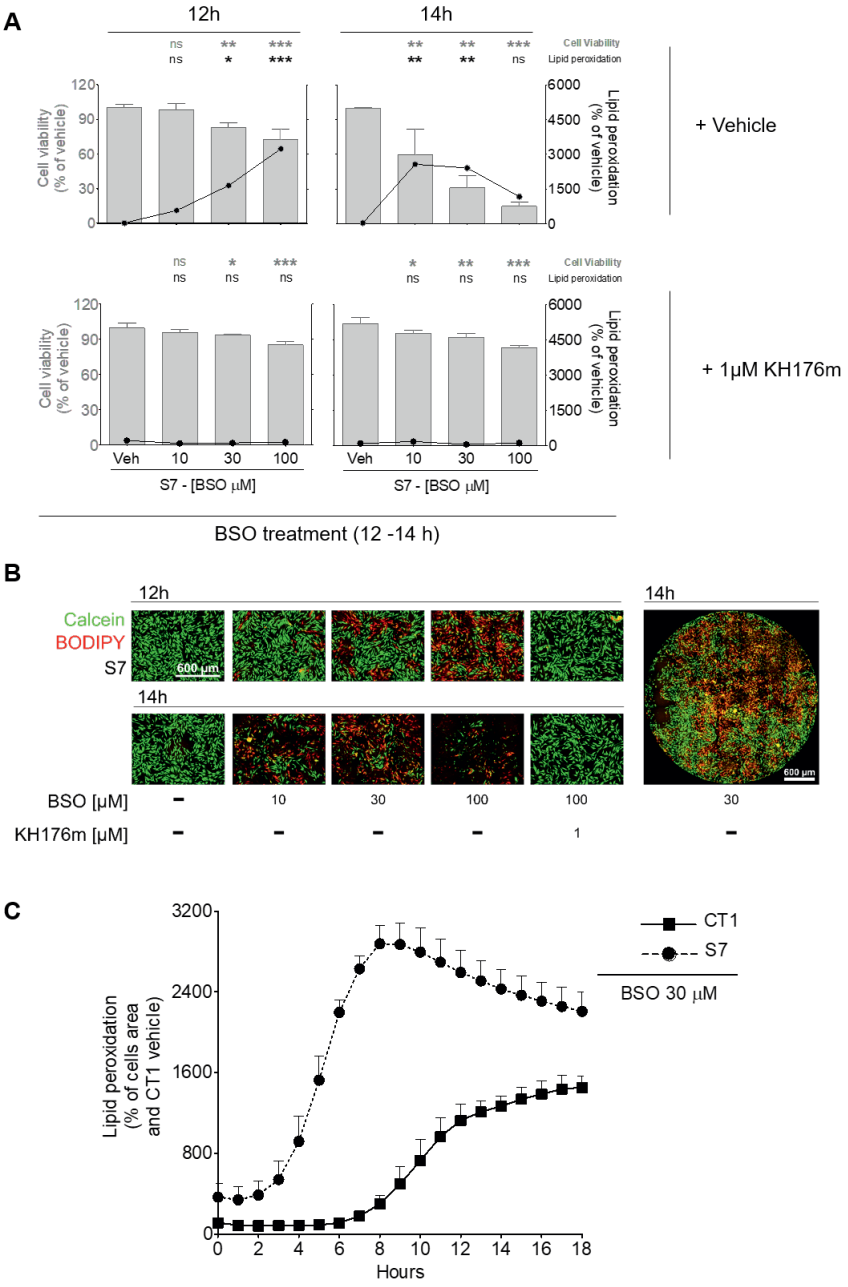


Figure 7.6: Kinetic of lipid peroxidation in cells treated with BSO. (Caption on the previous page.)

7.3.4 KH176m is a potent inhibitor of BSO-induced lipid peroxidation and cell death showing higher potency than ferrostatin-1

In our previous study, KH176m was shown to protect cells from BSO-induced cell death (Beyrath et al., 2018). We here evaluated the effect of KH176m on lipid peroxidation and cell death induced by different doses of BSO. Fig. 7.6A and B (bottom panels) show that KH176m completely abolished BSO-induced lipid peroxidation burst and cell death regardless of the BSO concentrations tested. Since lipid peroxidation increased just before cell death, we tested whether KH176m could still prevent cell death when incubated at different time following BSO treatment. KH176m was added at 0h, 8h, 10h or 12h after BSO and cell viability was measured at 14h. The results show that KH176m could rescue the cell viability in all conditions, even when incubated two hours prior to cell death measurement (Fig. 7.7).

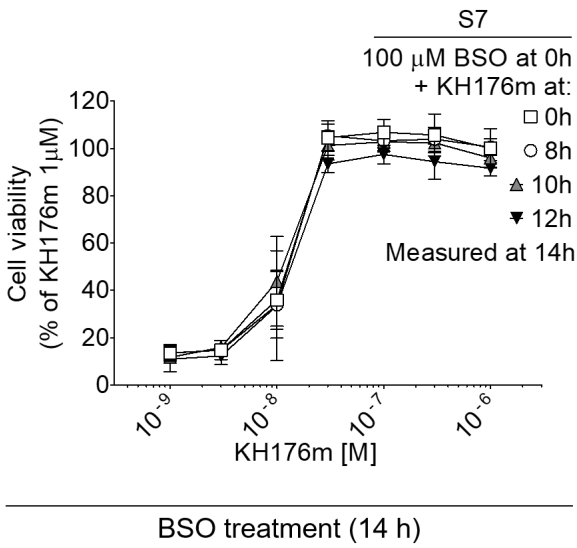


Figure 7.7: Dose- and time-response of KH176m in BSO-induced cell death. Cell viability data quantified from the calcein pictures of S7 PHSFs upon 14h treatment with 100 μM of BSO and 7 semi-logarithmic dilutions up to 1 μM of KH176m added at 0, 8, 10 and 12h after BSO treatment. (N = 3, n = 9).

Finally, KH176m potency was compared to Ferrostatin-1, the first identified inhibitor of ferroptosis (Dixon et al., 2012). KH176m showed higher potency than Ferrostatin-1 (Fig. 7.7) with the lowest doses able to fully rescue viability being 100 nM for Ferrostatin-1 and 30 nM for KH176m.

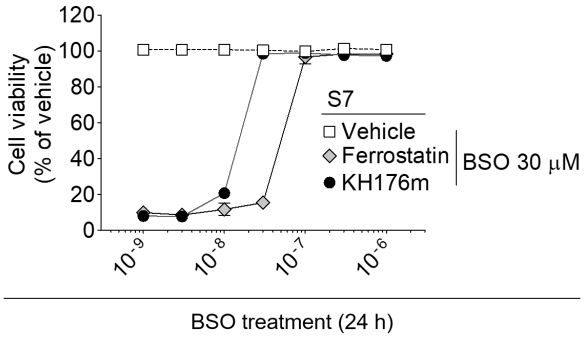


Figure 7.8: Dose –response of Ferrostatin-1 and KH176m prevention of BSO-induced cell death. Cell viability data quantified from the calcein pictures of S7 PHSFs upon 24h treatment with 30 μM of BSO in combination with 7 semi-logarithmic dilutions up to 1 μM of KH176m and Ferrostatin-1 (N = 1, n = 3).

7.4 Discussion

We here report preliminary results focusing on the cellular and molecular phenotypical characterization of the BSO-induced perturbation in cells derived from Leigh disease patients and healthy control. We identified a causative role of lipid peroxidation burst in the BSO-induced CI deficient LS patient cells pathological phenotype. Moreover, this can be fully inhibited by KH176m, a new potent inhibitor of lipid peroxidation and BSO-induced cell death. From a methodological point of view, our results stress the crucial importance of monitoring also the temporal dimensions performing cellular time-lapse measurements.

Previous work (Beyrath et al., 2018) revealed that while total cellular GSH level was decreased to a similar extent in both LS and CT cells upon BSO treatment, only the viability of LS cells with CI deficiency was affected. Since

CI is located into the mitochondria, we here studied whether mitochondrial GSH pool might be differently affected in LS CI cells upon BSO treatment as compared to healthy cells. Because, mitochondrial GSH only represents about 10% of total cellular GSH, we might have lacked sensitivity in our earlier experiment measuring the total cellular GSH level. However, here we show that no significant differences in GSH level could be detected in the crude mitochondrial fractions of LS and CT PHSFs. The procedures used to isolate mitochondria has perhaps prevented to detect small but physiologically relevant GSH concentration differences. More quantitative experiments to measure GSH consumption upon BSO in cell and mitochondria should be performed using for instance mass spectrometry or targeted and genetic sensors (Chandrasekharan et al., 2019; Chen et al., 2017; Jiang et al., 2017) to measure GSH in intact living cells.

In order to extend the characterization and identify LS pathological phenotypes we studied other cellular and mitochondrial indicators previously associated with mitochondrial dysfunction. Surprisingly cellular viability, mitochondrial morphofunction, ATP and lipid peroxidation were not affected neither in LS nor in CT cells when measured at 10h after BSO treatment. While only two hours later, at 12h, LS cell viability was significantly compromised, and at 18h, it was completely abolished. Although the LS cells used in this study have a documented deficiency in a mitochondrial enzyme (Distelmaier et al., 2009b), our measurements at the selected time points, did not identify any pathological mitochondrial phenotype responsible of the initiation of BSO-induced cell death. Therefore, further time-lapse measurements should be performed in the latest hours before cell death, provided the methods are available. Indeed, the low photostability and cell photo-toxicity of the fluorescent probes used to measure cell viability (calcein) and mitochondrial morphofunction (TMRM), but also the cell homogenization procedure used to measure GSH and ATP are not suitable for live kinetic measurement.

Lipid peroxidation, measured with the fluorescent sensor BODIPY, could be measured repeatedly over an 18h kinetic showing no detectable photo-toxicity and favorable photostability that allowed time-lapse monitoring. When cells

were analyzed in a time-course experiment we were able to identify a massive lipid peroxidation burst in the LS patient cells not detectable in the CT cells. Our results strongly indicate that the mechanism triggering BSO-induced cell death in LS cells is extremely fast reminding of a snap-action of other cell-death inducers such as TNF-related apoptosis-inducing ligand (TRAIL) (Albeck et al., 2008). Although the upstream complete depletion of GSH is equal in both LS and CT cells, LS cells seem to reach a sudden transition point leading to rapid lipid peroxidation burst and cell death. The mechanistic underlying this decision point remains to be deciphered.

Representative microscopy images in Fig. 7.6B, show little overlay of BODIPY (red) and calcein (green) signals identified by yellow regions. This suggests that lipid peroxidation, cell membrane disruption and cell death are extremely fast events difficult to be observed simultaneously with the method used. Indeed, the fluorescent calcein probe used to quantify cell viability is released as soon as cell membranes are disrupted because of lipid peroxidation. Limited yellow regions are identifiable in the right panel of Fig. 7.6B where the full well (10 $\times$ 10 images) was imaged at 14h after BSO treatment. Therefore, other methods to study kinetically and simultaneously cell death and lipid peroxidation are needed in order to study the chain of event. In the right panel of Fig. 7.6B, it is also interesting to note how the lipid peroxidation burst and loss of cell viability seem to propagate through cell to cell transmission, perhaps in a continuum of lipid radical chain reactions. This phenomenon could also explain the synchronicity observed in the BSO-induced cell death which affects the entire cell population in a very short time frame.

We further show that the redox compound KH176m could prevent both lipid peroxidation and LS cell death induced by BSO. Interestingly, the compound could rescue the cells even when incubated two hours before cells death. This together with the results displayed in Fig. 7.6 indicate that lipid peroxidation burst plays a pivotal role. The rescue of cell viability by KH176m happened in an all-or-nothing fashion, mirroring the BSO-induced cell death itself. This illustrates again an on/off mechanism due to the presence of a threshold effect decisive for initiating the cell death. Similar observations were made during

extrinsic apoptosis induced by TRAIL (Albeck et al., 2008), with the full permeabilization of mitochondrial membrane and the release of cytochrome c the events driving the decision to activate effector caspases leading to cell death. Based on these findings and the fact that LS cells carry a genetic defect and an enzymatic dysfunction in mitochondria (Distelmaier et al., 2009b), it is difficult to rule out the potential involvement of mitochondria as a key inducer of the BSO-induced LS cell death pathway. However, our results do not highlight any mitochondrial pathological phenotype at the selected time point of 10h after BSO treatment.

In our study, we used the BODIPY probe to evaluate the lipid peroxidation role in the cellular pathogenesis observed in LS cells. However, this probe is a general lipid peroxidation indicator and it does not allow to quantify the peroxidation of specific lipids. For instance, cardiolipin is an important phospholipid component of the inner mitochondrial membrane. This lipid plays a central role in many reactions and processes involved in mitochondrial physiological functionality and dynamics but also in the pathology development (Paradies et al., 2019). Cardiolipin is also particularly susceptible to lipid peroxidation and when transformed in oxidized-cardiolipin can induce an oxidative chain reaction with further oxidation of cardiolipin and other ROS species (Jacob et al., 2015). Oxidized-cardiolipin generation is also a crucial signaling platform during mitochondrial-driven cell death (Hauck and Bernlohr, 2016). It would therefore be of great interest to study cardiolipin role and also selectively measure cardiolipin oxidation in our models. Because the probe BODIPY does not allow to quantify the peroxidation of specific lipids, other methods need to be implemented. The fluorescent marker Nonyl Acridine Orange previously used to locate and quantify non-oxidized cardiolipin in living cells (Fernandez et al., 2004; Kaewsuya et al., 2007) could provide interesting information related to the unpretreated lipidic status. While lipidomics on cell lysate using mass spectrometry could be applied to identify and characterize specific phospholipids species and their oxidized forms including cardiolipin (Spickett and Pitt, 2015).

Oxidative stress can trigger different cell death pathways, unprogrammed as

necrosis, or programmed as apoptosis, necroptosis, oxytosis and ferroptosis. Some of these pathways can share similarities, can be partially overlapping, and it is sometimes difficult to define a neat distinction. Oxytosis and ferroptosis share very similar molecular mechanisms mainly differentiating by the experimental procedure, thus, should be regarded as two names for the same cell death pathway (Lewerenz et al., 2018). Ferroptosis can be induced by different chemical triggers that determine different molecular consequences and phenotypes with or without mitochondrial involvement (Gao et al., 2018). BSO, inducing a depletion of cellular GSH and therefore inhibition of GPX4 was described as a ferroptosis inducer (Dixon et al., 2012). Therefore, while the data collected in this study would point at ferroptosis being the cell death pathway induced by BSO in PHSFs derived from LS patients with CI deficiency, further work is warranted to understand the differential causes underlying the selective LS-patient cell death in our experiments.

Because no pathological aberrations were detected at the level of cellular ATP content, cellular and mitochondrial GSH content and mitochondrial morpho-function, we can speculate about the presence of alternative subcellular consequences not monitored in this study that could be triggered by the CI deficiency. The fact that mitochondria do not have a key role in a cell death pathway induced by GPX4 inhibition, like the BSO-induced, would be confirmed by recent findings. These show that mitochondria play instead a crucial role only in the ferroptosis induced by erastin treatment causing cysteine deprivation (Gao et al., 2018). While we could not detect mitochondrial aberrations, another study, in the cysteine deprivation induced ferroptosis, identified loss of mitochondrial membrane potential, enhanced mitochondrial fragmentation and reduced ATP levels (Neitemeier et al., 2017). In this study the BH3-only protein BID, a central mediator of mitochondrial driven apoptosis and oxytosis, is found to be the mediator of mitochondrial dysfunction downstream GSH depletion. BID indeed is described to acts as a crucial link between the lipid peroxidation burst and the following mitochondrial damage (Neitemeier et al., 2017). However, BID was there studied in a mouse hippocampal neuronal cell line HT22, where GSH depletion was induced by erastin-induced cysteine de-

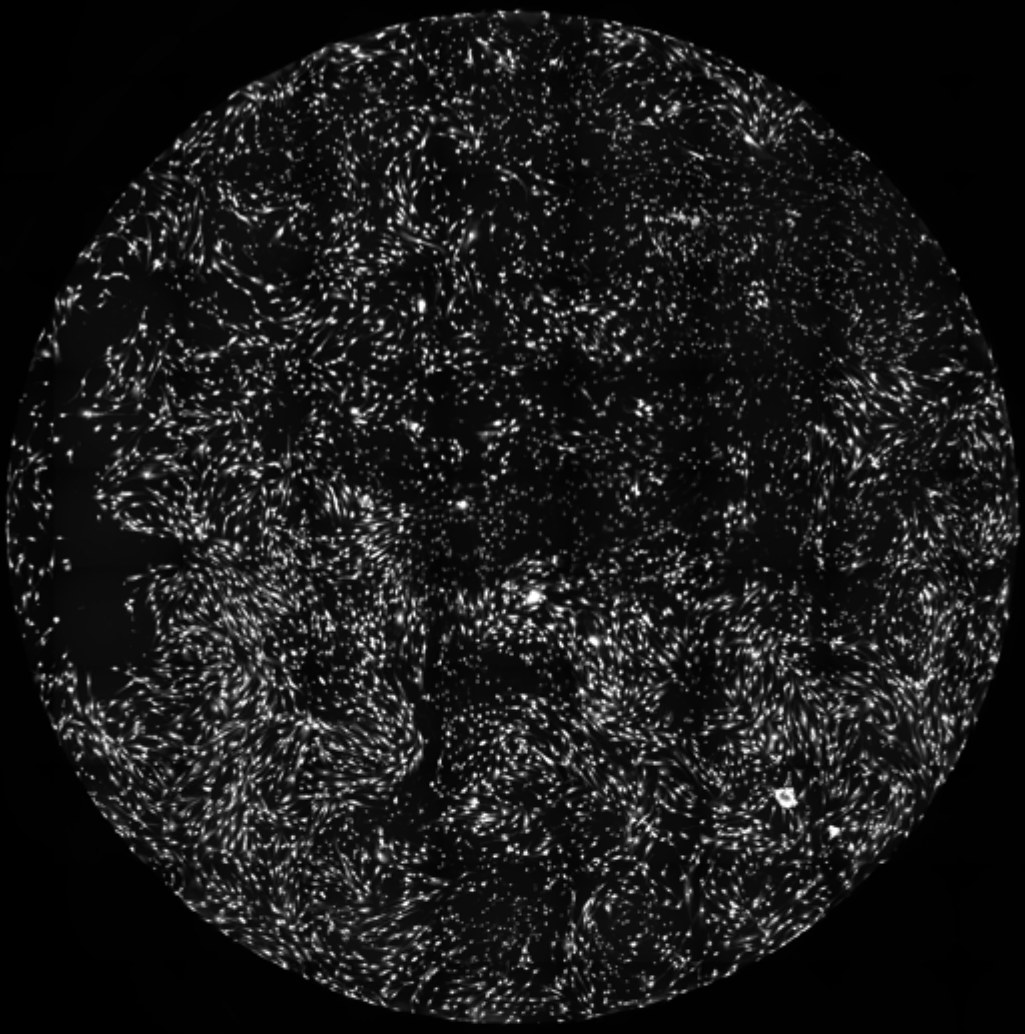
privation. Therefore, it would be interesting to characterize the role of BID in the LS cells with CI deficiency treated with BSO. Moreover, performing a molecular and phenotypical characterization at the mitochondrial level of the LS cells with CI deficiency treated with erastin and comparing those results with the BSO data could be also of interest.

Our clinical-stage small molecule KH176 was identified as lead compound upon selection among more than 200 unique and novel chemical entities for the treatment of mitochondrial disease as reported in a previous study (Beyrath et al., 2018). In that same study, it was also shown that the KH176, and KH176m, could counteract important cell biological consequences of CI dysfunctions.

Here, we demonstrated that KH176m could fully prevent lipid peroxidation burst and cell death also when added 12h after BSO treatment and only 2h before cell viability is compromised. This indicates that the compound protective mechanism acts downstream of GSH depletion and likely to be a direct inhibition of lipid peroxidation. The compound was earlier shown to interact with peroxiredoxins, a family of enzyme involved in reduction of hydrogen peroxide but also lipid peroxides, and that the peroxiredoxins activity was required for their activity in BSO cell death prevention. Further work is warranted to decipher whether peroxiredoxin are also involved in the prevention of lipid peroxidation by KH176m. Finally, KH176m was shown to be more potent in preventing BSO-induced cell death than Ferrostatin-1, a reference inhibitor of ferroptosis. In conclusion, the main question that remains to be answered is how, from a molecular point of view, CI deficiency causes a dramatically increase of lipid peroxidation production or a reduction of cellular ROS scavenging activity that is not detected in the CT cells. And are other biological features affected in the LS cells translating the CI deficiency to the lipid peroxidation burst and cell death?

In order to answer to these still open research questions, performing kinetic measurements and studying later time points (than the 10h time point studied) concomitantly with the LS loss of cells viability using targeted and genetic sensors for cytosolic and mitochondrial GSH (Chandrasekharan et al., 2019; Chen et al., 2017; Jiang et al., 2017) and ATP (De la Fuente-Herreruela et al., 2017;

Quintana-Cabrera et al., 2018; Sunnapu et al., 2017) in intact living cells and performing multiple mitochondrial morphofunction endpoint measurements focusing on the time window from 10h to 14h, could bring new interesting insight. Performing also mass spectrometry measurements to characterize and quantify oxidized lipids could be also informative. Furthermore, comparative analysis with alternative ferroptosis inducers, like erastin, could also help elucidating the pathomechanism induced by CI deficiency in LS cells.



Chapter 8

Summary, general discussion and future perspectives

8.1 Summary

The primary aim of this PhD project was to characterize cellular consequences of mitochondrial dysfunction at the phenotypical level for target discovery and drug testing. In order to do that, I focused on the development of novel automated live-cell imaging technologies and cell-based assays optimization. These were applied mainly to Primary Human Skin Fibroblasts (PHSFs) derived from healthy donors and Leigh Syndrome (LS) patients. LS is a severe neurological disorder usually becoming apparent in the first year of life by progressive loss of mental and movement abilities. This typically results in death within two to three years, usually due to respiratory failure (Gerards et al., 2016). The PHSFs derived from LS patients used in these studies have the most common mitochondrial oxidative phosphorylation (OXPHOS) enzyme defect associated with this disease phenotype, being isolated complex I (CI) deficiency (Fassone and Rahman, 2012; Ma et al., 2013).

Chapter 1 introduced mitochondrial structure, function and dysfunction from the molecular level and up to the clinics including drug development strategies. The importance mitochondria execute in relation to the overall human health status is highlighted. The concept of mitochondrial morphofunction is also introduced discussing the important interaction between structure and function. As morphofunction is a key indicator of the mitochondrial and overall cellular health status, and because of its biological relevance, it was measured or discussed in every chapter of this thesis. The chapter continues introducing the devastating clinical aspects of mitochondrial diseases and in particular CI deficiency and LS that are pathologies with a high unmet medical need. The general introduction ends with an overview on the drugs development process focusing on *in vitro* preclinical work. In particular cell-based phenotypic screening are presented as the main methodological approach used by pharmaceutical companies for target discovery and drug testing.

To evaluate how mitochondria contributed to disease and to perform preclinical *in vitro* drug development, a broad collection of technologies exists, both commercially available and in research laboratories. In **Chapter 2** we

presented a critical review of the literature on how live-cell high content microscopy can be used for image-based phenotypic profiling to assess mitochondrial (dys)function. Comprehensive guidelines about live cell imaging technologies were here presented to introduce the applications developed in the experimental chapters of this thesis. With that perspective, we discussed a selection of live-cell fluorescent reporters and imaging strategies and human cell models and discuss their pros/cons in mitochondrial research. We also presented an overview of live-cell high content microscopy applications used to detect disease-associated cellular phenotypes and perform cell-based drug screening.

Chapter 3 focused more specifically on how mitochondrial morphofunction can be studied combining high-content and high-throughput strategies. In this chapter, different applications which can be used to analyze genetic and/or drug-induced effects at the level of individual organelles, cells and cell populations are briefly discussed. In **Chapter 4** we presented a newly developed protocol to perform multiplexed high-content analysis of mitochondrial morphofunction. This allow unbiased and automated quantification of mitochondrial morphofunction, cellular and nuclear parameters in PHSFs. Cells were cultured in 96-well plates and stained with three fluorescent dyes targeting mitochondria, cytosol and nuclei. Multispectral fluorescence images were acquired using automated microscopy and processed to extract 44 descriptors. Subsequently, the descriptor data were subjected to univariate, bivariate and multivariate analysis. Although this protocol was specifically developed for PHSFs, this is transferable to other cell types. In **Chapter 5** this protocol was applied to the HT22 neuronal cell model. In this study, the mitochondrial morphofunctional analysis was used to analyze cellular metabolic flexibility using small-conductance Ca^{2+}-activated K^+ channels (SK) activation and investigating its phenotypical consequences. HT22 were treated with the chemical compound CyPPA to induce a pharmacological SK activation. In the presence of glucose in the culture medium, many cell models cultured in vitro generate almost all ATP via glycolysis rather than using the mitochondrial OXPHOS system (Crabtree, 1929). Therefore, cell culture medium

where glucose is replaced by galactose is a common experimental setting initially developed to induce or enhance pathological mitochondrial phenotypes (Robinson et al., 1992; Rossignol et al., 2004). This strategy enforce ATP production to rely on mitochondrial metabolism, prevent glycolysis upregulation and limit metabolic flexibility (Rossignol et al., 2004). In **Chapter 5**, in order to limit cellular compensatory mechanisms by the inhibition of glycolytic upregulation, we performed mitochondrial morphofunctional analysis of CyPPA-treated HT22 cells in galactose-based media and compared it with glucose-based media as control condition.

In **Chapter 6**, in order to induce a metabolic stress, enhancing the PSHF CI deficiency-induced aberrations, we also used the galactose-based medium strategy. We performed a cellular and mitochondrial phenotypical characterization of the mitochondrial diseased cells growing in galactose-based medium and we compared those to the same cells growing in a glucose-based medium. We investigated cell viability, mitochondrial morphofunction, reactive oxygen species (ROS) levels and ATP homeostasis. A panel of six cell lines were used, three derived from healthy donors and three derived from LS patients harboring mutations in nuclear DNA (nDNA)-encoded CI genes (NDUFS7, NDUFS8, NDUFV1). Following optimization of the cell culture protocol and of the glucose-based medium composition, LS fibroblasts died in the galactose medium, whereas control cells did not. LS cell death was dose-dependently inhibited by pyruvate, malate, oxaloacetate, α-ketoglutarate, aspartate, and exogenous NAD^+ (eNAD), but not by lactate, succinate, α-ketobutyrate, and uridine. Pyruvate and eNAD increased the cellular NAD^+ content in galactose-treated LS cells to a different extent and co-incubation studies revealed that pyruvate-induced rescue was not primarily mediated by NAD^+. Functionally, in LS cells glucose-by-galactose replacement increased mitochondrial fragmentation and mass, depolarized the mitochondrial membrane potential ($\Delta\psi$), increased H_2DCFDA-oxidizing ROS levels, increased mitochondrial ATP generation, and reduced the total cellular ATP content. These aberrations were differentially rescued by pyruvate and eNAD, supporting the conclusion that these compounds rescue galactose-induced LS cell death via different mecha-

nisms. These findings establish a cell-based strategy for intervention testing and enhance our understanding of CI deficiency pathophysiology.

Chapter 7, like Chapter 6, also presented a phenotypic and molecular characterization of PSHF CI deficiency-induced aberrations under a stress condition. In this study, redox stress was induced treating the cells with L-buthionine-(S,R)-sulfoximine (BSO) to reduce the concentration of glutathione (GSH), the main cellular antioxidant. A panel of six cell lines were used, three derived from healthy donors and three derived from LS patients harboring mutations in nuclear DNA (nDNA)-encoded CI genes (NDUFS7, NDUFS2, NDUFV1). In respect to Chapter 6, while NDUFS7 cell line was the same one used in both the studies, NDUFS2 was a different cell line mutated in a different gene of CI, NDUFV1 was a different cell line with a different mutation in the same gene of CI. We previously demonstrated that the GSH synthesis inhibitor BSO decreases cellular GSH content to a similar degree in PHSFs from LS patients and control healthy donors. Interestingly, BSO treatment greatly reduced the viability of LS patient cells (all harboring an isolated mitochondrial CI deficiency, whereas healthy controls cells (CT). However, the reason for this differential BSO effect is still unclear. In this last chapter we performed phenotypic and molecular profiling of LS and CT cells to investigate the effect of BSO prior to cell death induction. PHSF incubation with a non-toxic BSO concentration (1 μM) for 24h decreased mitochondrial and cytosolic GSH levels in LS and CT cells in a similar manner. No alterations in mitochondrial morphofunction, cellular ATP content or cellular lipid peroxidation state were observed up to 2 hours prior to cell death induction. However, when lipid peroxidation was measured from 12h to 18h after BSO treatment, an oxidative burst almost concomitant with the loss of cell viability was identified as LS-specific pathological phenotype. We previously demonstrated that KH176m, the metabolite of a new clinical-stage drug candidate KH176, fully inhibited BSO-induced LS cell death. Here we provide preliminary evidence that this cell death is paralleled by increased lipid peroxidation, which is prevented by KH176m. KH176m efficacy was also benchmarked against Ferrostatin-1, the first identified inhibitor of ferroptosis, a lipid peroxidation-dependent cell death. This

pilot study highlights a causative role for lipid peroxidation in the BSO-induced specific death of LS patient cells and enhances our understanding of KH176m mode-of-action.

8.2 General discussion

This thesis is part of a drug development strategy based on the technology transfer process of academic findings into industrial usable applications. The results generated with these studies all performed at Khondrion in collaboration with the Department of Biochemistry at the Radboudumc provide new methodological approaches to study mitochondrial dysfunction of *in vitro* cell models and new insight to better understand the pathology and design therapeutic strategies. One of the new methodological developments is the mitochondrial morphofunctional protocol discussed in Chapter 4. This protocol was applied in different experimental conditions in Chapter 4, 5, 6 and 7 where different research questions were addressed. In Chapter 4, 6 and 7 the protocol was applied to PHSFs, while in Chapter 5 it was applied to HT22 neuronal cells. Overall, this technology was able to discriminate drug-induced phenotypes modulation and to classify and quantify pathophysiological morphofunctional phenotypes of cell lines carrying pathogenic mutations compared to healthy controls.

In Chapter 7, the importance of another methodological approach was highlighted when indicating that cellular time-lapse monitoring, rather than end point measurements, was crucial to study fast and dynamic biological events. Within that context, kinetic measurement was optimized. This allowed to identify a pivotal role of lipid peroxidation for LS patient cell death that was otherwise detected with high technical difficulties or to easily pass undetected.

Another important experimental and methodological part of this thesis was focused on cell culture and stress assay optimization. Patients derived PHSF models are a precious source of information, however, despite the presence of the pathogenic mutations, often these *in vitro* cell models do not show robust pathological phenotypes suitable for preclinical drug development (Iannetti

et al., 2019). Therefore, two stress conditions (i and ii) have been optimized to enhance pathology, study mitochondrial dysfunction, identify new biological targets and perform drug interventions (to correct the aberrations and test drug efficacy and potency). The galactose-based medium (i) is a culture strategy described for the first time long ago (Robinson et al., 1992), that was here optimized and applied in Chapter 5 and 6. The galactose-based medium was used to inhibit metabolic flexibility in Chapter 5 and induce a metabolic stress in Chapter 6 where the medium was also pyruvate-free. The absence of pyruvate was here discovered to be crucial in inducing the LS patients derived PHSF death that was otherwise prevented. The BSO treatment (ii), inhibiting the main cellular antioxidant, was instead used to induce a cellular redox stress. Mitochondrial diseased cells derived from LS patients with CI deficiency responded with different sensitivity to both the galactose-based medium and the BSO treatment. The induction of a robust pathological phenotype provided models for target identifications and drug testing studies.

Chapter 6 identified NAD^+ shortage and the consequential reductive stress as hallmarks of CI deficiency in PSHF derived from LS patients when cultured in pyruvate-free galactose-based medium. Chapter 7 identified instead the lipid peroxidation aberration and the consequential oxidative stress as hallmarks of CI deficiency in PSHF derived from LS patients when treated with BSO. These two independent studies, applying different experimental conditions (the galactose-based medium and the BSO treatment) to the same cell models (PSHFs derived from LS patients with CI deficiency) and inducing different phenotypical consequences (reductive stress vs oxidative stress), might be the two faces of the same coin.

8.3 Future perspectives

In conclusion, cell-phenotypic profiling is a powerful technology that is continuously evolving according to the rapid technological advances of hardware and software development. The integration of these technological approaches with experimental biology has been and will be extremely advantageous for

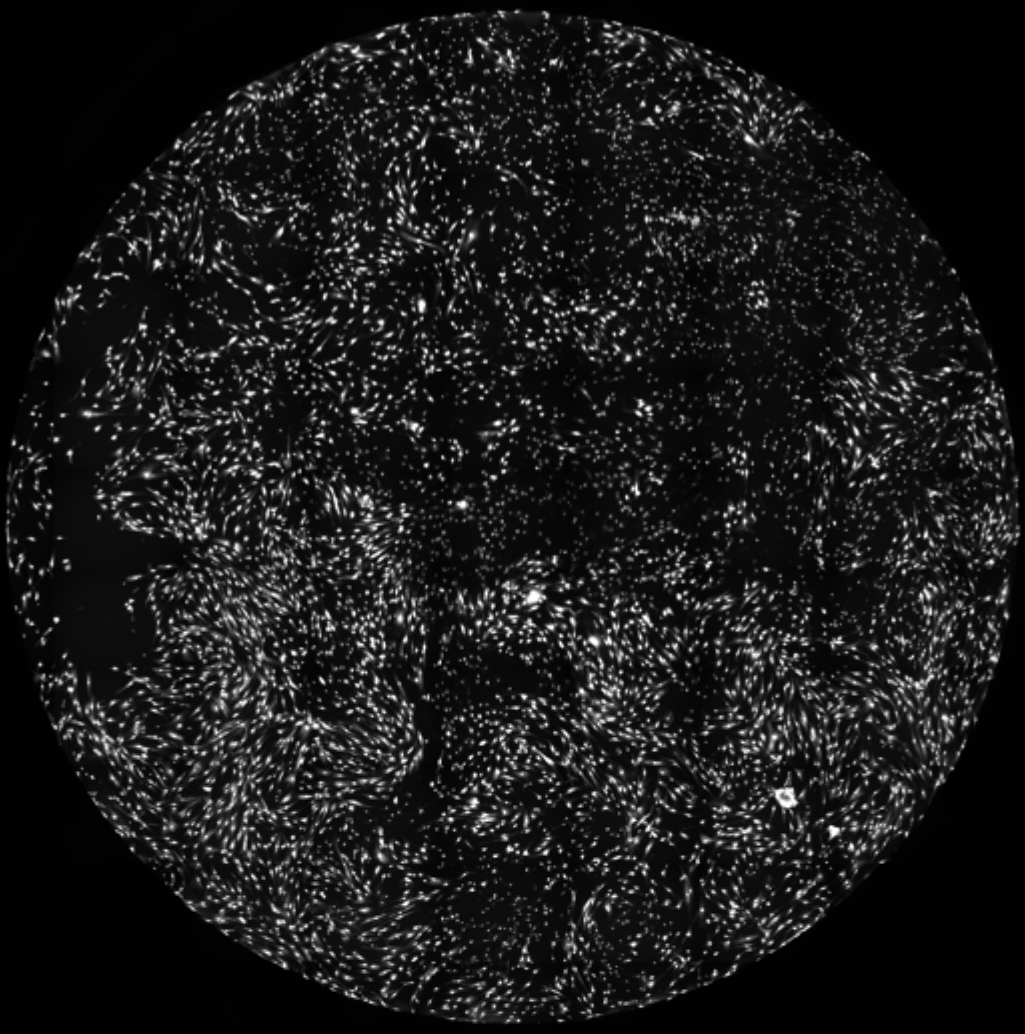
the understanding of the molecular basis of mitochondrial dysfunction. As a consequence, this will boost *in vitro* drug development and all translational medicine to get effective treatments from bench to bedside faster.

In particular, the field of 3D cell-based assays uses heterogenous and mature cell populations differentiated from induced pluripotent stem cell. These are combined in self-organized three-dimensional tissue cultures, called organoids, that represent a really promising tool (Dutta et al., 2017; Huch et al., 2017; Takahashi, 2018). Organoids presumably will offer more predictive models to better mimic the diseases phenotypes in a dish, discover new effective biological targets and develop new drugs faster and more effectively (Booij et al., 2019). Within this context phenotypic screening is maintaining a crucial role (Haasen et al., 2017) that more likely will remain dominant also in the next future.

In parallel to more advanced cell models, also new imaging detection methods are quickly developing. Free labeling microscopy techniques for time-lapse measurements and direct imaging of unstained living cells, are one promising example (Cotte et al., 2013; Kasprowicz et al., 2017). Making these label-free live cell imaging techniques quantitative, it is crucial to monitor fast and dynamic biological events in unperturbed and physiological conditions. Therefore, combining label-free time-lapse imaging techniques with targeted fluorescent dyes for end point measurements, will be an extremely powerful approach to facilitate experimental biology.

Despite the good promises and considerable technological advancements already happened in the last few years, pharmaceutical research organizations are still encountering considerable challenges with phenotypic screening. The trend indicated from the Eroom's law (Scannell et al., 2012) is still not inverted (Sam and Athri, 2019). Erooms's law specifically depicted a situation where drug discovery was becoming slower and more expensive over time, despite significant improvements in technology. Long time experimentation, unpredictable and often even irreproducible results are some of the current inherent obstacles associated with preclinical in vitro drug discovery. Errors in the experimental planning, execution and reporting is one of the major experimental biology bottlenecks. Even if rapid advances in technologies are happening, in

comparison with other industries, in biotech little has changed yet in the way research is conducted in most laboratories: manual work is still executed with pen, paper and pipettes.
Throughput, accuracy, efficiency and reproducibility are some of the necessary qualities, slowly moving biotech research to the next level. Within this context, full lab automation and digitalization are playing a major role in biotechnology, translational medicine, drug development... and mitochondrial dysfunction treatment development.



Chapter 9

Appendix: References, Nederlanse Samenvatting, Acknowledgments, RIMLS PhD Portfolio, Curriculum Vitae

References

Abeti, R., Parkinson, M. H., Hargreaves, I. P., Angelova, P. R., Sandi, C., Pook, M. A., Giunti, P., and Abramov, A. Y. (2016). 'Mitochondrial energy imbalance and lipid peroxidation cause cell death in Friedreich's ataxia'. *Cell death & disease*, 7:e2237.

Abraham, Y., Zhang, X., and Parker, C. N. (2014). Multiparametric Analysis of Screening Data: Growing Beyond the Single Dimension to Infinity and Beyond. *Journal of biomolecular screening*, 19(5):628–639.

Abramov, A. Y., Smulders-Srinivasan, T. K., Kirby, D. M., Acin-Perez, R., Enriquez, J. A., Lightowlers, R. N., Duchen, M. R., and Turnbull, D. M. (2010). Mechanism of neurodegeneration of neurons with mitochondrial DNA mutations. *Brain*, 133(3):797–807.

Ahmad, T., Aggarwal, K., Pattnaik, B., Mukherjee, S., Sethi, T., Tiwari, B. K., Kumar, M., Micheal, A., Mabalirajan, U., Ghosh, B., Sinha Roy, S., and Agrawal, A. (2013). Computational classification of mitochondrial shapes reflects stress and redox state. *Cell Death and Disease*.

Albeck, J. G., Burke, J. M., Spencer, S. L., Lauffenburger, D. A., and Sorger, P. K. (2008). Modeling a snap-action, variable-delay switch controlling extrinsic cell death. *PLoS biology*.

Archer, S. L. (2013). Mitochondrial Dynamics - mitochondrial fission and fusion in human diseases. *New England Journal of Medicine*, 369(23):2236–2251.

Auburger, G., Klinkenberg, M., Drost, J., Marcus, K., Morales-Gordo, B., Kunz, W. S., Brandt, U., Broccoli, V., Reichmann, H., Gispert, S., and Jendrach, M. (2012). Primary Skin Fibroblasts as a Model of Parkinson's Disease.

Barrientos, A. and Moraes, C. T. (1999). Titrating the effects of mitochondrial complex I impairment in the cell physiology. *Journal of Biological Chemistry*, 274(23):16188–16197.

Basit, F., Mpe Van Oppen, L., Schöckel, L., Bossenbroek, H. M., Van Emst-De Vries, S. E., Hermeling, J. C., Grefte, S., Kopitz, C., Heroult, M., Willems, P. H., and Koopman, W. J. (2017). Mitochondrial complex I inhibition triggers a mitophagy-dependent ROS increase leading to necroptosis and ferroptosis in melanoma cells.

Bast, A. and Haenen, G. R. (2013). Ten misconceptions about antioxidants.

Benard, G., Bellance, N., Jose, C., Melser, S., Nouette-Gaulain, K., and Rossignol, R. (2010). Multi-site control and regulation of mitochondrial energy production. *Biochimica et Biophysica Acta - Bioenergetics*, 1797(6-7):698–709.

Benard, G. and Rossignol, R. (2008). Ultrastructure of the Mitochondrion and Its Bearing on Function and Bioenergetics. *Antioxidants & Redox Signaling*, 10(8):1313–1342.

Bereiter-Hahn, J. and Vöth, M. (1994). Dynamics of mitochondria in living cells: shape changes, dislocations, fusion, and fission of mitochondria. *Microsc Res Tech.*, 27:198–219.

Bergin, E., Levine, J. S., Koh, J. S., and Lieberthal, W. (2000). Mouse proximal tubular cell-cell adhesion inhibits apoptosis by a cadherin-dependent mechanism. *American journal of physiology. Renal physiology*, 278(5):F758–68.

Beyrath, J., Pellegrini, M., Renkema, H., Houben, L., Pecheritsyna, S., Van Zandvoort, P., Van Den Broek, P., Bekel, A., Eftekhari, P., and Smeitink, J. A. M. (2018). KH176 Safeguards Mitochondrial Diseased Cells from Redox Stress-Induced Cell Death by Interacting with the Thioredoxin System/Peroxiredoxin Enzyme Machinery. *Scientific Reports*, 8(1).

Bilan, D. S. and Belousov, V. V. (2016). HyPer Family Probes: State of the Art. *Antioxidants & Redox Signaling*, 24(13):731–751.

Blanchet, L., Buydens, M. C., Smeitink, J. a. M., Willems, P. H. G. M., and Koopman, W. J. H. (2011). Isolated mitochondrial complex I deficiency: explorative data analysis of patient cell parameters. *Current pharmaceutical design*, 17(36):4023–33.

Blanchet, L., Grefte, S., Smeitink, J. A. M., Willems, P. H. G. M., and Koopman, W. J. H. (2014). Photo-induction and automated quantification of reversible mitochondrial permeability transition pore opening in primary mouse myotubes. *PLoS ONE*, 9(11).

Blanchet, L., Smeitink, J. A. M., van Emst-de Vries, S. E., Vogels, C., Pellegrini, M., Jonckheere, A. I., Rodenburg, R. J. T., Buydens, L. M. C., Beyrath, J., Willems, P. H. G. M., and Koopman, W. J. H. (2015). Quantifying small molecule phenotypic effects using mitochondrial morpho-functional fingerprinting and machine learning. *Scientific reports*, 5:8035.

Booij, T. H., Price, L. S., and Danen, E. H. (2019). 3D Cell-Based Assays for Drug Screens: Challenges in Imaging, Image Analysis, and High-Content Analysis. *SLAS Discovery*.

Brand, M. D. and Nicholls, D. G. (2011). Assessing mitochondrial dysfunction in cells. *The Biochemical journal*, 435(2):297–312.

Brandt, U. (2006). Energy converting NADH:quinone oxidoreductase (complex I). *Annual Review of Biochemistry*, 75(Complex I):69–92.

Bray, M.-A. and Carpenter, A. (2004). Advanced assay development guidelines for image-based high content screening and analysis. In Sittampalam, G., editor, *Assay guidance manual*. Eli Lilly & Company and the National Center for Advancing Translational Sciences, Bethesda, MD, USA.

Bray, M.-A. and Carpenter, A. (2012). Advanced Assay Development Guidelines for Image-Based High Content Screening and Analysis. *Assay Guidance Manual*.

Breuer, M. E., Willems, P. H., Smeitink, J. A., Koopman, W. J., and Nooteboom, M. (2013). Cellular and animal models for mitochondrial complex i deficiency: A focus on the NDUFS4 subunit. *IUBMB Life*, 65(3):202–208.

Brigelius-flohé, R. and Maiorino, M. (2013). Glutathione peroxidases. *Biochimica et Biophysica Acta*, pages 3298–3303.

Bro, R. &. S. A. (2014). Principal component analysis. *Anal. Methods*, 6:2812–2831.

Bros, H., Hauser, A., Paul, F., Niesner, R., and Infante-Duarte, C. (2015). Assessing Mitochondrial Movement Within Neurons: Manual Versus Automated Tracking Methods. *Traffic*.

Brown, J. (2009). Choosing the right number of components of factors in PCA and EFA. *Shiken: JALT testing & evaluation SIG Newsletter*, 13:19–23.

Buchser, W., Collins, M., Garyantes, T., Guha, R., Haney, S., and Lemmon, V. (2012). Assay Development Guidelines for Image-Based High Content Screening, High Content Analysis and High Content Imaging. *Assay Guid Man, Bethesda, Eli Lilly & Company and the National Center for Advancing Translational Sciences*, pages 1–69.

Chan, D. (2012). Fusion and fission: Interlinked processes critical for mitochondrial health. *Annu. Rev. Genet.*, 46:256–287.

Chandel, N. (2014). Mitochondria as signalling organelles. *BMC Biol.*, 12(34).

Chandrasekharan, A., Varadarajan, S. N., Lekshmi, A., Lupitha, S. S., Darvin, P., Chandrasekhar, L., Pillai, P. R., Santhoshkumar, T. R., and Pillai, M. R. (2019). A high-throughput real-time in vitro assay using mitochondrial targeted roGFP for screening of drugs targeting mitochondria. *Redox Biology*.

Chazotte, B. (2011). Labeling mitochondria with mitotracker dyes. *Cold Spring Harbor Protocols*, 6(8):990–992.

Chen, J., Jiang, X., Zhang, C., MacKenzie, K. R., Stossi, F., Palzkill, T., Wang, M. C., and Wang, J. (2017). Reversible Reaction-Based Fluorescent Probe for Real-Time Imaging of Glutathione Dynamics in Mitochondria. *ACS Sensors*, 2(9):1257–1261.

Chen, X., Zhong, Z., Xu, Z., Chen, L., and Wang, Y. (2010). 2',7'-Dichlorodihydrofluorescein as a fluorescent probe for reactive oxygen species measurement: Forty years of application and controversy. *Free Radical Research*, 44(6):587–604.

Christensen, C. E., Karlsson, M., Winther, J. R., Jensen, P. R., and Lerche, M. H. (2014). Non-invasive In-cell Determination of Free Cytosolic [NAD+]/[NADH] Ratios Using Hyperpolarized Glucose Show Large Variations in Metabolic Phenotypes. *Journal of Biological Chemistry*, 289(4):2344–2352.

Cogliati, S., Enriquez, J. A., and Scorrano, L. (2016). Mitochondrial Cristae: Where Beauty Meets Functionality. *Trends in Biochemical Sciences*, 41(3):261–273.

Collins, T. J., Berridge, M. J., Lipp, P., and Bootman, M. D. (2002). Mitochondria are morphologically and functionally heterogeneous within cells. *EMBO Journal*, 21(7):1616–1627.

Connolly, N. M. C., Theurey, P., Adam-Vizi, V., Bazan, N. G., Bernardi, P., Bolaños, J. P., Culmsee, C., Dawson, V. L., Deshmukh, M., Duchen, M. R., Düssmann, H., Fiskum, G., Galindo, M. F., Hardingham, G. E., Hardwick, J. M., Jekabsons, M. B., Jonas, E. A., Jordán, J., Lipton, S. A., Manfredi, G., Mattson, M. P., McLaughlin, B., Methner, A., Murphy, A. N., Murphy, M. P., Nicholls, D. G., Polster, B. M., Pozzan, T., Rizzuto, R., Satrústegui, J., Slack, R. S., Swanson, R. A., Swerdlow, R. H., Will, Y., Ying, Z., Joselin, A., Gioran, A., Moreira Pinho, C., Watters, O., Salvucci, M., Llorente-Folch, I., Park, D. S., Bano, D., Ankarcrona, M., Pizzo, P., and Prehn, J. H. M. (2017). *Guidelines on experimental methods to assess mitochondrial dysfunction in cellular models of neurodegenerative diseases*. Springer US.

Corrado, M., Scorrano, L., and Campello, S. (2012). Mitochondrial dynamics in cancer and neurodegenerative and neuroinflammatory diseases. *International Journal of Cell Biology*, 2012.

Cotte, Y., Toy, F., Jourdain, P., Pavillon, N., Boss, D., Magistretti, P., Marquet, P., and Depeursinge, C. (2013). Marker-free phase nanoscopy. *Nature Photonics*, 7(2):113–117.

Crabtree, H. G. (1929). Observations on the carbohydrate metabolism of tumours. *Biochemical Journal*, 23(3):536–545.

De la Fuente-Herreruela, D., Gónzalez-Charro, V., Almendro-Vedia, V. G., Morán, M., Martín, M. Á., Lillo, M. P., Natale, P., and López-Montero, I. (2017). Rhodamine-based sensor for real-time imaging of mitochondrial ATP in living fibroblasts. *Biochimica et Biophysica Acta (BBA) - Bioenergetics*, 1858(12):999–1006.

Dietlmeier, J., Ghita, O., Duessmann, H., Prehn, J. H. M., and Whelan, P. F. (2013). Unsupervised mitochondria segmentation using recursive spectral clustering and adaptive similarity models. *Journal of Structural Biology*, 184(3):401–408.

Distelmaier, F., Koopman, W. J. H., Testa, E. R., De Jong, A. S., Swarts, H. G., Mayatepek, E., Smeitink, J. A. M., and Willems, P. H. G. M. (2008). Life cell quantification of mitochondrial membrane potential at the single organelle level. *Cytometry Part A*, 73(2):129–138.

Distelmaier, F., Koopman, W. J. H., Van Den Heuvel, L. P., Rodenburg, R. J., Mayatepek, E., Willems, P. H. G. M., and Smeitink, J. A. M. (2009a). Mitochondrial complex i deficiency: From organelle dysfunction to clinical disease. *Brain*, 132(4):833–842.

Distelmaier, F., Valsecchi, F., Forkink, M., van Emst-de Vries, S., Swarts, H. G., Rodenburg, R. J., Verwiel, E. T., a.M. Smeitink, J., Willems, P. H., and Koopman, W. J. (2012). Trolox-Sensitive Reactive Oxygen Species Regulate Mitochondrial Morphology, Oxidative Phosphorylation and Cytosolic Calcium Handling in Healthy Cells. *Antioxidants & Redox Signaling*, 17(12):1657–1669.

Distelmaier, F., Valsecchi, F., Liemburg-Apers, D. C., Lebiedzinska, M., Rodenburg, R. J., Heil, S., Keijer, J., Fransen, J., Imamura, H., Danhauser, K., Seibt, A., Viollet, B., Gellerich, F. N., Smeitink, J. A., Wieckowski, M. R., Willems, P. H., and Koopman, W. J. (2015). Mitochondrial dysfunction in primary human fibroblasts triggers an adaptive cell survival program that requires AMPK-α. *Biochimica et Biophysica Acta - Molecular Basis of Disease*, 1852(3):529–540.

Distelmaier, F., Visch, H. J., Smeitink, J. A. M., Mayatepek, E., Koopman, W. J. H., and Willems, P. H. G. M. (2009b). The antioxidant Trolox restores mitochondrial membrane potential and Ca2+-stimulated ATP production in human complex i deficiency. *Journal of Molecular Medicine*, 87(5):515–522.

Dixon, S. J., Lemberg, K. M., Lamprecht, M. R., Skouta, R., Zaitsev, E. M., Gleason, C. E., Patel, D. N., Bauer, A. J., Cantley, A. M., Yang, W. S., Morrison, B., and Stockwell, B. R. (2012). Ferroptosis: An iron-dependent form of nonapoptotic cell death. *Cell*, 149(5):1060–1072.

Dmitriev, R. I. and Papkovsky, D. B. (2015). Intracellular probes for imaging oxygen concentration: how good are they? *Methods and Applications in Fluorescence*, 3(3):034001.

Dolga, A. M., Netter, M. F., Perocchi, F., Doti, N., Meissner, L., Tobaben, S., Grohm, J., Zischka, H., Plesnila, N., Decher, N., and Culmsee, C. (2013). Mitochondrial small conductance SK2 channels prevent glutamate-induced oxytosis and mitochondrial dysfunction. *Journal of Biological Chemistry*, 288:10792–10804.

Donato, M. T., Tolosa, L., Jimenez, N., Castell, J. V., and Gomez-Lechon, M. J. (2012). High-Content Imaging Technology for the Evaluation of Drug-Induced Steatosis Using a Multiparametric Cell-Based Assay. *Journal of Biomolecular Screening*, 17(3):394–400.

Dong, H., Cheung, S., Liang, Y., Wang, B., Ramalingam, R., and Wang, P. (2013). "Stain-omics": Identification of mitotracker labeled proteins in mammalian cells. *Electrophoresis.*, 34:1957–64.

Dutta, D., Heo, I., and Clevers, H. (2017). Disease Modeling in Stem Cell-Derived 3D Organoid Systems.

El-Hattab, A. W., Zarante, A. M., Almannai, M., and Scaglia, F. (2017). Therapies for mitochondrial diseases and current clinical trials. *Molecular Genetics and Metabolism*, 122(3):1–9.

Eliceiri, K. W., Berthold, M. R., Goldberg, I. G., Ibáñez, L., Manjunath, B. S., Martone, M. E., Murphy, R. F., Peng, H., Plant, A. L., Roysam, B., Stuurman, N., Swedlow, J. R., Tomancak, P., and Carpenter, A. E. (2012). Biological imaging software tools. *Nature Methods*, 9(7):697–710.

Enns, G. M., Kinsman, S. L., Perlman, S. L., Spicer, K. M., Abdenur, J. E., Cohen, B. H., Amagata, A., Barnes, A., Kheifets, V., Shrader, W. D., Thoolen, M., Blankenberg, F., and Miller, G. (2012). Initial experience in the treatment of inherited mitochondrial disease with EPI-743. *Molecular Genetics and Metabolism*, 105(1):91–102.

et al. Tigges, J. (2014). The hallmarks of fibroblast aging. *Mech. Ageing Dev.*, 138:26–44.

Falchi, A., Isola, R., Diana, A., Putzolu, M., and Diaz, G. (2005). Characterization of depolarization and repolarization phases of mitochondrial membrane potential fluctuations induced by tetramethylrhodamine methyl ester photoactivation. *FEBS J.*, 272:1649–1659.

Farrand, L., Kim, J. Y., Im-Aram, A., Suh, J. Y., Lee, H. J., and Tsang, B. K. (2013). An Improved Quantitative Approach for the Assessment of Mitochondrial Fragmentation in Chemoresistant Ovarian Cancer Cells. *PLoS ONE*.

Fassone, E. and Rahman, S. (2012). Complex I deficiency: Clinical features, biochemistry and molecular genetics. *Journal of Medical Genetics*, 49(9):578–590.

Feng, Y., Mitchison, T. J., Bender, A., Young, D. W., and Tallarico, J. A. (2009). Multi-parameter phenotypic profiling: using cellular effects to characterize small-molecule compounds. *Nature Reviews Drug Discovery*, 8(7):567–578.

Fernandez, M. I. G., Ceccarelli, D., and Muscatello, U. (2004). Use of the fluorescent dye 10-N-nonyl acridine orange in quantitative and location assays of cardiolipin: A study on different experimental models. *Analytical Biochemistry*, 328(2):174–180.

Folmes, C. D., Martinez-Fernandez, A., Perales-Clemente, E., Li, X., McDonald, A., Oglesbee, D., Hrstka, S. C., Perez-Terzic, C., Terzic, A., and Nelson, T. J. (2013). Disease-causing mitochondrial Heteroplasmy segregated within induced pluripotent stem cell clones derived from a patient with MELAS. *Stem Cells*, 31(7):1298–1308.

Forkink, M., Manjeri, G. R., Liemburg-Apers, D. C., Nibbeling, E., Blanchard, M., Wojtala, A., Smeitink, J. A., Wieckowski, M. R., Willems, P. H., and Koopman, W. J. (2014). Mitochondrial hyperpolarization during chronic complex i inhibition is sustained by low activity of complex II, III, IV and v. *Biochimica et Biophysica Acta - Bioenergetics*, 1837(8):1247–1256.

Forkink, M., Smeitink, J. A., Brock, R., Willems, P. H., and Koopman, W. J. (2010). Detection and manipulation of mitochondrial reactive oxygen species in mammalian cells. *Biochimica et Biophysica Acta (BBA) - Bioenergetics*, 1797(6):1034–1044.

Forkink, M., Willems, P. H. G. M., Koopman, W. J. H., and Grefte, S. (2015). Live-cell assessment of mitochondrial reactive oxygen species using dihydroethidine. *Methods in molecular biology (Clifton, N.J.)*, 1264:161–9.

Frey, P. A. (1996). The Leloir pathway: a mechanistic imperative for three enzymes to change the stereochemical configuration of a single carbon in galactose. *The FASEB Journal*, 10(4):461–470.

Friedman, J. and J., N. (2014). Mitochondrial form and function. *Nature*, 505:335–343.

Gammage, P. A., Moraes, C. T., and Minczuk, M. (2017). Mitochondrial Genome Engineering: The Revolution May Not Be CRISPR-Ized. *Trends in Genetics*, 34(2):101–110.

Gao, M., Yi, J., Zhu, J., Minikes, A. M., Monian, P., Thompson, C. B., and Jiang, X. (2018). Role of Mitochondria in Ferroptosis. *Molecular Cell*, pages 1–10.

Gáspár, T., Domoki, F., Lenti, L., Katakam, P. V. G., James, A., Bari, F., and Busija, D. W. (2009). Immediate neuronal preconditioning by NS1619. *Brain Res*, 1285:196–207.

Gaude, E., Schmidt, C., Gammage, P. A., Dugourd, A., Blacker, T., Chew, S. P., Saez-Rodriguez, J., O'Neill, J. S., Szabadkai, G., Minczuk, M., and Frezza, C. (2018). NADH Shuttling Couples Cytosolic Reductive Carboxylation of Glutamine with Glycolysis in Cells with Mitochondrial Dysfunction. *Molecular Cell*, 69(4):648–663.e7.

Gerards, M., Sallevelt, S. C., and Smeets, H. J. (2016). Leigh syndrome: Resolving the clinical and genetic heterogeneity paves the way for treatment options. *Molecular Genetics and Metabolism*, 117(3):300–312.

Gerencser, A. A., Mookerjee, S. A., Jastroch, M., and Brand, M. D. (2016). Measurement of the absolute magnitude and time courses of mitochondrial membrane potential in primary and clonal pancreatic beta-cells. *PLoS ONE*, 11(7).

Gibbs, R. M., Lipnick, S., Bateman, J. W., Chen, L., Cousins, H. C., Hubbard, E. G., Jowett, G., LaPointe, D. S., McGredy, M. J., Odonkor, M. N., Repetti, G., Thomas, E., and Rubin, L. L. (2018). Toward Precision Medicine for Neurological and Neuropsychiatric Disorders. *Cell Stem Cell*, 23(1):21–24.

Giuly, R. J., Martone, M. E., and Ellisman, M. H. (2012). Method: Automatic segmentation of mitochondria utilizing patch classification, contour pair classification, and automatically seeded level sets. *BMC Bioinformatics*.

Gomes, L. C., Di Benedetto, G., and Scorrano, L. (2011). Essential amino acids and glutamine regulate induction of mitochondrial elongation during autophagy. *Cell Cycle*, 10(16):2635–2639.

Gomes, L. C. and Scorrano, L. (2011). Mitochondrial elongation during autophagy: A stereotypical response to survive in difficult times. *Autophagy*, 7(10):1251–1253.

Gorman, G. S., Chinnery, P. F., DiMauro, S., Hirano, M., Koga, Y., McFarland, R., Suomalainen, A., Thorburn, D. R., Zeviani, M., and Turnbull, D. M. (2016). Mitochondrial diseases. *Nature Reviews Disease Primers*, 2.

Grier, J., Hirano, M., Karaa, A., Shepard, E., and Thompson, J. L. P. (2018). Diagnostic odyssey of patients with mitochondrial disease: Results of a survey. *Neurol. Genet.*, 4(e230).

Grobarczyk, B., Franco, B., Hanon, K., and Malgrange, B. (2015). Generation of Isogenic Human iPS Cell Line Precisely Corrected by Genome Editing Using the CRISPR/Cas9 System. *Stem Cell Reviews and Reports*, 11(5):774–787.

Guillery, O., Malka, F., Frachon, P., Milea, D., Rojo, M., and Lombès, A. (2008). Modulation of mitochondrial morphology by bioenergetics defects in primary human fibroblasts. *Neuromuscular Disorders*, 18(4):319–330.

Haasen, D., Schopfer, U., Antczak, C., Guy, C., Fuchs, F., and Selzer, P. (2017). How Phenotypic Screening Influenced Drug Discovery: Lessons from Five Years of Practice. *ASSAY and Drug Development Technologies*, 15(6):239–246.

Halliwell, B. and Gutteridge, J. M. (1985). Free radicals in biology and medicine. *Journal of Free Radicals in Biology & Medicine*, 1(4):331–332.

Hatakeyama, H., Katayama, A., Komaki, H., Nishino, I., and Goto, Y. I. (2015). Molecular pathomechanisms and cell-type-specific disease phenotypes of MELAS caused by mutant mitochondrial tRNA(Trp). *Acta neuropathologica communications*, 3:52.

Hauck, A. K. and Bernlohr, D. A. (2016). Oxidative stress and lipotoxicity. *Journal of Lipid Research*, 57(11):1976–1986.

Held, M., Schmitz, M. H. a., Fischer, B., Walter, T., Neumann, B., Olma, M. H., Peter, M., Ellenberg, J., and Gerlich, D. W. (2010). CellCognition: time-resolved phenotype annotation in high-throughput live cell imaging. *Nature methods*, 7(9):747–754.

Hoitzing, H., Johnston, I. G., and Jones, N. S. (2015). What is the function of mitochondrial networks? A theoretical assessment of hypotheses and proposal for future research. *BioEssays*, 37(6):687–700.

Homolya, L., Hollo, Z., Germann, U. A., Pastan, I., Gottesman, M. M., and Sarkadi, B. (1993). Fluorescent cellular indicators are extruded by the multidrug resistance protein. *Journal of Biological Chemistry*.

Honrath, B., Krabbendam, I. E., Culmsee, C., and Dolga, A. M. (2017). Small conductance Ca2+-activated K+ channels in the plasma membrane, mitochondria and the ER: Pharmacology and implications in neuronal diseases. *Neurochemistry International*, 109:13–23.

Hosios, A. M. and Vander Heiden, M. G. (2018). The redox requirements of proliferating mammalian cells. *Journal of Biological Chemistry*, page jbc.TM117.000239.

Huch, M., Knoblich, J. A., Lutolf, M. P., and Martinez-Arias, A. (2017). The hope and the hype of organoid research. *Development*, 144(6):938–941.

Hugelier, S., De Rooi, J. J., Bernex, R., Duwé, S., Devos, O., Sliwa, M., Dedecker, P., Eilers, P. H., and Ruckebusch, C. (2016). Sparse deconvolution of high-density super-resolution images. *Scientific Reports*.

Hüser, J., Rechenmacher, C., and Blatter, L. (1998). Imaging the permeability transition in single mitochondria. *Biophys. J.*, 74:2129–2137.

Iannetti, E. F., Prigione, A., Smeitink, J. A. M., Koopman, W. J. H., Beyrath, J., and Renkema, H. (2019). Live-Imaging Readouts and Cell Models for Phenotypic Profiling of Mitochondrial Function. *Frontiers in Genetics*, 10(March):1–9.

Iannetti, E. F., Smeitink, J. A. M., Beyrath, J., Willems, P. H. G. M., and Koopman, W. J. H. (2016). Multiplexed high-content analysis of mitochondrial morphofunction using live-cell microscopy. *Nature Protocols*, 11(9):1693.

Iannetti, E. F., Smeitink, J. A. M., Willems, P. H. G. M., Beyrath, J., and Koopman, W. J. H. (2018). Rescue from galactose-induced death of Leigh Syndrome patient cells by pyruvate and NAD⁺. *Cell Death & Disease*, 9(11):1135.

Iannetti, E. F., Willems, P. H. G. M., Pellegrini, M., Beyrath, J., Smeitink, J. A. M., Blanchet, L., and Koopman, W. J. H. (2015). Toward high-content screening of mitochondrial morphology and membrane potential in living cells. *The international journal of biochemistry & cell biology*, 63:66–70.

Imamura, H., Huynh Nhat, K. P., Togawa, H., Saito, K., Iino, R., Kato-Yamada, Y., Nagai, T., and Noji, H. (2009). Visualization of ATP levels inside single living cells with fluorescence resonance energy transfer-based genetically encoded indicators. *Proceedings of the National Academy of Sciences*, 106(37):15651–15656.

Inak, G., Lorenz, C., Lisowski, P., Zink, A., Mlody, B., and Prigione, A. (2017). Concise Review: Induced Pluripotent Stem Cell-Based Drug Discovery for Mitochondrial Disease. *Stem cells (Dayton, Ohio)*, 35(7):1655–1662.

Iuso, A., Scacco, S., Piccoli, C., Bellomo, F., Petruzzella, V., Trentadue, R., Minuto, M., Ripoli, M., Capitanio, N., Zeviani, M., and Papa, S. (2006). Dysfunctions of cellular oxidative metabolism in patients with mutations in the NDUFS1 and NDUFS4 genes of complex I. *Journal of Biological Chemistry*, 281(15):10374–10380.

Jacob, S. F., Wü, M. L., Delgado, M. E., and Rehm, M. (2015). An Analysis of the Truncated Bid-and ROS-dependent Spatial Propagation of Mitochondrial Permeabilization Waves during Apoptosis. *The Journal of biological chemistry*.

Jiang, X., Chen, J., Bajić, A., Zhang, C., Song, X., Carroll, S. L., Cai, Z.-L., Tang, M., Xue, M., Cheng, N., Schaaf, C. P., Li, F., MacKenzie, K. R., Ferreon, A. C. M., Xia, F., Wang, M. C., Maletić-Savatić, M., and Wang, J. (2017). Quantitative real-time imaging of glutathione. *Nature Communications*, 8:16087–16163.

Kaewsuya, P., Danielson, N. D., and Ekhterae, D. (2007). Fluorescent determination of cardiolipin using 10-N-nonyl acridine orange. *Analytical and Bioanalytical Chemistry*, 387(8):2775–2782.

Kandel, J., Chou, P., and Eckmann, D. M. (2015). Automated detection of whole-cell mitochondrial motility and its dependence on cytoarchitectural integrity. *Biotechnology and Bioengineering*.

Karamanlidis, G., Lee, C. F. F., Garcia-Menendez, L., Kolwicz, S. C. C., Suthammarak, W., Gong, G., Sedensky, M. M. M., Morgan, P. G. G., Wang, W., and Tian, R. (2013). Mitochondrial Complex I Deficiency Increases Protein Acetylation and Accelerates Heart Failure. *Cell Metabolism*, 18(2):239–250.

Kasprowicz, R., Suman, R., and O'Toole, P. (2017). Characterising live cell behaviour: Traditional label-free and quantitative phase imaging approaches. *International Journal of Biochemistry and Cell Biology*, 84:89–95.

Kim, J. A., Han, E., Eun, C. J., Tak, Y. K., and Song, J. M. (2012). Real-time concurrent monitoring of apoptosis, cytosolic calcium, and mitochondria permeability transition for hypermulticolor high-content screening of drug-induced mitochondrial dysfunction-mediated hepatotoxicity. *Toxicology Letters*, 214(2):175–181.

Kim, T. K. and Eberwine, J. H. (2010). Mammalian cell transfection: The present and the future. *Analytical and Bioanalytical Chemistry*, 397(8):3173–3178.

King, M. P. and Attardi, G. (1989). Human cells lacking mtDNA: repopulation with exogenous mitochondria by complementation. *Cell*, 246(4929):500–503.

Kirby, D. M., Crawford, M., Cleary, M. A., Dahl, H.-H. M. H., Dennett, X., and Thorburn, D. R. (1999). Respiratory chain complex I deficiency: An underdiagnosed energy generation disorder. *Neurology*, 52(6):1255–1255.

Kitami, T., Logan, D. J., Negri, J., Hasaka, T., Tolliday, N. J., Carpenter, A. E., Spiegelman, B. M., and Mootha, V. K. (2012). A chemical screen probing the relationship between mitochondrial content and cell size. *PLoS ONE*, 7(3):1–7.

Koene, S. and Smeitink, J. (2009). Mitochondrial medicine: Entering the era of treatment. *Journal of Internal Medicine*, 265(2):193–209.

Komor, A. C., Badran, A. H., and Liu, D. R. (2017). CRISPR-Based Technologies for the Manipulation of Eukaryotic Genomes. *Cell*, 168(1-2):20–36.

Koopman, W. J., Forkink, M., Smeitink, J. A., Brock, R., and Willems, P. H. (2010). Mammalian Mitochondrial Complex I: Biogenesis, Regulation, and Reactive Oxygen Species Generation. *Antioxidants & Redox Signaling*, 12(12).

Koopman, W. J., Visch, H. J., Verkaart, S., van den Heuvel, L. W., Smeitink, J. A., and Willems, P. H. (2005a). Mitochondrial network complexity and pathological decrease in complex I activity are tightly correlated in isolated human complex I deficiency. *American Journal of Physiology. Cell Physiology*, 289(4):C881–90.

Koopman, W. J. H., Beyrath, J., Fung, C.-W., Koene, S., Rodenburg, R. J., Willems, P., and Smeitink, J. A. M. (2016). Mitochondrial disorders in children: Toward development of small-molecule treatment strategies. *EMBO Molecular Medicine*, 8(4):311–327.

Koopman, W. J. H., Distelmaier, F., Esseling, J. J., Smeitink, J. A. M., and Willems, P. H. G. M. (2008). Computer-assisted live cell analysis of mitochondrial membrane potential, morphology and calcium handling. *Methods*, 46(4):304–311.

Koopman, W. J. H., Distelmaier, F., Smeitink, J. A., and Willems, P. H. (2013). OXPHOS mutations and neurodegeneration. *The EMBO Journal*, 32(1):9–29.

Koopman, W. J. H., Hink, M. A., Verkaart, S., Visch, H. J., Smeitink, J. A. M., and Willems, P. H. G. M. (2007a). Partial complex I inhibition decreases mitochondrial motility and increases matrix protein diffusion as revealed by fluorescence correlation spectroscopy. *Biochimica et Biophysica Acta - Bioenergetics*, 1767(7):940–947.

Koopman, W. J. H., Verkaart, S., van Emst-de Vries, S. E., Grefte, S., Smeitink, J. A. M., and Willems, P. H. G. M. (2006a). Simultaneous quantification of oxidative stress and cell spreading using 5-(and-6)-chloromethyl-2',7'-dichlorofluorescein. *Cytometry Part A*, 69A(12):1184–1192.

Koopman, W. J. H., Verkaart, S., Visch, H.-J., van der Westhuizen, F. H., Murphy, M. P., van den Heuvel, L. W. P. J., Smeitink, J. a. M., and Willems, P. H. G. M. (2005b). Inhibition of complex I of the electron transport chain causes O2-. -mediated mitochondrial outgrowth. *American journal of physiology. Cell physiology*, 288(6):C1440–C1450.

Koopman, W. J. H., Verkaart, S., Visch, H. J., van Emst-de Vries, S., Nijtmans, L. G. J., Smeitink, J. A. M., and Willems, P. H. G. M. (2007b). Human NADH:ubiquinone oxidoreductase deficiency: radical changes in mitochondrial morphology? *American journal of physiology. Cell physiology*, 293(1):C22–9.

Koopman, W. J. H., Visch, H.-J., Smeitink, J. A. M., and Willems, P. H. G. M. (2005c). Simultaneous quantitative measurement and automated analysis of mitochondrial morphology, mass, potential, and motility in living human skin fibroblasts. *Cytom. Part A*, 69A:1–12.

Koopman, W. J. H., Visch, H.-J. J., Smeitink, J. A. M., and Willems, P. H. G. M. (2006b). Simultaneous quantitative measurement and automated analysis of mitochondrial morphology, mass, potential, and motility in living human skin fibroblasts. *Cytometry Part A*, 69(1):1–12.

Koopman, Werner. Willems, Peter and Smeitink, J., Koopman, W. J., Willems, P. H., and Smeitink, J. A. (2012). Monogenic Mitochondrial Disorders. *New England Journal of Medicine*, 366(12):1132–41.

Krabbendam, I. E., Honrath, B., Culmsee, C., and Dolga, A. M. (2017). Mitochondrial Ca2+ -activated K+ channels and their role in cell life and death pathways. *Cell Calcium*, 69:101–111.

Krabbendam, I. E., Honrath, B., Dilberger, B., Iannetti, E. F., Branicky, R. S., T., M., Evers, B., Dekker, F. J., Koopman, W. J. H., Beyrath, J., Bano, D., Schmidt, M., Bakker,

B. M., Hekimi, S., Culmsee, C., Eckert, G., and Dolga, A. M. (2019). SK channel-mediated metabolic escape to glycolysis inhibits 1 ferroptosis and supports stress resistance in C. elegans. *Cell Death & Disease*.

Kümmel, A., Selzer, P., Beibel, M., Gubler, H., Parker, C. N., and Gabriel, D. (2011). Comparison of multivariate data analysis strategies for high-content screening. *Journal of biomolecular screening*, 16(3):338–47.

Lackner, L. L. (2014). Shaping the dynamic mitochondrial network. *BMC Biology*, 12:22–25.

Lake, N. J., Compton, A. G., Rahman, S., and Thorburn, D. R. (2016). Leigh syndrome: One disorder, more than 75 monogenic causes. *Annals of Neurology*, 79(2):190–203.

Lansing-Taylor, D. (2007). Past, present and future of high content screening and the field of cellomics. In Lansing-Taylor, D., Haskins, J.R., Giuliano, K., editor, *High content screening: A powerful approach to systems cell biology and drug discovery*. Humana Press, Totowa, NJ, USA.

Lautenschläger, J., Lautenschläger, C., Tadic, V., Süße, H., Ortmann, W., Denzler, J., Stallmach, A., Witte, O. W., and Grosskreutz, J. (2015). Novel computer vision algorithm for the reliable analysis of organelle morphology in whole cell 3D images - A pilot study for the quantitative evaluation of mitochondrial fragmentation in amyotrophic lateral sclerosis. *Mitochondrion*.

Lehmann, D. and McFarland, R. (2018). Overview of Approaches to Mitochondrial Disease Therapy. *Journal of Inborn Errors of Metabolism and Screening*, 6:232640981775296.

Leipnitz, G., Mohsen, A. W., Karunanidhi, A., Seminotti, B., Roginskaya, V. Y., Markantone, D. M., Grings, M., Mihalik, S. J., Wipf, P., Van Houten, B., and Vockley, J. (2018). Evaluation of mitochondrial bioenergetics, dynamics, endoplasmic reticulum-mitochondria crosstalk, and reactive oxygen species in fibroblasts from patients with complex i deficiency. *Scientific Reports*, 8(1):1–14.

Lemasters, J. J. and Ramshesh, V. K. (2007). Imaging of Mitochondrial Polarization and Depolarization with Cationic Fluorophores. *Methods in Cell Biology*, 80(06):283–295.

Leonard, A. P., Cameron, R. B., Speiser, J. L., Wolf, B. J., Peterson, Y. K., Schnellmann, R. G., Beeson, C. C., and Rohrer, B. (2015). Quantitative analysis of mitochondrial morphology and membrane potential in living cells using high-content imaging, machine learning, and morphological binning. *Biochimica et Biophysica Acta - Molecular Cell Research*, 1853(2):348–360.

Lewerenz, J., Ates, G., Methner, A., Conrad, M., and Maher, P. (2018). Oxytosis/ferroptosis-(Re-) emerging roles for oxidative stress-dependent non-apoptotic cell death in diseases of the central nervous system. *Frontiers in Neuroscience*, 12(APR).

Liang, C., Ahmad, K., and Sue, C. M. (2014). The broadening spectrum of mitochondrial disease: Shifts in the diagnostic paradigm. *Biochimica et Biophysica Acta (BBA) - General Subjects*, 1840(4):1360–1367.

Liemburg-Apers, D. C., Imamura, H., Forkink, M., Nooteboom, M., Swarts, H. G., Brock, R., Smeitink, J. A., Willems, P. H., and Koopman, W. J. (2011). Quantitative glucose and ATP sensing in mammalian cells. *Pharmaceutical Research*, 28(11):2745–2757.

Liemburg-Apers, D. C., Schirris, T. J., Russel, F. G., Willems, P. H., and Koopman, W. J. (2015). Mitoenergetic Dysfunction Triggers a Rapid Compensatory Increase in Steady-State Glucose Flux. *Biophysical Journal*, 109(7):1372–1386.

Liemburg-Apers, D. C., Wagenaars, J. A. L., Smeitink, J. A. M., Willems, P. H. G. M., and Koopman, W. J. H. (2016). Acute stimulation of glucose influx upon mitoenergetic dysfunction requires LKB1, AMPK, Sirt2 and mTOR–RAPTOR. *Journal of Cell Science*, 129(23):4411–4423.

Lihavainen, E., Kislin, M., Toptunov, D., Khiroug, L., and Ribeiro, A. S. (2015). Automatic quantification of mitochondrial fragmentation from two-photon microscope images of mouse brain tissue. *Journal of Microscopy*.

Lihavainen, E., Mäkelä, J., Spelbrink, J. N., and Ribeiro, A. S. (2012). Mytoe: Automatic analysis of mitochondrial dynamics. *Bioinformatics*.

Lin, M. T. and Beal, M. F. (2006). Mitochondrial dysfunction and oxidative stress in neurodegenerative diseases. *Nature*, 443(7113):787–795.

Little, D., Luft, C., Mosaku, O., Lorvellec, M., Yao, Z., Paillusson, S., Kriston-Vizi, J., Gandhi, S., Abramov, A. Y., Ketteler, R., Devine, M. J., and Gissen, P. (2018). A single cell high content assay detects mitochondrial dysfunction in iPSC-derived neurons with mutations in SNCA. *Scientific reports*.

Lopez-Fabuel, I., Le Douce, J., Logan, A., James, A. M., Bonvento, G., Murphy, M. P., Almeida, A., and Bolaños, J. P. (2016). Complex I assembly into supercomplexes determines differential mitochondrial ROS production in neurons and astrocytes. *Proceedings of the National Academy of Sciences*, 113(46):13063–13068.

Lorenz, C., Lesimple, P., Bukowiecki, R., Zink, A., Inak, G., Mlody, B., Singh, M., Semtner, M., Mah, N., Auré, K., Leong, M., Zabiegalov, O., Lyras, E.-M. M., Pfiffer, V., Fauler,

B., Eichhorst, J., Wiesner, B., Huebner, N., Priller, J., Mielke, T., Meierhofer, D., Izsvák, Z., Meier, J. C., Bouillaud, F., Adjaye, J., Schuelke, M., Wanker, E. E., Lombès, A., and Prigione, A. (2017). Human iPSC-Derived Neural Progenitors Are an Effective Drug Discovery Model for Neurological mtDNA Disorders. *Cell Stem Cell*, 20(5):659–674.e9.

Lunt, S. Y. and Vander Heiden, M. G. (2011). Aerobic Glycolysis: Meeting the Metabolic Requirements of Cell Proliferation. *Annual Review of Cell and Developmental Biology*, 27(1):441–464.

Ma, Y. Y., Wu, T. F., Liu, Y. P., Wang, Q., Song, J. Q., Li, X. Y., Shi, X. Y., Zhang, W. N., Zhao, M., Hu, L. Y., Yang, Y. L., and Zou, L. P. (2013). Genetic and biochemical findings in Chinese children with Leigh syndrome. *Journal of Clinical Neuroscience*.

Makrecka-Kuka, M., Krumschnabel, G., and Gnaiger, E. (2015). High-Resolution Respirometry for Simultaneous Measurement of Oxygen and Hydrogen Peroxide Fluxes in Permeabilized Cells, Tissue Homogenate and Isolated Mitochondria. *Biomolecules*, 5(3):1319–1338.

Malka, F., Guillery, O., Cifuentes-Diaz, C., Guillou, E., Belenguer, P., and Lombès, A. (2005). Separate fusion of outer and inner mitochondrial membranes. *EMBO Rep.*, 6:853–9.

Marí, M., Morales, A., Colell, A., García-Ruiz, C., Kaplowitz, N., and Fernández-Checa, J. C. (2013). Mitochondrial glutathione: Features, regulation and role in disease. *Biochimica et Biophysica Acta - General Subjects*, 1830(5):3317–3328.

Marroquin, L. D., Hynes, J., Dykens, J. A., Jamieson, J. D., and Will, Y. (2007). Circumventing the Crabtree Effect: Replacing Media Glucose with Galactose Increases Susceptibility of HepG2 Cells to Mitochondrial Toxicants. *Toxicological Sciences*, 97(2):539–547.

Massart, D. and Al., E. (1997). *Handbook of Chemometrics and Qualimetrics*. Elsevier, Amsterdam, The Netherlands.

McClatchey, P. M., Keller, A. C., Bouchard, R., Knaub, L. A., and Reusch, J. E. (2016). Fully automated software for quantitative measurements of mitochondrial morphology. *Mitochondrion*.

McDonagh, B. (2017). Detection of ROS induced proteomic signatures by mass spectrometry. *Frontiers in Physiology*, 8(JUL):1–7.

Mertens, J., Paquola, A. C., Ku, M., Hatch, E., Böhnke, L., Ladjevardi, S., McGrath, S., Campbell, B., Lee, H., Herdy, J. R., Gonçalves, J. T., Toda, T., Kim, Y., Winkler, J., Yao, J., Hetzer, M. W., and Gage, F. H. (2015). Directly Reprogrammed Human Neurons Retain Aging-Associated Transcriptomic Signatures and Reveal Age-Related Nucleocytoplasmic Defects. *Cell Stem Cell*, 17(6):705–718.

Meyer, A. J. and Dick, T. P. (2010). Fluorescent Protein-Based Redox Probes. *Antioxidants & Redox Signaling*, 13(5):621–650.

Meyer, J. N., Leung, M. C., Rooney, J. P., Sendoel, A., Hengartner, M. O., Kisby, G. E., and Bess, A. S. (2013). Mitochondria as a target of environmental toxicants. *Toxicological Sciences*, 134(1):1–17.

Mishra, P. and Chan, D. C. (2016). Metabolic regulation of mitochondrial dynamics. *Journal of Cell Biology*.

Mitchell, P. (1961). Coupling of Phosphorylation to Electron and Hydrogen Transfer by a Chemi-Osmotic type of Mechanism. *Nature*.

Mitchell, P. and Moyle, J. (1967). Chemiosmotic hypothesis of oxidative phosphorylation. *Nature*, 213(5072):137–139.

Morris, G., Berk, M., Carvalho, A. F., Maes, M., Walker, A. J., and Puri, B. K. (2018). Why should neuroscientists worry about iron? The emerging role of ferroptosis in the pathophysiology of neuroprogressive diseases. *Behavioural Brain Research*, 341:154–175.

Mukhopadhyay, P. (2008). Simple quantitative detection of mitochondrial superoxide production in live cells. *Biochemical and Biophysical Research Communications*, 358(1):203–208.

Mumcuoglu, E. U., Hassanpour, R., Tasel, S. F., Perkins, G., Martone, M. E., and Gurcan, M. N. (2012). Computerized detection and segmentation of mitochondria on electron microscope images. *Journal of Microscopy*.

Murphy, M. P. (2009). How mitochondria produce reactive oxygen species. *The Biochemical journal*, 417(1):1–13.

Nadanaciva, S., Dillman, K., Gebhard, D. F., Shrikhande, A., and Will, Y. (2010). High-Content Screening for Compounds That Affect mtDNA-Encoded Protein Levels in Eukaryotic Cells. *Journal of Biomolecular Screening*, 15(8):937–948.

Neitemeier, S., Jelinek, A., Laino, V., Hoffmann, L., Eisenbach, I., Eying, R., Ganjam, G. K., Dolga, A. M., Oppermann, S., and Culmsee, C. (2017). BID links ferroptosis to mitochondrial cell death pathways. *Redox Biology*.

Nicholls, D. G. (2006). Simultaneous monitoring of ionophore- and inhibitor-mediated plasma and mitochondrial membrane potential changes in cultured neurons. *Journal of Biological Chemistry*, 281(21):14864–14874.

Nicholls, D. G. (2012). Fluorescence Measurement of Mitochondrial Membrane Potential Changes in Cultured Cells. In *Humana Press*, pages 119–133.

Nicholls, D. G. (2018). Fluorescence measurement of mitochondrial membrane potential changes in cultured cells. In *Methods in Molecular Biology*, pages 119–133. Humana Press.

Nicolaisen, J., Nillson, L., Pettersen, I., Willems, P., Lorens, J., and Koopman, W. (2014). Automated quantification and integrative analysis of 2D and 3D mitochondrial shape and network properties. *PLoS One*, 9:e101365.

Nielson, J. R. and Rutter, J. P. (2018). Lipid-mediated signals that regulate mitochondrial biology. *Journal of Biological Chemistry*, 293(20):7517–7521.

Nightingale, H., Pfeffer, G., Bargiela, D., Horvath, R., and Chinnery, P. F. (2016). Emerging therapies for mitochondrial disorders.

Nikolaisen, J., Nilsson, L. I. H., Pettersen, I. K. N., Willems, P. H. G. M., Lorens, J. B., Koopman, W. J. H., and Tronstad, K. J. (2014). Automated quantification and integrative analysis of 2D and 3D mitochondrial shape and network properties. *PLoS ONE*, 9(7):1–16.

Niyazov, D. M., Kahler, S. G., and Frye, R. E. (2016). Primary Mitochondrial Disease and Secondary Mitochondrial Dysfunction: Importance of Distinction for Diagnosis and Treatment. *Molecular syndromology*, 7(3):122–37.

Nomura, Y., Takayama, T., Sato, M., Takahashi, E., Feng, Z., and Nakamura, T. (2009). Mitochondria-Targeted Green Fluorescent Protein for Quantitative Monitoring of Mitochondrial Morphology in Living Cells. *Letters in Drug Design & Discovery*, 6(5):319–322.

Nooteboom, M., Forkink, M., and Willems, P.H.G.M. Koopman, W. (2012). Live-cell quantification of mitochondrial functional parameters. In Badoer, E., editor, *Neuromethods 70: Visualization techniques, from immunohistochemistry to Magnetic Resonance Imaging*.

Nunnari, J. and Suomalainen, A. (2012). Mitochondria: In sickness and in health. *Cell*, 148(6):1145–1159.

Oparka, M., Walczak, J., Malinska, D., van Oppen, L. M., Szczepanowska, J., Koopman, W. J., and Wieckowski, M. R. (2016). Quantifying ROS levels using CM-H 2 DCFDA and HyPer. *Methods*, 109:3–11.

PALADE, G. E. (1953). An electron microscope study of the mitochondrial structure. *The journal of histochemistry and cytochemistry : official journal of the Histochemistry Society*.

Pap, E., Drummen, G., Winter, V., Kooij, T., Rijken, P., Wirtz, K., Op den Kamp, J., Hage, W., and Post, J. (1999). Ratio-fluorescence microscopy of lipid oxidation in living cells using C11-BODIPY581/591. *FEBS Letters*, 453(3):278–282.

Paradies, G., Paradies, V., Ruggiero, F. M., and Petrosillo, G. (2019). Role of Cardiolipin in Mitochondrial Function and Dynamics in Health and Disease: Molecular and Pharmacological Aspects. *Cells*, 8(7):728.

Parikh, S., Goldstein, A., Koenig, M. K., Scaglia, F., Enns, G. M., Saneto, R., and Al., E. (2015). Diagnosis and management of mitochondrial disease: a consensus statement from the Mitochondrial Medicine Society HHS Public Access. *Genetics in medicine*.

Patananan, A. N., Wu, T.-H., Chiou, P.-Y., and Teitell, M. A. (2016). Modifying the Mitochondrial Genome.

Pegoraro, G. and Misteli, T. (2017). High-Throughput Imaging for the Discovery of Cellular Mechanisms of Disease. *Trends in Genetics*, 33(9):604–615.

Peng, J. Y., Lin, C. C., Chen, Y. J., Kao, L. S., Liu, Y. C., Chou, C. C., Huang, Y. H., Chang, F. R., Wu, Y. C., Tsai, Y. S., and Hsu, C. N. (2011). Automatic morphological subtyping reveals new roles of caspases in mitochondrial dynamics. *PLoS Computational Biology*, 7(10).

PERA, M. F. (2011). The dark side of induced pluripotency. *Stem Cells*, 471.

Perales-Clemente, E., Cook, A. N., Evans, J. M., Roellinger, S., Secreto, F., Emmanuele, V., Oglesbee, D., Mootha, V. K., Hirano, M., Schon, E. A., Terzic, A., and Nelson, T. J. (2016). Natural underlying mtDNA heteroplasmy as a potential source of intra-person hiPSC variability. *The EMBO Journal*, 35(18):e201694892.

Persson, M., Løye, A. F., Mow, T., and Hornberg, J. J. (2013). A high content screening assay to predict human drug-induced liver injury during drug discovery. *Journal of Pharmacological and Toxicological Methods*, 68(3):302–313.

Pfeffer, G., Horvath, R., Klopstock, T., Mootha, V. K., Suomalainen, A., Koene, S., Hirano, M., Zeviani, M., Bindoff, L. A., Yu-Wai-Man, P., Hanna, M., Carelli, V., McFarland, R., Majamaa, K., Turnbull, D. M., Smeitink, J., and Chinnery, P. F. (2013). New treatments for mitochondrial disease-no time to drop our standards. *Nature Reviews. Neurology*, 9(8):474–481.

Picard, M., Shirihai, O., Gentil, B., and Burelle, Y. (2013). Mitochondrial morphology transitions and functions: implications for retrograde signalling? *Am. J. Physiol. Regul. Integr. Comp. Physiol. 3*, 4:393–406.

Picard, M., Taivassalo, T., Gouspillou, G., and Hepple, R. T. (2011). Mitochondria: isolation, structure and function. *The Journal of Physiology*, 589(18):4413–4421.

Pitkanen, S. and Robinson, B. H. (1996). Mitochondrial complex I deficiency leads to increased production of superoxide radicals and induction of superoxide dismutase. *The Journal of clinical investigation*, 98(2):345–351.

Pittelli, M., Felici, R., Pitozzi, V., Giovannelli, L., Bigagli, E., Cialdai, F., Romano, G., Moroni, F., and Chiarugi, A. (2011). Pharmacological Effects of Exogenous NAD on Mitochondrial Bioenergetics, DNA Repair, and Apoptosis. *Molecular pharmacology*, 80(6).

Pouvreau, S. (2014). Genetically encoded reactive oxygen species (ROS) and redox indicators. *Biotechnology Journal*, 9(2):282–293.

Prime, T. A., Forkink, M., Logan, A., Finichiu, P. G., McLachlan, J., Li Pun, P. B., Koopman, W. J., Larsen, L., Latter, M. J., Smith, R. A., and Murphy, M. P. (2012). A ratiometric fluorescent probe for assessing mitochondrial phospholipid peroxidation within living cells. *Free Radical Biology and Medicine*, 53(3):544–553.

Quintana-Cabrera, R., Quirin, C., Glytsou, C., Corrado, M., Urbani, A., Pellattiero, A., Calvo, E., Vázquez, J., Enríquez, J. A., Gerle, C., Soriano, M. E., Bernardi, P., and Scorrano, L. (2018). The cristae modulator Optic atrophy 1 requires mitochondrial ATP synthase oligomers to safeguard mitochondrial function. *Nature Communications*.

Rajendran, M., Dane, E., Conley, J., and Tantama, M. (2016). Imaging Adenosine Triphosphate (ATP). *The biological bulletin*.

Rambold, A. S., Kostelecky, B., Elia, N., and Lippincott-Schwartz, J. (2011). Tubular network formation protects mitochondria from autophagosomal degradation during nutrient starvation. *Proceedings of the National Academy of Sciences*, 108(25):10190–10195.

Ramos-Ibeas, P., Barandalla, M., Colleoni, S., and Lazzari, G. (2017). Pyruvate antioxidant roles in human fibroblasts and embryonic stem cells. *Molecular and Cellular Biochemistry*, 429(1-2):1–14.

Reis, Y., Bernardo-Faura, M., Richter, D., Wolf, T., Brors, B., Hamacher-Brady, A., Eils, R., and Brady, N. R. (2012). Multi-parametric analysis and modeling of relationships between mitochondrial morphology and apoptosis. *PLoS ONE*, 7(1).

Reitzer, J. and Wice, M. (1979). Evidence That Glutamine, Not Sugar, Is the Major Energy Source for cultured HeLa Cells. *The Journal of biological chemistry*, 254(8).

Reuven, N., Adler, J., Meltser, V., and Shaul, Y. (2013). The Hippo pathway kinase Lats2 prevents DNA damage-induced apoptosis through inhibition of the tyrosine kinase c-Abl. *Cell Death and Differentiation*, 20(10):1330–1340.

Ringnér, M. and Ringner, M. (2008). What is principal component analysis? *Nat Biotechnol*, 26(3):303–304.

Ristow, M., Schmeisser, K., and Ristow M, S. K. (2014). Mitohormesis: Promoting health and lifespan by increased levels of reactive oxygen species (ROS). *Dose-Response*, 12(2):288–341.

Rizk, A., Paul, G., Incardona, P., Bugarski, M., Mansouri, M., Niemann, A., Ziegler, U., Berger, P., and Sbalzarini, I. F. (2014). Segmentation and quantification of subcellular structures in fluorescence microscopy images using Squassh. *Nature Protocols*.

Rizzuto, R., Brini, M., Pizzo, P., Murgia, M., and Pozzan, T. (1995). Chimeric green fluorescent protein as a tool for visualizing subcellular organelles in living cells. *Current Biology*, 5(6):635–642.

Robinson, B., Petrova-Benedict, R., Buncic, J., and Wallace, D. (1992). Nonviability of cells with oxidative defects in galactose medium: A screening test for affected patient fibroblasts. *Biochemical Medicine and Metabolic Biology*, 48(2):122–126.

Robinson, B. H. (1996). Use of fibroblast and lymphoblast cultures for detection of respiratory chain defects. *Methods in enzymology*, 264:454–64.

Robinson, K. M., Janes, M. S., Pehar, M., Monette, J. S., Ross, M. F., Hagen, T. M., Murphy, M. P., and Beckman, J. S. (2006). Selective fluorescent imaging of superoxide in vivo using ethidium-based probes. *Proceedings of the National Academy of Sciences*, 103(41):15038–15043.

Rodenburg, R. J. (2016). Mitochondrial complex I-linked disease. *Biochimica et Biophysica Acta - Bioenergetics*, 1857(7):938–945.

Rodenburg, R. J. T. (2011). Biochemical diagnosis of mitochondrial disorders. *Journal of Inherited Metabolic Disease*, 34(2):283–292.

Rossignol, R., Gilkerson, R., Aggeler, R., Yamagata, K., Remigton, S. J., and Capaldi, R. (2004). Energy substrate modulates mitochondrial structures and oxidative capacityin cancer cells. *Cancer Research*, 64:985–993.

Rowland, A. and Voeltz, G. (2012). Endoplasmic reticulum-mitochondria contacts: function of the junction. *Nat. Rev. Mol. Cell Biol.*, 13:607–625.

Russ, J. C. and Neal, F. (2016). *The Image Processing Handbook.* CRC press, Boca Raton, FL, USA.

Saha, K. and Jaenisch, R. (2010). Technical challenges in using human induced pluripotent stem cells to model disease. *Cell Stem Cell*, 5(6):584–595.

Sam, E. and Athri, P. (2019). Web-based drug repurposing tools: A survey.

Sawa, K., Uematsu, T., Korenaga, Y., Hirasawa, R., Kikuchi, M., Murata, K., Zhang, J., Gai, X., Sakamoto, K., Koyama, T., and Satoh, T. (2017). Krebs Cycle Intermediates Protective against Oxidative Stress by Modulating the Level of Reactive Oxygen Species in Neuronal HT22 Cells. *Antioxidants*, 6(1):21.

Sbalzarini, I. F. (2016). Seeing Is Believing: Quantifying Is Convincing: Computational Image Analysis in Biology. pages 1–39. Springer, Cham.

Scannell, J. W., Blanckley, A., Boldon, H., and Warrington, B. (2012). Diagnosing the decline in pharmaceutical R&D efficiency. *Nature Reviews Drug Discovery*, 11(March):191–200.

Schirris, T. J. J., Renkema, G. H., Ritschel, T., Voermans, N. C., Bilos, A., and Van Engelen, B. G. M. (2015). Statin-Induced Myopathy Is Associated with Mitochondrial Complex III Inhibition. *Cell Metab.*, 22:399–407.

Schöckel, L., Glasauer, A., Basit, F., Bitschar, K., Truong, H., Erdmann, G., Algire, C., Hägebarth, A., Willems, P. H., Kopitz, C., Koopman, W. J., and Héroult, M. (2015). Targeting mitochondrial complex I using BAY 87-2243 reduces melanoma tumor growth. *Cancer & Metabolism*, 3(1):11.

Schrepfer, E. and Scorrano, L. (2016). Mitofusins, from mitochondria to metabolism. *Mol. Cell*, 61:683–694.

Sharma, L. K., Fang, H., Liu, J., Vartak, R., Deng, J., and Bai, Y. (2011). Mitochondrial respiratory complex I dysfunction promotes tumorigenesis through ROS alteration and AKT activation. *Human Molecular Genetics*, 20(23):4605–4616.

Shrader, W. D., Amagata, A., Barnes, A., Enns, G. M., Hinman, A., Jankowski, O., Kheifets, V., Komatsuzaki, R., Lee, E., Mollard, P., Murase, K., Sadun, A. A., Thoolen, M., Wesson, K., and Miller, G. (2011). α-Tocotrienol quinone modulates oxidative stress response and the biochemistry of aging. *Bioorganic and Medicinal Chemistry Letters*, 21(12):3693–3698.

Sieprath, T., Corne, T. D., Willems, P. H., Koopman, W. J., and de Vos, W. H. (2016). Integrated high-content quantification of intracellular ROS levels and mitochondrial morphofunction. *Advances in Anatomy Embryology and Cell Biology*, 219(286):149–177.

Sirenko, O. and Cromwell, E. F. (2018). Determination of Hepatotoxicity in iPSC-Derived Hepatocytes by Multiplexed High Content Assays. In *Methods in molecular biology (Clifton, N.J.)*, volume 1683, pages 339–354.

Sjöstrand, F. S. (1953). Electron microscopy of mitochondria and cytoplasmic double membranes: Ultra-structure of rod-shaped mitochondria. *Nature*.

Smeitink, J., Van Den Heuvel, L., and DiMauro, S. (2001). The genetics and pathology of oxidative phosphorylation.

Smeitink, J. A., Zeviani, M., Turnbull, D. M., and Jacobs, H. T. (2006). Mitochondrial medicine: A metabolic perspective on the pathology of oxidative phosphorylation disorders.

Smith, K., Piccinini, F., Balassa, T., Koos, K., Danka, T., Azizpour, H., and Horvath, P. (2018). Phenotypic Image Analysis Software Tools for Exploring and Understanding Big Image Data from Cell-Based Assays. *Cell Systems*, 6(6):636–653.

Smolina, N., Bruton, J., Kostareva, A., and Sejersen, T. (2017). *Assaying Mitochondrial Respiration as an Indicator of Cellular Metabolism and Fitness*. Humana Press, New York, NY.

Sommer, C. and Gerlich, D. W. (2013). Machine learning in cell biology – teaching computers to recognize phenotypes. *Journal of Cell Sciience*, 126(Pt 24):5529–5539.

Spickett, C. M. and Pitt, A. R. (2015). Oxidative lipidomics coming of age: Advances in analysis of oxidized phospholipids in physiology and pathology. *Antioxidants and Redox Signaling*, 22(18):1646–1666.

Spinazzola, A. and Zeviani, M. (2009). Mitochondrial Diseases: A Cross-Talk Between Mitochondrial and Nuclear Genomes. In *Advances in experimental medicine and biology*, volume 652, pages 69–84.

Sternberg, S. (1983). Biomedical image processing. *Computer*, 16:22–34.

Stroud, D. A., Surgenor, E. E., Formosa, L. E., Reljic, B., Frazier, A. E., Dibley, M. G., Osellame, L. D., Stait, T., Beilharz, T. H., Thorburn, D. R., Salim, A., and Ryan, M. T. (2016). Accessory subunits are integral for assembly and function of human mitochondrial complex I. *Nature*, pages 1–17.

Sunnapu, O., Kotla, N. G., Maddiboyina, B., Marepally, S., Shanmugapriya, J., Sekar, K., Singaravadivel, S., and Sivaraman, G. (2017). Rhodamine-Based Fluorescent Turn-On Probe for Facile Sensing and Imaging of ATP in Mitochondria. *ChemistrySelect*, 2(25):7654–7658.

Swerdlow, R. H. (2007). Mitochondria in cybrids containing mtDNA from persons with mitochondriopathies. In *Journal of Neuroscience Research*.

Swinney, D. C. (2013). Phenotypic vs. Target-based drug discovery for first-in-class medicines. *Clinical Pharmacology and Therapeutics*, 93(4):299–301.

Takahashi, K., Tanabe, K., Ohnuki, M., Narita, M., Ichisaka, T., Tomoda, K., and Yamanaka, S. (2007). Induction of Pluripotent Stem Cells from Adult Human Fibroblasts by Defined Factors. *Cell*.

Takahashi, T. (2018). Organoids for Drug Discovery and Personalized Medicine. *Annual Review of Pharmacology and Toxicology*.

Tapia, P. C. (2006). Sublethal mitochondrial stress with an attendant stoichiometric augmentation of reactive oxygen species may precipitate many of the beneficial alterations in cellular physiology produced by caloric restriction, intermittent fasting, exercise and dietary p. *Medical Hypotheses*, 66(4):832–843.

Tasel, S. F., Mumcuoglu, E. U., Hassanpour, R. Z., and Perkins, G. (2016). A validated active contour method driven by parabolic arc model for detection and segmentation of mitochondria. *Journal of Structural Biology*.

Taylor, D. L. (2007). Past, present, and future of high content screening and the field of cellomics. *Methods in molecular biology (Clifton, N.J.)*, 356:3–18.

Taylor, D. L., Woo, E. S., and Giuliano, K. A. (2001). Real-time molecular and cellular analysis: The new frontier of drug discovery. *Current Opinion in Biotechnology*, 12(1):75–81.

Teixeira, J., Basit, F., Swarts, H. G., Forkink, M., Oliveira, P. J., Willems, P. H., and Koopman, W. J. (2018). Extracellular acidification induces ROS- and mPTP-mediated death in HEK293 cells. *Redox Biology*, 15(November 2017):394–404.

Titov, D. V., Cracan, V., Goodman, R. P., Peng, J., Grabarek, Z., and Mootha, V. K. (2016). Complementation of mitochondrial electron transport chain by manipulation of the NAD+/NADH ratio. *Science (New York, N.Y.)*, 352(6282):231–235.

Tolosa, L., Gómez-Lechón, M. J., Pérez-Cataldo, G., Castell, J. V., and Donato, M. T. (2013). HepG2 cells simultaneously expressing five P450 enzymes for the screening of hepatotoxicity: Identification of bioactivable drugs and the potential mechanism of toxicity involved. *Archives of Toxicology*, 87(6):1115–1127.

Toyama, E. Q., Herzig, S., Courchet, J., Lewis, T. L., Loson, O. C., Hellberg, K., Young, N. P., Chen, H., Polleux, F., Chan, D. C., and Shaw, R. J. (2016). AMP-activated protein kinase mediates mitochondrial fission in response to energy stress. *Science*, 351(6270):275–281.

Tretter, L., Sipos, I., and Adam-Vizi, V. (2004). Initiation of Neuronal Damage by Complex I Deficiency and Oxidative Stress in Parkinson's Disease. *Neurochemical Research*, 29(3):569–577.

Tronstad, K., Nooteboom, M., Nilsson, L., Nikolaisen, J., Sokolewicz, M., Grefte, S., Pettersen, I., Dyrstad, S., Hoel, F., Willems, P., and Koopman, W. (2014). Regulation And Quantification Of Cellular Mitochondrial Morphology And Content. *Current Pharmaceutical Design*, 20:5634–5652.

Tukey, J. (1977). *Exploratory Data Analysis.* Addison-Wesley, Boston, USA, 1st edition.

Twig, G., Elorza, A., Molina, A. J., Mohamed, H., Wikstrom, J. D., Walzer, G., Stiles, L., Haigh, S. E., Katz, S., Las, G., Alroy, J., Wu, M., Py, B. F., Yuan, J., Deeney, J. T., Corkey, B. E., and Shirihai, O. S. (2008). Fission and selective fusion govern mitochondrial segregation and elimination by autophagy. *EMBO Journal*.

Twig, G. and Shirihai, O. S. (2010). The Interplay Between Mitochondrial Dynamics and Mitophagy. *Antioxidants & Redox Signaling*.

Valsecchi, F., Monge, C., Forkink, M., De Groof, A. J., Benard, G., Rossignol, R., Swarts, H. G., Van Emst-De Vries, S. E., Rodenburg, R. J., Calvaruso, M. A., Nijtmans, L. G., Heeman, B., Roestenberg, P., Wieringa, B., Smeitink, J. A., Koopman, W. J., and Willems, P. H. (2012). Metabolic consequences of NDUFS4 gene deletion in immortalized mouse embryonic fibroblasts. In *Biochimica et Biophysica Acta - Bioenergetics*, volume 1817, pages 1925–1936.

Verkaart, S., Koopman, W. J. H., Cheek, J., van Emst-de Vries, S. E., van den Heuvel, L. W. P. J., Smeitink, J. A. M., and Willems, P. H. G. M. (2007a). Mitochondrial and cytosolic thiol redox state are not detectably altered in isolated human NADH:ubiquinone oxidoreductase deficiency. *Biochimica et Biophysica Acta - Molecular Basis of Disease*, 1772(9):1041–1051.

Verkaart, S., Koopman, W. J. H., van Emst-de Vries, S. E., Nijtmans, L. G. J., van den Heuvel, L. W. P. J., Smeitink, J. A. M., and Willems, P. H. G. M. (2007b). Superoxide production is inversely related to complex I activity in inherited complex I deficiency. *Biochimica et Biophysica Acta - Molecular Basis of Disease*, 1772(3):373–381.

Victor, M. B., Richner, M., Olsen, H. E., Lee, S. W., Monteys, A. M., Ma, C., Huh, C. J., Zhang, B., Davidson, B. L., Yang, X. W., and Yoo, A. S. (2018). Striatal neurons directly converted from Huntington's disease patient fibroblasts recapitulate age-associated disease phenotypes. *Nature Neuroscience*, 21(3):341–352.

Vierbuchen, T., Ostermeier, A., Pang, Z. P., Kokubu, Y., Südhof, T. C., and Wernig, M. (2010). Direct conversion of fibroblasts to functional neurons by defined factors. *Nature*, 463(7284):1035–1041.

Vincent, A. E., Ng, Y. S., White, K., Davey, T., Mannella, C., Falkous, G., Feeney, C., Schaefer, A. M., McFarland, R., Gorman, G. S., Taylor, R. W., Turnbull, D. M., and Picard, M. (2016). The Spectrum of Mitochondrial Ultrastructural Defects in Mitochondrial Myopathy. *Scientific Reports*, 6(April):1–12.

Vinogradov, A. and Grivennikova, V. (2001). The mitochondrial complex I: progress in understanding of catalytic properties. *IUBMB life*, 52(3-5):129–134.

Vives-Bauza, C., Yang, L., and Manfredi, G. (2007). Assay of Mitochondrial ATP Synthesis in Animal Cells and Tissues. pages 155–171.

Wai, T. and Langer, T. (2016). Mitochondrial dynamics and metabolic regulation. *Trends Endocrinol. Metab.*, 27:105–117.

Wang, X. M., Terasaki, P. I., Rankin, G. W., Chia, D., Hui Ping Zhong, and Hardy, S. (1993). A new microcellular cytotoxicity test based on calcein AM release. *Human Immunology*.

Westermann, B. (2010). Mitochondrial fission and fusion in cell life and death. *Nat. Rev. Mol. Cell Biol.*, 11:872–884.

Wiemerslage, L. and Lee, D. (2016). Quantification of mitochondrial morphology in neurites of dopaminergic neurons using multiple parameters. *Journal of Neuroscience Methods*, 262:56–65.

Wilkins, H. M., Carl, S. M., and Swerdlow, R. H. (2014). Cytoplasmic hybrid (cybrid) cell lines as a practical model for mitochondriopathies. *Redox Biology*, 2:619–631.

Willems, P. H., Smeitink, J. A., and Koopman, W. J. (2009). Mitochondrial dynamics in human NADH:ubiquinone oxidoreductase deficiency.

Willems, P. H. G. M., Valsecchi, F., Distelmaier, F., Verkaart, S., Visch, H. J., Smeitink, J. A. M., and Koopman, W. J. H. (2008). Mitochondrial Ca2+ homeostasis in human NADH:ubiquinone oxidoreductase deficiency. *Cell Calcium*, 44(1):123–133.

Willems, P. H. G. M., Rossignol, R., Dieteren, C. E. J., Murphy, M. P., and Koopman, W. J. H. (2015). Perspective Redox Homeostasis and Mitochondrial Dynamics. *Cell Metab.*, 22:207–218.

Woolley, J. F., Stanicka, J., and Cotter, T. G. (2013). Recent advances in reactive oxygen species measurement in biological systems. *Trends in Biochemical Sciences*, 38(11):556–565.

Yang, L., Venneti, S., and Nagrath, D. (2017). Glutaminolysis: A Hallmark of Cancer Metabolism. *Annual Review of Biomedical Engineering*, 19(1):163–194.

Yang, W. S., Kim, K. J., Gaschler, M. M., Patel, M., Shchepinov, M. S., and Stockwell, B. R. (2016). Peroxidation of polyunsaturated fatty acids by lipoxygenases drives ferroptosis. *Proceedings of the National Academy of Sciences*, page 201603244.

Yang, Y. and Balcarcel, R. R. (2003). 24-well plate spectrophotometric assay for preliminary screening of metabolic activity. *Assay and drug development technologies*, 1(3):461–468.

Yang, Y., McBride, K. M., Hensley, S., Lu, Y., Chedin, F., and Bedford, M. T. (2014). Arginine Methylation Facilitates the Recruitment of TOP3B to Chromatin to Prevent R Loop Accumulation. *Molecular Cell*, 53(3):484–497.

Ye, N., Qin, J., Shi, W., Liu, X., and Lin, B. (2007). Cell-based high content screening using an integrated microfluidic device. *Lab on a Chip*, 7(12):1696–1704.

Yokota, M., Hatakeyama, H., Okabe, S., Ono, Y., and Goto, Y. I. (2015). Mitochondrial respiratory dysfunction caused by a heteroplasmic mitochondrial DNA mutation blocks cellular reprogramming. *Human Molecular Genetics*, 24(16):4698–4709.

Yokota, M., Hatakeyama, H., Ono, Y., Kanazawa, M., and Goto, Y. I. (2017). Mitochondrial respiratory dysfunction disturbs neuronal and cardiac lineage commitment of human iPSCs. *Cell Death and Disease*, 8(1):e2551–11.

Yoshida, T., Kakizuka, A., and Imamura, H. (2016). BTeam, a Novel BRET-based Biosensor for the Accurate Quantification of ATP Concentration within Living Cells. *Scientific Reports*, 6(December):1–9.

Yoshihara, T., Hirakawa, Y., Hosaka, M., Nangaku, M., and Tobita, S. (2017). Oxygen imaging of living cells and tissues using luminescent molecular probes. *Journal of Photochemistry and Photobiology C: Photochemistry Reviews*, 30:71–95.

Yun J, F. T., Yun, J., and Finkel, T. (2014). Mitohormesis. *Cell Metabolism*, 19(5):757–766.

Zanella, F., Lorens, J. B., and Link, W. (2010). High content screening: Seeing is believing. *Trends in Biotechnology*, 28(5):237–245.

Zanna, C., Ghelli, A., Porcelli, A. M., Karbowski, M., Youle, R. J., Schimpf, S., Wissinger, B., Pinti, M., Cossarizza, A., Vidoni, S., Valentino, M. L., Rugolo, M., and Carelli, V. (2008). OPA1 mutations associated with dominant optic atrophy impair oxidative phosphorylation and mitochondrial fusion. *Brain*, 131(2):352–367.

Zhang, X. and Gao, F. (2015). Imaging mitochondrial reactive oxygen species with fluorescent probes: Current applications and challenges. *Free Radical Research*, 49(4):374–382.

Zheng, W., Thorne, N., and McKew, J. C. (2013). Phenotypic screens as a renewed approach for drug discovery. *Drug Discovery Today*, 18(21-22):1067–1073.

Zhong, Q., Busetto, A. G., Fededa, J. P., Buhmann, J. M., and Gerlich, D. W. (2012). Unsupervised modeling of cell morphology dynamics for time-lapse microscopy. *Nature Methods*, 9(7):711–713.

Zhu, Y., Zhao, K.-k., Tong, Y., Zhou, Y.-l., Wang, Y.-x., Zhao, P.-q., and Wang, Z.-y. (2016). Exogenous NAD+ decreases oxidative stress and protects H2O2-treated RPE cells against necrotic death through the up-regulation of autophagy. *Scientific Reports*, 6:26322.

Zick, M., Rabl, R., and Reichert, A. S. (2009). Cristae formation-linking ultrastructure and function of mitochondria. *Biochimica et Biophysica Acta - Molecular Cell Research*, 1793(1):5–19.

Zielonka, J. and Kalyanaraman, B. (2010). Hydroethidine- and MitoSOX-derived red fluorescence is not a reliable indicator of intracellular superoxide formation: Another inconvenient truth. *Free Radical Biology and Medicine*, 48(8):983–1001.

Zorova, L. D., Popkov, V. A., Plotnikov, E. Y., Silachev, D. N., Pevzner, I. B., Jankauskas, S. S., Babenko, V. A., Zorov, S. D., Balakireva, A. V., Juhaszova, M., Sollott, S. J., and Zorov, D. B. (2018). Mitochondrial membrane potential. *Analytical Biochemistry*, 552:50–59.

Nederlandse samenvatting

Het belangrijkste doel van dit promotieonderzoek was het karakteriseren van de consequenties voor de cel van het disfunctioneren van mitochondriën. Dit is gedaan op fenotypische niveau voor *Target Discovery* en het testen van geneesmiddelen. Om dit te doen heb ik mij gericht op het ontwikkelen van nieuwe geautomatiseerde l*ive-cell imaging* technieken en de optimalisatie van cel-gebaseerde assays. Deze technieken zijn toegepast op de *Primary Human Skin Fibroblasts* (PHSF) afgenomen van zowel gezonde donoren als van patiënten met het Syndroom van Leigh (SvL). SvL is een ernstige neurologische afwijking die zich meestal openbaart in het eerste levensjaar door het versneld verliezen van mentale en motorieke capaciteiten. De patiënt overlijdt typisch binnen twee tot drie jaar, meestal door het falen van het ademhalingssysteem (Gerards et al., 2016). De bij de SvL patiënten afgenomen PHSF's, die in deze studie gebruikt zijn, vertonen de meest voorkomende mitochondriale oxidatieve phosphorylyse (OXPHOS) enzym afwijking, namelijk het tekort aan het geïsoleerde complex I (Fassone and Rahman, 2012; Ma et al., 2013).

Hoofdstuk 1 introduceert de structuur, de functie en het disfunctioneren van mitochondriën van moleculair tot klinische niveau, inclusief de strategie om drugs te ontwikkelen. Het belang van mitochondriën op de gezondheid van de mens wordt benadrukt. Het concept van de mitochondriale morphofunctie wordt ook behandeld. Dit concept benadrukt de belangrijke interactie tussen vorm en functioneren. De morphofunctie is een essentiële indicator van de mitochondriale en algemene gezondheidstoestand van de cel, en wordt in elk hoofdstuk van dit proefschrift gemeten of bediscussieerd. Het hoofdstuk gaat verder met de beschrijving van de ernstige klinische aspecten van mitochondriale ziektes, specifiek het tekort aan CI en SvL zijn ziektebeelden waarvoor geen goede behandeling bestaat. De introductie wordt afgesloten met een overzicht van het proces van het ontwikkelen van geneesmiddelen met een focus op *in vitro* pre-klinisch werk. Cell-based fenotypisch screening wordt gepresenteerd als de belangrijkste methodologische aanpak die door farmaceutische bedrijven wordt gebruikt voor *Target Discovery* en het testen van drugs.

Er bestaat een groot aantal technologieën voor het evalueren van de bijdrage van mitochondriën aan ziektes en voor het uitvoeren van preklinisch *in vitro* geneesmiddelen ontwikkeling. Sommige van deze technieken zijn commercieel beschikbaar, andere alleen nog in het laboratorium. In **Hoofdstuk 2** presenteer ik een kritisch overzicht van de literatuur over het gebruik van *live-cell*, hoge resolutie microscopie dat gebruikt wordt voor het karakteriseren van het disfunctioneren van mitochondriën door middel van fenotypische profilering gebaseerd op beelden. Gedetailleerde richtlijnen voor *live-cell imaging* technieken worden hier gepresenteerd om de ontwikkelde technieken in de experimentele hoofdstukken van dit proefschrift te introduceren. Vanuit dit perspectief bediscussieer ik een selectie van *live-cell* fluorescentie reporters, de gebruikte imaging strategie en modellen van de menselijk cel met hun voor- en nadelen. We presenteren ook een overzicht van *live-cell* toepassing van microscopie die gebruikt worden voor het detecteren van cellulaire fenotypes gekoppeld aan ziektes en voor het uitvoeren van cel gebaseerde screening van geneesmiddelen.

Hoofdstuk 3 richt zich op hoe mitochondriaal morphofunction kan worden bestudeerd en gecombineerd met high-content en high-troughput strategieën. Het hoofdstuk behandelt verschillende toepassingen hiervan, die worden gebruikt om genetische en door geneesmiddelen veroorzaakte effecten op het niveau van individuele organellen, cellen en cel populaties te analyseren. In **Hoofdstuk 4** presenteren wij een nieuw protocol dat ontwikkeld is om gemultiplexde *high-content* analyses van mitochondriale morphofunctie uit te voeren. Dit maakt het mogelijk om de mitochondriale morphofunctie en de cellulaire en nucleaire parameters in de PHSF's onbevooroordeeld en geautomatiseerd te kwantificeren. Cellen werden gekweekt op 96-*well* kweekplaten en verkleurd met drie fluorescentie kleurenstoffen die gericht zijn op mitochondriën, cytosol en kernen. Beelden van multi-spectrale fluorescentie zijn verkregen met geautomatiseerde microscopie waaruit de waarde van 44 descriptoren geëxtraheerd zijn. Deze data werd vervolgens onderworpen aan univariate, bivariate en multivariate analyse. Hoewel dit protocol specifiek voor PHSF's ontwikkeld is kan het ook worden toegepast op andere cel types. In **Hoofdstuk 5** wordt dit pro-

tocol toepast op het HT22 neuronaal cel model. Mitochondriale morphofunctionele analyse werd gebruikt om de flexibiliteit van het cellulaire metabolisme te analyseren met lage-geleiding Ca^{2+}-geactiveerde K^+ kanalen om vervolgens de fenotypische consequenties te onderzoeken. HT22 werd behandeld met de chemische verbinding CyPPA om farmacologische SK-activering te induceren. Bij aanwezigheid van glucose in het cultuur medium produceren veel *in vitro* gekweekte cel modellen bijna alle ATP via glycolyse in plaats van met het mitochondriale OXPHOS systeem (Crabtree, 1929). Daarom is het een algemeen gebruikte experimentele opzet om glucose te vervangen door galactose in het cultuur medium om pathologische mitochondriale fenotypes te induceren of te versterken (Robinson et al., 1992; Rossignol et al., 2004). Deze strategie forceert dat de ATP productie afhangt van het mitochondriale metabolisme, dat glycolyse opregulering wordt voorkomen en dat metabolische flexibiliteit wordt beperkt (Rossignol et al., 2004). Om de cellulaire compensatie mechanismes van de inhibitie van glycolytische opregulering te beperken, hebben wij in Hoofdstuk 5 de mitochondriale morphofunctionele analyse van de met CyPPA behandelde HT22 cellen uitgevoerd in galactose- en glucose gebaseerde media.

In **Hoofdstuk 6** gebruiken wij ook de op galactose gebaseerde medium strategie waarmee een metabolische stress wordt opgewerkt die de afwijkingen van het PSHF CI tekort verstrekt. Wij hebben een cellulaire en mitochondriale fenotype karakterisering uitgevoerd van de cellen met een mitochondriale ziekte die in een galactose gebaseerd medium groeien en die vergeleken met cellen die in een glucose gebaseerd medium groeien. We onderzochten de levensvatbaarheid van de cel, de mitochondriale morfofunctie, de reactieve zuurstof species en de ATP-homeostase. Een paneel van 6 cellijnen werd gebruikt, drie afgeleid van gezonde donoren en drie van patiënten met LS die mutaties vertonen in de CI genen (NDUFS7, NDUFS8, NDUFV1) gecodeerd in het nucleaire DNA (n-DNA). Na een optimalisaties van het celcultuur protocol en van de samenstelling van het op glucose gebaseerde medium, stierven de LS fibroplasten in het galactose medium terwijl de control cellen bleven leven. De sterfte onder LS-cellen werd afhankelijk van de dosering geremd door pyruvaat,

malaat, oxaloacetaat, α-ketoglutaraat, aspartaat en exogeen NAD^+ (eNAD), maar niet door lactaat, succinaat, α-ketobutyraat en uridine. Pyruvaat en eNAD verhoogde het gehalte van cellulair NAD^+ in de met galactose behandelde LS-cellen in verschillende mate. Co-incubatie studies lieten zien dat de door pyruvaat geinduceerde redding niet primair door NAD^+ wordt gemedieerd. De vervanging van glucose door galactose in de LS-cellen verhoogde de mitochondriale fragmentatie en massa, depolariseerde de mitochondriale membraan potentiaal ($\Delta\psi$, verhoogde het H2DCFDA-oxiderende ROS-niveau, verhoogde de vorming van de mitochondriale ATP en verminderde het totale cellulaire ATP-gehalte. Deze afwijkingen werden op een verschillende manier gered door pyruvate en eNAD wat de conclusie ondersteunt dat deze verbindingen via verschillende mechanismes de sterfte van LS-cellen veroorzaakt door galactose beperken. Deze bevindingen leggen een nieuwe cel-gebaseerde strategie vast voor het testen van interventies en versterken ons begrip van de pathofysiologie van het tekort aan CI.

Hoofdstuk 7 presenteert net als hoofdstuk 6 een fenotypische en moleculaire karakterisering van door CI-tekort geïnduceerde afwijkingen in PSHF's, onder een conditie van stress. In deze studie wordt een redox stress opgelegd door de cellen te behandelen met L-buthionine-(S,R)-sulfoximine (BSO) wat de concentratie van de belangrijkste cellulaire oxidant, glutathion (GSH), vermindert. Net als in hoofdstuk 6 werden zes cellijnen gebruikt, drie van gezonde donoren en drie van patiënten met LS met mutaties in de CI genen ((NDUFS7, NDUFS2, NDUFV1). De NDUFS7 cellijn was dezelfde als in hoofdstuk 6, echter de ander twee wijken af: de NDUFS2 was een andere cellijn met een mutatie in een ander gen van het CI, NDUFV1 heeft een andere mutatie op hetzelfde gen van het CI. We hebben eerder laten zien dat de GSH syntheseinhibitor BSO het cellulaire GSH gehalte in dezelfde mate verminderd in PSHF's van LS patiënten als in gezonde controle donoren. Het was interessant dat de BSO behandeling de levensvatbaarheid van cellen van LS patiënten sterk reduceert (allemaal met een geïsoleerde mitochondriale CI tekort), terwijl CT cellen levensvatbaar bleven. De oorzaak voor dit verschil in invloed is nog niet bekend. In dit laatste hoofdstuk voerden wij ook een fenotypische

en moleculaire profilering uit van LS- en CT cellen om het effect van BSO te bestuderen voordat de celsterfte werd geïnduceerd. De incubatie gedurende 24 uur van PSHF's met een niet-giftige BSO-concentratie (1 μM) verminderde de mitochondriale en cytosolische GSH-niveaus in LS en CT cellen op dezelfde wijze. Geen afwijkingen in de mitochondriale morfofunctie, het cellulaire ATP gehalte of de cellulaire lipide peroxidatie toestand werd geobserveerd tot 2 uur voordat de cel sterfte werd geinduceerd. Als de lipide peroxidatie toestand echter op een latere tijdstip (12 of 18 uur) werd gemeten werd een uitbarsting waargenomen tegelijkertijd met een vermindering van de levensvatbaarheid van de cel die geidentificieerd kan worden als een LS-specifiek pathologisch fenotype. We hebben eerder gedemonstreerd dat KH176m, het metaboliet van een nieuwe geneesmiddel KH176 dat in de klinisch fase is, de BSO-geinduceerde celsterfte volledig stopt. Hier geven wij voorlopige bewijs dat deze celsterfte wordt vergezeld door een verhoogde lipide peroxidatie, wat KH176m kan voorkomen. De effectiviteit van KH176m werd ook vergeleken met Ferrosttin-1, de eerste geindentificieerde inhibitor van ferroptose, een celsterfte die ook afhankelijk is van lipide peroxidatie. Deze verkennende studie benadrukt de causale rol van lipide peroxidatie op de door BSO veroorzaakte sterfte van cellen van LS patienten en verstrekt ons begrip van het werkingsmechanisme van KH176m.

Acknowledgements

It took me a while... but I finally got there!

I would like to open this acknowledgement in an unusual way, acknowledging myself. Because I made it! A PhD journey is not a walk in the park, it was tough. Unfortunately "biology in the lab takes too long and it fails too often" because most of the time "things turned out as they were bound to do and not as I expected", but also because jumping in the ocean when you cannot swim can be scary and if you get too nervous you can even drown.

I made it and I considered this an exceptional once in a lifetime training both from a professional and personal point of view.

Therefore, I am incredibly grateful for this great opportunity it was offered to me in the far 2013 by Khondrion's executive team with my promotor Prof. dr. Jan Smeitink, my co-promotors Dr. Julien Beyrath and Dr. Werner Koopman. You taught me a lot guiding me during this exciting scientific endeavour. You made a scientist of me.

Thanks to Sarhita, you were my colleague and pillar at Khondrion, we started together this long journey sitting side by side, we went through a lot, work and not related and we came out stronger and much closer. You are my Paranymph, you are my French sister.

Thanks to all the Khondrion's team Peter, Mina, Lisanne, Svetlana, Lionel, Herma, Sjenet, Xiaolan, Xin and Iris. We spent a lot of good time together and this thesis is here also because of all your input and support. Thanks also to my two students Matthijs and Chesco, I was very lucky with you. You did a great job which significantly contributed to the experimental work of this thesis.

Thanks to Giuseppe Gasparre, to Ivi and all the genetica medica lab in Bologna. My scientific and mitochondrial journey started back there during my bachelor internship and without your great guidance and training I would have never got so far.

Thanks to the awesome Marie Curie ITN European project Mitochondrial European Educational Training (MEET). This was the bridge which connected

me to Nijmegen and gave me an extraordinary opportunity during three amazing years. Thanks to Sarah (again), Renaud, Serena, Michele, Mika, Mara, Manar and Silvia, it was a lot of fun meeting up all of you around Europe for conferences and trainings.

Thanks to Renaud (again), you were my MEET Buddy, you are my Paranymph, you are my French brother.

Thanks to lo Zio Giuseppe, Timmeche, Ndonell and Alessia, you were great (literally or not) flat mates, you were my life after work in Nijmegen. You were my family.

Thanks Jurre & Ila for being that other part of my Nijmegen family, we met up right back at the beginning of all in 2013, but we got together again only later when I most needed you.

Thanks to my Respora buddies, il Prosciutto Till and il Maestro Jurre (again). We woke up way before the sunrise and went to bed way after the sunset to make of a dream a reality, we fought long with determination and we smartly surrendered when we realized we gave our best.

Again, thanks Jurre (third time), you are my Paranymph and my Dutch brother.

Thank you Angela, Stefania, Antoine and Cindy, when I arrived in Nijmegen you were the "old guard", in one way or another it was a lot of fun with you all.

Thank you Federico, Simone, Giuliana, Riccardo you were the little Italy always ready to BBQ and party like real Erasmus.

Thank you Professor del mio cuore Diego, you showed me how to smile no matter what.

Thanks to the UNIVV football team and to Paolo, Sergio, Nicco, Paco and Brian because kicking a ball and/or drinking few beers to many it was just a lot of fun with you.

Grazie Robertina e Stefy perché l'asse Nijmegen – Bruxelles era solidissimo e spendere quei bei weekend insieme era una gran rifugio dalla nostre settimane lavorative, era un fantastico rifugio per le nostre menti, cuori...e per i nostri stomaci.

Thanks to my Dutch mum Geertje, you welcomed me in your beautiful family with kindness. And thank you Frank for the careful revisions of this thesis, for the Dutch summary and for your constant special and genuine interest in my research and in any other initiative I take. Thank you Jacchi, Ellen (the funny sister :-) I owe you a few crates of beers for the layman translation) and Lotte, Jessi and Fabian, opa & oma Aart & Anneke, Pim & Ria.

Grazie Papá.

Ci ha lasciato proprio nel mezzo di questo mio cammino di dottorato, ma avresti tanto voluto vedermi difendere questa tesi. Tu sei sempre stata la persona "più grande, paziente, e saggia, che mi capivi quando ero più giovane e mi davi saggi consigli per aiutarmi a farmi strada". Tu mi ha insegnato un grande senso di responsabilità, mi hai spiegato che se altri intorno a me riescono quando io affanno, non devo fare altro che guardare a me stesso e a come io posso migliorare senza criticare le situazioni o gli altri. Mi hai insegnato come come dare tutto il meglio di me per essere poi felice dei risultati per quelli che sono. Tu se la parte razionale, matematica, logica di me. Se sono riuscito a finire questa tesi è tanto merito della forte etica del dovere e della perseveranza che mi ha donato. Mi hai insegnato come usare un'agenda, a non bivaccare ma a sfruttare ed ottimizzare il tempo fin dalle scuole elementari. Grazie per questa bellissima lezione durata 30 anni che ha fatto di me l'uomo che sono oggi.

Grazie Mamma.

Mi hai insegnato come rispettare ed amare gli altri. Tu sei la parte emotiva, dolce e gentile di me. Mi hai insegnato come lavorare sodo giorno dopo giorno per gli altri, dando tutto me stesso senza risparmiarmi. Mi hai mostrato come amare il prossimo, tuo marito, i tuoi figli, un vicino o anche uno sconosciuto per strada. Grazie per la tua affettuosa natura, per suggerirmi che non devo essere io a risolvere tutti problemi del mondo, e per ricordarmi di essere sempre grato per tutto quello che ho.

Grazie alle mie sorelle Maria e Marta e ai miei fratelli Riccardo e Damiano. Come piccolino di casa ho imparato tanto da tutti voi che mi avete sempre portato dietro, io vi guardavo con rispetto ammirazione cercando di imitarvi.

Gli ultimi anni sono stati duri per noi ma ne siamo usciti tanto legati. In vario modo siete tutti bellissimi esempi di vita e dopo tutti questi anni continuo ad ammirarvi con tanto affetto.
Thanks to my Anna. Thank you, amore to be with me every day. Thank you amore for listening to my crazy excitement one evening and my anxious moaning the evening after. Thank you for being there every evening. And thank you for all the amazing support with this thesis, from questioning it scientifically to reviewing it textually and for all the crazy and beautiful work on the layout. This thesis is also partially yours. Ti amo da pazzi.

PHD PORTFOLIO

Name PhD candidate: **Eligio F. Iannetti**	**PhD period: 01-10-2013 – 01-10-2017**
Department: **Kindergeneeskunde (Khondrion)**	*Promotor(s):* **Prof Dr J.A.M., Smeitink**
Graduate School: **Radboud Institute for Molecular Life Sciences**	*Co-promotor(s):* **Dr W.J.H. Koopman, Dr. J. Beyrath**

	Year(s)	ECTS
TRAINING ACTIVITIES		
a) Courses & Workshops		
- MIC Course Imaging May 2014	2014	1
- Chemometrics school	2014	1
- Live imaging microscopy of mitochondria, UNIBO - Bologna (Italy)	2014	0.8
- XF EXTRACELLULAR flux analysis, Seahorse BV – Bologna (Italy)	2015	0.8
- Principles of Systems Biology	2015	0.8
- Cellular Imaging in Four Dimensions; principles and applications	2015	0.8
- Science MEET business, Valencia (Spain)	2015	1.75
- MEET course in SCIENCE COMMUNICATION, Rome (Italy)	2015	2
- Laser-captured microdissection, UNEW - New Castle (UK)	2016	0.5
- The MEET winterschool, Nijmegen	2016	0.5
- Entrepreneurship and innovation for PhD students, Nijmegen	2017	2
b) Seminars & lectures^		
- Mitochondria, metabolism and cell cycle control: An imaging perspective	2014	0.1
- Introduction to Machine Learning with a Focus on Clinical Data	2014	0.1
c) Symposia & congresses^		
- EUROMIT 2014, Tampere (Finland)	2014	1.75
- Poster presentation at EUROMIT 2014	2014	0.55
- Mitochondrial Medicine Course, Bologna (Italy)	2014	0.25
- Oral Presentation at the Mitochondrial Medicine Course	2014	0.5
- PhD retreat 2015, Veldhoven	2015	0.5
- Poster presentation at the PhD retreat 2015, Veldhoven	2015	0.5
- 11th MiP conference, Luční Bouda, (Czech Republic)	2015	0.25
- Oral presentation at the 11th MiP conference	2015	0.5
- The MEET mini-congress on mitochondrial medicine, Nijmegen	2016	0.25
- Oral presentation at the MEET mini-congress on mitochondrial medicine	2016	0.5
- The MEET Symposium, Nijmegen	2016	0.25
- Mitochondrial Medicine conference, Cambridge (UK)	2016	0.75
- Poster presentation Mitochondrial Medicine conference, Cambridge (UK)	2016	0.5
- EBEC - European Bionergetic, 2016, Riva del Garda (Italy)	2016	1.5
- Poster presentation at the EBEC	2016	0.5
- PhD retreat 2016, Veldhoven	2016	0.5
- Poster presentation at the PhD retreat 2016, Veldhoven	2016	0.5
- PhD retreat 2017, Veldhoven	2017	0.5
- Oral presentation at the PhD retreat 2017, Veldhoven	2017	0.5
- SysmedPD consortium 1st year Progress Meeting, Leiden	2017	0.5
- Oral presentation at SysmedPD consortium 1st year Progress Meeting	2017	0.5
- SysmedPD consortium 2nd year Progress Meeting, Lubeck	2017	0.5
- Oral presentation at SysmedPD consortium 2nd year Progress Meeting	2017	0.5
d) Other		
- Research Secondment at CNIC, Madrid Spain	2015	2
- Organizing the MEET Winterschool & mini-congress	2015-2016	1
- Organizing the MEET Symposium	2015-2016	2
TEACHING ACTIVITIES		
e) Lecturing		
f) Supervision of internships / other		
- Master of Science Student internship coaching	2016	2
- Bachelor of Science Student internship coaching	2017	2
TOTAL		**34.2**

List of publications

1. Krabbendam, I. E., Honrath, B., Dilberger, B., **Iannetti, E. F**., Branicky R. S., Meyer T., Evers, B., Dekker F. J., Koopman W. J. H., Beyrath, J., Bano, D., Schmidt, M., Bakker, B. M., Hekimi, S., Culmsee, C., Eckert, G.P., Dolga A. M. SK channel-mediated metabolic escape to glycolysis inhibits 1 ferroptosis and supports stress resistance in C. elegans. *Under revision at Cell Death & Disease.*

2. **Iannetti, E. F.**, Prigione, A., Smeitink, J. A. M., Koopman, W. J. H., Beyrath, J., and Renkema, H. (2019). Live-Imaging Readouts and Cell Models for Phenotypic Profiling of Mitochondrial Function. *Frontiers in Genetics. 10*, 1–9.

3. **Iannetti, E. F.**, Smeitink, J. A. M., Willems, P. H. G. M., Beyrath, J., and Koopman, W. J. H. (2018). Rescue from galactose-induced death of Leigh Syndrome patient cells by pyruvate and NAD+. *Cell Death & Disease. 9,* 1135.

4. **Iannetti, E. F.**, Smeitink, J. A. M., Beyrath, J., Willems, P. H. G. M., and Koopman, W. J. H. (2016). Multiplexed high-content analysis of mitochondrial morphofunction using live-cell microscopy. *Nature Protocols. 11*, 1693.

5. **Iannetti, E. F.**, Willems, P. H. G. M., Pellegrini, M., Beyrath, J., Smeitink, J. A. M., Blanchet, L., Koopman, W. J. H. (2015). Toward high-content screening of mitochondrial morphology and membrane potential in living cells. *The International Journal of Biochemistry & Cell Biology. 63*, 66–70.

Curriculum Vitae

Eligio F. Iannetti was born on March 23rd, 1987 in Teramo (Italy) where he also grew up.

He obtained a bachelor's degree in biological sciences in 2010 from Università di Bologna (Italy) with an experimental thesis on mitochondrial molecular genetics. He obtained a master's degree in Molecular and Cellular Biology in 2013 also from Università di Bologna (Italy) with an experimental thesis on mitochondrial genetics, molecular biology and virology with applications to cancer research.

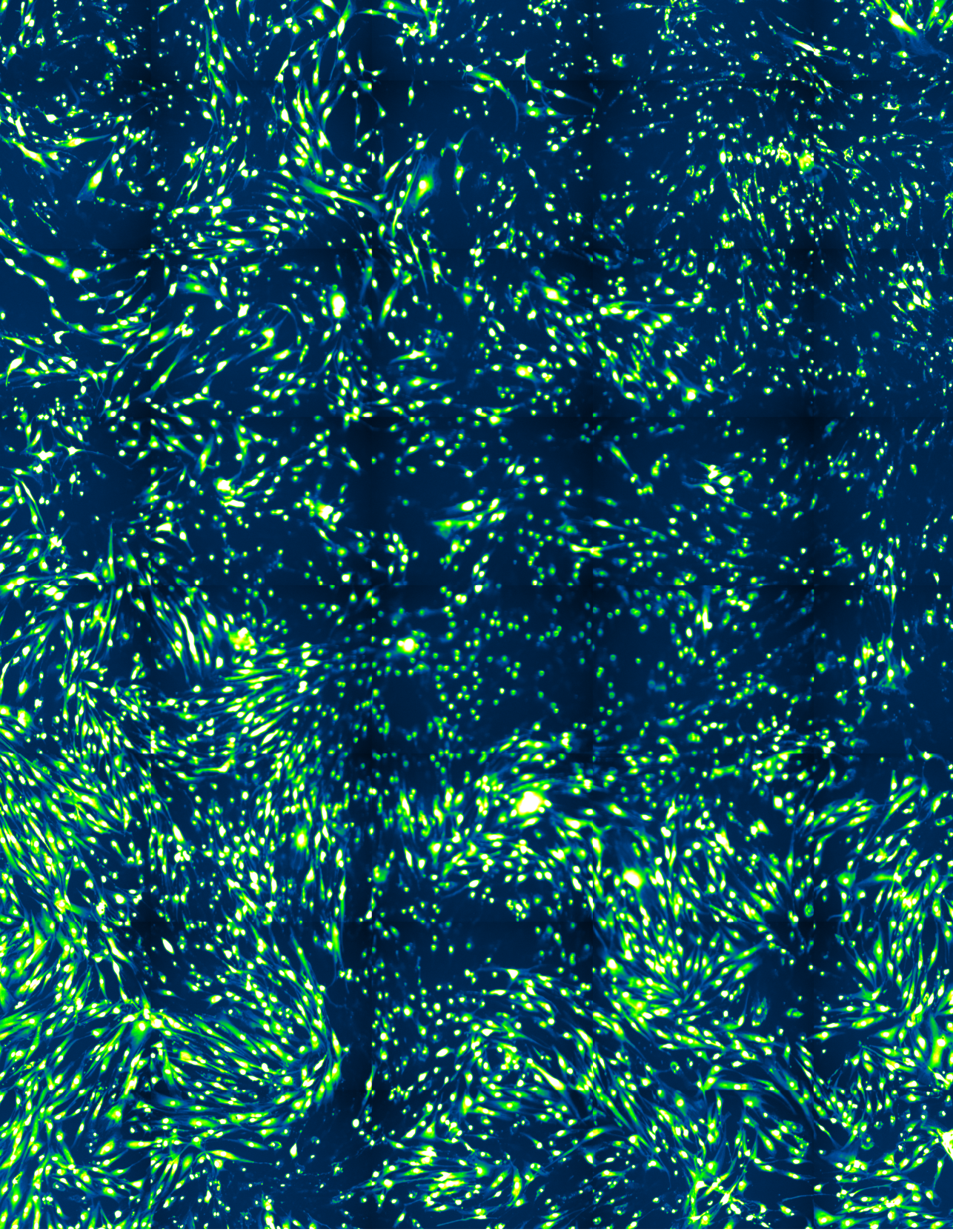
After a short research internship in Birmingham University (UK) studying cancer genetics, Eligio was selected as Early Stage Researcher in the Marie Curie International Training Network Mitochondrial European Educational Training project. Therefore, in October 2013 he moved to Nijmegen (The Netherlands) to start a PhD project focusing on cell-phenotypic profiling of mitochondrial dysfunction for target discovery and drug testing. The PhD research was performed at Khondrion in collaboration with the Department of Biochemistry of the Radboud University Medical Center (Radboudumc) under the supervision of Dr. Julien Beyrath, Dr. Werner Koopman and Prof. Jan Smeitink. Khondrion, founded as a spinoff of the Radboudumc, is now a clinical-stage pharmaceutical company discovering and developing therapies targeting mitochondrial disease. Eligio's PhD thesis was part of Khondrion's drug development strategy. The results provided new methodological approaches to study mitochondrial dysfunction of in vitro cell models and new insight to better understand the pathology and design therapeutic strategies.

During his PhD time at the Radboud University research community ($\geq$ 5.000 researchers), Eligio realized that intellectual and technological resource sharing was not optimal and that research laboratories could have been better connected. Therefore, he founded Respora, a startup selling IT services to academic communities to support researchers' communication, resource and knowledge sharing, productivity and creativity.

At the end of 2018, Eligio left the Netherlands to look for new career oppor-

tunties at the intersection between entrepreneurship, science and technology. After a short period collaborating with a Cambridge (UK) based early stage deep science startup accelerator, Panacea Stars, he joined a London based startup, Experoment. The mission was to automate and standardize experimental biology to increase reproducibility and eliminate human errors by a centralized robotic cloud research laboratory.

While exploring the European scientific startup ecosystem, Eligio got in contact with Valitacell, a biotech company based in Dublin (Ireland) motivated to accelerate the manufacture of life-saving medicines like biologics and cell therapy by enhancing the bioprocess monitoring and optimization. From September 2019, Eligio works at Valitacell as an Innovation Associate, combining his passion for technology, live cell imaging and assay development together with a business oriented and customer facing role.



Institute for Molecular Life Sciences

Radboudumc